UNIVERSITÉ DE STRASBOURG

EDSC
Ecole Doctorale des
Sciences Chimiques

ÉCOLE DOCTORALE DES SCIENCES CHIMIQUES

Laboratoire d'Electrochimie et de Chimie Physique du Corps Solide

THÈSE présentée par :

YANG Shu

soutenue le : 10, NOVEMBRE 2017

pour obtenir le grade de : **Docteur de l'université de Strasbourg**

Discipline/ Spécialité : Chimie

Réduction électrocatalytique des NO_x sur des nanoparticules métalliques stabilisées par des polyoxométallates

THÈSE dirigée par :

Pr. RUHLMANN Laurent, Université de Strasbourg
Dr. BONNEFONT Antoine, Université de Strasbourg

RAPPORTEURS :

Pr. PROUST Anna, Université Pierre et Marie Curie-Paris 6
Pr. COLBEAU-JUSTIN Christophe, Université Paris-Sud

AUTRES MEMBRES DU JURY :

Pr. SAVINOVA Elena, Université de Strasbourg
Pr. MIALANE Pierre, Université de Versailles Saint-Quentin en Yvelines

Acknowledgements

Firstly, I have to show my gratitude to the jury members for grading my thesis:

Prof. Laurent Ruhlmann, Université de Strasbourg
Dr. Antoine Bonnefont, Université de Strasbourg
Prof. Anna Proust, Université Pierre et Marie Curie-Paris 6
Prof. Christophe Colbeau-Justin, Université Paris-Sud
Prof. Elena Savinova, Université de Strasbourg
Prof. Pierre Mialane, Université de Versailles Saint-Quentin en Yvelines

This study is conducted at Laboratoire d'Electrochimie et de Chimie Physique du Corps Solide under the direction of Prof. Laurent Ruhlmann and Dr. Antoine Bonnefont.

I have to thank Prof. Laurent Ruhlmann for giving me the opportunity to work in the group. Prof. Ruhlmann with his passion and expertise had been supporting and inspiring me strongly through the entire period of this thesis. Prof. Ruhlmann has been an example not only with respect to expertise but also the attitude towards scientific research.

Besides Prof. Ruhlmann, I need to show my appreciation to Dr. Antoine Bonnefont who has been supporting me all the time. Dr. Antoine Bonnefont with his patience, rigorousness and great availability has been with me together to face the challenges and overcome the obstacles in the study, notably at the time when writing this manuscript.

Moreover, I would like to show my appreciation to the working conditions and the possibilities of academic conferences worldwide. Apart from that I have to give credit to all the group members at Laboratoire d'Electrochimie et de Chimie Physique du Corps Solide for contributing to my study, particularly DR. Jean-Paul Gisselbrecht for sharing his experiences in scientific work, programming and analysis of experiment results and Prof. Corinne Boudon for all the helpful discussions and advices during all these years.

I would like to express my gratitude to the partners of the scientific collaboration that have enriched the outcome of my thesis. In this context I would like to address:

- Prof. Pierre Mialane and DR. Anne Dolbecq (Institut Lavoisier, Université de Versailles Saint-Quentin en Yvelines), who helped us to synthesize the samples Cu-substituted POMs and metal-organic framework (MOFs) compounds.
- Dr. Rana Farha and Prof. Michel Goldmann (Université Pierre et Marie Curie-Paris 6) for AFM measurement.
- Eric Rivière (Institut de Chimie Moléculaire et des Matériaux d'Orsay, University of Paris-sud) for magnetic measurement.

I am especially grateful to Dr. Huo Zhaohui, Dr. Zang Dejin for their great helps and advices in scientific research. I'd like to thank all the interns who had worked with me.

I would like to thank my family and my friends, for all the support, good company given, understanding and love. Without their supports, this work would be more difficult and perhaps even impossible to reach.

Last, I would like to express my great gratitude to the Labex Chemistry of Complex Systems of the University of Strasbourg for the financial supporting.

List of publications

1. Oms, O., **Yang, S.**, Salomon, W., Marrot, J., Dolbecq, A., Rivière, R., Bonnefont, A., Ruhlmann, L. & Mialane, P. Heteroanionic materials based on copper clusters, bisphosphonates and polyoxometalates: magnetic properties and comparative electrocatalytic NO_x reduction studies. *Inorg. Chem.* **55**, 1551-1561 (2016).

2. Huo, Z.H., Zang, D.J., **Yang, S.**, Farha, R., Goldmann, M., Hasenknopf, B., Xu, H.L. & Ruhlmann, L. Synthesis and characterization of Lindqvist-type polyoxometalate–porphyrin copolymers. *Electrochim. Acta,* **179**, 326-335 (2015).

3. Salomon, W., Lan, Y.L., Rivière, E., **Yang, S.**, Roch-Marchal, C., Dolbecq, A., Simonnet-Jégat, C., Steunou, N., Leclerc-Laronze, N., Ruhlmann, L., Mallah, T., Wernsdorfer, W. & Mialane, P. Single-molecule magnet behavior of individual polyoxometalate molecules incorporated within biopolymer or metal-organic framework matric. *Chem. Eur. J,* **22**, 6564 –6574 (2016).

4. Salomon, W., Roch-Marchal, C., Mialane, P., Rouschmeyer, P., Serre, C., Haouas, M., Taulelle, F., **Yang, S.**, Ruhlmann, L. & Dolbecq, A. Immobilization of polyoxometalates in the Zr-based metal organic framework UiO-67. *Chem. Commun,* **51**, 2972—2975 (2015).

List of presentations

1. **Yang, S.**, Oms, O., Mialane, P., Dolbecq, A., Bonnefont, A., Ruhlmann, L. ***Poster*** 'Cu-substituted heteropolyanions for the electrocatalytic reduction of NO_x'. Journées Scientifiques Institut de Chimie de Strasbourg UMR 7177, 29 - 30 Octobre 2015, Faculté de Chimie, Strasbourg, France.

2. **Yang, S.**, Ruhlmann, L., Bonnefont, A. ***Oral presentation*** 'Réduction électrocatalytique des NO_x sur des nanoparticules métalliques stabilisées par des polyoxométallates'. GECOM-CONCOORD 2016, 16-20 Mai 2016, Obernai, France.

3. **Yang, S.**, Ruhlmann, L., Bonnefont, A. ***Poster*** 'Electrocatalytic reduction of NO_x on polyoxometalate-stabilized nanoparticles'. 67th Annual Meeting of the International Society of Electrochemistry, 21 - 26 Août 2016, The Hague, the Netherlands.

4. **Yang, S.**, Bonnefont, A., Ruhlmann, L. ***Oral presentation*** 'Cu or Ag nanoparticles stabilized by polyoxometalates for the NO_x reduction'. Symposium 'Diverse Facets of Chemistry' Osaka University – Strasbourg University, 11-12 May 2017, ISIS, Strasbourg France.

RESUME

L'électrocatalyse des réactions impliquant de petites molécules (CO_2, H_2O, O_2, NO_3^-...) est au cœur de plusieurs problèmes énergétiques et environnementaux cruciaux pour l'avenir. Cependant, la conception d'électrocatalyseurs sélectifs, efficaces mais aussi économiques et respectueux de l'environnement pour ces réactions reste un défi majeur. L'électrochimie de ces molécules implique des processus de transfert multi-électroniques complexes avec la formation de différentes espèces et produits intermédiaires résultant en une lente cinétique de réaction. Pour de telles réactions, le développement de nouveaux catalyseurs hybrides tandem efficaces et sélectifs, impliquant différents types de sites actifs catalysant les transformations des intermédiaires de réaction, est nécessaire. Le but principal de cette thèse est d'explorer le potentiel des polyoxométallates (POMs) associés aux nanoparticules métalliques pour catalyser la réduction des nitrates et des nitrites. Pour ces matériaux hybrides, on s'attend à ce que les nanoparticules métalliques et les entités POMs fonctionnent en parallèle et synergie pour catalyser les différentes étapes de réduction des NO_X (nitrates, nitrite, etc…).

A travers le monde entier, l'expansion et l'intensification de l'agriculture ont conduit à une utilisation croissante des engrais, ce qui a dégradé la qualité de l'eau des rivières, des lacs et des eaux marines. Le nitrate est le contaminant chimique le plus courant dans les aquifères des eaux souterraines. Dans la nature, le nitrate et ses dérivés nitrites peuvent provoquer l'eutrophisation dans les rivières et empêcher l'élimination du phosphore dans le système de purification de l'eau.[1] Une quantité élevée d'ions nitrate (40 ppm) dans l'eau potable a été identifiée comme une cause de la méthémoglobinémie (syndrôme 'baby-blue'), qui est une maladie sanguine fatale chez les nourrissons de moins de six mois.[2] Le nitrate et le nitrite peuvent aussi provoquer certains cancers, comme par exemple le cancer colorectal et le cancer de la vessie, chez les animaux de laboratoire.[3] Pour ces raisons, le développement de nouveaux catalyseurs efficaces et sélectifs devient une mission urgente. Dans le corps humain, le nitrate peut être transformé en nitrite dans la salive par la microflore par voie orale. Par conséquent, ces deux composés sont souvent discutés conjointement.[4]

Un système catalytique prometteur doit être capable à transformer les ions nitrates en diazote gazeux, gaz inoffensif, de manière efficace et pas cher. Les processus biologiques et les processus physico-chimiques comme l'osmose inverse et l'échange d'ions sont les méthodes les plus largement appliquées pour éliminer les ions de nitrate de l'eau potable, certains

inconvénients évidents sont connus. Par exemple, le système de dénitrification biologique peut être contaminé par les bactéries mortes, tandis que les processus physicochimiques actuels ne peuvent pas réduire le nitrate pour former des composés inoffensifs, mais seulement les concentrer (saumure), ce qui nécessite un traitement ultérieur.[5] Dans ce sens, le processus électrocatalytique apparaît comme la technologie la plus prometteuse.[6]

Les difficultés principales de l'électroréduction des ions nitrates et / ou nitrites sont dues à : i) la cinétique de réaction lente qui engendre des surtensions et un courant à appliquer élevé ; ii) le grand nombre d'espèces et de produits intermédiaires possibles :

$\mathrm{NO_3^- + 4H_3O^+ + 3e^- \rightleftharpoons NO(g) + 6H_2O} \qquad \mathrm{E^0 = 0{,}958\ V/ENH}$

$\mathrm{2NO_3^- + 12H_3O^+ + 10e^- \rightleftharpoons} N_2\mathrm{(g) + 18H_2O} \qquad \mathrm{E^0 = 1{,}246\ V/ENH}$

$\mathrm{NO_3^- + 10H_3O^+ + 8e^- \rightleftharpoons NH_4^+ + 13H_2O} \qquad \mathrm{E^0 = 0{,}875\ V/ENH}$

$\mathrm{2NO_2^- + 6H_3O^+ + 4e^- \rightleftharpoons N_2O(g) + 9H_2O} \qquad \mathrm{E^0 = 1{,}396\ V/ENH}$

$\mathrm{NO_2^- + 6H_3O^+ + 4e^- \rightleftharpoons NH_3OH^+ + 7H_2O} \qquad \mathrm{E^0 = 0{,}673\ V/ENH}$

$\mathrm{NO_2^- + 8H_3O^+ + 6e^- \rightleftharpoons NH_4^+ + 10H_2O} \qquad \mathrm{E^0 = 0{,}897\ V/ENH}$

Par conséquent, l’électrocatalyse de la réduction des NOx avec une formation sélective de produit, tel que le diazote (N_2) pour la dépollution environnementale de l'eau, sans produire d'autres produits restant polluants et indésirables tels que l'ammoniaque, est un défi.

Dans la littérature, différent types de catalyseur ont déjà publiés. Dans les enzymes naturelles telles que la nitrate réductase, on peut catalyser la réduction du nitrate en nitrite, le complexe molybdopterine (molybdène-soufre) étant le site actif comme présenté en Figure 1.[7] D'autres catalyseurs moléculaires ont également été étudiés comme les complexe de Mo. Cependant, la plupart des études ont été menées avec des catalyseurs monométalliques et bimétalliques. Sur la base des études publiées, le Pt et le Pd massifs ont été très efficaces pour la réduction des nitrites tandis que le Pd est sélectif vis-à-vis de la formation de N_2.[8] Dans le cas de la réduction des nitrates, le Cu et l'Ag ont été considérés comme les catalyseurs monométalliques les plus efficaces.[9] L’étape cinétiquement déterminante sur ces deux électrodes métalliques est considérée comme étant la réduction des nitrates en nitrites :

$\mathrm{NO_3^- + 2H_3O^+ + 2e^- \rightleftharpoons NO_2^- + 3H_2O} \qquad \mathrm{E^0 = 0{,}835\ V/ENH}$

D'autres améliorations de l'efficacité catalytique nécessitent un niveau de complexité accrue dans la conception du catalyseur.

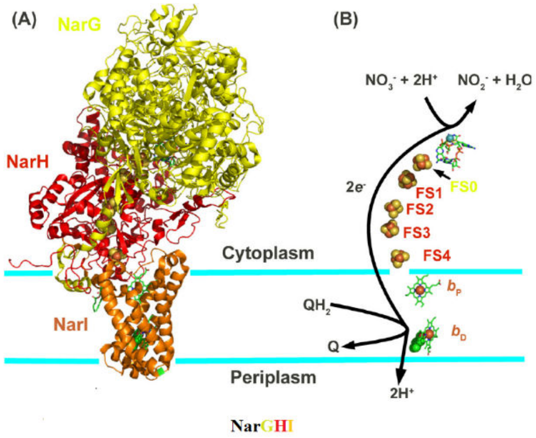

Figure 1 : Réductase de nitrate NarGHI en tant que le complexe molybdoenzyme de fer-soufre (CISM). A) Les trois sous-unités de NarGHI sont incorporées dans la membrane cytoplasmique avec les sous-unités NarGHI orientées vers le compartiment cytoplasmique. B) Le transport d'électrons de NarGHI pour la réduction des nitrates. (Réimprimé à partir de la référence 7 avec l'autorisation d'Elsevier).

Dans ce travail de thèse, le travail se concentrera sur le développement de nouveaux catalyseurs associant des polyoxométallates (POMs) et des nanoparticules (NPs). Les POMs sont des clusters inorganiques anioniques du type métal-oxygène constitués d'élément métalliques dans leur état d'oxydation le plus élevé, avec des propriétés électroniques, magnétiques et catalytiques remarquables. Diverses structures de POMs ont été étudiées, parmi lesquelles les types Lindqvist, Anderson, Keggin et Dawson (Figure 2) sont les plus connus. Ces composés sont très intéressants pour la catalyse ou la photocatalyse car il est possible d'ajuster leurs potentiels redox et leurs propriétés d'absorption du rayonnement UV suivant leurs structures, leurs charges, etc... En présence d'un donneur sacrificiel et sous illumination, les POMs peuvent être utilisés comme photocatalyseurs pour réduire des ions métalliques et former les nanoparticules métalliques correspondantes. Selon les études qui sont déjà publiées, les polyoxométallates (POMs) ont démontré la capacité de stabiliser les nanoparticules montrant qu'ils jouent à la fois le rôle de catalyseur et de surfactant.[10]

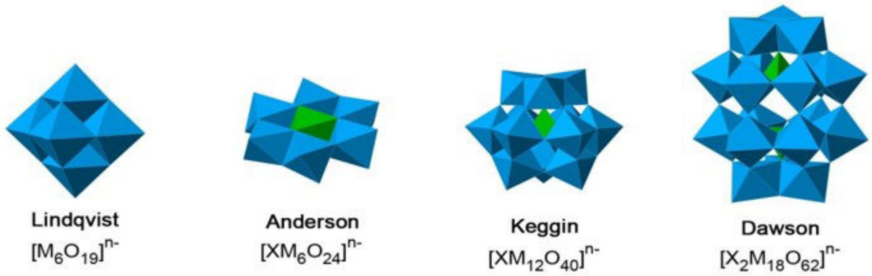

Figure 2 : Représentation de différentes structures de polyoxométallates (POMs).

La possibilité d'insérer des métaux de transition tout en conservant leurs structures rend les POMs intéressants pour de nombreux application en catalyse pour des réactions telles que l'oxydation des oléfines par $[Ru^{III}(H_2O)(SiW_{11}O_{39})]^{5-}$, la réduction de diméthylsulfoxyde (DMSO) par $[Ru^{III}(H_2O)(PW_{11}O_{39})]^{4-}$, la réduction de CO_2 par $(TOA)_6[\alpha\text{-}(\ )Co^{II}(SiW_{11}O_{39})]$, etc.[10]

En particulier, la réduction des ions nitrite peut être catalysée par divers POMs tels que $[SiW_{12}O_{40}]^{4-}$.[11] La catalyse est observée dès que l'on atteint le potentiels de réduction de POM. Celle-ci est également très dépendante du pH. Trois couples redox successifs en réduction sont observés pour $[SiW_{12}O_{40}]^{4-}$. Les deux premiers processus (pics I et II) sont indépendants du pH dans une plage de pH de 1 à 5 tandis que le troisième processus (pic III) est dépendant du pH (60 mV / pH). Le courant cathodique est proportionnel à la racine carrée de la vitesse de balayage pour l'ensemble des trois réductions, ce qui indique un processus contrôlé par la diffusion. À pH < 2, une augmentation significative du courant catalytique pour l'ensemble des trois pics cathodiques peut être observée après l'ajout de $NaNO_2$ dans la solution. L'activité sur le processus I est illustrée sur la Figure 3. Le meilleur courant catalytique est obtenu à pH 1, ensuite le courant catalytique diminue avec l'augmentation du pH. À pH > 3, aucune réponse catalytique n'est observée dans la gamme de + 0,1 V à - 0,6 V par rapport à Ag/AgCl, mais un courant catalytique est observé à la troisième vague de réduction (Figure 3).

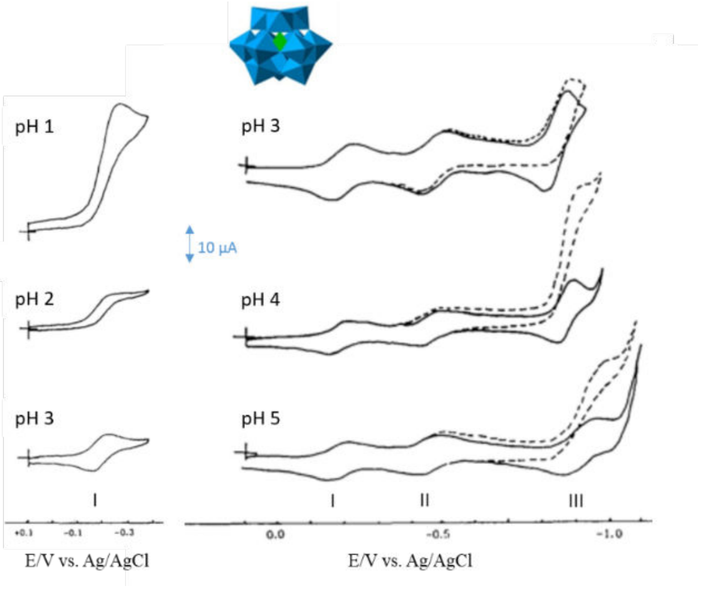

Figure 3 : CVs de 1 mmol·L^{-1} $[SiW_{12}O_{40}]^{4-}$ avec l'électrode en carbone vitreux dans des solutions de pH variable avec 2 mmol·L^{-1} $NaNO_2$, vitesse de balayage : 10 mV·s^{-1}. (Reproduit à partir de la référence 11 avec l'autorisation d'Elsevier).

Cependant, seuls des POMs substitués par des ions Cu^{II}, Ni^{II} et quelques POMs substitués par le Fe ont montré une activité pour la réduction des nitrates.

En 2001, Keita et ses collègues ont publié un POM de type Dawson $[Cu^{II}P_2W_{15}Mo_2]^{8-}$ qui était actif pour la réduction des nitrates à pH 3.[12] Un travail de comparaison entre $[Cu^{II}P_2W_{15}Mo_2]^{8-}$, $[P_2W_{15}Mo_2O_{61}]^{10-}$ et $[P_2W_{15}Mo_3O_{62}]^{6-}$ a également été mené. Il a été démontré que la présence d'ions Cu^{II} était indispensable pour catalyser la réduction des nitrates. Après cela, d'autres études ont été menées pour augmenter le nombre d'ions Cu^{II} dans la structure du POM conduisant à concevoir des POM tels que $[Cu^{II}_{20}Cl(OH)_{24}(H_2O)_{12}(P_8W_{48}O_{184})]^{25-}$ montrant que 'intensité du courant catalytique augmente avec le nombre d'atomes de Cu dans la structure.[13] Cependant, au stade actuel, l'étude de la réduction des ions nitrates a été menée uniquement en solution. En effet, en raison de la grande solubilité en solution aqueuse, les POMs ne sont pas de bons candidats pour être utilisés comme catalyseur hétérogène. Récemment, Imar et ses collègues ont immobilisé un polyoxométallate substitué par des ions Cu^{II} et des nanoparticule d'argent sur la surface de l'électrode en présence de polymères. Les films préparés ont montré une activité pour la réduction des nitrates.[14]

Dans la présente thèse, nous allons essayer de comprendre les facteurs d'influence sur l'efficacité de la catalyse de réduction des nitrates en utilisant différents POMs substitués avec des ions Cu^{II} puis comparer leurs activités catalytiques lorsque ces mêmes dérivés sont associés à des complexes d'alendronate de cuivre (CuAle). La réduction photocatalytique des ions d'argent en présence de POM a été largement étudiée dans notre groupe, la taille et la forme des nanoparticules d'argent peuvent être contrôlée en fonction des conditions de formation (concentration en POMs et Ag(I), température, concentration du donneur sacrificiel d'électron). Ainsi, les nanoparticules d'Ag@POM seront étudiées pour leur capacité à former un catalyseur hétérogène pour la réduction des nitrates et / ou des nitrites. Dans la dernière partie, les POMs seront immobilisés dans des matrices MOFs (**Metal-Organic Frameworks**) afin d'améliorer la stabilité des catalyseurs pendant la réaction catalytique. L'association de POMs aux MOFs permet aussi de réaliser un catalyseur hétérogène pour la réduction des NO_x. Nous allons étudier si les POMs conservent leurs propriétés électrochimiques et leurs propriétés électrocatalytiques après leur insertion dans les matrices MOFs.

I. Réduction de NO_x sur électrode de Cu ou d'Ag en présence ou en absence de polyoxométallates.

D'après les travaux publiés, les électrodes en Cu et en Ag sont des catalyseurs intéressants pour la réduction de nitrate. La quantité de catalyseur métallique peut être considérablement réduite en utilisant des nanoparticules au lieu des matériaux massifs. Cependant, les nanoparticules doivent être protégées par un agent de recouvrement afin d'empêcher leurs agglomérations, ce qui entraînerait une diminution de l'efficacité catalytique. A cet égard, les POMs sont des composés très prometteurs, car ils peuvent être utilisés à la fois comme des agents stabilisants (surfactants) pour stabiliser les nanoparticules métalliques et aussi comme des co-catalyseurs pour le processus en tandem puisque les POMs sont également actifs pour la réduction des nitrates et des nitrites. L'association des POMs avec des nanoparticules métalliques catalytiques peut conduire à améliorer les propriétés catalytiques et peut permettre d'ajuster la sélectivité de la réaction.

Dans ce travail, la réduction de nitrate et de nitrite est d'abord étudiée sur électrode de Cu ou électrode d'Ag, avec ou sans la présence de POM à pH 5 (1 mol·L^{-1} $CH_3COOLi + CH_3COOH$) et à pH 1 (0,5 mol·L^{-1} $Na_2SO_4 + H_2SO_4$), afin de comprendre le rôle de l'entité de POM dans la réduction électrocatalytique. Dans ce but, le polyanion du type Keggin $[SiW_{12}O_{40}]^{4-}$ est choisi pour sa capacité à catalyser la réduction des ions nitrites.[11]

La propriété électrochimique de $[SiW_{12}O_{40}]^{4-}$ a d'abord été étudiée sur électrode de Cu et électrode d'Ag à pH 1 et 5. Les résultats sont comparés avec ceux obtenus sur électrode de carbone vitreux (GC). Trois vagues de réduction sont observées sur électrode GC (Figure 4) à pH 1 et pH 5 qui sont attribuées à la réduction successives d'atomes W^{VI}. Les deux premiers processus (-0,25 V et -0,50 V *vs.* ECS) sont indépendante du pH alors que troisième processus mesuré à -0,72 V à pH 1 et à -0,95 V à pH 5 varie avec le pH de la solution (60 mV/pH). L'intensité de courant du premier pic de réduction est proportionnelle à la racine carrée de la vitesse de balayage, ce qui indique le courant est limité par la diffusion du POM à l'électrode. En revanche, seulement deux réductions successives sont observées sur électrode de Cu et électrode d'Ag du fait que les surfaces métalliques sont plus actives pour le dégagement de dihydrogène H_2 (Figure 4). A pH 1, $[SiW_{12}O_{40}]^{4-}$ se réduit à des potentiels légèrement positifs sur électrodes de Cu et d'Ag par rapport à l'électrode de carbone vitreux. A pH 5, $[SiW_{12}O_{40}]^{4-}$ se réduit plus difficilement sur électrode d'Ag avec un décalage plus négatif de 30 mV pour le processus I et de 50 mV. Ces modifications des potentiels redox reflètent une forte interaction entre les POMs et la surface métallique affectant ainsi les propriétés électrochimiques. L'intensité de courant est proportionnelle à la vitesse de balayage indiquant que le POM $[SiW_{12}O_{40}]^{4-}$ est bien adsorbé à la surface d'électrodes métalliques.

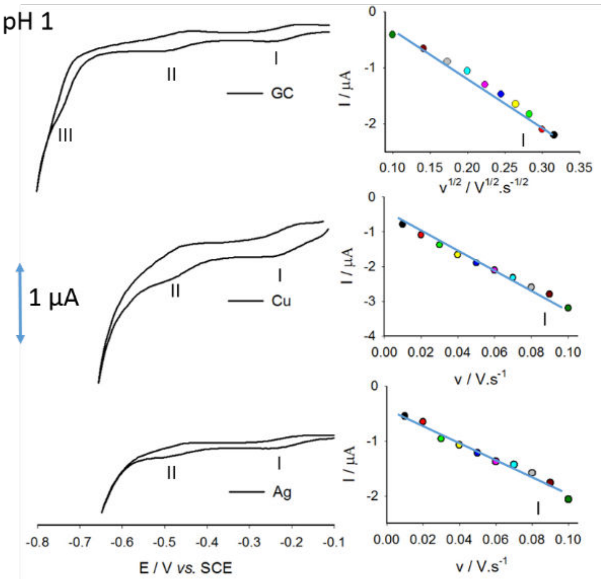

Figure 4 : CVs de $[SiW_{12}O_{40}]^{4-}$ *sur électrode de GC, de Cu ou d'Ag à pH 1 (0,5 mol·L*$^{-1}$ *Na*$_2$*SO*$_4$ *+ H*$_2$*SO*$_4$*), v = 2 mV·s*$^{-1}$*.*

Les propriétés électrocatalytiques de $[SiW_{12}O_{40}]^{4-}$ ont étudiées dans les mêmes milieux. Pour mieux comparer les propriétés catalytiques, le début de catalyse est défini au potentiel où la différence de courant $\triangle I = I_0 - I_{NOx}$ est égale à 0,5 µA, ce qui correspond à 7,15 µA/cm^2. I_0 est défini comme $I_{électrode}$ quand aucun POM n'est présent dans la solution. $I_{électrode+POM}$ correspond au courant mesuré lorsque le POM est ajouté dans la solution. Cette valeur 0,5 µA permet de comparer les performances catalytiques des différents systèmes, car il est assez faible pour déterminer le potentiel de départ auquel la réduction catalytique se produit sans influence significative du transport de masse. Le courant est dans le même temps, suffisamment élevée par rapport au courant de base.

Dans les deux solutions, l'électrode GC n'est pas active pour la réduction des nitrites. Après l'ajout de $[SiW_{12}O_{40}]^{4-}$, une augmentation de courant, qui devient catalytique, est observée au potentiel de la première réduction du couple $W^{VI/V}$ dans la solution à pH 1. A pH 5, cette augmentation est observée seulement à la troisième réduction de $W^{VI/V}$, en accord avec des travaux déjà publiés.[15] Dans la cas de l'emploi d'électrodes de Cu et d'Ag, l'électrode massive seule est déjà active pour la catalyse de la réduction des ions nitrites. Le potentiel de départ est mesuré à -0,26 V à pH 1 sur électrode Cu (Figure 5A). Le courant augmente dans toute la gamme de potentiel mesuré sur électrode Ag mais l'intensité du courant est trop faible pour définir le potentiel de départ pour le début de la catalyse.

Après l'addition de $[SiW_{12}O_{40}]^{4-}$, l'intensité de courant catalytique augmente de façon significative. Le départ de la catalyse de la réduction des nitrites est avancé aux potentiels similaires pour les deux électrodes de Cu et d'Ag (-0,18 V et -0,19 V). Une synergie entre le Cu et le POM est observée dans la plage de potentiel entre -0,40 V et -0,57 V *vs.* ECS à pH 1 (Figure 5B et 5C). Des observations similaires sont obtenues à pH 5.

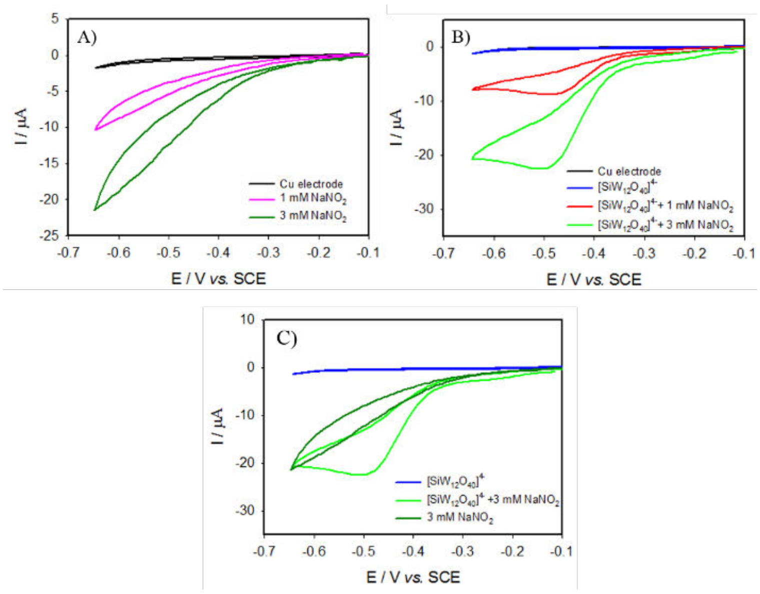

Figure 5 : Electroréduction de HNO_2 sur l'électrode de Cu en absence de $K^+{}_4[SiW_{12}O_{40}]^{4-}$ (A) ou en présence de 0.1 mmol·L^{-1} $K^+{}_4[SiW_{12}O_{40}]^{4-}$ (B). (C) comparaison de (A) et (B).

Dans le cas de la réduction des ions nitrates, l'électrode de carbone vitreux n'est pas active même en présence du POM. Sur électrode de Cu, les ions NO_3^- commencent à se réduire de manière électrocatalytique à -0,63 V *vs.* ECS à pH 1 alors que dans le cas d'Ag, le potentiel du départ de la catalyse est difficile à mesurer à pH 1. En présence de POM, l'activité catalytique du Cu pour la réduction des ions NO_3^- est exaltée au-delà de -0,52 V *vs.* ECS. De plus, le courant de réduction augmente avec la quantité de NO_3^- ajoutée. Des résultats similaires sont obtenues à pH 5.

Sur électrode d'Ag, l'activité catalytique pour la réduction des ions NO_3^- est moins importante que sur électrode de Cu. Cependant, après l'ajout de POM en solution, le courant catalytique devient plus important et le potentiel catalytique est mesuré à -0,57 V. Dans la solution à pH 5, seul une faible augmentation de courant catalytique est observée sur électrode d'Ag, mais en présence de POM, aucun changement n'est observé. Cela démontre que $[SiW_{12}O_{40}]^{4-}$ inhibe l'activité de l'Ag dans cette condition. La Figure 6 montre la réduction électrocatalytique des ions nitrates sur les trois types d'électrodes (GC, Cu et Ag) à pH 1 et à pH 5 en présence de POMs.

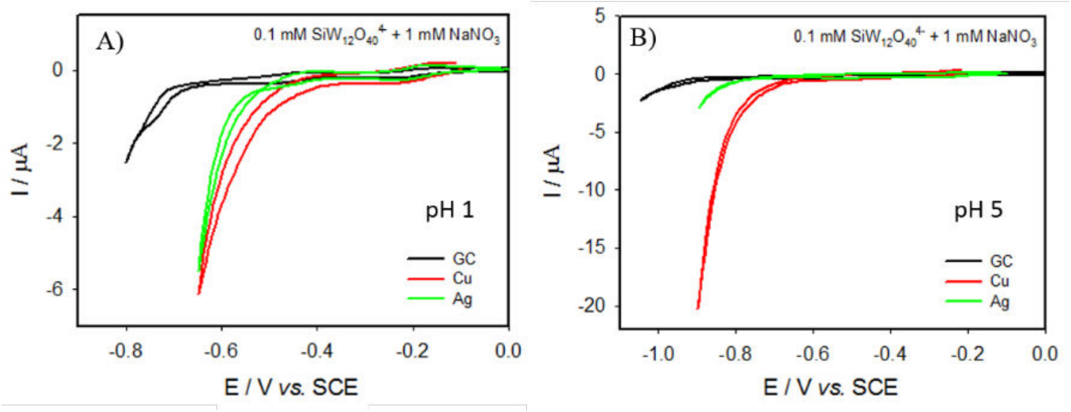

Figure 6 : Réduction de 1 mmol·L^{-1} $NaNO_3$ en présence de 0,1 mmol·L^{-1} $[SiW_{12}O_{40}]^{4-}$ sur les électrodes de GC, Cu ou Ag, v = 2 mV·s^{-1}.

Dans ces deux cas, la présence de POM conduit à une amélioration de l'activité catalytique des électrodes dans les conditions adaptées. Par la suite, on pourra également utiliser les POMs pour décorer les nanoparticules de Cu ou d'Ag en espérant une amélioration des performances catalytiques des matériaux obtenus.

II. Propriétés électrochimiques et électrocatalytiques du polyoxométallate/alendronate substitué au Cu

En sus de l'activité catalytique de l'électrode métallique massivede Cu, on a constaté que les POMs substitués avec des ions cuivriques Cu^{II} possèdent également une activité significative pour la réduction du nitrate. Ainsi, l'élaboration de POM à substitution métallique fonctionnalisés par des ligands exogènes peut permettre d'ajuster les propriétés de POM. Les POMs fonctionnalisé avec des ligands Alendronate (Ale = $[H_2O_3PC(C_3H_6NH_2(OH)PO_3H_2)]$) ont démontré une bonne stabilité en milieu aqueux en raison de la capacité de chélation des entités bisphosphonates.[16]

Dans ce chapitre, on a d'abord étudié trois polyoxométallates (CuPOM) contenant des atomes de Cu^{II} :

- $Na_{16}[Cu^{II}_4(H_2O)_2(P_2W_{15}O_{56})_2]\cdot 50H_2O$ (**$P_2W_{15}Cu_4$**),
- $NaK_4[(A\text{-}\beta\text{-}SiW_9O_{34})Cu^{II}_4(OH)_3(H_2O)(H_3N(CH_2)_3COO)_2]_3\cdot 18H_2O$ (**SiW_9Cu_4**),
- $K_{12}[(SbW_9O_{33})_2\{Cu^{II}(H_2O)\}_3]\cdot 41H_2O$ (**$Sb_2W_{18}Cu_3$**).

Les ions cuivriques Cu^{II} sont encapsulés dans différents types d'unités de POM (du type Keggin ou Dawson). Leurs propriétés électrochimiques et aussi leurs propriétés catalytiques pour la réduction NO_3^- et NO_2^- ont été étudiées à pH 5 (1 mol·L^{-1} $CH_3COOLi + CH_3COOH$) et à pH 1 (0,5 mol·L^{-1} $Na_2SO_4 + H_2SO_4$).

Ensuite, un cluster de cuivre (complexé avec un ligand alendronate, Ale : $[Cu_6(Ale)_4(H_2O)_4]^{4-}$ a été ajouté à chacun des trois complexes de CuPOM préalablement étudiés pour obtenir les composés CuPOM/CuAle :

- $Na_{20}[\{(P_2W_{15}O_{56})_2Cu^{II}_4(H_2O)_2\}\{Cu^{II}_6(O_3PC(O)(C_3H_6NH_3)PO_3)_4(H_2O)_4\}]\cdot 50H_2O$ **(P_2W_{15}CuAle)**,
- $Na_{12}[\{SiW_9O_{34}Cu^{II}_3(Ale)(H_2O)\{Cu^{II}_6(O_3PC(O)(C_3H_6NH_3)PO_3)_4(H_2O)_4\}\}\cdot 50H_2O$ **(SiW_9CuAle),**
- $Na_8Li_{29}[\{(SbW_9O_{33})_2Cu^{II}_3(H_2O)_{2.5}Cl_{0.5}\}_2\{Cu^{II}_6(O_3PC(O)(C_3H_6NH_3)PO_3)_4(H_2O)_4\}_3]\cdot 163H_2O$ **(SbW_9CuAle)**.

Deux types d’ion Cu^{II} coexistent dans ces trois composés : une partie est encapsulée dans le POM alors que l’autre partie est complexée par le ligand alendronate (Ale).

Ces composés sont été synthétisés dans le groupe de Prof. Pierre Mialane et le DR. Anne Dolbecq, Institut Lavoisier, UMR 8180, Université de Versailles Saint-Quentin-en-Yveline. Les structures de ces composés sont présentées sur le Figure 7.

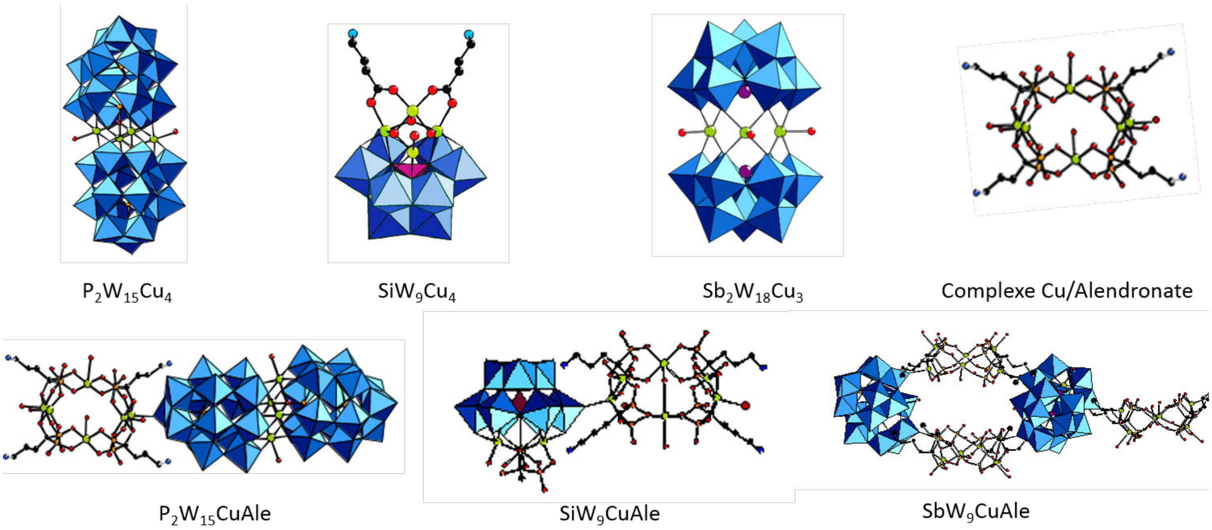

Figure 7 : Représentation des différentes structures de CuPOMs et de CuPOM/CuAle.

Les propriétés électrochimiques ont été étudiées à pH 1 et pH 5. La réduction des ion Cu^{II} sont observées pour tous ces composés étudiés. Deux pics de réductions sont observés à pH 1 correspondant à la réduction des Cu^{II} en Cu^{I}, puis des Cu^{I} en Cu^{0}. A pH 1, un seul pic en réduction est observé indiquant que le Cu^{I} n'est pas assez stable durant la mesure électrochimique et sa dismutation en Cu^{II} et Cu^{0}. Cette différence peut être expliquée par une meilleure stabilité du complexe Cu^{I} en présence d'ions acétate contenu dans le tampon acétate à pH 5, qui est un ligand fort.[17] Lors du balayage de potentiel retour, un grand pic de réoxydation anodique est observé vers 0,00 V *vs.* ECS. Il correspond à la réoxydation des Cu^{0} en Cu^{II}. Une réduction réversible de W^{VI} en W^{V} du POMs est également observée à un potentiel plus négatif, bien au-delà de la réduction des atomes de cuivre (Figure 8A). A pH 1 et pH 5, la réduction de W^{VI} n'est pas bien définie ou difficile à détecter, du fait d'un dépôt important du Cu^{0} mais également d'un grand nombre d'électrons transférés pour la réduction des atomes de Cu. Lors de la réduction de l'ensemble des atomes de cuivre, les nanoparticules de Cu^{0} sont formées *in situ.* Ces nanoparticules continuent à se déposer à la surface de l'électrode de carbone vitreux durant le balayage en réduction lorsque l'on atteint la première réduction des W. Afin de mieux étudier le premier pic de réduction Cu^{II}/Cu^{I}, le balayage est arrêté après ce premier pic (Figure 8B). La réduction des atomes Cu^{II} en Cu^{I}, est réversible et le courant de pic mesuré est proportionnelle à la racine carrée de la vitesse de balayage. Ces résultats indiquent que le courant est limité par la diffusion du POM vers la surface de l'électrode. Les ions Cu dans les composés CuPOM/Ale devraient se réduire à des potentiels plus positifs que les ions Cu dans CuPOM, indique les Cu complexé par ligand Ale (plus facile à réduire). Ceci n'a pas été observé lors de notre étude où il est difficile de distinguer la réduction des CuAle et CuPOM, qui se réduisent au même potentiel. Le seul changement étant les potentiels de réduction (plus facile à réduire pour CuPOM/CuAle que pour CuPOM).

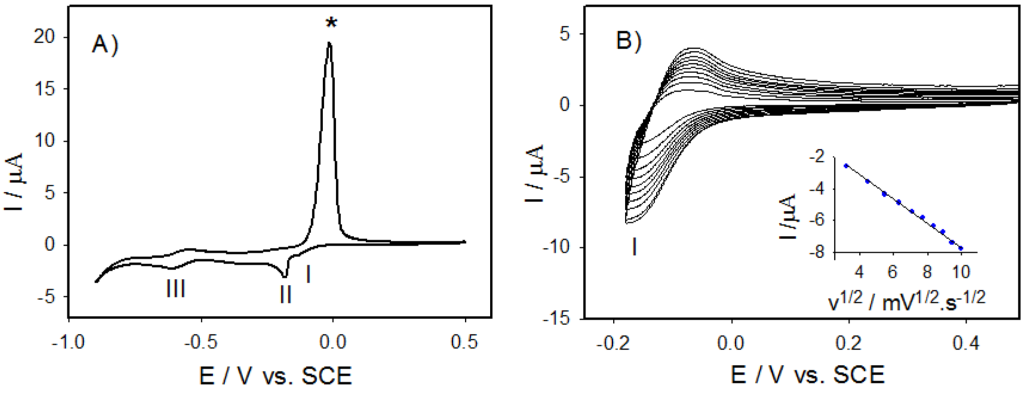

Figure 8 : A) CV de $P_2W_{15}CuAle$ à pH 5 (1 mol·L^{-1} CH_3COOLi + CH_3COOH), v = 2 mV·s^{-1}. B) CVs du processus I (couple Cu^{II}/Cu^{I}) en variant de la vitesse de balayage de 10 à 100 mV·s^{-1}.

L'étude par coulométrie à potentiel imposé est réalisée pour s'assurer que tous les atomes de Cu^{II} dans la structure sont bien réduits au second pic de réduction (Cu^{I}/Cu^{0}). L'étude AFM a montré que le film ou dépôt devient plus dense et rugueux si le temps de dépôt augmente. Un changement de couleur est observé sur l'électrode ITO. Ces composés ont été aussi étudiés par Microbalance à Cristal de Quartz Electrochimique (EQCM), où la masse de dépôt est calculée à partir de l'équation de Sauerbrey :

$$f = -2f_0^2\,\Delta m/\sqrt{\mu.\rho}$$

f_0: fréquence fondamentale de résonance, ρ: densité du cristal (2,684 g/cm^3), A: area (0,2 cm^2), μ: module de cisaillement de quartz (2,947×10^{11} g/cm·s^{-2}).

Le dépôt de Cu^0 en présence de CuPOM/CuAle démarre plus tôt qu'en présence du CuPOM seul, ce qui montre que le Cu complexé par ligand Ale sont plus facile à réduire, ce qui semble cohérent par rapport aux mesures électrochimiques (Figure 9). La masse déposée augmente généralement avec le nombre des ions cuivriques Cu^{II} présent dans la structure. Cependant, puisque les espèces de POM adsorbées sur les nanoparticules de Cu, la présence du POM (surfactant) contribue également au changement de la masse. Des interprétations plus quantitatives doivent ainsi être prises avec beaucoup de précaution.

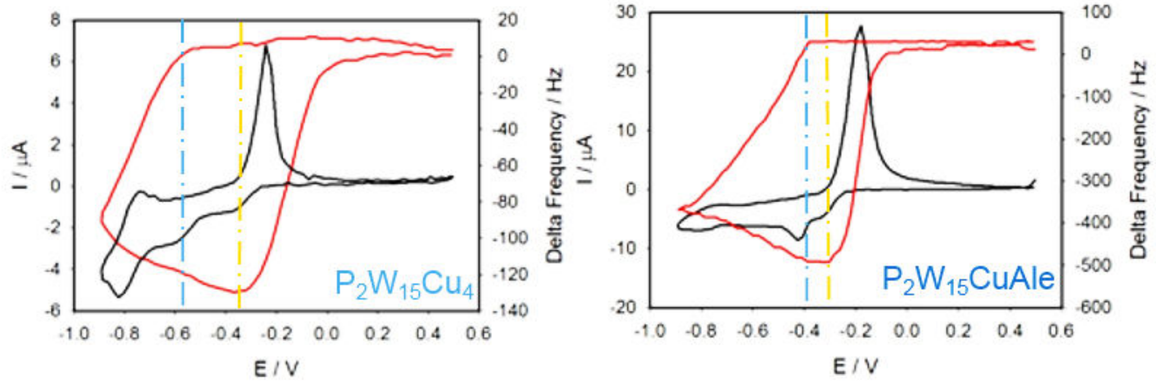

Figure 9 : Microbalance à Cristal de Quartz Electrochimique (EQCM) de $P_2W_{15}Cu_4$ et $P_2W_{15}CuAle$ à pH 5(1 mol·L^{-1} CH_3COOLi + CH_3COOH), v = 2 mV·s^{-1}.

La réduction électrocatalytique de NO_2^- a été étudiée d'abord avec les trois CuPOMs (sans le complexe CuAle). Deux vagues de courant catalytique sont observées lors de l'ajout de $NaNO_2$: la première activité est observée au potentiel du couple redox Cu$^{II/I}$ (processus I) et correspond à la réduction NO_2^- par Cu^I complexé. La deuxième activité est située au niveau du potentiel de réduction du W (processus III, couple W$^{VI/V}$). Cette seconde activité catalytique correspond à la réduction de NO_2^- par le W^V réduit du POM et est beaucoup plus importante que la première activité. Au processus II, réduction des ions cuivreux en cuivre (Cu$^{I/0}$), on observe une absence d'activité catalytique. Les propriétés catalytiques de ces composés sont comparées en mesurant le potentiel catalytique du début de la catalyse et la densité de courant catalytique. **$P_2W_{15}Cu_4$**

est le plus actif pour la réduction de nitrite quelle que soit la concentration initiale en $NaNO_2$ (Figure 10).

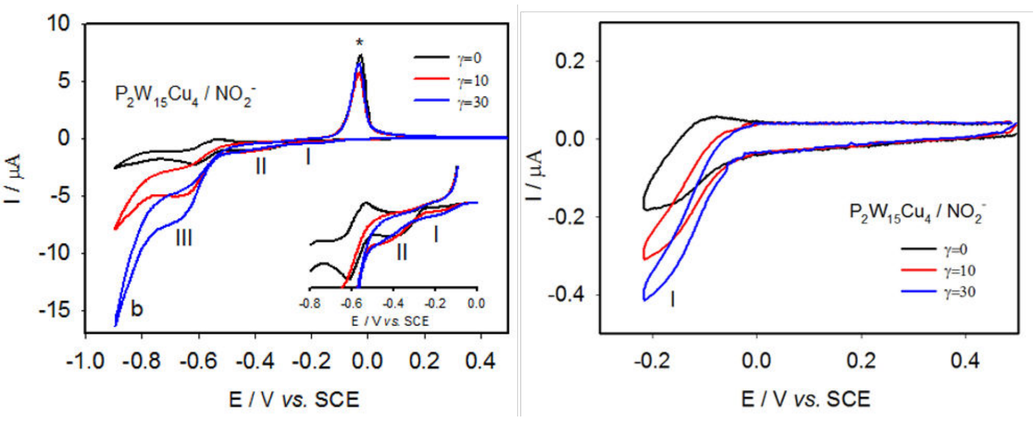

Figure 10 : Réduction des ions nitrite par $P_2W_{15}Cu_4$ à pH 5 (1 mol·L^{-1} CH_3COOLi + CH_3COOH), $v = 2$ mV·s^{-1}.

Après l'addition de complexes CuAle, ces composés montrent des propriétés catalytiques similaires à celles du CuPOM seul. Néanmoins, le courant catalytique est plus important sans doute dû au fait d'un nombre d'ions cuivriques plus élevée dans la structure. Une augmentation de courant est observée également après la réduction de W^{VI}, indiquant que le Cu électrodéposé à la surface de l'électrode affecte la réduction de nitrite dans le potentiel de l'évolution du dihydrogène. Parmi les composés CuPOM/CuAle, **P_2W_{15}CuAle** est le plus actif. Si on compare **P_2W_{15}CuAle** et **$P_2W_{15}Cu_4$**, la catalyse démarre plus tôt pour **P_2W_{15}CuAle** avec la densité de courant cinétique plus importante.

Quant à la réduction de NO_3^-, **$P_2W_{15}Cu_4$** et **SiW_9Cu_4** ont montré une activité intéressante au potentiel de réduction du couple $W^{VI/V}$ (Figure 11). Cette activité est due à la fois de la présence de nanoparticules de Cu formées *in situ* en synergie avec celle du POM réduit. **$Sb_2W_{18}Cu_3$** est inactif pour la réduction de NO_3^-, ceci a été attribué au blocage de la surface des nanoparticules de cuivre par les unités POMs libérées (surfactant). De plus, pour **$Sb_2W_{18}Cu_3$**, aucun courant catalytique n'est observé sur électrode de Cu pour la réduction de NO_3^-, ce qui confirme que **$Sb_2W_{18}Cu_3$** est susceptible de « bloquer » la surface de l'électrode inhibant la catalyse de la réduction des nitrates. Cela montre que la formation de CuNPs et ses propriétés catalytiques peuvent être modulées par le type de POMs présents.

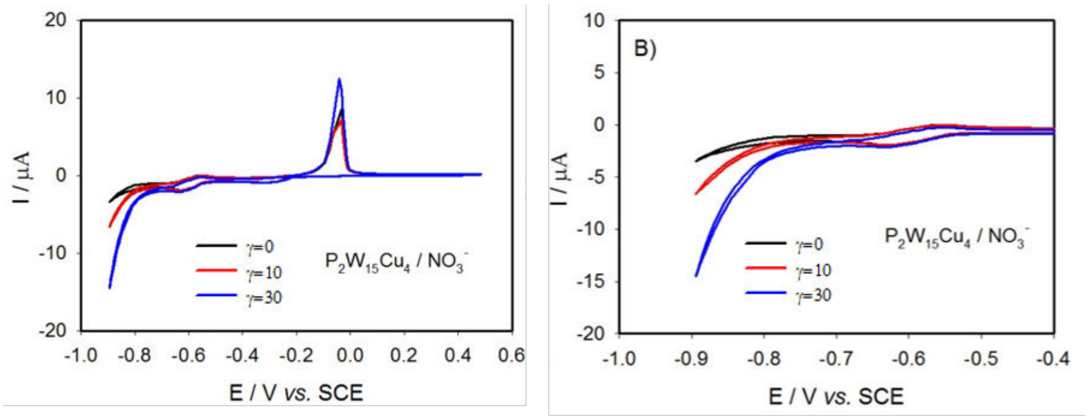

Figure 11 : Réduction de nitrate par $P_2W_{15}Cu_4$ à pH 5 (1 mol·L^{-1} CH_3COOLi + CH_3COOH), v = 2 mV·s^{-1}.

Les composés **P_2W_{15}CuAle** et **SiW_9CuAle** sont également actifs pour la réduction de NO_3^- mais pas **SbW_9CuAle**. Cela montre que l'unité de POM « SbW_9 » peut toujours « bloquer » la surface des nanoparticules de Cu formées *in situ* et inhiber la catalyse, même si le nombre d'ions d'ions cuivriques dans la structure de départ augmente. Dans tous les cas, le courant de réduction est plus important avec le composé contenant le complexe CuAle additionnel. Ceci est sans doute dû à l'augmentation du nombre d'atomes de Cu^{II} dans la structure. Comparant le départ de la catalyse et la densité de courant catalytique, **P_2W_{15}CuAle** est considéré comme le catalyseur le plus actif pour la réduction de nitrate à la fois à pH 1 et à pH 5.

L'effet du pH du milieu (pH = 1, 2, 3 ou 5) a été également étudié pour la réduction de NO_2^- / HNO_2 pour **P_2W_{15}CuAle**, où le composé a montré les meilleures performances pour la réduction des nitrites. La meilleure activité est obtenue dans la solution à pH 2 pour les deux activités (couple $Cu^{II/I}$ et première réduction des atomes de W^{VI}).

Si l'on varie la concentration de nitrate dans la solution, une dépendance linéaire du courant sur la concentration en nitrate a été obtenue avec **P_2W_{15}CuAle** dans la gamme de 0 à 20 mmol·L^{-1} dans une solution à pH 1, tandis qu'une gamme plus étroite de 0 à 10 mmol·L^{-1} a été obtenue dans un milieu à pH 5. Il est donc possible d'envisager l'élaboration de capteurs d'ion nitrate dans ce domaine de concentration.

III. Electroréduction de NO_x par nanoparticules Ag stabilisées par le POM (surfactant)

Selon la littérature, l'argent est aussi un bon catalyseur pour la réduction de NO_3^-.[9] Dans cette partie, des nanoparticules d'Ag sont préparées en utilisant les propriétés photoréductrice du POM* $[SiW_{12}O_{40}]^{4-*}$ excité sous illumination UV en présence d'un donneur d'électron sacrificiel tel que le propan-2-ol. Pour simplifier, sous illumination UV, le POM passe dans un état excité et réagit avec propan-2-ol pour former le POM réduit et des nanoparticules d'argent stabilisées par le POM : Ag@$SiW_{12}O_{40}$. Ce mécanisme fonctionne après une phase d'initiation qui permet l'augmentation la taille de la nanoparticule. Un mécanisme plus précis a été publié par le groupe de L. Ruhlmann et est présenté sur la Figure 12.[18] La formation des nanoparticules est suivie par spectroscopie UV-visible. Le couleur de la solution change au jaune ce qui confirme la formation de nanoparticules de l'argent. Après 15 min, une solution devient gris-bleu indiquant la présence de POM réduit (en solution ou en surface des nanoparticules). Les nanoparticules obtenues ont été caractérisées par microscopie électronique en transmission (MET). Les nanoparticules Ag@$SiW_{12}O_{40}$ sont de forme ronde avec un diamètre moyen environ 20 nm. Ces nanoparticules sont stables dans le temps pendant quelques mois d'après des mesures en spectroscopie UV-visible.

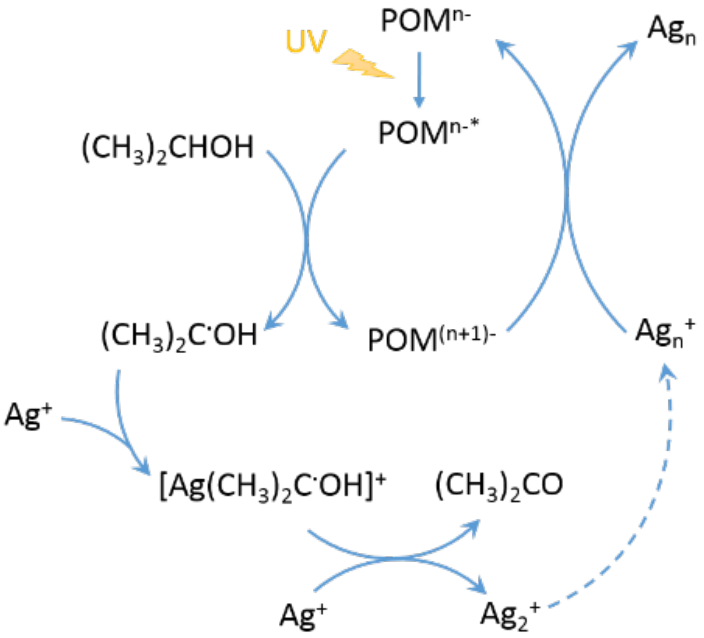

Figure 12 : Photoréduction des ions Ag^+ avec polyoxométallates en présence de $(CH_3)_2CHOH$.

Les formes et les tailles des nanoparticules d'Ag@$SiW_{12}O_{40}$ formées peuvent être modulées en variant la concentration initiale de POM. La concentration de POM plus élevée conduit à la formation rapide des nanoparticules Ag@$SiW_{12}O_{40}$ qui sont mono-dispersées avec une distribution de taille uniforme. Dans le cas d'une concentration en POMs trop faible, la quantité de POMs ne permet pas une adsorption sur toute la surface des nanoparticules d'argent induisant une tendance à l'agrégation des AgNPs. Les POMs adsorbés à la surface de nanoparticules ne peuvent pas être observé directement par MET. Cependant, en utilisant l'analyse dispersive en énergie (« Energy Dispersive X-ray spectrometry », EDX), la présence des éléments Ag, W et Si montre la présence des POMs sur la surface de nanoparticules, montrant que le POM agit bien comme surfactant.

Pour étudier les propriétés électrocatalytiques des nanoparticules d'Ag@$SiW_{12}O_{40}$, elles doivent être déposées sur une surface de carbone vitreux qui servira de collecteur de courant. Pour préparer l'électrode modifiée, une quantité fixée de la solution d'Ag@$SiW_{12}O_{40}$ est déposée à la surface, puis on laisse sécher à l'air afin d'éliminer le solvant (H_2O et le donneur sacrificiel d'électron : le propan-2-ol). La quantité de catalyseur déposé peut être modulée suivant le nombre de dépôt réalisé. La propriété électrochimique de cette électrode modifiée est ensuite étudiée, où la réduction de W^{VI} en W^{V} des POMs et l'oxydation de Ag^{0} en Ag^{I} sont observées (Figure 13), entraînant dans ce cas la libération des ions Ag^{I} qui diffusent dans la solution et ne peut pas être réduits à nouveau sur l'échelle de temps du balayage. Ainsi, la mesure doit être limitée après 0,1 V *vs.* ECS afin d'éviter l'oxydation de l'Ag^{0}.

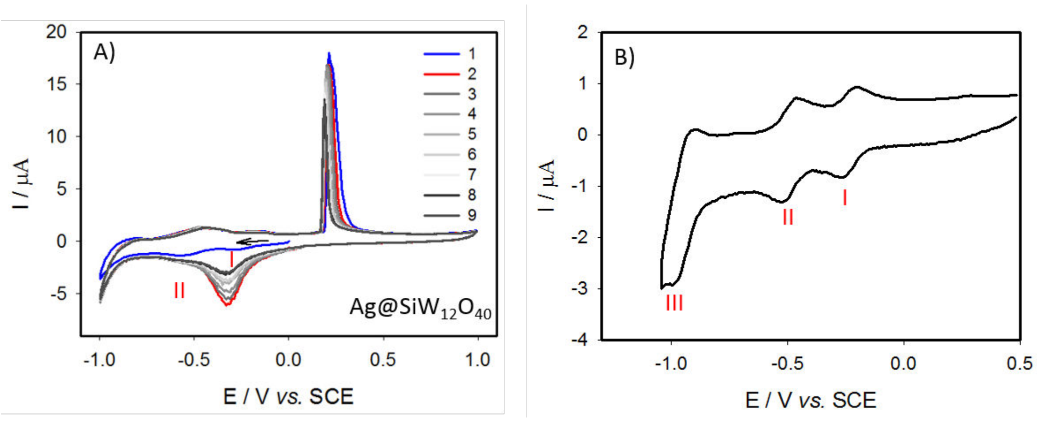

Figure 13 : A) CVs de la solution de nanoparticules Ag@$SiW_{12}O_{40}$. B) CV de $[SiW_{12}O_{40}]^{4-}$ en solution pH 5 (1 $mol{\cdot}L^{-1}$ $CH_3COOLi + CH_3COOH$), $v = 20\ mV{\cdot}s^{-1}$.

La masse déposée à la surface de l'électrode est estimée en utilisant la Microbalance à Cristal de Quartz (« QCM » en anglais). Le résonateur est un cristal de quartz pris en sandwich entre deux électrodes de carbone soumises à un champ électrique alternatif à travers le cristal, générant un mouvement vibratoire du cristal à sa fréquence de résonance. Cette fréquence de résonance est sensible au changement de masse à la surface de l'électrode. Dans le cas de notre expérience, un changement de masse entre 58 à 110 $\mu g{\cdot}cm^{-2}$ est obtenu, indiquant que la concentration des nanoparticules d'Ag@$SiW_{12}O_{40}$ est de l'ordre de 2,80 à 4,42 $g{\cdot}L^{-1}$ suivant l'expérience. On a aussi observé que la fréquence de résonance du quartz atteint presque sa valeur initiale à chaque fois que 5 µL solution des nanoparticules d'Ag@$SiW_{12}O_{40}$ est déposée (avant évaporation). Cela suggère que la plupart des nanoparticules se retirent de la surface de l'électrode au contact de l'eau. Pour améliorer la fixation des nanoparticules à la surface, 2 µL solution of 5 wt. % Nafion doit être ajouté en surface à la fin du processus de dépôt.

L’effet du Nafion est vérifié par la voltampérométrie cyclique. Après l’ajout de Nafion, les pics redox sont mieux définis et plus symétriques. Le courant associé aux processus POM redox n’augmente pas avec le nombre de cycles de dépôt, des maxima pour les courants de pics étant obtenu avec 15 µL de solution de nanoparticules d’Ag@$SiW_{12}O_{40}$ déposé et l’ajout 2 µL Nafion. Cela suggère que seules de petites fractions des particules sont reliées manière électrique au collecteur de courant de carbone vitreux.

Pour comparer les propriétés catalytiques, le potentiel de départ est défini où la différence de courant $\triangle I = I_0 - I_{NOx}$ est égal à 1 µA en présence of 5 mmol·L^{-1} $NaNO_x$ dans la solution. Notez que la valeur $\triangle I$ choisie est supérieure à celle utilisée avec les catalyseurs CuPOM qui était de 0,5 µA. En effet, les courants de fond des électrodes de GC modifiées par Ag@$SiW_{12}O_{40}$ sont significativement augmentés par rapport à l'électrode de GC non modifiée et une valeur $\triangle I$ plus élevée doit être choisie pour une détermination fiable du potentiel de déclenchement de la réduction des NO_X.

L’activité catalytique pour la réduction de NO_2^- ou HNO_2 suivant le pH est étudiée à partir d’un dépôt de 15 µL solution de Ag@$SiW_{12}O_{40}$ + 2 µL Nafion. Le résultat est ensuite comparé avec $[SiW_{12}O_{40}]^{4-}$ seul dans les solutions en utilisant une électrode non modifiée de carbone vitreux, à pH 1 et à pH 5 comme dans les parties précédentes. On observe dans ce cas (GC non modifié + $[SiW_{12}O_{40}]^{4-}$ + $NaNO_2$) que la catalyse de la réduction du nitrite est observée au potentiel de la première réduction du W^{VI} du POM à pH 1 et au potentiel de la troisième réduction à pH 5.

En présence de nanoparticules d’Ag@$SiW_{12}O_{40}$ fixé à la surface de l’électrode (GC) la catalyse débute à un potentiel plus positif avec des intensités de courant plus forte. A pH 1, une augmentation de courant est observée dans toute la gamme de potentiel mesurée (-0,65 V à 0,00 V *vs.* ECS) même avant 0 V. Cela peut être attribué à l’activité d’Ag dans milieu acide. Le courant catalytique est plus important aux potentiels de réduction de W^{VI}. Ce résultat démontre que l’ajout de POM aux nanoparticules d’Ag@$SiW_{12}O_{40}$ conduit à une amélioration significative du courant catalytique. A pH 5, l’association de POM aux nanoparticules d’Ag@$SiW_{12}O_{40}$ n’a pas influencé le potentiel de départ de la catalyse comparé avec $[SiW_{12}O_{40}]^{4-}$ seul en solution. Cependant, le courant catalytique mesuré est 4 fois plus grand ce qui peut s’expliquer en partie par une surface spécifique plus grande. Ces résultats sont présentés sur la Figure 14.

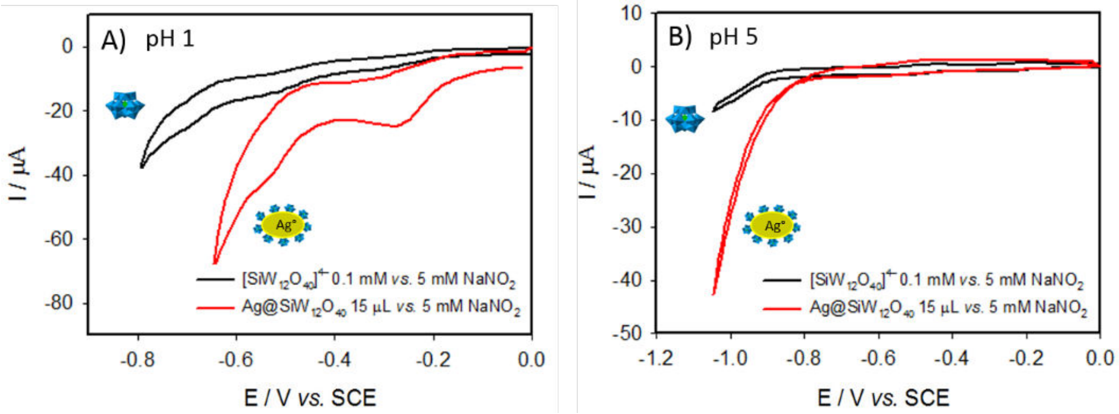

Figure 14 : Réduction de nitrite par Ag@$SiW_{12}O_{40}$ déposé à la surface d'électrode ou par $[SiW_{12}O_{40}]^{4-}$ dans la solution à pH 5 ((1 mol·L^{-1} CH_3COOLi + CH_3COOH) et à pH 1 (0,5 mol·L^{-1} Na_2SO_4 + H_2SO_4), v = 20 mV·s^{-1}.

Quant à la réduction catalytique de NO_3^-, l'activité catalytique n'est observée qu'après la première réduction des W^{VI} du POM. La catalyse démarre à -0,52 V à pH 1 et à -0,91 V à pH 5 (Figure 15). Enfin le courant catalytique augmente avec la quantité de nitrate ajoutée entre 1 - 200 mmol·L^{-1}. Une dépendance linéaire est obtenue en général entre 50 mmol·L^{-1} et 200 mmol·L^{-1}. Ainsi, un capteur pour le nitrate basé sur le système d'Ag@$SiW_{12}O_{40}$ pourrait être élaboré dans ce domaine de concentrations.

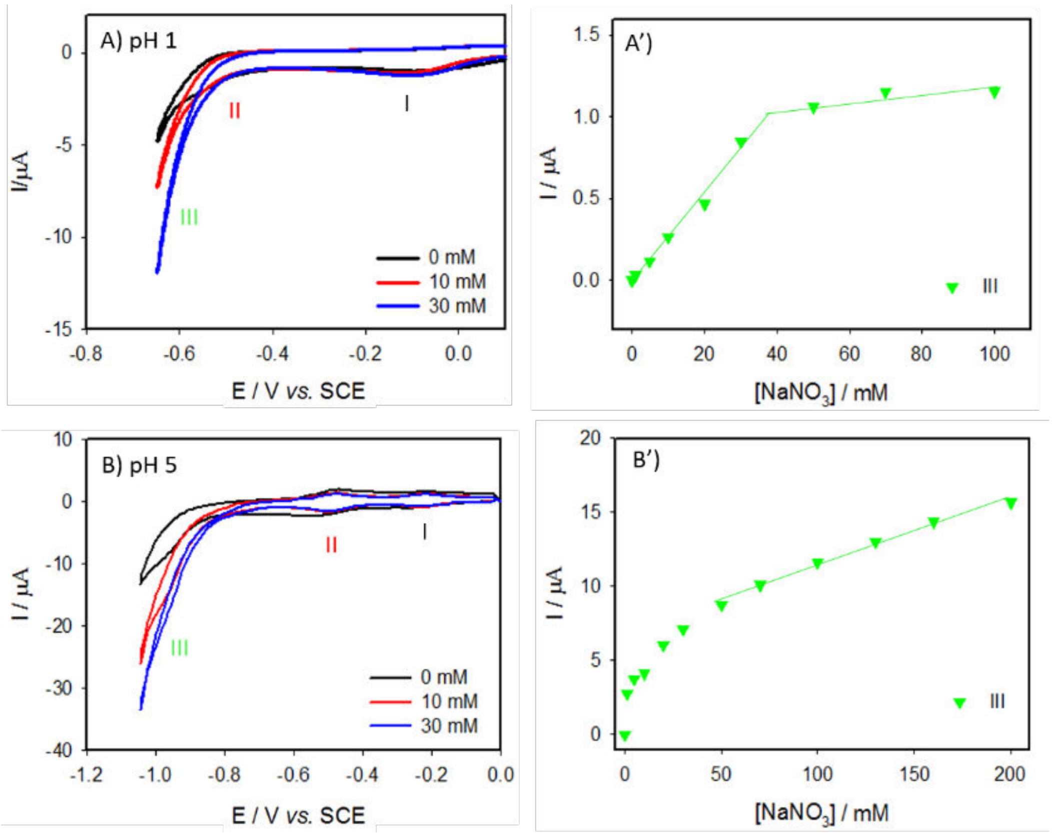

Figure 15 : Réduction de nitrate par Ag@$SiW_{12}O_{40}$ déposé à la surface d'électrode à pH 5 (1 mol·L^{-1} CH_3COOLi + CH_3COOH) et à pH 1 (0,5 mol·L^{-1} Na_2SO_4 + H_2SO_4), v = 20 mV·s^{-1}.

La stabilité de film est vérifiée avec 750 cycles de réaction (balayage itératif) en présence of 200 mmol·L^{-1} de $NaNO_2$, où plus de 65% de courant catalytique de départ est conservé.

L'électroréduction de nitrate sur les trois différents systèmes est comparée : sur l'électrode d'Ag, sur l'électrode d'Ag en présence de 0,1 mmol·L^{-1} de $[SiW_{12}O_{40}]^{4-}$ ou sur l'électrode modifiée avec Ag@$SiW_{12}O_{40}$/Nafion (Figure 16). La présence de POM sur la surface d'Ag peut empêcher l'évolution de l'hydrogène, d'où une plus grande plage de potentiel qui peut être appliquée pour le système GC/Ag@$SiW_{12}O_{40}$/Nafion. Comme on l'avait déjà montré dans la première partie, $[SiW_{12}O_{40}]^{4-}$ ajouté directement dans la solution peut bloquer accès de nitrate ions à la surface de l'électrode d'Ag. Ici, on a démontré que le système Ag@$SiW_{12}O_{40}$/Nafion est un meilleur catalyseur que l'électrode d'Ag seul avec une amélioration notable du courant catalytique.

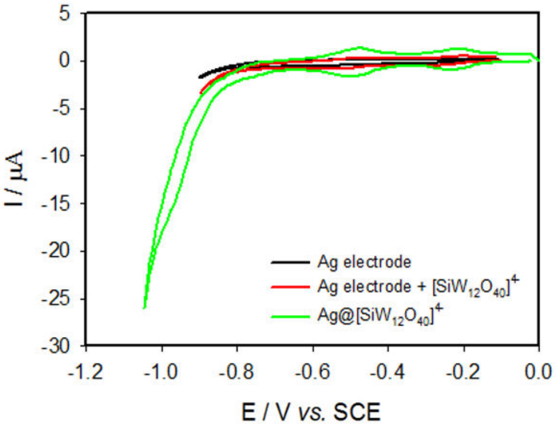

Figure 16 : Réduction de nitrate pour trois différents systèmes (Ag, Ag+$[SiW_{12}O_{40}]^{4-}$ ou GC/Ag@$SiW_{12}O_{40}$/Nafion) à pH 5 (1 mol·L^{-1} CH_3COOLi + CH_3COOH), v = 20 mV·s^{-1}.

IV. Immobilisation de polyoxométallates dans les matrices 'Metal-Organic Frameworks' (POM @ MOF)

Les polyoxométallates (POMs) possèdent des propriétés catalytiques intéressante pour diverses applications. Cependant, leurs inconvénients sont de faible surface spécifique, de faible stabilité dans des conditions catalytiques et une solubilité élevée dans le milieu aqueux. Ainsi, l'insertion de POMs dans les cavités de « Metal-Organic Frameworks » (MOFs) constitue une stratégie intéressante d'accès aux catalyseurs hétérogènes à base de POM.

Les «Metal-Organic Frameworks» (MOFs) sont des matériaux cristallins poreux dont la structure est définie par des ions métalliques ou des clusters métalliques qui sont connecté à des liants organiques bi- ou multimodaux avec des interactions fortes.[5] La structure microporeuse des MOFs fournit des surfaces jusqu'à 5900 $m^2 \cdot g^{-1}$ et les volumes de pores spécifiques jusqu'à 2 $cm^3 \cdot g^{-1}$ avec une dimension de pore variable.[19] La caractéristique de MOFs, telle que ses dimensions de pores, leurs formes, leurs dimensions et leurs environnements chimiques, peuvent être finement contrôlées pour des applications spécifiques.

Les composés POMs encapsulés dans le MOFs (POM@MOF) permettent d'augmenter la stabilité du POM et ses surfaces spécifiques et également de réaliser une catalyse sélective en fonction de la taille des pores.[20] Les composés POM@MOF sont fixés à la surface de l'électrode de graphite pyrolytique (PG) ce qui permet une étude de leurs propriétés redox, par exemple dans une solution à pH 2,5. Deux types d'étude ont été réalisés :

- Trois type de POMs $[PW_{12}O_{40}]^{3-}$ (**PW_{12}**), $[PW_{11}O_{39}]^{7-}$ (**PW_{11}**) et $[P_2W_{18}O_{62}]^{6-}$ (**P_2W_{18}**) sont insérés dans le MOF $[Zr^{IV}{}_6O_4(OH)_4(C_{14}H_8O_4)_6]$ (**UiO-67**). Dans la structure d'**UiO-67**, les unités octaédriques inorganiques Zr_6 sont liées à 12 autres sous-unités inorganiques à travers des ligands de dicarboxylate de biphényle formant une structure cubique à face centrée (Ø = 27,1 Å). Ce MOF présente deux types de cages : une super-tétraédrique (Ø ~ 11,5 Å) et une super-octaédrique (Ø ~ 18Å), accessibles par des fenêtres triangulaires microporeuses (Ø ~ 8 Å). **P_2W_{18}** et **PW_{12}** possèdent des propriétés électrocatalytiques identiques en solution ou après encapsulation dans le MOF (Figure 17). Dans le cas de **PW_{11}**, seulement trois processus de réduction successifs sont observés au lieu de quatre mesurés en solution (sans le MOF). Cette différence est attribuée à la complexation de **PW_{11}** avec le complexe de Zr^{IV} du MOF UiO-67. L'intensité de courant est proportionnelle à la vitesse de balayage, indiquant que le POM est bien immobilisé dans la cage de MOF. Il a été démontré que les POMs encapsulés à l'intérieur des cages du MOF peuvent conserver leurs propriétés électrochimiques.[21]

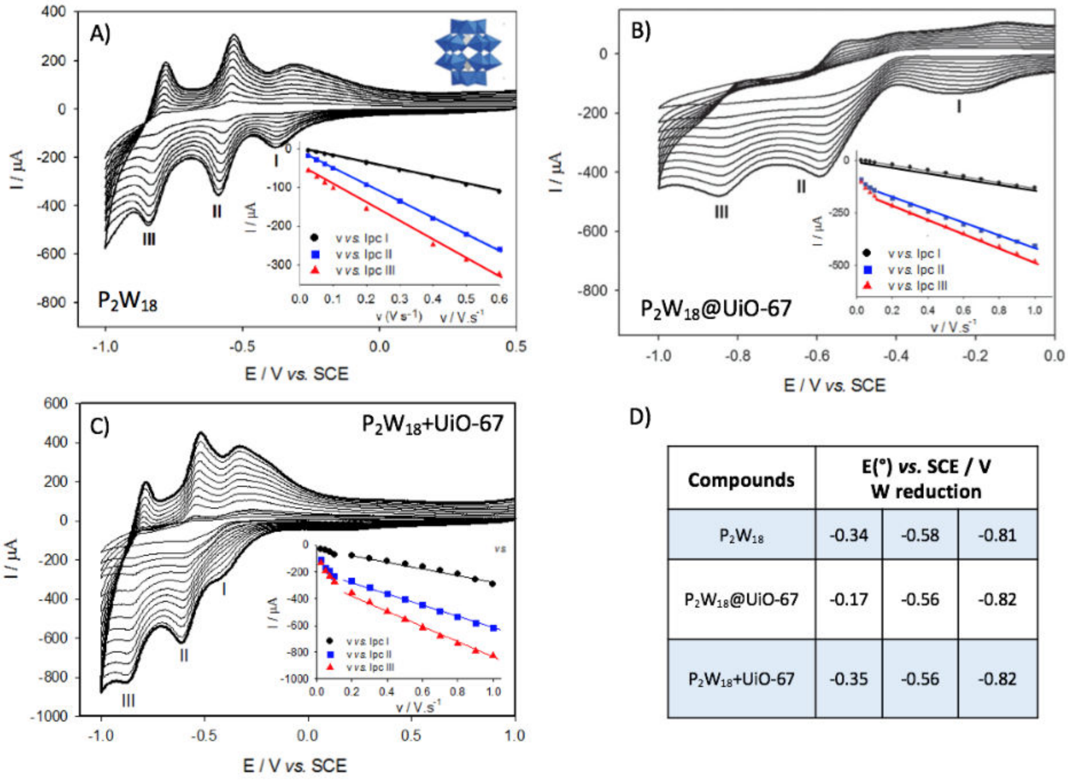

Compounds	E(°) *vs.* SCE / V W reduction		
P_2W_{18}	-0.34	-0.58	-0.81
P_2W_{18}@UiO-67	-0.17	-0.56	-0.82
P_2W_{18}+UiO-67	-0.35	-0.56	-0.82

Figure 17 : CVs de trois systèmes (A) P_2W_{18}*, (B)* P_2W_{18}*@UiO-67 and (C)* P_2W_{18}*+UiO-67 (mélange mécanique des deux solides) immobilisés sur l'électrode de PG à différent vitesse de balayage de 0,025 à 1,000 V·s*$^{-1}$*. D) Potentiels de réduction pour chaque système sur électrode de PG à pH 2,5 0,5 mol·L*$^{-1}$ Na_2SO_4 *+* H_2SO_4*.*

- $[(FeW_9O_{34})_2Fe_4(H_2O)_2]^{10-}$ (**Fe_6W_{18}**) a été stabilisé dans trois types de support : la gélatine et deux MOFs différents : $[Zr^{IV}{}_6O_4(OH)_4(C_{14}H_8O_4)_6]$ (**UiO-67**) et $[Cr^{III}{}_3(H_2O)_3O(C_8H_4O_4)_3]NO_3$ (**MIL-101{Cr}**). Le MOF **MIL-101 (Cr)** est construit à partir de trimères d'octaèdres Cr^{III} liées par des anions de téréphtalate, ce qui crée une structure 3D avec deux types de méso-cages (Ø ~ 29 et 34 Å) accessibles par des fenêtres microporeuses (Ø = 11 et 16 Å). **Fe_6W_{18}** conservent également ces propriétés électrochimiques dans les deux MOFs, mais pas dans la gélatine, probablement en raison du caractère isolant celle-ci.[22] Une étude préliminaire sur la réduction catalytique des nitrites est réalisée pour **Fe_6W_{18}@MOF** où une activité intéressante est obtenue à la deuxième réduction de Fe^{III}. Cette activité catalytique est améliorée après le troisième pic de réduction de Fe^{III}. Cependant, la stabilité de ce catalyseur hétérogène sur la surface de l'électrode pendant la réduction de la catalyse reste un défi. L'ajout d'une couche de Nafion à la surface du catalyseur pourrait être envisagé.

En conclusion, l'objet de ce travail est de développer des nouveaux catalyseurs pour réduire de manière catalytique les ions nitrites (NO_2^-/HNO_2) et nitrates (NO_3^-) dans l'eau, mais également d'essayer de comprendre des facteurs qui vont influencer ces réductions catalytiques. On a montré que la présence de polyoxométallates induit un effet positif pour la réduction catalytique de ions nitrate et nitrite avec l'électrode de Cu et d'Ag.

Les nanoparticules décorées par des POMs (CuPOM et Ag@POM) sont formées avec deux méthodes différentes (électroréduction *in situ* ou photoréduction sous illumination UV en présence d'un donneur sacrificiel d'électron et en présence d'ions POMs). Ces deux types de nanoparticules sont actives pour la réduction des NO_3^- et des NO_2^-/HNO_2 à pH 1 et à pH 5. On a montré également que la formation des nanoparticules et ses propriétés catalytiques peuvent être modulées par le type de POMs utilisé. De plus, les nanoparticules du type Ag@POM ont montré une bonne stabilité vis-à-vis de l'électroréduction des ions nitrite.

Dans le cas de POMs encapsulés dans des matrices MOF, les unités POM conservent leurs propriétés électrochimiques, les POM@MOF montrent également de bonnes activités vis-à-vis de la réduction des nitrites.

La poursuite de ce travail inclut la caractérisation des nanoparticules protégées par des POMs en utilisant la spectroscopie de photoélectrons induits rayon-X, la microscopie électronique à transmission in situ (TEM *in situ*), etc. L'identification des produits et leur quantification doit être effectué à l'aide de la spectrométrie de masse électrochimique différentielle (DEMS), de la chromatographie en phase gazeuse (GC) et de la spectroscopie infrarouge à transformée de Fourier (FT-IR).

Plus particulièrement, dans le système CuPOMs/CuAle, le CuAle complexe devrait être étudié indépendamment afin de mieux comprendre l'influence de l'environnement chimique des ions Cu. Pour les systèmes Ag@POM et POM@MOF, le POM pourra être modulé de manière à trouver les candidats les mieux adaptés. En outre, le film de catalyseur doit être fixé de manière optimale à la surface de l'électrode en faisant varier la quantité de Nafion ou en incorporant le catalyseur dans une matrice polymère.

Réferences

1. World Health Organization. *Nitrate and nitrite in drinking water, background document for development of WHO guidelines for drinking-water quality*. (World Health Organization, 2011).
2. Brinkmann, T., Santonja, G. G., Yukseler, H., Roudier, S. & Sancho, L. D. *Best Available Techniques (BAT) reference document for common waste water and waste gas treatment/management systems in the chemical sector*. (European Integrated Pollution Prevention and Control Bureau, 2016).
3. Knobeloch, L., Salna, B., Hogan, A., Postle, J. & Anderson, H. Blue babies and nitrate-contaminated well water. *Environ. Health Perspect.* **108,** 675–678 (2000).
4. Soares, M. I. M. Biological denitrification of groundwater. *Water Air Soil Pollut.* **123,** 183–193 (2000).
5. Samatya, S., Kabay, N., Ksel, Y., ßerref Arda, M. S. & Yü Ksel, M. Removal of nitrate from aqueous solution by nitrate selective ion exchange resins. *React. Funct. Polym.* **66,** 1206–1214 (2006).
6. Duca, M. & Koper, M. T. M. Powering denitrification: the perspectives of electrocatalytic nitrate reduction. *Energy Environ. Sci.* **5,** 9726–9742 (2012).
7. Magalon, A., Fedor, J. G., Walburger, A. & Weiner, J. H. Molybdenum enzymes in bacteria and their maturation. *Coord. Chem. Rev.* **255,** 1159–1178 (2011).
8. Salomé, O., Soares, G. P., Rfão, J. J. M., Fernando, M. & Pereira, R. Pd-Cu and Pt-Cu Catalysts Supported on Carbon Nanotubes for Nitrate Reduction in Water. *Ind. Eng. Chem. Res.* **49,** 7183–7192 (2010).
9. Dima, G. E., De Vooys, A. C. A. & Koper, M. T. M. Electrocatalytic reduction of nitrate at low concentration on coinage and transition-metal electrodes in acid solutions. *J. Electroanal. Chem.* 554–555**,** 15–23 (2003).
10. Pope, M. T. & Müller, A. Polyoxometalate chemistry. *Angew. Chem., Int. Ed.* **30**, 34–48 (1991).
11. Dong, S., Xi, X. & Tian, M. Study of the electrocatalytic reduction of nitrite with silicotungstic heteropolyanion. *J. Electroanal. Chem.* **385,** 227–233 (1995).
12. Keita, B., Abdeljalil, E., Nadjo, L., Contant, R. & Belgiche, R. First examples of efficient participation of selected metal-ion-substituted heteropolyanions in electrocatalytic nitrate reduction. *Electrochem. commun.* **3,** 56–62 (2001).
13. Mal, S. S., Bassil, B. S., Ibrahim, M., Nellutla, S., Tol, J., Dalal, N. S., Fernandez, J. A. Lopez, X., Poblet, J. M., Biboum, R. N., Keita, B. & Kortz. U. Wheel-shaped Cu_{20}-tungstophosphate $[Cu_{20}X(OH)_{24}(H_2O)_{12}-(P_8W_{48}O_{184})]^{25-}$ ion (X = Cl, Br, I) and the role of the halide guest. *Inorg. Chem.* **48**, 11636–11645 (2009).
14. Imar, S., Maccato, C., Dickinson, C., Vagin, M. & Mccormac, T. Enhancement of nitrite and nitrate electrocatalytic reduction through the employment of self-assembled layers of nickel- and copper-substituted crown-type heteropolyanions. *Langmuir* **31**, 2584–2592 (2015).
15. Xi, X. & Dong, S. Electrocatalytic reduction of nitrite using Dawson-type tungstodiphosphate anions in aqueous solutions, adsorbed on a glassy carbon electrode and doped in polypyrrole film. *J. Mol. Catal. A Chem. A* **114,** 257–265 (1996).
16. El Moll, H., Dolbecq, A., Marrot, J., Rousseau, G., Haouas, M., Taulelle, F., Rogez, G., Rousseau, G., Keita, B. & Pierre Mialane. A stable hybrid bisphosphonate polyoxometalate single-molecule magnet. *Chem. - A Eur. J.* **18**, 3845–3849 (2012).
17. Rorabacher, Davide, B. & Schroeder, R. R. Electrochemistry of copper. (Encyclopedia of Electrochemistry, 2007).
18. Costa-Coquelard, C., Schaming, D., Lampre, I. & Ruhlmann, L. Photocatalytic reduction of Ag_2SO_4 by the Dawson anion α-$[P_2W_{18}O_{62}]^{6-}$ and tetracobalt sandwich complexes. *Appl. Catal. B Environ.* **84,** 835–842 (2008).
19. Férey, G., Mellot-Drazieks, C., Serre, C., Millange, F., Dutour, J., Surblé, S. & Margiolaki, I.A chromium terephthalate-based solid with unusually large pore volumes and surface area. *Science* **309,** 2040–2042 (2005).
20. Hao, X.-L., Ma, Y.-Y., Zang, H.-Y., Wang, Y.-H., Li, Y.-G. & Wang, E.-B. A Polyoxometalate encapsulating cationic metal-organic framework as a heterogeneous catalyst for desulfurization. *Chem. - A Eur. J.* **21**, 3778–3784 (2015).
21. Salomon, W. Roch-Marchal, C., Mialane, P., Rouschmeyer, P., Serre, C., Haouas, M., Taulelle, F., Yang, S., Ruhlmann L. & Dolbecq, A. Immobilization of polyoxometalates in the Zr-based metal organic framework UiO-67. *Chem. Commun.* **51**, 2972–2975 (2015).
22. Salomon, W., Lan, Y. L., Rerière, E., Yang, S., Roch-Marchal, C., Dolbecq, A., Simonnet-Jégat, C., Steunou, N., Leclerc-Laronze, N., Ruhlmann, L., Mallah, T., Wernsdorfer, W. & Mialane, P. Single-molecule magnet behavior of individual polyoxometalate molecules incorporated within biopolymer or metal-organic framework matrices. *Chem. - A Eur. J.* **22**, 6564–6574 (2016).

List of Abbreviations

AFM	Atomic-Force Microscopy
Ale	Alendronate = $[H_2O_3PC(C_3H_6NH_2(OH)PO_3H_2]$
CuAle	$[Cu_6(Ale)_4(H_2O)_4]^{4-}$
cryo-TEM	cryogenic Transmission Electron Microscopy
CT	Charge Transfer
CV	Cyclic Voltammetry
DEMS	Differential Electrochemical Mass Spectroscopy
DMF	N,N-DiMethylFormamid
EDX	Energy-Dispersive X-ray spectroscopy
EQCM	Electrochemical Quartz Crystal Microbalance
Fe_6W_{18}	$[(FeW_9O_{34})_2Fe_4(H_2O)_2]^{10-}$
FT-IR	Fourier-Transformed Infrared Spectroscopy
GC	Glassy Carbon
HOMO	Highest Occupied Molecular Orbital
in-situ TEM	*in-situ* Transmission Electron Microscopy
IR	Infrared Reflection
ITO	Indium Tion Oxide
LbL	Layer-by-Layer
LUMO	Lowest Unoccupied Molecular Orbital
MIL-101(Cr)	$[Cr^{III}_3(H_2O)_3O(C_8H_4O_4)_3]NO_3$ (MIL for Material Institute Lavoisier)
MOF	Metal-Organic Frameworks
MV	Mixed-Valent
NP(s)	Nanoparticle(s)
PG	Pyrolytic Graphite
POM(s)	Polyoxometalate(s)
PVA	Poly(Vinyl Acetate)

PVP	PolyVinylPyrrolidone
PW_{11}	$[PW_{11}O_{39}]^{7-}$
P_2W_{15}	$Na_{12}[\alpha\text{-}P_2W_{15}O_{56}]\cdot 24H_2O$
$P_2W_{15}Cu_4$	$Na_{16}[Cu_4(H_2O)_2(P_2W_{15}O_{56})_2]\cdot 50H_2O$
$P_2W_{15}CuAle$	$Na_{20}[\{(P_2W_{15}O_{56})_2Cu_4(H_2O)_2\}\{Cu_6(O_3PC(O)(C_3H_6NH_3)PO_3)_4(H_2O)_4\}]\cdot 50H_2O$
P_2W_{18}	$[P_2W_{18}O_{62}]^{6-}$
RHE	Reversible Hydrogen Electrode
SBA	Strong Base Anion
SbW_9	$Na_9[\alpha\text{-}SbW_9O_{33}]\cdot 19.5H_2O$
SbW_9CuAle	$Na_8Li_{29}[\{(SbW_9O_{33})_2Cu_3(H_2O)_{2.5}Cl_{0.5}\}_2\{Cu_6(O_3PC(O)(C_3H_6NH_3)\text{-}PO_3)_4(H_2O)_4\}_3]\cdot 163H_2O$
$Sb_2W_{18}Cu_3$	$K_{12}[(SbW_9O_{33})_2\{Cu(H_2O)\}_3]\cdot 41H_2O$
SCE	Saturated Calomel Electrode
SEM	Scanning Electron Microscopy
SiW_9	$Na_{10}[A\text{-}\alpha\text{-}SiW_9O_{34}]\cdot xH_2O$
SiW_9Cu_4	$NaK_4[(A\text{-}\beta\text{-}SiW_9O_{34})Cu_4(OH)_3(H_2O)(H_3N(CH_2)_3COO)_2]_3\cdot 18H_2O$
SiW_9CuAle	$Na_{12}[\{SiW_9O_{34}Cu_3(Ale)(H_2O)\}\{Cu_6(O_3PC(O)(C_3H_6NH_3)PO_3)_4(H_2O)_4\}]\cdot 50H_2O$
UiO-67	$[Zr^{IV}{}_6O_4(OH)_4(C_{14}H_8O_4)_6]$ (UiO for University of Oslo)
upd	under-potential deposition
UV	Ultraviolet
XPS	X-ray Photoelectron Spectroscopy
XRD	X-Ray power Diffraction
$\triangle E_p$	Peak-to-peak separation

Table of Contents

CHAPTER III ELECTROCHEMICAL AND ELECTROCATALYTIC PROPERTIES OF CU-SUBSTITUTED POLYOXOMETALATE/ALENDRONATE - 66 -

General Introduction

Electrocatalysis of reactions involving small molecules (CO_2, H_2O, O_2, NO_3^-…) is at the heart of several crucial energy and environmental issues for the future. However, the design of selective, efficient but also cheap and environmental friendly electrocatalysts for these reactions remains a major challenge. The electrochemistry of these molecules involves complex multi-electron transfer processes with the formation of different intermediate species and products resulting in a sluggish reaction kinetics. For such reactions, the development of new synergistic hybrid catalysts, involving various kind of active sites catalyzing the transformation for each reaction intermediates in order to achieve both efficiency and selectivity is needed. The main purpose of this thesis is to explore the potential of hybrid catalyst composed polyoxometalates associated with metal nanoparticles for catalyzing the nitrate reduction. In these catalysts, the metallic nanoparticles and the POM entities are expected to work in tandem to catalyze the different steps of the nitrate reduction pathway.

Due to the wide utilization of fertilizers in agriculture, the increase of the concentration of nitrate ions in groundwater becomes a serious problem.[1] As groundwater is one of the most important source of drinking water, nitrate ions in water can directly affect human health. Nitrite ions are often discussed at the same time with nitrate ions, because nitrate can be converted to nitrite in saliva and nitrite is one important intermediate species of nitrate reduction. High concentration of nitrate and/or nitrite has been demonstrated as a cause of methemoglobinemia, which is a fatal disease for infants under six months.[2] Some studies have shown that an extremely high dose of nitrates and/or nitrite could cause several types of cancer.[3] Hence, the development of efficient and clean technology is needed to eliminate nitrate from waters. While biological processes and physicochemical processes are the most widely applied methods to remove nitrate ions from drinking water,[3] some obvious disadvantages are known. The biological denitrification system might be contaminated by the dead bacteria, while the physiochemical processes cannot reduce nitrate to harmless compounds but only concentrate them from water to brine, thus further treatment is required.[4,5,6]

Therefore, the development of electrochemical processes which is able to reduce nitrate to anoxic nitrogenated species is a promising approach. Electrochemical processes present also others advantages such as low cost and the possibility to combine with diverse treatment processes.

As mentioned above, the main difficulties of the electroreduction of nitrate and/or nitrite ions are due to: i) the sluggish reaction kinetics which cause high reaction overpotential and current; ii) the large number of possible intermediate species and products. Therefore, the achievement of a selective product formation, for example toward nitrogen for environmental water depollution without producing other undesired products such as ammonia is a challenge.[7,8]

In the literature, different types of catalyst have been studied for nitrate and nitrite reductions. In natural enzymes, such as nitrate reductase, which can catalyze nitrate to nitrite, the molybdopterin (molybdenum-sulfur) complex being the active site.[9] Other molecular catalysts have been also investigated such as Mo complex.[10] However, most of the studies were carried out with monometallic and bimetallic catalysts. Based on the published studies, Pt and Pd were found to be very efficient for nitrite reduction while Pd is selective towards the formation of N_2.[11,12] In the case of nitrate reduction, Cu and Ag were considered as the most efficient monometallic catalyst.[8,13] Further improvements of the catalytic efficiency requires an increased level of complexity in the catalyst design.

In this thesis, the work will focus on the development of new catalyst associating polyoxometalates (POMs) and nanoparticles (NPs). POMs are inorganic anionic clusters formed by oxo species of transition metals with one or more bridging oxygen atom.[14] The possibility to insert transition-metal cations while keeping the structure intact makes POMs interesting for many catalytic reactions such as olefins oxidation by $[Ru^{III}(H_2O)(SiW_{11}O_{39})]^{5-}$,[15] DMSO reduction by $[Ru^{III}(H_2O)(PW_{11}O_{39})]^{4-}$,[16] CO_2 reduction by $(TOA)_6[\alpha\text{-}(\square)Co^{II}(SiW_{11}O_{39})]$,[17] etc.

In particular, the nitrite ions reduction can be catalyzed by various POMs such as $[SiW_{12}O_{40}]^{4-}$ and the catalysis occurring at the POM reduction potentials.[18] However, only Cu-, Ni-substituted POMs and few Fe-substituted POMs have been found to be active towards nitrate reduction. In 2001, Keita and co-workers have published a Dawson-type POM $[Cu^{II}P_2W_{15}Mo_2]^{8-}$ which was active for nitrate reduction in pH 3 solution. A comparing work between $[Cu^{II}P_2W_{15}Mo_2]^{8-}$, $[P_2W_{15}Mo_2O_{61}]^{10-}$ and $[P_2W_{15}Mo_3O_{62}]^{6-}$ have been also reported. It was shown that the presence of Cu ions was indispensable to catalyze nitrate reduction.[19] After that, some studies have been performed to increase the number of Cu ions in the POMs structure leading to design the POMs such as $[Cu^{II}_{20}Cl(OH)_{24}(H_2O)_{12}(P_8W_{48}O_{184})]^{25-}$.[20,21] They have shown that the catalytic current intensity increases with the number of Cu atoms in structure.

However, at current stage, nitrate reduction study was used only for testing the properties of POMs in solution. Due to the high solubility in aqueous solution, POMs are not good candidates to be used as heterogeneous catalyst.

POMs are also well known to interact with the surface of metals. POMs being able to act as stabilizer at nanoparticles' surface and protect them from agglomeration.[22] Recently, Iamr and his co-workers have immobilized Cu-substituted POMs and prepared AgNPs on electrode surface in the presence of polymers.[23] The prepared films were active for nitrate reduction.

In the present thesis, we will try to understand the influencing factors on nitrate catalysis by using different Cu-substituted POMs and compare the activities when POM are associated with copper alendronate complexes. The photocatalytic reduction of silver ions in the presence of POM was widely studied in our group.[24,25] The size and shape of the silver nanoparticles can be controlled depending on the operating conditions. Thus, Ag@POM nanoparticles will be investigated for their ability to form heterogeneous catalyst toward nitrate and/or nitrite reduction. At the last part, the POMs have been immobilized into metal-organic frameworks (MOFs) in order to improve the stability during the reduction reaction. We will investigate if POMs conserve their electrochemical properties and catalytic properties after being inserted into MOFs.

References

1. Bogardi, I., Kuzelka, R. D. & Ennenga, W. *Nitrate contamination: exposure, consequence and control*. (Springer, 1991).
2. World Health Organization. *Nitrate and nitrite in drinking water, background document for development of WHO guidelines for drinking-water quality*. (World Health Organization, 2011).
3. Brinkmann, T., Santonja, G. G., Yukseler, H., Roudier, S. & Sancho, L. D. *Best Available Techniques (BAT) reference document for common waste water and waste gas treatment/management systems in the chemical sector*. (European Integrated Pollution Prevention and Control Bureau, 2016).
4. Soares, M. I. M. Biological denitrification of groundwater. *Water Air Soil Pollut.* **123**, 183–193 (2000).
5. Bohdziewicz, J., Bodzek, M. & Wąsik, E. The application of reverse osmosis and nanofiltration to the removal of nitrates from groundwater. *Desalination* **121**, 139–147 (1999).
6. Samatya, S., Kabay, N., Ksel, Y., ßerref Arda, M. S. & Yü Ksel, M. Removal of nitrate from aqueous solution by nitrate selective ion exchange resins. *React. Funct. Polym.* **66**, 1206–1214 (2006).
7. Duca, M. & Koper, M. T. M. Powering denitrification: the perspectives of electrocatalytic nitrate reduction. *Energy Environ. Sci.* **5**, 9726-9742 (2012).
8. Rosca, V., Duca, M., de Groot, M. T. & Koper, M. T. M. Nitrogen cycle electrocatalysis. *Chem. Rev.* **109**, 2209–2244 (2009).
9. Magalon, A., Fedor, J. G., Walburger, A. & Weiner, J. H. Molybdenum enzymes in bacteria and their maturation. *Coord. Chem. Rev.* **255**, 1159–1178 (2011).
10. Majumdar, A., Pal, K. & Sarkar, S. Necessity of fine tuning in Mo(iv) bis(dithiolene) complexes to warrant nitrate reduction. *Dalt. Trans.* **11**, 1927–1938 (2009).
11. Duca, M., Van Der Klugt, B. & Koper, M. T. M. Electrocatalytic reduction of nitrite on transition and coinage metals. *Electrochim. Acta* **68**, 32–43 (2012).
12. Wada, K., Hirata, T., Hosokawa, S., Iwamoto, S. & Inoue, M. Effect of supports on Pd-Cu bimetallic catalysts for nitrate and nitrite reduction in water. *Catal. Today* **185**, 81–87 (2012).
13. Dima, G. E., De Vooys, A. C. A. & Koper, M. T. M. Electrocatalytic reduction of nitrate at low concentration on coinage and transition-metal electrodes in acid solutions. *J. Electroanal. Chem.* **554–555**, 15–23 (2003).
14. Pope, M. T. & Müller, A. Polyoxometalate chemistry. *Angew. Chem., Int. Ed.* **30**, 34–48 (1991).
15. Tayebee, R. Epoxidation of some olefins with hydrogen peroxide catalyzed by heteropolyoxometalates. *Asian J. Chem.* **20**, 8–14 (2008).
16. Rong, C. & Pope, M. T. Lacunary polyoxometalate anions are acceptor ligands characterization of some tungstoruthenate heteropolyanions and their atom transfer reactivity. *J Am Chem Soc* **114**, 2932–2938 (1992).
17. Girardi, M., Blanchard, S., Griveau, S., Simon, P., Fontecave, M., Bedioui, F. & Proust, A. Electro-assisted reduction of CO_2 to CO and formaldehyde by $(TOA)_6[SiW_{11}O_{39}Co(\_)]$ polyoxometalate. *Eur. J. Inorg. Chem.* **2015**, 3642–3648 (2015).
18. Dong, S., Xi, X. & Tian, M. Study of the electrocatalytic reduction of nitrite with silicotungstic heteropolyanion. *J. Electroanal. Chem.* **385**, 227–233 (1995).
19. Keita, B., Abdeljalil, E., Nadjo, L., Contant, R. & Belgiche, R. First examples of efficient participation of selected metal-ion-substituted heteropolyanions in electrocatalytic nitrate reduction. *Electrochem. commun.* **3**, 56–62 (2001).
20. Mal, S. S., Bassil, B. S., Ibrahim, M., Nellutla, S., Tol, J., Dalal, N. S., Fernandez, J. A. Lopez, X., Poblet, J. M., Biboum, R. N., Keita, B. & Kortz. U. Wheel-shaped Cu_{20}-tungstophosphate $[Cu_{20}X(OH)_{24}(H_2O)_{12}\text{-}(P_8W_{48}O_{184})]^{25-}$ ion (X = Cl, Br, I) and the role of the halide guest. *Inorg. Chem.* **48**, 11636–11645 (2009).
21. Zhang, Z., Qi, Y., Qin, C., Li, Y., Wang, E.B., Wang, X., Su, Z. & Xu, L. Two multi-copper-containing heteropolyoxotungstates constructed from the lacunary keggin polyoxoanion and the high-nuclear spin cluster. *Inorg. Chem.* **46**, 8162–8169 (2007).
22. Troupis, A., Gkika, E., Hiskia, A. & Papaconstantinou, E. Photocatalytic reduction of metals using polyoxometallates: recovery of metals or synthesis of metal nanoparticles. *C. R. Chim.* **9,** 851–857 (2006).
23. Imar, S., Maccato, C., Dickinson, C., Vagin, M. & Mccormac, T. Enhancement of nitrite and nitrate electrocatalytic reduction through the employment of self-assembled layers of nickel- and copper-substituted crown-type heteropolyanions. *Langmuir* **31**, 2584–2592 (2015).
24. Costa-Coquelard, C., Schaming, D., Lampre, I. & Ruhlmann, L. Photocatalytic reduction of Ag_2SO_4 by the Dawson anion α-$[P_2W_{18}O_{62}]^{6-}$ and tetracobalt sandwich complexes. *Appl. Catal. B Environ.* **84,** 835–842 (2008).
25. Ruhlmann, L., Costa-Coquelard, C., Sorgues, S. & Lampre, I. Photocatalytic reduction of Ag_2SO_4 by dawson-derived sandwich complex. *Macromol. Symp.* **270**, 117–122 (2008).

Chapter I

Introduction and literature review

Chapter I Introduction and literature review

1 Nitrate and Nitrite: environmental issues and electrocatalytic reduction

1.1 Environmental issues and general treatments

1.1.1 Environmental issues

Groundwater is the most important source of drinking water, especially in areas lack of surface water.[1] As the quality of groundwater directly affects human health, its contaminations are a serious concern. Nitrate is the most common chemical contaminant in the groundwater, which may cause public health risk and environmental pollution. The nitrate ion (NO_3^-) is one of the most stable species in the nitrogen cycle, but it can be reduced in environment to nitrite ion (NO_2^-) by microbial action.[2] Nitrite ion is less stable than nitrate and it can be easily reduced to other compounds or be oxidized to nitrate. In human body, nitrate can be converted to nitrite in saliva by oral microflora. Hence, these two compounds are often discussed together.

Throughout the world, the expansion and intensification of agriculture have led to increasing utilizations of fertilizers, which has degraded the water quality. The most common inorganic nitrogen fertilizers contain nitrate and/or ammonium, which are necessary for plants growth. When the nitrate supply is higher than the amount needed by the plants, the nitrate excess accumulates into the soil or moves with the ground water. This results into the eutrophication of water and may cause harmful algal blooms, water column anoxia and fish mortality.[3] Vegetables that contain the highest concentration of nitrate are spinach, salad mix, mustard greens and cole slaw. Sodium nitrite is also used as a food preservative and antibacterial agent especially in prepared meats (such as ham and bacon) due to its ability to block the growth of bacteria (clostridium botulinum and listeria monocytogenes). It also contributes to the characteristic color and flavor of the cured meat.[4]

Even though healthy human adults can be exposed to large amounts of nitrate in a short term, long-term effects are still uncertain. High concentration（$>10\ mg\cdot L^{-1}$）of nitrate in water or 3 $mg\cdot L^{-1}$ nitrite in drinking water have been identified as a cause of methemoglobinemia (also called ‘blue baby syndrome’),[5] which causes fatal blood disorder in infants under six months of age. The symptom of nitrate/nitrite poisoning infants is the blue or lavender skin color, especially around eyes and mouth. The cause of methemoglobinemia is generally that the red blood cells are unable to carry oxygen from the lungs to the other part of the body. Some studies show that consuming nitrate-contaminated drinking water during early pregnancy may increase the risk of birth defects.[6] An extremely high dose of nitrate could cause several types of cancer, for example colorectal, bladder, urothelial, gastric and brain tumor, in laboratory animals. Consume high dose of nitrite-contaminated water in short-term can cause adrenal hypertrophy in laboratory animals. Growth inhibition is observed in rats after two years of oral administration with 5% sodium nitrate. Another long-term effect of nitrite in various animals is vitamin A deficiency. Nitrite can deplete vitamin A in non-ruminants by destroying it in the gut lumen under acidic condition.[6] Nitrite can also form N-nitroso compounds in stomach and these N-nitroso compounds are carcinogenic in all animal species tested.[6]

As a result, legislation generally limits the nitrate level in water and the maximum concentration in the range of 10 - 40 ppm is set out in most countries based on the World Health Organization guideline.[6] Water containing more than 40 ppm nitrate is not considered as drinkable. Nitrite level in drinking water is usually below 0.1 ppm.[6] Consequently, the development of efficient and clean technology to eliminate nitrate from water has attracted considerable attention.

1.1.2 General treatments

Nitrate easily dissolves in water and is very difficult to remove. Simple household treatments as filtration, disinfection and boiling are not efficient for nitrate removal. Nowadays, biological processes and/or physicochemical processes are used to remove nitrate ions from drinking water. Biological denitrification is a type of anaerobic respiration that uses nitrate as an electron acceptor, by microbiological reduction of nitrate into its elemental state nitrogen.[7,8] This proceeds through a stepwise reduction of intermediate species, like nitrite, nitric oxide, nitrous oxide, dinitrogen, etc. In the nature, there are more than twenty species of strictly denitrifying bacteria, hence the preparation of the biofilm is not obvious. However, there some shortcomings of this method. First, without the addition of a carbon source, biological denitrification is difficult. Second, it may lead to contamination by dead bacteria. The absence of contamination should be checked before utilization in drinking water treatment. The last issue is the presence of residual organics.

Reverse osmosis is a filtration method which allows water to pass through microscopic pores in a filter membrane under high pressure. In such a way, only the pure water is able to get through.[9,10] Other contaminants like nitrate and other inorganic chemicals (Ca and Mg) are physically too large and thus unable to pass through the pores of the systems. This method can reject about 83 - 92% of the nitrate in drinking water. Problems associated with reverse osmosis membranes include high cost and the fouling, compaction and deterioration with time. These problems are caused by deposition of soluble materials, organic matter, suspended and colloidal particles, pH variations and chlorine exposure, which means that the reverse osmosis process requires pretreatment.

The ion exchange process involves the passage of nitrate-containing water through a Strong Base Anion (SBA) exchange resins bed on which nitrate ions are exchanged for chloride or bicarbonate ions until the resin exhausted.[11] The exhausted resin is regenerated by using a concentrated solution of sodium chloride or sodium bicarbonate. This method is efficient except for water containing high amount of sulfate ions, due to the competition between sulfate ions and nitrate ions.

Even though ion exchange process and reverse osmosis processes are identified as the Best Available Technologies (BAT) by United Stated Environmental Protection Agency (USEPA) for nitrate removing technique,[5] these two processes cannot transfer nitrate into harmless compounds but can only concentrate nitrate from water to brine, which require further treatment. None of these methods is satisfactory for the durable treatment of groundwater. In this thesis, reductions of nitrate and nitrite by electrochemical technique are investigated. With this method, nitrate can be reduced to anoxic nitrogenated species. The others advantages of electrocatalytic denitrification, such as low cost, no requirement of addition of chemicals and the possibility to combined with other treatment processes, make electrochemical techniques attached much attentions.[12]

1.2 Electrocatalytic reduction of nitrate and nitrite

Electrochemical process is generally operated in room temperature under atmospheric pressure. Nitrate and/or nitrite are reduced at the cathode to form other nitrogen-containing compounds (such as nitrogen, ammonia or nitrous oxide). However, metal ions present in the electrolyte can also be reduced at the cathode to form solid deposited surface on the cathode as parasite reaction.[13] At the anode, the main reaction is the oxidation of water to oxygen gas. Only few technologies can reduce nitrate to N_2 based on the published reports.

1.2.1 Mechanism of nitrate reduction

Nitrate reduction is a very complex process. The main cathodic products during electroreduction of nitrate are NO_2^-, NO_2, NO, N_2O, N_2, NH_2OH, NH_2NH_2 and NH_3, as nitrogen has oxidation states from +5 to -3.[14] During electrochemical reduction, a mixture of products is often observed and it is still not clear if the products are obtained in a sequence of electron transfer steps or in parallel reduction mechanisms. Because of this, the determination of the number of transferred electrons in the reduction is not sufficient to identify the products. The experimental parameters like the pH of solution, the electrode potential and the cathode material influence the reaction products. The mechanisms for nitrate reduction are still poorly understood. Based on natural denitrification, formation of N_2 is performed through a stepwise reaction:[14]

$$NO_3^- \rightarrow NO_2^- \rightarrow NO \rightarrow N_2O \rightarrow N_2$$

Thermodynamically, several products such as NO (g), N_2 (g) or ammonium ion (NH_4^+) can be obtained during the reduction of nitrate ions:

$$NO_3^- + 4H_3O^+ + 3e^- \rightleftharpoons NO(g) + 6H_2O \qquad E^0 = 0.958\ V/NHE \qquad (1)$$

$$2NO_3^- + 12H_3O^+ + 10e^- \rightleftharpoons N_2(g) + 18H_2O \qquad E^0 = 1.246\ V/NHE \qquad (2)$$

$$NO_3^- + 10H_3O^+ + 8e^- \rightleftharpoons NH_4^+ + 13H_2O \qquad E^0 = 0.875\ V/NHE \qquad (3)$$

The desired process is the reduction of NO_3^- to N_2 (reaction 2) but the reaction rate is slow. In the literature, it is commonly accepted that the rate-determining step of nitrate reduction is the formation of nitrite. The redox half-equation of NO_3^-/NO_2^- is written as:

$$NO_3^- + 2H_3O^+ + 2e^- \rightleftharpoons NO_2^- + 3H_2O \qquad E^0 = 0.835\ V/NHE \qquad (4)$$

Once formed, nitrite is one of the most reactive compounds in the nitrogen cycle and nitrite reduction is considerate as the selectivity-determining step. The list of nitrite reduction products and the corresponding equilibrium potentials are given below:

$$2NO_2^- + 8H_3O^+ + 6e^- \rightleftharpoons N_2(g) + 12H_2O \qquad E^0 = 1.520\ V/NHE \qquad (5)$$

$$NO_2^- + 2H_3O^+ + e^- \rightleftharpoons NO(g) + 3H_2O \qquad E^0 = 1.202\ V/NHE \qquad (6)$$

$$2NO_2^- + 6H_3O^+ + 4e^- \rightleftharpoons N_2O(g) + 9H_2O \qquad E^0 = 1.396\ V/NHE \qquad (7)$$

$$NO_2^- + 6H_3O^+ + 4e^- \rightleftharpoons NH_3OH^+ + 7H_2O \qquad E^0 = 0.673\ V/NHE \qquad (8)$$

$$NO_2^- + 8H_3O^+ + 6e^- \rightleftharpoons NH_4^+ + 10H_2O \qquad E^0 = 0.897\ V/NHE \qquad (9)$$

Both nitrate and nitrite reductions consume proton. Thus, low pH favors the reaction from the thermodynamics point of view. As mentioned before, the formation of N_2 is going through N_2O in natural denitrification. The reaction can be written as:[15]

$$N_2O + 2H_3O^+ + 2e^- \rightleftharpoons N_2(g) + 3H_2O \qquad E^0 = 1.770\ V/NHE \qquad (10)$$

This step is difficult to achieved because only few catalysts are able to perform the reduction of N_2O before this intermediate desorbs from the surface and lost to the electrolyte as a product.[14]

The high overpotential, the sluggish reaction kinetics and the side products during multi-electron transfer reactions are the main problems during nitrate reduction. The catalyst should be not only efficient but also selective to promote the formation of N_2 rather than other toxic products. Hence, the development of efficient catalysts has been widely investigated.

1.2.2 Catalysts for the nitrate and nitrite reduction

1.2.2.1 Monometallic catalysts

Nitrite reduction has been widely studied on different metal surfaces. In solution, the nitrite is affected by the pH-dependent homogeneous-phase equilibrium, such as the acid-base equilibrium HNO_2/NO_2^- ($pK_a = 3.39$).[16] Therefore, NO_2^- is predominant in neutral/alkaline pH media, while HNO_2 is dominant at $pH < 2$. The electrocatalytic responses might then also be expected with the pH. Besides, HNO_2 decomposes slowly into NO and NO_2 in acidic media, which is also a reactive substance on most metal and non-metal electrodes:

$$2HNO_2(aq) \rightleftarrows NO(aq) + NO_2(aq) + H_2O \qquad (11)$$

It was also found that nitrite reduction in acidic media is not sensitive to the nature of the anion of the supporting electrolyte.[17]

A comparing work of nitrite reduction on transition metals (Ru, Rh, Ir, Pd and Pt) and coinage metals (Cu, Ag and Au) was published by Duca and his co-workers[18] in both acidic media and alkaline media. In acidic media, a direct HNO_2 reduction is observed for all of these electrodes except Ir. The formation of NO obtained from HNO_2 disproportionation in solution and followed by an overall reaction to form N_2O is observed on all of the active metals:

$$NO_{ads} + NO_{aq} + 2H_3O^+ + 2e^- \rightleftarrows N_2O + 3H_2O \tag{12}$$

In alkaline media, the activity of transition metals is ranked as Rh ~ Ru > Pt > Ir. Based on Tafel slope analysis, the rate-determining step is assumed to be the conversion of NO_2^- to NO species. No N_2O is detected in solution, which indicates that NO is strongly adsorbed on metal surface.[18] Duca and his co-workers[18] have proposed a model for the electrocatalytic NO reduction where the presence of NO in solution is necessary for the formation of N_2O and N_2, which occurs through a weakly adsorbed NO dimer that can only form when NO is in solution. This dimer is a necessary precursor for N_2O formation, while N_2 is formed directly by N_2O reduction. Among coinage metals, only Cu is active for nitrite reduction in alkaline media and the final product is NH_3. A high overpotential for nitrite reduction on Ag or Au surface is obtained which occurs simultaneously with hydrogen evolution.[19]

Nitrate reduction on Pt surface has already been investigated at the beginning of last century. In acidic media, the activity of Pt surface is very low toward nitrate reduction.[20] Since the nitrate is reduced at potential close to the hydrogen evolution onset, high coverage of hydrogen inhibits the adsorption of nitrate, which leads to a decrease of catalytic activity. The main product from the nitrate reduction on Pt surface is characterized by Infrared Reflection (IR) measurements. The presence of adsorbed NO is observed at a fixed potential in nitrate reduction (0.122 V *vs.* RHE in 0.5 $mol{\cdot}L^{-1}$ H_2SO_4). Based on Differential Electrochemical Mass Specstroscopy (DEMS) measurement, neither N_2O nor N_2 is formed during the nitrate reduction and the final products are NH_2OH and NH_3.

Koper and his co-workers[21] have reported a comparison works toward nitrate reduction on various metal electrodes in acid solution. Among the transition metals, the catalytic activity is ranked as: Rh > Ru > Ir > Pd ≈ Pt. The reaction order on noble metal in acidic media is usually lower than one, which suggests that adsorption step proceeds the rate-determining step. On the coinage metal, Cu is the most active surface for nitrate reduction followed by Ag and Au (Cu > Ag > Au).[21] The DEMS measurement in 0.5 mol·L^{-1} H_2SO_4 shows that the product on Cu surface is NO, whereas no N_2O is produced.[18] On Cu surface, the chemisorption energy (ca. 100 kJ·mol^{-1})[22] is much lower than the one on Pt surface, thus NO_{ads} is able to desorb from Cu electrode to form NO_{sol}. Thus, the formation of N_2O is expected because the reaction from NO to N_2O is a non-catalytic reaction on Cu surface.[23] However, N_2O and N_2 are not observed on bulk Cu, due to the oxidation of Cu by the nitrate and NO solution. In contrast, the gaseous products (N_2O and N_2) are observed with a Pd electrode covered by a full monolayer of under-potential deposition (upd) Cu, which is attributed to the higher stability toward oxidation of the upd Cu layer compared to bulk Cu electrode.[24] The details will be presented in the following part devoted to bimetallic catalysis. The above mechanism makes Cu a better choice for nitrate reduction even though its activity can be influenced by H_{ads} and anions present in solution like with Pt electrode. Tafel slopes for nitrate reduction on different transition metals and coinage metals are found close to 120 mV/decade, suggesting that the first electron transfer step is the rate-determining step. Thus, the rate-determining step is:

$$\mathrm{NO_3^- + 2H_3O^+ + 2e^- \rightleftharpoons NO_2^- + 3H_2O} \qquad \mathrm{E^0 = 0.835\ V/NHE} \qquad (4)$$

Other metals such as mercury, indium, cadmium and tin have also been studied toward nitrate reduction in acidic media.[15] A high overpotential is found with these metals. Kyriacou and his co-workers[25] have observed a significant negative potential -2.8 V *vs.* Ag/AgCl with tin which is able to reduce nitrate to dinitrogen in 0.1 mol·L^{-1} K_2SO_4 with a high selectivity (92%).

1.2.2.2 Bimetallic catalysts for nitrate and nitrite reduction

While copper electrode is shown to be able to catalyze nitrate reduction, a high selectivity toward the formation of dinitrogen is still difficult to achieve.

More recently, bimetallic and trimetallic catalysts have attracted more attention for their high activity and selectivity. Vorlop and Tacke have firstly demonstrated the effectiveness of bimetallic catalysts in 1989.[26] They studied bimetallic system composed of a precious metal (Pt or Pd) and a promoter (Cu, Ni, Fe, Sn, In or Ag). In this bimetallic system, the promoter catalyzes nitrate to nitrite reduction and the precious metal is involved in the reduction of nitrite into further products. Pd has better conversion efficiency and selectivity than Pt. As Cu is an active catalyst, despite its instability at potential in alkaline solution (0.1 mol·L^{-1} KOH),[27] bimetallic catalysts composed of Pd and Cu have been widely studied in acidic[28,24] and alkaline[29,24] media. As mentioned before, Pd-Cu bimetallic electrode is a good catalyst for the selective reduction of nitrate to N_2. The Cu sites take care of the fast reduction of nitrate to NO and N_2O, whereas Pd is the most selective and best catalyst for the reduction of NO and N_2O to N_2. The metal ratio is a key role in the catalytic performance. Okuhara and his co-workers[30] have investigated the influence of the Pd/Cu radio. As presented in Fig. I.1, the hydrogenation step occurs during the NO_2^- reduction. Pd sites with different coordinative unsaturation at the Pd particles surfaces show different selectivities for hydrogenation. The edge and corner sites of Pd possess high abilities for hydrogenation and consequently increase the formation of NH_3. The terrace sites of the Pd have mild hydrogenationability and N_2 would be favorably formed.

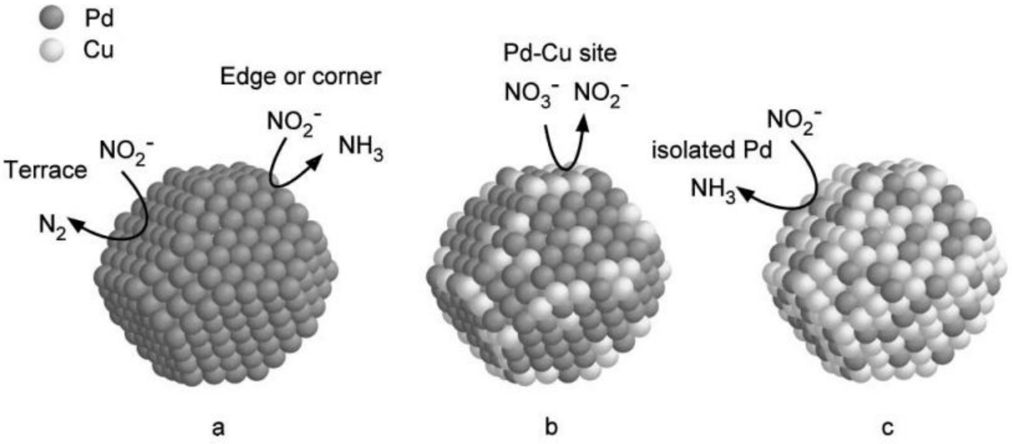

Figure I.1: Model elaborated from XRD patterns of Pd and Pd-Cu particles a) 5 wt% Pd, b) 5 wt% Pd - 0.6 wt% Cu, c) 5 wt% Pd - 3 wt%. (Reprinted from the reference 30 with the permission from Elsevier).

Other metal, like tin, can also enhance the selectivity to N_2 formation on Pd surface. Generally, mechanism for NO_x reduction with bimetallic catalysts is assumed to be the same than with monometallic catalyst. The rate-determining step is still the first electron transfer and the reaction order is lower than one.

Pt have also been studied even though it is not the best catalyst. The most promising combination with Pt is Pt/Sn.[31,32] Other combinations such as Cu–Ni[33], Pt-Ge[34] and Pt-Bi[35] also exhibit a catalytic effect but the selectivity towards N_2 remains a challenge.

1.2.2.3 Enzymatic and molecular catalyst

The clearest indication for the mechanism towards nitrate reduction reaction comes from the investigation of natural enzymes. Nitrate reductase catalyzes the reduction of nitrate to nitrite in the nitrogen cycle. Most of them have a molybdopterin (molybdenum-sulfur) complex as active site. With the addition of other co-factors such as iron-sulfurs and hemes, the electron transfers can be mediated within the enzyme. An example of nitrate reductase is shown in Fig. I.2.[36] Other electrochemical studies have modified nitrate reductase on graphite or gold electrodes. An overview of the catalytic mechanism of selected nitrate reductase is described in references 37 and 38.

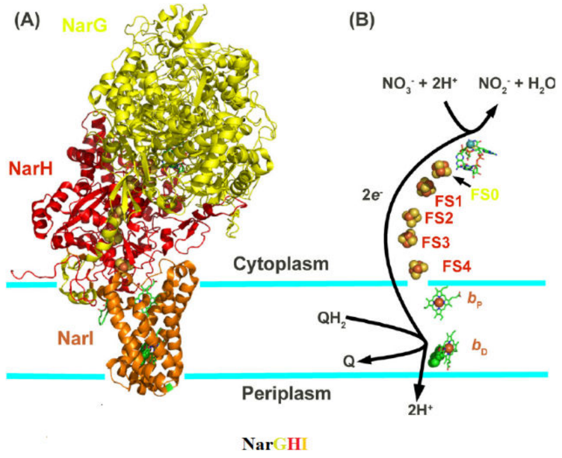

Figure I.2: Nitrate reductase NarGHI as an archetypal complex iron-sulfur molybdoenzyme (CISM). A) The three subunits of NarGHI are embedded in the cytoplasmic membrane with the NarGHI subunits oriented towards the cytoplasmic compartment. B) The NarGHI electron transport for nitrate reduction. (Reprinted from reference 36 with the permission from Elsevier).

As the metal centre Mo is considered as the active site for catalysis, other Mo complexes were tested for their ability to reduce nitrate.[39] Mo center is capable of forming a bond to an oxygen atom of a nitrate ion and produce nitrite.[40]

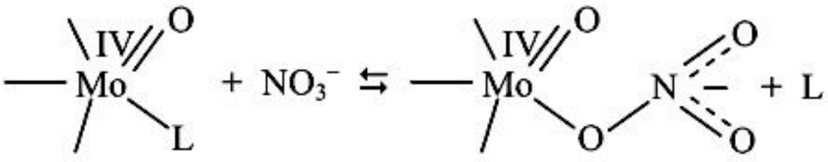

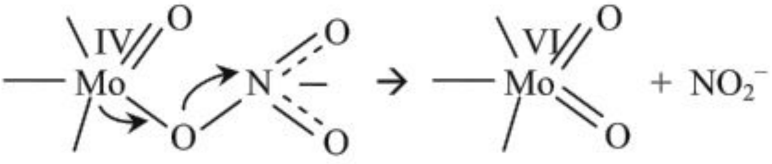

Figure I.3: Mechanism of nitrate reduction by Mo complex (Reprinted from reference 40 with the permission from Springer).

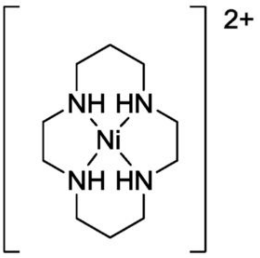

Metal cyclams (cyclam = 1,4,8,11-tetra-azacyclotetradecane) catalyze also nitrate reduction and have been reported by Taniguchi and his coworkers for the first time.[41] The Co- and Ni-cyclams have been studied on a mercury electrode and the main product is hydroxylamine. Metal phthalocyanine-modified electrode have been studied in alkaline media where the main product is ammonia.[42]

More recently, polyoxometalates (POMs) have been considered for their catalytic properties towards nitrite and nitrate reduction, due to the possibility to insert transition metals into structure as well as their ability to form nanoparticles. The details will be presented in the next part.

2 Polyoxometalates

Polyoxometalates (POMs) are inorganic anionic clusters formed by oxo species of transition metals with one or more bridging oxygen atom. POMs normally contain at least three metal atoms, mainly from group V or VI (vanadium, niobium, tantalum, molybdenum and tungsten) in their highest oxidation state with (heteropolyoxometalates) or without (isopolyoxometalates) heteroatoms.[43] They have been known since the XIX century and the ammonium salt of $[PMo_{12}O_{40}]^{3-}$ is the first compound discovered by Berzelius.[44] Keggin is the first phosphotungstic anion and its structure was elucidated in 1934.[45] Only after the discovery of their applications in various domain such as catalysis and non-linear optics, these compounds have been widely studied.

2.1 Structure of polyoxometalates

Various structures of POMs have been studied, among which the Lindqvist, Anderson, Keggin and Dawson types (Fig. I.4, left) are the most well known.

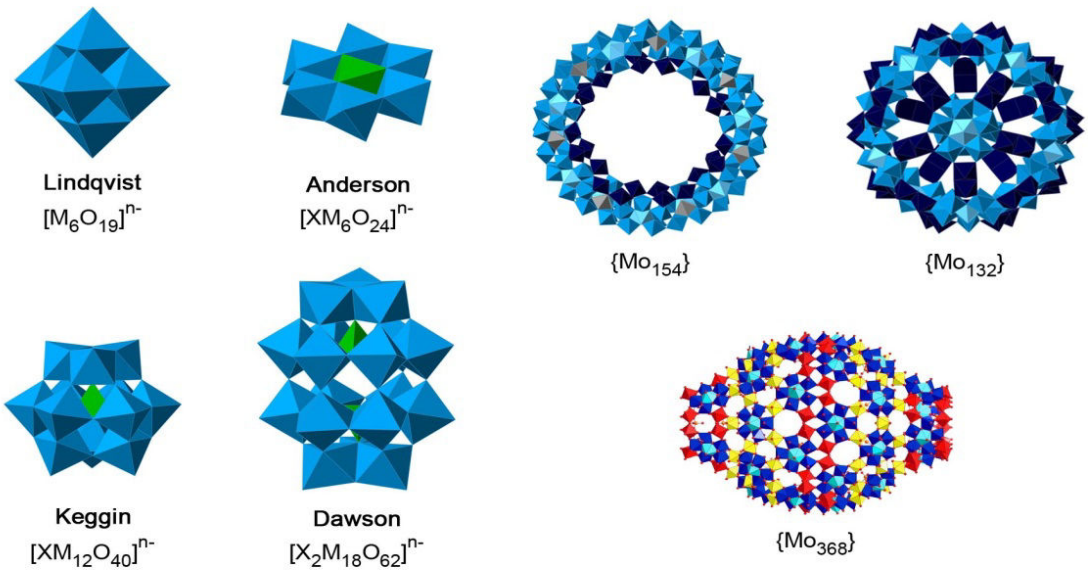

Figure I.4: Representation of different structures of polyoxometalates (POMs).

Most POMs are based on molybdenum or tungsten and POMs containing vanadium, niobium or tantalum also exist. Modification of these compounds can be made by removing M = O (mainly M = Mo or W) entities and replacing them by other transition metals or groups. New structures were also obtained by joining two or more known structures via transition metal ions. For example, the synthesis of nano-wheel $\{Mo_{154}\}$[46], nano-sphere $\{Mo_{132}\}$[47] and a giant cluster $\{Mo_{368}\}$[48] have been published (Fig. I.4, right). As a consequence, the number of compounds, which can be prepared, is very large and can be designed according to the requirements.

Lacunary POMs are derived from plenary parent structures by loss of one or more addenda atoms. For example, the corresponding lacunary POMs for Keggin type $[XM_{12}O_{40}]^{n-}$ or Dawson type $[X_2M_{18}O_{62}]^{n-}$ are $[XM_{11}O_{39}]^{n-}$ and $[X_2M_{17}O_{61}]^{n-}$ respectively.[49] Incorporation of metal ions in these vacant sites usually preserves the POMs structure but sometime can also lead to isomerization or even loss or gain of tungsten. In any case, the resulting products are usually good candidates for magnetic, electrochemical and catalytic studies.

The functionalized polyoxometates are allowed to tune the redox and acid-base properties and solubility of POMs, in order to enhance their stability and catalysis activities.[50] For example, Proust and her co-workers[51] have reported the first carbene derivative polyoxometalate [(*cis*-RuL^{Me}_2)($(PW_9O_{34})_2$(*cis*-WO_2)]$^{13-}$ (L^{Me} = 1,3-dimethyllimidazoli-dine-2-ylidene) represented in Fig. I.5A. Mialane and his co-workers[52] have reported a spherical Keggin-type structure $[((Ni^{II}(H_2O))_2(\mu_{1.1}\text{-}N_3)(A\text{-}\alpha\text{-}PW_{10}O_{37}))^{6-}$, which is the first structurally characterized azido POM (Fig. I.5B). The magnetic studies reveal that the Ni^{II} centers are ferromagnetic coupling in a Ni^{II} μ-1,1-azido complex. Photochromic POM compounds can be obtained by covalently grafting a photochromic group such as amino group. The complexes $Na_6(N(C_2H_5)_2H_2)_2[(Mo_3O_8)_4(O_3PC(C_3H_6NH_3)(O)PO_3)_4]{\cdot}25H_2O$ and $Na_7(N(C_4H_9)_4)[(Mo_3O_8)_4\text{-}(O_3PC(C_3H_6NH_3)(O)PO_3)_4]{\cdot}43H_2O$ as well as their association with spiropyran have been investigated (Fig I.5C).[53] More details in functionalization of POMs were presented in references 54-56.

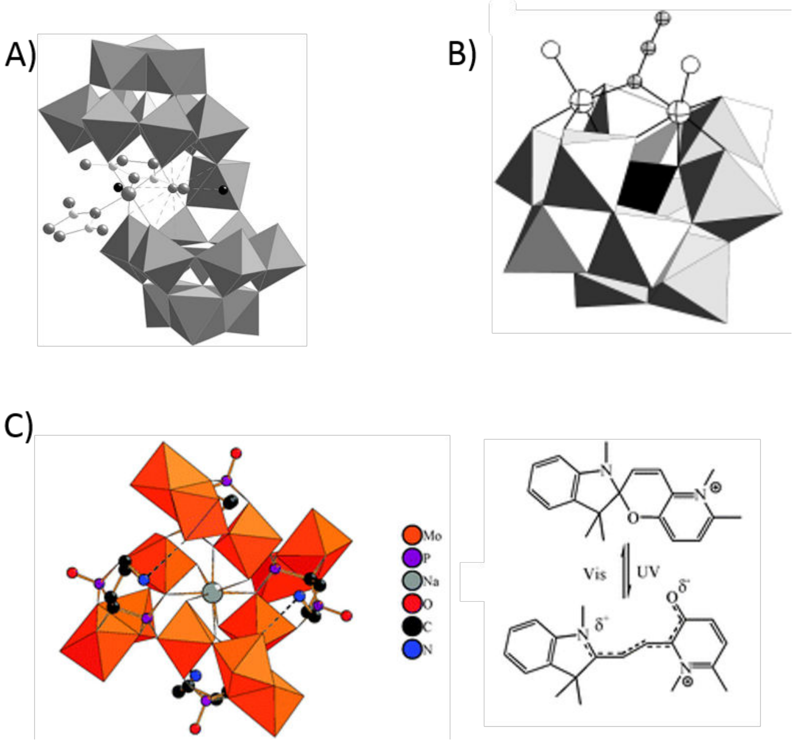

Figure I.5: Structures of A) $Na_4K_9[(PW_9O_{34})_2(cis\text{-}WO_2)(cis\text{-}RuL^{Me}_2)]\cdot 23H_2O$ reprinted from reference 51, Copyright (2017) American Chemical Society. B) $[(Ni^{II}(H_2O))_2(\mu_{1.1}\text{-}N_3)(A\text{-}\alpha\text{-}PW_{10}O_{37})]^{6-}$ reprinted from reference 52 with the permission from John Wiley and Sons. C) Structure of $[(Mo_3O_8)_4(O_3PC(C_3H_6NH_3)(O)PO_3)_4]^{8-}$ unit and the representation of the closed and open forms of the spiropyran countercation SP^+. These representations are reprinted from reference 53 with the permission from Royal Society of Chemistry.

2.2 Properties of polyoxometalates

2.2.1 Stability

The stability is a major concern in catalytic reaction. Generally, POMs possess good thermal stabilities. The stability of some Keggin-type POMs decreases in the order: $H_3[PW_{12}O_{40}]$ (465°C) > $H_4[SiW_{12}O_{40}]$ (445°C) > $H_3[PMo_{12}O_{40}]$ (375°C) > $H_4[SiMo_{12}O_{40}]$ (350°C).[55] Substituting metals and counter cations often affect the stabilities of POMs, the substituted POMs are usually unstable than their unsubstituted parents.

POMs usually have remarkable stability in acidic and neutral aqueous solution, as well as oxidative stabilities. Indeed, POMs are only stable in certain pH range because at high pH, the polyhedral subunits leave the skeletons in the presence of water and the structure decomposes.

2.2.2 Molecular magnetism

Polyoxometalates (POMs) are used as an example in molecular magnetism for studying the magnetic exchange and the electron delocalization.[56] Magnetic POMs have been classified into two groups namely the spin-localized POMs and the spin-delocalized mixed-valence (MV) POMs.

In spin-localized POMs, the magnetic moments remain localize on the 3d or 4f magnetic metal ions. Various paramagnetic cations can be encapsulated by lacunary POMs at specific sites, creating well-defined magnetic molecular with controlling of the nuclearity and the type of magnetic interactions. Co^{II}-substituted POM has been widely studied on magnetic exchange ion. A high-spin $S = 3/2$ with an unquenched orbital momentum, hence exhibiting a large spin anisotropy.[57]

The electron acceptor ability of POMs allows to prepare the mixed-valent (MV) POMs. POMs are the only example in coordination chemistry of high-nuclearity MV clusters. The electronic complexity of MV POMs is much higher than that of the spin-localized magnetic clusters. Bi-reduced $[PW_{12}O_{40}]^{5-}$ is considered as a typical example of diamagnetic MV POM. The diamagnetism of this Keggin-type POMs is due to a multi-route super-exchange mechanism.[58] A strong stabilization of the singlet is observed with this POM. The study have also been performed on Wells-Dawson type POMs in which electrons move in two central 6-membered rings.[59] The single ground state stabilization is obtained as in the case of Keggin-type POM.

Recently, POMs are used as model systems in molecular magnetism towards the design of single-molecule magnets (SMMs) and as molecular spin-qubits in nanospintronic devices. A detail description is summarized by Clemente-Juan, Coronado and their co-workers.[56]

2.2.3 Photochemical behaviors of POMs

In spectroscopy, POMs are characterized by O-M charge transfer bands in the UV-near visible area. The photoexcitation of POMs in this wavelength range induces the electron transfer from their highest occupied molecular orbital (HOMO) to their lowest unoccupied molecular orbital (LUMO).[60] The absorption spectra of several different types of POMs are shown in Fig. I.6.

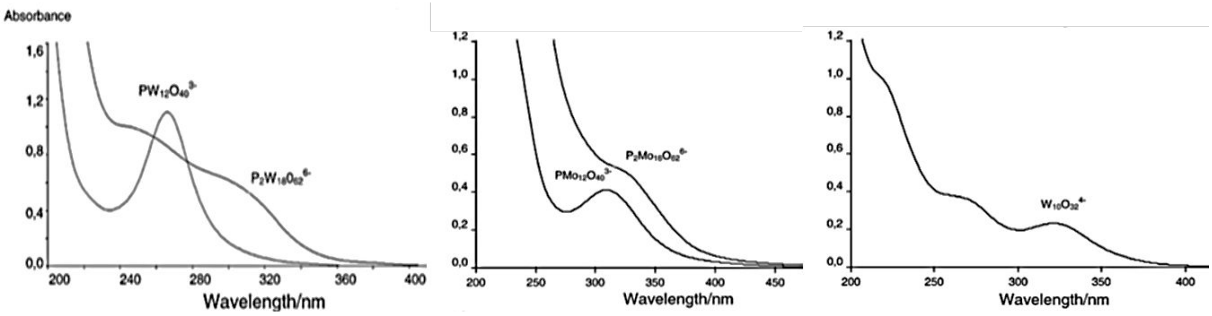

Figure I.6: Examples of UV-visible spectra of certain POMs. (Reprinted from reference 61 with permission from Royal Society of Chemistry).

In the presence of electron donors such as alcohol, the excited POM ($POM^{*,n-}$) is easily converted to the reduced POM ($POM^{*,(n+1)-}$), which subsequently reacts with electron acceptors and return to the original POM. The reduced POM becomes blue due to the intra electron transfer between adjacent metal ions, M-M charge transfer (CT) bands (also called intervalence band, M^{VI}-O-M^{V} →M^{V}-O-M^{VI}, if M = Mo or W) and an absorption can be observed around 500 - 700 nm. The absorbance of reduced POM increases with the number of the exchanged electrons as shown in Fig. I.7A'. The color of POM-containing solution becomes intense blue after exchanging five or six electrons (red line and blue line in Fig I.7A').

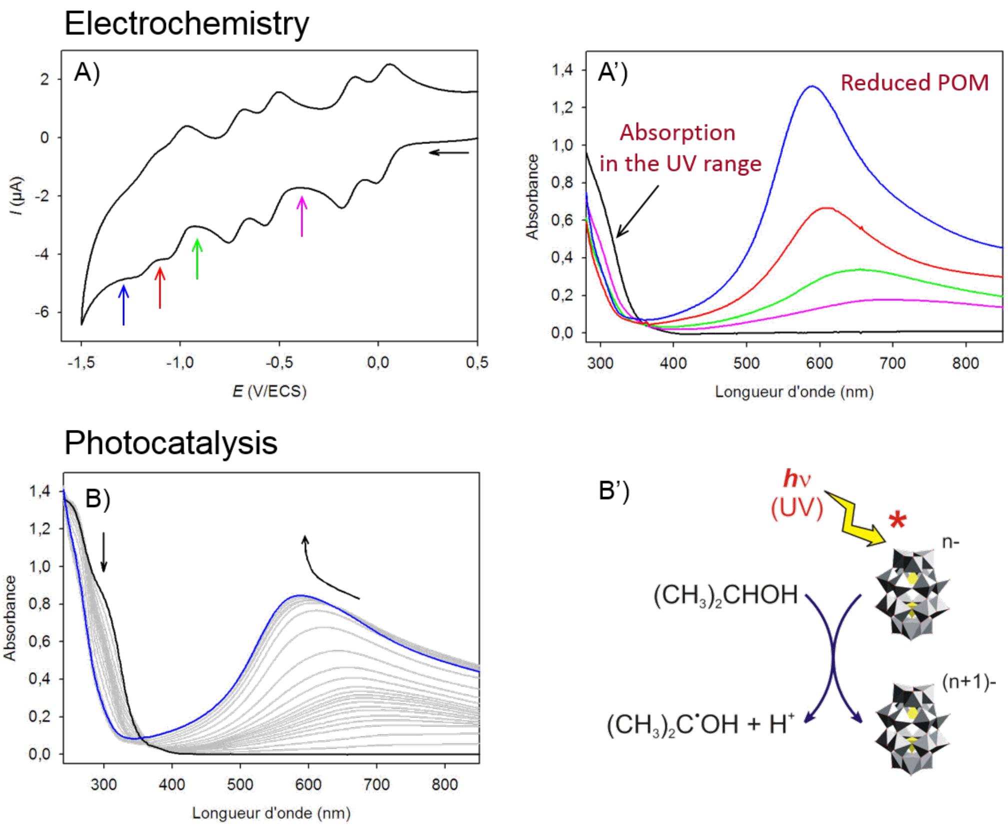

Figure I.7: A) Cyclic voltammogram of 2.5×10^{-5} mol·L^{-1} α-$K_6[P_2W_{18}O_{62}]$ in the solution of 0.5 mol·L^{-1} Na_2SO_4 at pH 5.5, present six reversible monoelectronics reductions waves. A') UV-visible spectra of 2.5×10^{-5} mol·L^{-1} α-$K_6[P_2W_{18}O_{62}]$ in the solution of 0.5 mol·L^{-1} Na_2SO_4 at pH 5.5 (—) without electrolysis; (—) electrolysis at -0.40 V vs. SCE; (—) electrolysis at -0.90 V vs. SCE; (—) electrolysis at -1.12 V vs. SCE; (—) electrolysis at -1.30 V vs. SCE. B) UV-visible spectra during the photocatalysis of a solution contains 2.5×10^{-5} mol·L^{-1} α-$K_6[P_2W_{18}O_{62}]$ and 0.13 mol·L^{-1} propan-2-ol. B') illustration of photocatalysis of POM under UV illumination in the presence of propan-2-ol.

Similar UV-visible spectra can be obtained by using photocatalysis with the same concentration of POM under illumination of UV light, in the presence of 0.13 mol·L^{-1} propan-2-ol as shown in Fig.I.7B. With a long enough illumination time, the intensity of the absorbance of the intervalence band is stabilized around 0.85. The absorbance value is in fact between 0.65 (red line in Fig. I.7A', 5 electrons exchanged) and 1.30 (blue line in Fig. I.7A', 6 electrons exchanged) which corresponds to the maximum intensity obtained after complete electrolysis after the fifth and the sixth reduction wave. This observation indicates that the solution obtained in photocatalysis is a mixture of 5-times reduced POM$^{(n+5)-}$ and 6-times reduced POM$^{(n+6)-}$. Hence, the maximum of exchanged electrons in solution with 0.13 mol·L^{-1} propan-2-ol seems to be six electrons in the case of the Dawson-type polyoxometalate (Unpublished work from prof. Laurent Rulmann).

2.2.4 Electrochemical behaviors of POMs

The redox properties of polyoxometalates are characterized by their ability to accept as well as to release several electrons in distinct redox steps, while keeping their structure intact. The reduction is often accompanied by protonation in acidic media depending on the pK_a of the produced polyoxometalates. A pH increase shifts the redox potentials to more negative values and often splits the two-electron waves to two one–electron pH-independent waves.

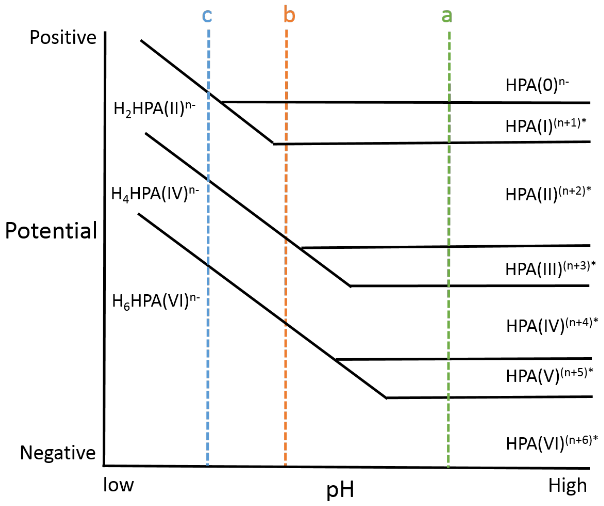

Figure I.8: Schematic representation of electrochemical behavior of heteropolyanions (HPA), the roman numerals show the number of electrons added to the oxidized anion 0: $(HPA)^{n-}$ (Reproduced from reference 49. Copyright (2017) American chemical society).

The relationship between the potentials of the reversible redox pairs of heteropolyanions (HPAs) and pH is represented in Fig. I.8.[49] It represents well the redox behaviors of the Dawson-type POM. By decreasing pH, the two one-electron waves convert to one two-electron wave, which is generally accompanied by the addition of two protons. A change of redox potentials about 50 mV/pH is observed when decreasing pH, thus the potentials measured in the line b and the line c can be obtained with certain POMs. However, all the case represented in Fig. I.8 can be observed just depending of the pH of the solution.

The electrochemical behavior of each POM exhibits a different feature due to their different redox potentials, pK_a and stabilities.

2.3 Photocatalytic properties of POMs

2.3.1 Photocatalytic oxidation of organic pollutant

The irradiation with UV-near visible light makes POMs powerful oxidizing agents, which are capable to ‘destroy’ a great variety of organic compounds.

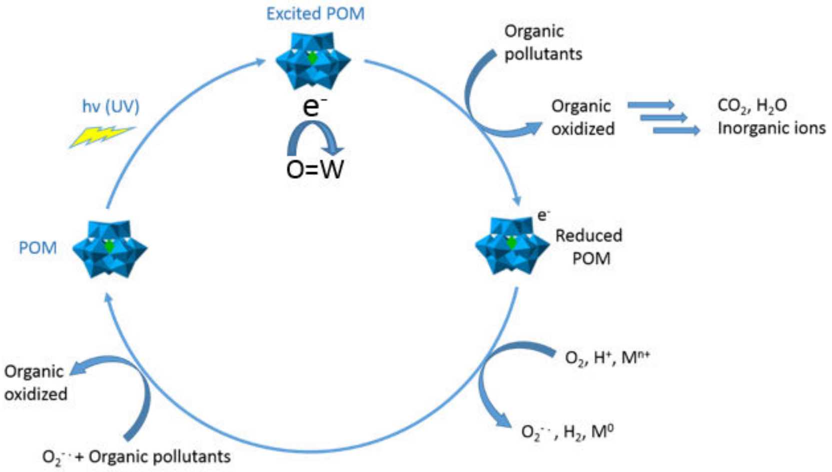

Figure I.9: Photocatalytic circle of degradation of organic pollutants.

Under UV illumination, POMs pass into its excited state, POM^*. The excited POM anions often possess better performance than their ground states and they are able to oxidize the organic substrates (organic pollutants). After oxidation to intermediate products, organic pollutants can be fully mineralized to CO_2, H_2O and inorganic anions in aerated media. At the same time, reduced POMs are formed and further they can be re-oxidized by dioxygen (aerated solution). The reactions are given below:

$$\mathrm{POM} \overset{\mathrm{hv}}{\rightarrow} \mathrm{POM}^*$$

$$\mathrm{POM}^* + \text{organic pollutants} \rightarrow \mathrm{POM}^- + \text{oxidation products}$$

$$^{\cdot}\mathrm{OH} + \text{organic pollutants} \rightarrow \text{oxidation products} \rightarrow\rightarrow\rightarrow \mathrm{CO_2} + \mathrm{H_2O} + \text{inorganic anions}$$

$$\mathrm{POM}^- + \mathrm{O_2} \rightarrow \mathrm{POM} + \mathrm{O_2^{-\cdot}}$$

$$\mathrm{O_2^{-\cdot}} + \text{organic pollutants} \rightarrow\rightarrow\rightarrow \text{oxidation products} \rightarrow\rightarrow$$

$$\rightarrow \mathrm{CO_2} + \mathrm{H_2O} + \text{inorganic anions}$$

POMs can only be active in UV range. Some photosensitizers, such as fullerene, complexes of ruthenium and porphyrin, can be added to POMs in order to absorb the visible light. For instance, our group has published the method electro-copolymerization of different organo-POMs with zinc β-octaethylporphyrin (ZnOEP) on ITO electrode to build original photovoltaic electrode. The photocurrent response is used to examine the photovoltaic performance.[62]

Heterogeneous POMs photocatalysts can be also modified on other support materials such as TiO_2, ZrO_2, etc. Moreover, $[Ru^{III}(H_2O)SiW_{11}O_{39}]^{5-}$ have been shown to catalyze photoreduction of CO_2 to CO in the presence of amines as reducing agents.[63]

2.3.2 Photocatalytic reduction-precipitation of metal ions

Recovery of metal in environment is also an attractive topic because many metals are toxic (such as chromium and mercury) or valuable (such as copper, silver, gold, palladium and platinum).

Papaconstantinou and his co-workers[64] have firstly reported $[PW_{12}O_{40}]^{3-}$ stabilized Ag, Au, Pt and Pd metal nanoparticles by reacting the corresponding metal-salt ($Ag^{I}NO_3$, $HAu^{III}Cl_4$, $K_2Pt^{IV}Cl_6$ and $Pd^{II}Cl_2$) with $H_3[PW_{12}O_{40}]$ in the presence of propan-2-ol or 2,4-dichlorophenol. The formation of metal nanoparticles can be followed by UV–visible spectroscopy. Color change of the solution is generally observed during the reduction. Fig. I.10 shows an example of NP@POM formation in solution.

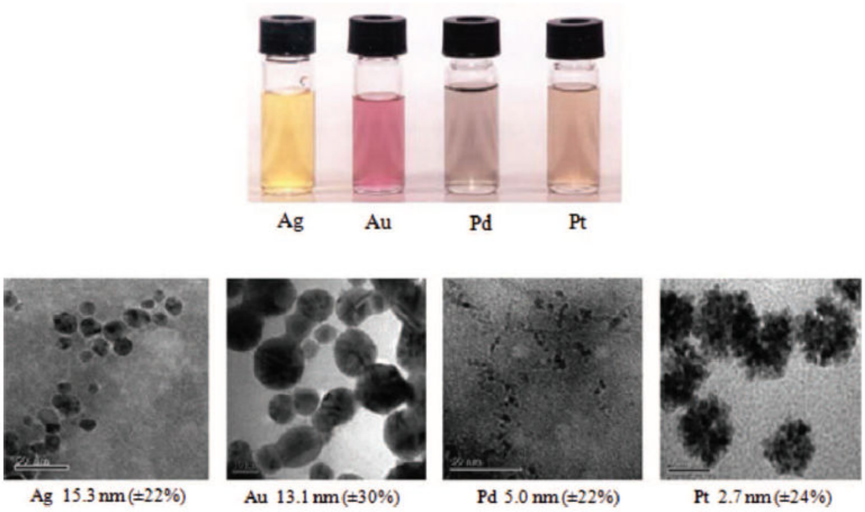

Figure I.10: (Upper) photos of different nanoparticles solutions obtained upon mixing of a reduced $[SiW_{12}O_{40}]^{5-}$ ($c = 3.5\times10^{-4}$ mol·L^{-1}) with the corresponding metal ions solution $Ag^{I}NO_3$, $H_2Pt^{IV}Cl_6$, $Pd^{II}Cl_2$ ($c = 10^{-4}$ mol·L^{-1}) and $HAu^{III}Cl_4$ (final concentration 10^{-3} mol·L^{-1}), pH 5, $\theta = 20$°C (Reprinted from reference 64 with the permission from John Wiley and Sons).

A more detail mechanism of reduction of Ag^+ by the Dawson-type POM α-$[P_2W_{18}O_{62}]^{6-}$ was reported by Ruhlmann and his co-workers.[65] Under illumination of UV light, a direct photochemical excitation of POM is observed in the presence of propan-2-ol, which may be written as:

$$\alpha - [P_2W_{18}O_{62}]^{n-} + (CH_3)_2CHOH \overset{hv}{\rightarrow} \alpha - [P_2W_{18}O_{62}]^{(n+1)-} + (CH_3)_2C^{\cdot}OH + H^+$$

In fact, Ag^+ reduction occurs immediately at the onset of the irradiation without introduction time, which suggests that the Ag^+ reduction begins from the first reduced forms of POM. However, the reduction of Ag^+ by reduced POM is not thermodynamically favored, considering that the potential of the (Ag^+/Ag^0) is -1.75 V *vs.* NHE (with only one Ag(0)). This potential has been deduced from radiolysis experiments.[66] Two explanations were suggested:

- The complexation between Ag^+ and POM may lead to a change in the redox potentials. In fact, the electric field created by the charges is in favor of the electron transfer from the reduced POM to Ag^+. Moreover, the possibility of the reduction of Ag^+ in the complex by an excited reduced POM cannot be excluded, all the more, a compound in the excited state is always better reductant than when it is in the ground state.

- An initiation step is possible with a complexation of Ag^+ and alcohol radicals produced upon the photoreduction of the POM. The mechanism can be written as:

  $$(CH_3)_2C^{\cdot}OH + Ag^+ \rightarrow [Ag(CH_3)_2C^{\cdot}OH]^+$$
  $$[Ag(CH_3)_2C^{\cdot}OH]^+ + Ag^+ \rightarrow Ag_2^+ + (CH_3)_2CO + H^+$$

  The association and coalescence reactions of Ag^+ ions and silver clusters lead to the formation of silver nanoparticles with the increase of the nuclearity.

  $$Ag^0 + Ag^+ \rightarrow Ag_2^+$$
  $$2Ag_2^+ \rightarrow Ag_4^{2+}$$
  $$Ag_m^{x+} + Ag_p^{y+} \rightarrow Ag_{(m+p)}^{(x+y)+}$$

  Besides, the redox potential of silver clusters increases with their nuclearity (n). Hence, the direct reduction of the Ag_n^+ clusters by the reduced POMs become thermodynamically favorable when the redox potential of the AgNPs becomes higher than the potential of the couple E^0 ($POM^{n-}/POM^{(n+1)-}$). The illustration of this mechanism is shown in Fig. I.11.

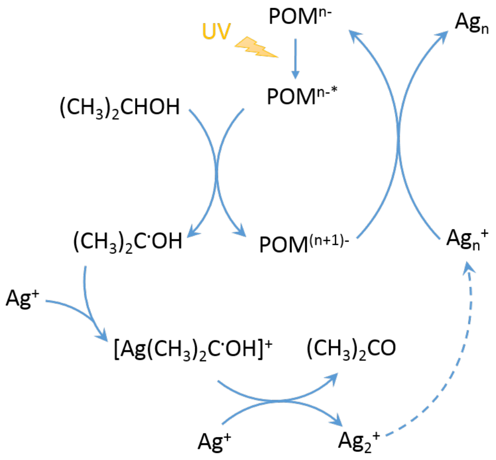

Figure I.11: Mechanism of the photoreduction of silver ions in the presence of POM.

The nanoparticles formed during this process can be imaged by using cryogenic Transmission Electron Microscopy (cryo-TEM) as published by Weinstock and his co-workers.[67] The picture shows clearly a monolayer of POMs at surface of Au nanoparticles, which can protect nanoparticles from agglomeration.

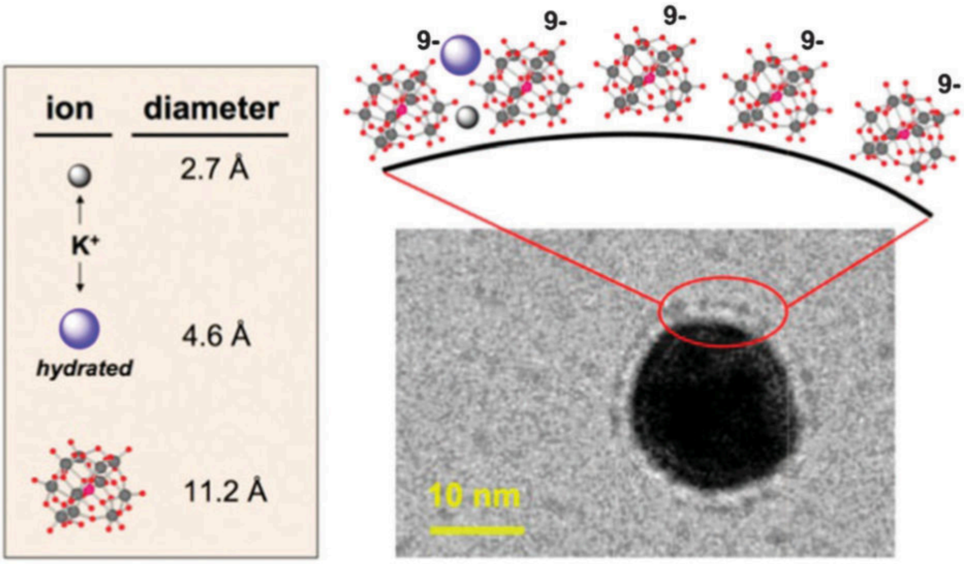

Figure I.12: Scale model of $[AlW_{11}O_{39}]^{9-}$ and K^+ counter cations on the surface of a 14-nm Au nanoparticle. The left diagram illustrates the crystallographic and hydrated sizes of K^+ relative to a scale model of $[AlW_{11}O_{39}]^{9-}$ (Reprinted from reference 67. Copyright (2017) American Chemical Society).

A selective reduction of certain metal ions from a mixture can be achieved by using POMs with suitable redox potentials. Reduced POMs are able to reduce metal ions efficiently with more positive redox potentials, while leave intact metal ions with more negative redox potential. Illumination of $[SiW_{12}O_{40}]^{4-}$ (1 mmol·L^{-1}) in a pH 3 solution (0.1 mol·L^{-1} $NaClO_4$) containing Pd^{II} (0.1 mmol·L^{-1}), Cu^{II} (1 mmol·L^{-1}) and Ni^{II} (0.7 mmol·L^{-1}) leads to complete formation of the corresponding NPs. For instance, the reduction of the Pd^{II} to Pd^0 is completed in 1 hour under UV illumination while leaving Cu^{II} and Ni^{II} ions intact. Ni^{II} ions cannot attract electrons from the reduced POMs due to its more negative reduction potential. In the case of Cu^{II} ions, photoreduction of Cu^{II} by $[SiW_{12}O_{40}]^{4-}$ have been reported, but note that copper do not precipitate immediately upon irradiation with UV-near Vis light. An induction period is observed at the start of metal deposition, attributed to the formation of the "stable" Cu^{I} intermediates.[68] It needs to mention that no characterization of formed copper nanoparticles is presented in their work. However, in the presence of Pd^{II}, the nanoparticles of palladium is easier to be obtained due to the greater redox potential compare to Cu^{II}/Cu^{I} reduction (E^0 (Pd^{II}/Pd^0) = +0.987 V and E^0 (Cu^{II}/Cu^{I}) = +0.153 V *vs.* NHE).[69]

2.4 Electrocatalysis by POM

Polyoxometalates (POMs) have also been studied for their ability as donors or acceptors of several electrons without structural change. The possibility to insert different transition-metal cations into structure makes POMs interesting for various catalytic reactions. Several examples of electrocatalytic reactions are given below.

2.4.1 Electrocatalytic oxidation by POMs

The oxidation catalytic reactions in the presence of POMs are often observed with transition metal-substituted heteropolyanions. The transition metals accept oxygen from oxygen donors and formed oxometal species M=O which are able to oxidize various compounds.

- NAD(P)H oxidation:[49] $NAD(P)H/NAD(P)^+$ is an important redox couple in biological system. Nadjo and his co-workers have demonstrated several vanado-tungsto phosphoric POMs such as α_2-$[P_2V^VW_{17}O_{62}]^{7-}$, which satisfies all the necessary criteria for the oxidation of NADH. The overall reduction reaction is presented as:

  $$2\alpha_2-[P_2V^VW_{17}O_{62}]^{7-}+NADH \rightleftharpoons 2\alpha_2-[P_2V^{IV}W_{17}O_{62}]^{8-}+NAD^++H^+$$

  The stoichiometry of NADH to POM was found to be 1:2 by spectrophotometry and coulometry. This indicates that POM acts as a one-electron oxidant. Others POMs such as α_2-$[P_2W_{17}O_{61}]^{8-}$ and α_2-$[P_2W_{17}MoO_{62}]^{8-}$ are also active in pH 7 solution (phosphate buffer).

- Me$_2$SO oxidation:[70] Me$_2$SO can be oxidized to Me$_2$SO$_2$ by $[Ru^{III}(H_2O)PW_{11}O_{39}]^{4-}$ in 1 mol·L^{-1} Na$_2$SO$_4$ + H$_2$SO$_4$ (pH 0) at 1.1 V *vs.* SCE in room temperature. The current efficiency can reach up to 92%.

- Alcohol oxidation:[71,72,73] alcohols (such as 1-phenyl-ethanol, benzylalcohol, propan-2-ol, ethanol, etc) can be oxidized in pH range from 1 to 6 with different transition-metal substituted POMs to form cyclohexanone, benzoic acid and other compounds.

- Olefins oxidation:[74,75] $[Ru^{III}(H_2O)SiW_{11}O_{39}]^{5-}$ catalyzes olefins oxidation at Pt electrode in 34% H$_2$O$_2$ (20 mmol·L^{-1}) + CH$_2$Cl$_2$ (20 mL) electrolysis to form aldehyde. Another example is to modify a POM with prepared Au nanoparticles over γ-Al$_2$O$_3$ by wet impregnation method. These catalysts are active for epoxidation of olefins under mild conditions.

2.4.2 Electrocataytic reduction by POMs

Electrocatalytic reduction by POMs is largely studied either in solution or after modified on electrode surface.

Homogeneous catalysis

- Chlorate ion reduction:[49] $[SiMo_{12}O_{40}]^{4-}$ and $[PMo_{12}O_{40}]^{3-}$ have been demonstrated to be active for chlorate ion reduction in acidic media (0.5 mol·L^{-1} H$_2$SO$_4$). The chlorate ion is reduced by the six electron reduced species in the presence of hydrogen to form chloride and water.

- Bromate reduction:[76] the reduction of bromate to bromide is catalyzed by reduced POM such as $[Nd^{III}(SiMo_7W_4O_{30})_2]^{13-}$ in acidic solutions (pH = 2.3 and pH = 3.8). The overpotential of bromate reduction is dependent on pH.

- H_2O_2 reduction:[77,78] a series of Fe-substituted POMs is active for H_2O_2 reduction such as $[Fe^{III}(H_2O)(SiW_{11}O_{39})]^{5-}$ and $\alpha_2\text{-}[Fe^{III}(H_2O)(P_2W_{17}O_{61})]^{8-}$. The Fe^{III} is the active site during the reduction reaction in aqueous system.

- DMSO reduction:[70] DMSO is reduced to dimethyl sulfide by $[Ru^{III}(H_2O)\ (PW_{11}O_{39})]^{4-}$ in sulfate solution (pH 2) with a turnover number of 30 and with ca. ~50% current efficiency.

- CO_2 reduction:[79] CO_2 can be reduced to CO and HCHO by $(TOA)_6[\alpha\text{-}(_\square)Co^{II}SiW_{11}O_{39}]$ (TOA = tetraoctyl ammonium; $_\square$ = vacant position of the coordination sphere of Co) at -1.5 V *vs.* Hg/ Hg_2Cl_2 in CH_2Cl_2 + 0.1 $mol{\cdot}L^{-1}$ $TBAPF_4$. The catalyst is selective towards CO_2 reduction, because no H_2 produced during electrolysis.

- *Heterogeneous catalysis*

For heterogeneous catalysis with POMs, emphasis is given to the fixation of the POM catalysts on solid surface, to achieve good recovery and recyclability besides high activity. Several methods have been used to fix active soluble POMs:

- Adsorption POMs on electrode surface: this is the easiest way to fix POMs on electrode by soaking electrode in an acidic aqueous POMs solution. Rong and Anson[80] reported a series of both Keggin-type, Dawson-type and transition-metal substituted POMs can adsorb spontaneously on glassy carbon and edge pyrolytic graphite (PG) electrode. Other supports such as gold and mercury electrode were also studied.[80] The adsorbed POMs increase the negative charge on the surface thus influencing the heterogeneous electron-transfer rate. A three-dimensional multilayer catalyst containing $[SiW_{12}O_{40}]^{4-}$ and poly(4-vinyl-pyridine) (PVP) was prepared by Layer-by-Layer method. The properties can be modulated by varying the soaking time. Other examples of POMs/polycations films are reported and based on their electrocatalytic studies, POMs conserve their catalytic properties after being fixed on electrode surface.[81]

- Entrap POMs in polymer: POMs can be entrapped to a polymer-coated surface by electrostatic incorporation or be immobilized simultaneously with the electropolymerization step. Polymer matrixes like poly(aniline)[82], poly(thiophene)[83], poly(acetylene)[84] and poly(1-naphthol)[85] were studied. In many cases, POMs incorporated in polymer films exhibit similar electrochemical and electrocatalytic properties to POMs dissolved in solution.

- Electrodeposition POMs on electrode surface: POMs can be electrodeposited on electrode surface under a constant potential: Keita and Nadjo reported firstly the electrodeposition of $[SiW_{12}O_{40}]^{4-}$ on electrode in 1985.[86] After their seminal work, a large number of papers have been published about this method.[43,87,88]

Other methods including the encapsulation by MOFs[89,90] (metal organic frameworks) and the combination with various C/Si-based materials[91] have been also investigated.

3 Electroreduction of NO_x by polyoxometalates (POMs)

Electrocatalytic reduction of nitrate ions remains a big challenge since it is a multi-electronic process involving many intermediate species. POMs are multi-electron reservoirs thus a very promising candidate for nitrate reduction, especially transition-metal substituted POMs. Nitrite and nitric oxide are the most important intermediates during the electroreduction reactions, therefore their catalysis by POMs was also broadly studied.

3.1 Nitrite reduction

Electrocatalytic activity of POMs towards the reduction of NO_2^-/HNO_2 and NO was studied by Toth and his coworkers.[92] Since then, nitrite reduction is used as a classical test of the electrocatalytic properties of POMs.

In 1995, Dong and his co-workers[93] investigated, in more details, a Keggin-type POM $[SiW_{12}O_{40}]^{4-}$ which is active for nitrite reduction on glassy carbon electrode. Three redox peaks are observed while the first two waves (waves I and II) are independent of pH in a pH range of 1 to 5 and the third (wave III) shifts with pH (60 mV/pH). The cathodic current is proportional to the square root of the scan rate, indicating a diffusion-controlled process. At pH < 2, a significant current increase for all the three cathodic peaks can be observed after adding $NaNO_2$

into solution. The activity on the wave I is shown in Fig. I.13. left panel. The best current is obtained at pH 1 and then the catalytic current decreases at higher pH. At pH > 3, no catalytic response is observed in the range of +0.1 V to -0.4 V *vs.* Ag/AgCl, but a remarkable catalytic current occurs only at the third wave (see Fig. I.13 right panel).

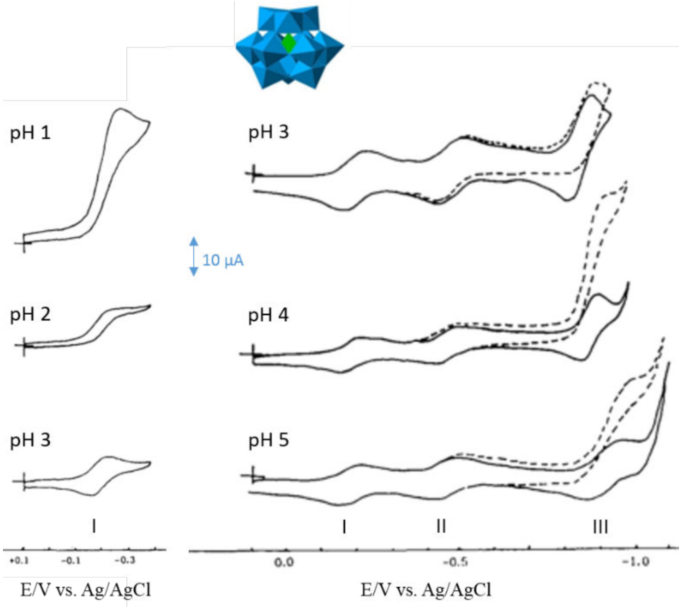

Figure I.13: Cyclic voltammograms of 1 mmol·L^{-1} [$SiW_{12}O_{40}$]$^{4-}$ at a glassy carbon electrode in solutions of varying pH with 2 mmol·L^{-1} $NaNO_2$, scan rate: 10 mV·s^{-1}. (Reproduced from reference 93 with the permission from Elsevier).

In a further work, they showed that the Fe^{III}-substituted Keggin POM and Fe^{III}-substituted Dawson POM have similar electrocatalytic properties.[78] McCormac and co-workers[94] have studied a series of transition-metal substituted (Ni^{II}, Co^{II}, Mn^{III}, Mn^{II}, Cu^{II} and Fe^{III}) Dawson-type POMs for their catalytic properties towards nitrite reduction (see Table I.1). All of these compounds are active at pH 2.0 with similar activity. At pH 4.5, the transition metals enhance the electrocatalytic efficiency. Fe^{II} and Cu^{II}-substituted POMs possess similar activities while the ones for Ni^{II} and Co^{II}-substituted POMs are lower. Hence, the presence of these metals and of the POMs units is necessary for the catalysis. Mn^{III}- and Mn^{II}-substituted Dawson-type POMs show no electroactivity during nitrite reduction at pH 4.5, a blockage effect is observed with the combination of Mn and POM unit.

POM	Electrocatalytic efficiency at pH 2	Electrocatalytic efficiency at pH 4.5
$[\alpha\text{-}P_2W_{18}O_{62}]^{6-}$	***	*
$[\alpha_2\text{-}P_2W_{17}O_{61}]^{10-}$	***	*
$[Fe^{III}(OH)_2(\alpha_2\text{-}P_2W_{17}O_{61})]^{7-}$	***	***
$[Cu^{II}(OH)_2(\alpha_2\text{-}P_2W_{17}O_{61})]^{8-}$	***	***
$[Ni^{II}(OH)_2(\alpha_2\text{-}P_2W_{17}O_{61})]^{8-}$	***	**
$[Co^{II}(OH)_2(\alpha_2\text{-}P_2W_{17}O_{61})]^{8-}$	***	**
$[Mn^{II}(OH)_2(\alpha_2\text{-}P_2W_{17}O_{61})]^{8-}$	***	-
$[Mn^{III}(OH)_2(\alpha_2\text{-}P_2W_{17}O_{61})]^{7-}$	***	-

*** Efficient for low concentrations of nitrite; ** Efficient for concentrations of nitrite where $[NO_2^-] = 20[POM]$;
* Not efficient for low concentrations of nitrite; - No electrocatalysis observed.

Table I.1: Electrocatalytic efficiencies of the unsubstituted and substituted Dawson-type POMs towards nitrite reduction at pH 2.0 and 4.5. (Reproduced from reference 94 with the permission from Elsevier).

Keita and co-workers[95] have shown the influence of Mo atom in two series of Fe- or Cu-substituted Dawson type POMs, which are α_2-$P_2W_{12}Mo_xO_{61}M$ and α_2-$P_2W_{13}Mo_xO_{61}M$ (where $_x$ is from 2 to 5 and M is the substituted metal cations), for nitrite reduction. Whatever the pH, the presence of Mo was beneficial for the reduction current intensity as well as the overpotential of the catalytic wave. This observation is in line with the fact that Mo is known as the active site in nitrite reductase.

The studies mentioned above involved homogeneous catalysis by POMs in solution. Some other studies have tried to fix POMs at a solid surface to design a heterogeneous catalyst.

For instance, a multilayer film of PDDA/$[P_2W_{18}O_{62}]^{6-}$ (PDDA = poly(diallymethylammonium chloride) is deposited on PVA/ITO (PVA = poly(vinyl alcohol)) through electrospining method (Fig. I.14). For long enough deposition time, PDDA/$[P_2W_{18}O_{62}]^{6-}$ selectively adsorbed on PVA nanofibers. $[P_2W_{18}O_{62}]^{6-}$ preserves its redox properties and the intensities of the current increase with the number of deposited layers. After adding $NaNO_2$, an increase of current is also observed from the first redox wave in pH 1 solution showing the electrocatalytical reduction of HNO_2.[96]

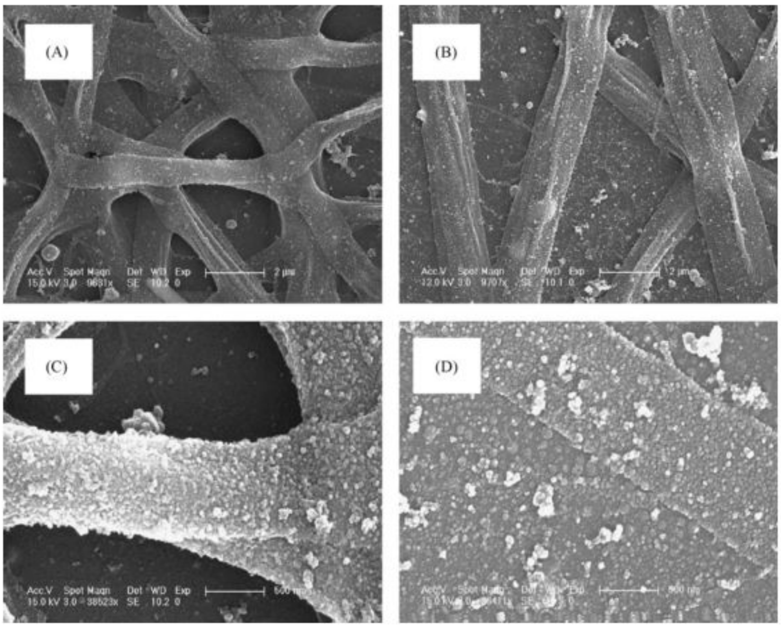

Figure I.14: SEM images of (PDDA/$[P_2W_{18}O_{62}]^{6-}$) deposited on the ITO electrode modified with PVA nanofibers with a electrospun time of 25 minutes (A, C) and 10 minutes (B, D). (Reprinted from reference 96 with the permission from Elsevier).

Liu and his co-workers[97] have immobilized POMs on an electrode surface embedded in a polyelectrolyte matrix to build an electrochemical sensor for NO detection. The reduction current is proportional to the NO concentration in a range from 1 $\text{nmol}\cdot\text{L}^{-1}$ to 10 $\mu\text{mol}\cdot\text{L}^{-1}$, which can be used as a low cost and water-based environment-friendly NO sensor.

3.2 Nitrate reduction

Many POMs are active for nitrite reduction, but only few transition-metal substituted POMs have demonstrated possess an activity for nitrate reduction in the homogeneous phase or after deposition on a support surface.

In 2001, electrocatalytic reduction of nitrate was achieved in the presence of POMs by Keita and coworkers.[98] $[Cu^{II}P_2W_{15}Mo_2]^{8-}$ Dawson-type POM was shown to be active for nitrate reduction just after the copper (II) reduction wave in pH 3 solution (Fig. I.15). A comparison study with $[P_2W_{15}Mo_2O_{61}]^{10-}$ and $[P_2W_{15}Mo_3O_{62}]^{6-}$ clarified the influence of the presence of copper ion. The electrocatalysis of nitrate reduction starts after the electrodeposited copper and in a potential domain that Mo^{VI} and W^{VI} are reduced. Hence, the final products might be different from those reduced on Cu bulk electrode. A Ni^{II}-substituted POM $[Ni^{II}P_2W_{15}Mo_2]^{8-}$ is also active for nitrate reduction, which mimic the catalytic effect of metal ion cyclams and related complexes.

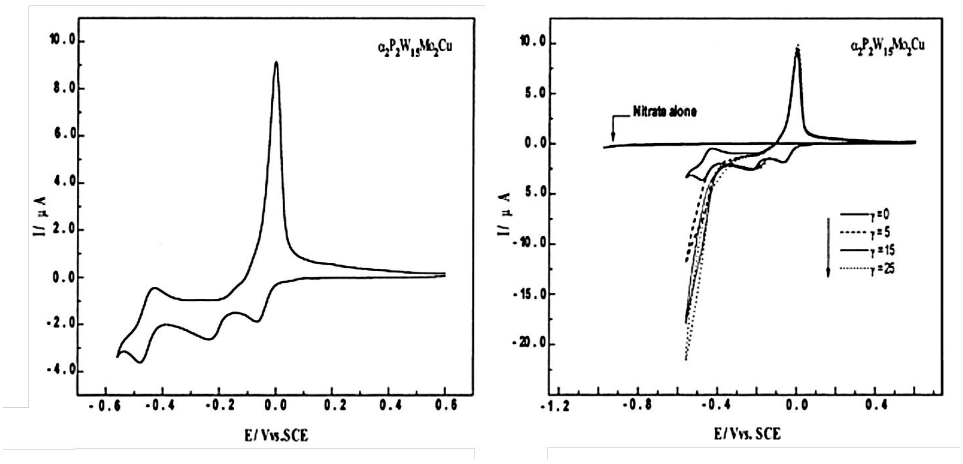

Figure I.15: Left) Cyclic voltammogram of the three first waves of 5×10^{-4} *mol·L*$^{-1}$ $[\alpha_2\text{-}P_2W_{15}Mo_2Cu]^{8-}$ *in 0.2 mol·L*$^{-1}$ $Na_2SO_4 + H_2SO_4$ *(pH = 3), scan rate: 2 mV·s*$^{-1}$*. (Right) after adding of increasing amounts of nitrate with the excess parameter* $\gamma = C^{\circ}_{NO3-}/C^{\circ}_{POM}$*. (Reprinted from reference 98 with the permission from Elsevier).*

Since then, various types of transition-metal substituted POMs for nitrate reduction were reported, most of them contains Cu or Ni ions.[99,100,101] Only few metal-substituted POMs have been demonstrated to be active for nitrate reduction. $[Fe^{III}_6(OH)_3(A\text{-}\alpha\text{-}GeW_9O_{34}(OH)_3)_2]^{11-}$ is active for nitrate reduction in pH 3 (0.4 mol·L^{-1} $CH_3COONa + CH_3COOCH$) when the first W reduction process was reached (Fig. I.16A).[102]

In 2007, Nadjo and his co-workers[103] demonstrated $[\{Sn^{II}(H_2O)(CH_3)_2\}_{24}\{Sn^{II}(CH_3)_2\}_{12}(A\text{-}PW_9O_{34})_{12}]^{36-}$ for nitrate reduction (Fig. I.16B). The single reversible wave of W (at -0.585 V *vs.* SCE) in POMs becomes irreversible at pH 2. The pH dependency of nitrate reduction is studied and the catalytic pattern moves to more negative potential by increasing pH. Nitrite ions reduced at a potential that 0.15 V more positive than nitrate with this POM. This POM is also active toward NO reduction. A sharp peak is observed during NO reduction at the potential of W reduction and it continues to increase with time.

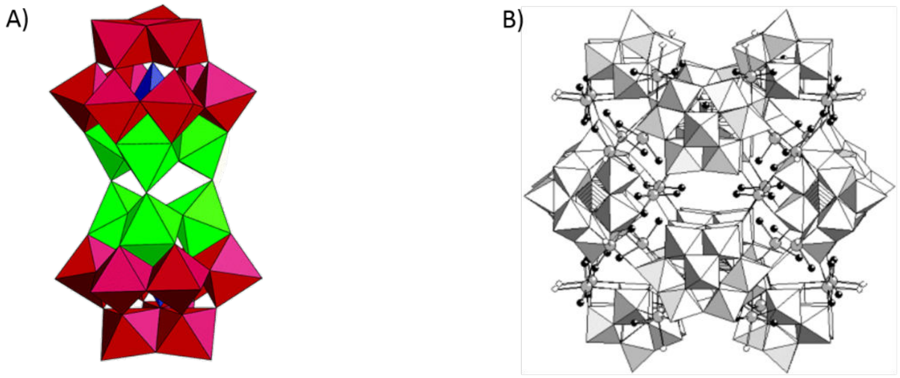

$[Fe^{III}_6(OH)_3(A\text{-}\alpha\ GeW_9O_{34}(OH)_3)_2]^{11-}$ $[\{Sn^{II}(H_2O)(CH_3)_2\}_{24}\{Sn^{II}(CH_3)_2\}_{12}(A\text{-}PW_9O_{34})_{12}]^{36-}$

Figure I.16: Structures of A) $[Fe^{III}_6(OH)_3(A\text{-}\alpha\text{-}GeW_9O_{34}(OH)_3)_2]^{11-}$ *reprinted from reference 102, Copyright (2017) American Chemical Society. B)* $[\{Sn^{II}(H_2O)(CH_3)_2(H_2O)\}_{24}\{Sn^{II}(CH_3)_2\}_{12}(A\text{-}PW_9O_{34})_{12}]^{36-}$ *reprinted from reference 103 with the permission from John Wiley and Sons.*

In 2007, two Cu-substituted POMs $Na_{16}[Cu^{II}_{14}(OH)_4(H_2O)_{16}(SiW_8O_{31})_4]\cdot 20.5H_2O$ and $K_{10}Na_{14}[Cu^{II}_{10}(H_2O)_2(N_3)_4(GeW_9O_{34})_2(GeW_8O_{31})_2]\cdot 30H_2O$ for nitrate reduction in pH 5 acetate solution were reported (Fig. I.17). The catalysis starts at the potential domain of W^{VI} reduction and the current intensity increases with the quantity of nitrate added.[104]

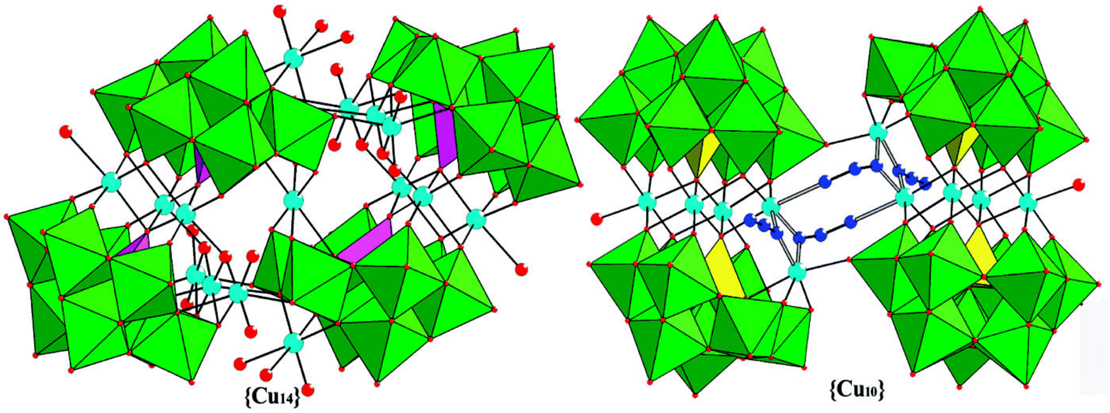

Figure I.17: Structures of $Na_{16}[Cu^{II}_{14}(OH)_4(H_2O)_{16}(SiW_8O_{31})_4]\cdot 20.5H_2O$ *and* $K_{10}Na_{14}[Cu^{II}_{10}(H_2O)_2(N_3)_4\text{-}GeW_9O_{34}]_2(GeW_8O_{31})_2]\cdot 30H_2O$ *reprinted from reference 104, Copyright (2017) American Chemical Society.*

Based on the published work, the catalysis efficiency increases with the number of Cu ions in structure. POM containing 20 Cu(II) atoms $[Cu^{II}_{20}Cl(OH)_{24}(H_2O)_{12}(P_8W_{48}O_{184})]^{25-}$ has been designed (Fig. I.18A). After then, Mal and his co-workers modified $[Cu^{II}_{20}Br(OH)_{24}(H_2O)_{12}(P_8W_{48}O_{184})]^{25-}$ and room-temperature ionic liquid 1-butyl-3-methylimidazolium tetrafluoroborate on a solid surface, which is the first example of electrocatalytic nitrate reduction by a polyanions entrapped in room-temperature ionic liquid films. The electrocatalytic process takes place at the potential of the first W reduction wave.[105]

3.3 POM@NPs for nitrate and nitrite reduction

Few studies have associated transition-metal substituted POMs with nanoparticles. $[Cu^{II}_{20}Cl(OH)_{24}(H_2O)_{12}(P_8W_{48}O_{184})]^{25-}$ ($Cu_{20}TP$) and $[Ni^{II}_4(P_8W_{48}O_{148})(WO_2)]^{28-}$ (Ni_4TP) were fixed on a PDDA modified glassy carbon electrode and then dipped in a solution of Ag nanoparticles which formed PDDA/Cu_{20}TP/AgNP and PDDA/Ni_4TP/AgNP systems respectively (Fig. I.18). The thickness of the films can be modified by changing the number of the soaking cycles. The redox process assigned to both POM species or AgNP are distinguishable.[106]

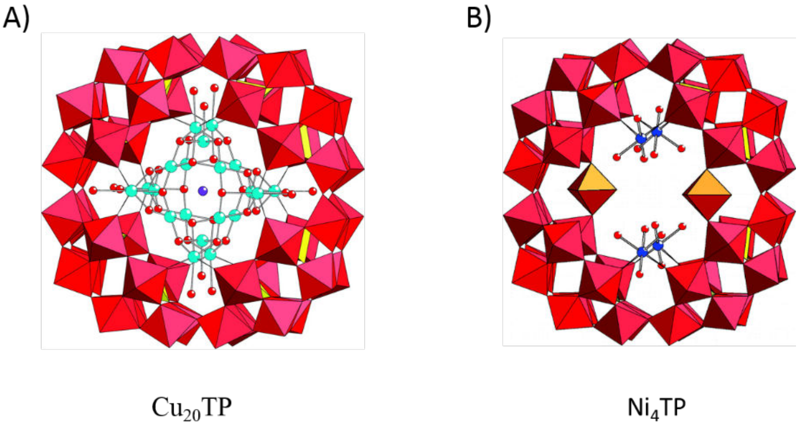

Figure I.18: A) Representation of $[Cu^{II}_{20}Cl(OH)_{24}(H_2O)_{12}(P_8W_{48}O_{184})]^{25-}$ ($Cu_{20}TP$) reprinted from reference 106. Copyright (2017) American Chemical Society. B) Representation of $[Ni^{II}_4(P_8W_{48}O_{148})(WO_2)]^{28-}$ (Ni_4TP) reprinted from reference 107. Copyright (2017) American Chemical Society.

The employment of AgNPs can increase the conductivity and porosity of the films. The electrocatalytic performance of developed films toward the reduction of nitrite and nitrate, which is showed in Fig. I.19, exhibits similar activity and starts at almost the same potential (-0.43 V *vs.* Ag/AgCl) in pH 4.5 solution.[106]

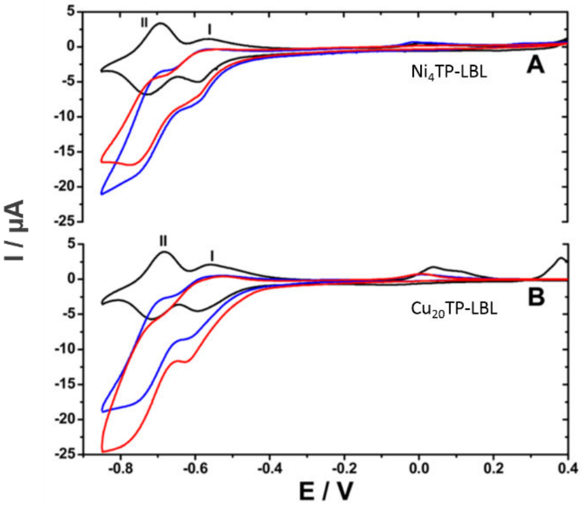

Figure I.19: Nitrite (red line, c=5 mmol·L^{-1}) and nitrate (blue line, c=5 mmol·L^{-1}) electrocatalytic reduction on Ni_4TP- (A) and Cu_{20}TP-based LBL films-modified electrodes. Working electrode: glassy carbon, number of assembly: 16, pH 4.5 0.1 mol·L^{-1} Na_2SO_4 + 20 mmol·L^{-1} CH_3COOH, scan rate: 10 mV.s^{-1}. (Reproduced from reference 106. Copyright (2017) American Chemical Society).

In this study, AgNPs were prepared by mixing with poly(ethylenimine) (PEI) and heating for 15 minutes. It is curious that even though AgNPs can be directly prepared with adapted POM in room temperature under illumination of UV. However, there is no published work examined the formed Ag@POM nanoparticles properties toward NO_x catalysis according to our knowledge.

In summary, polyoxometalate chemistry offers the possibility to prepare a large variety of compounds with tuned redox and catalytic properties. Non-substituted POMs, such as the Keggin-type POM $[SiW_{12}O_{40}]^{4-}$ and Dawson-type POM α-$[P_2W_{18}O_{62}]^{6-}$, are active only for the nitrite reduction, while catalytic activities for both nitrite and nitrate reductions can be achieved by using transition-metal substituted POM such as $[Cu^{II}P_2W_{15}Mo_2]^{8-}$, $[Cu^{II}_{20}Cl(OH)_{24}(H_2O)_{12}(P_8W_{48}O_{184})]^{25-}$ and $[Fe^{III}_6(OH)_3(A\text{-}\alpha\text{-}GeW_9O_{34}(OH)_3)_2]^{11-}$. However, more detailed investigations are needed, in particular to elucidate the role of the transition metal in the catalytic mechanism.

POMs have also the ability to adsorb on the surface of metals. Therefore, tandem catalysis, with improved efficiencies might be expected by associating POMs with catalytically active metallic nanoparticles. In this thesis, we have associated POMs and nanoparticles by different approaches. Under cathodic polarization, Cu@POM nanoparticles can be electrodeposited on a substrate resulting in significant activity toward the NO_x reduction. Another approach consists in the formation of Ag@POM by photocatalytic reduction of silver salt in the presence of a sacrificial donor. In this thesis, the preparation of these M@POM compounds and their characterization by various techniques will be described and their ability for nitrate and nitrite reductions will be explored.

References

1. Bogardi, I., Kuzelka, R. D. & Ennenga, W. *Nitrate contamination: exposure, consequence, and control.* (Springer, 1991).
2. Mahler, R. L., Colter, A. & Hirnyck, R. *Nitrate and groundwater. quality water for idaho.* (University of Idaho, 2007).
3. Mateo-sagasta, J. & Burke, J. *Agriculture and water quality interactions: a global overview.* (Senior water polycy officer, 2010).
4. Gilchrist, M., Winyard, P. G. & Benjamin, N. Dietary nitrate - Good or bad? *Nitric Oxide.* **22**, 104–109 (2010).
5. Brinkmann, T., Santonja, G. G., Yukseler, H., Roudier, S. & Sancho, L. D. *Best Available Techniques (BAT) Reference document for common waste water and waste gas treatment/management systems in the chemical sector.* (European Integrated Pollution Prevention and Control Bureau, 2016).
6. World Health Organization. *Nitrate and nitrite in drinking water, background document for development of WHO guidelines for drinking-water quality.* (World Health Organization, 2011).
7. Soares, M. I. M. Biological denitrification of groundwater. *Water Air Soil Pollut.* **123**, 183–193 (2000).
8. Hell, F. Biological denitrification of ground water – 8 years full scale experiences with the BIODEN-process. *Recent Prog. Slow Sand Altern. Biofiltration Process.* (IWA, 2006).
9. Bohdziewicz, J., Bodzek, M. & Wąsik, E. The application of reverse osmosis and nanofiltration to the removal of nitrates from groundwater. *Desalination* **121**, 139–147 (1999).
10. Malaeb, L. & Ayoub, G. M. Reverse osmosis technology for water treatment: state-of-the-art review. *Desalination* **267**, 1–8 (2011).
11. Samatya, S., Kabay, N., Yüksel, U., Arda, M., & YüKsel, M. Removal of nitrate from aqueous solution by nitrate selective ion exchange resins. *React. Funct. Polym.* **66**, 1206–1214 (2006).
12. Haque, I.-U., & Tariq, M. Electrochemical reduction of nitrate: a review. *J. Chem. Soc. Pakistan* **32**, 396–418 (2010).
13. Fanning, J. C. The chemical reduction of nitrate in aqueous solution. *Coord. Chem. Rev.* **199**, 159–179 (2000).
14. Duca, M. & Koper, M. T. M. Powering denitrification: the perspectives of electrocatalytic nitrate reduction. *Energy Environ. Sci.* **5**, 9726-9742 (2012).
15. Rosca, V., Duca, M., de Groot, M. T. & Koper, M. T. M. Nitrogen cycle electrocatalysis. *Chem. Rev.* **109**, 2209–2244 (2009)
16. Parkt, J.-Y. & Lee, Y.-N. Solubility and decomposition kinetics of nitrous acid in aqueous solution. *J . Phys. Chem* **92**, 6294–6302 (1988).
17. Duca, M., Kavvadia, V., Rodriguez, P., Lai, S.C.S., Hoogenboom, T. & Koper, M. T. M. New insights into the mechanism of nitrite reduction on a platinum electrode. *J. Electroanal. Chem.* **649**, 59–68 (2010).
18. Duca, M., Van Der Klugt, B. & Koper, M. T. M. Electrocatalytic reduction of nitrite on transition and coinage metals. *Electrochim. Acta* **68**, 32–43 (2012).
19. Cattarin, S. Electrochemical reduction of nitrogen oxyanions in 1 M sodium hydroxide solutions at silver, copper and $CuInSe_2$ electrodes. *J. Appl. Electrochem.* **22**, 1077–1081 (1992).
20. Petrii, O. A. & Safonova, T. Y. Electroreduction of nitrate and nitrite anions on platinum metals: a model process for elucidating the nature of the passivation by hydrogen adsorption. *J. Elecrrounal. Chem. Elsevier Sequoia S.A* **331**, 897–912 (1992).
21. Dima, G. E., De Vooys, A. C. A. & Koper, M. T. M. Electrocatalytic reduction of nitrate at low concentration on coinage and transition-metal electrodes in acid solutions. *J. Electroanal. Chem.* **554–555**, 15–23 (2003).
22. Neurock. M, Santen, R. A. van, Biemolt, W. & Jansen, A. P. J. Atomic and molecular oxygen as chemical precursors in the oxidation of ammonia by copper. *J Am Chem Soc* **116**, 6860–6872 (1994).
23. De Vooys, A. C. A., Koper, M. T. M., Van Santen, R. A. & Van Veen, J. A. R. Mechanistic study on the electrocatalytic reduction of nitric oxide on transition-metal electrodes. *J. Catal.* **202**, 387–394 (2001).
24. De Vooys, A. C. A., Van Santen, R. A. & Van Veen, J. A. R. Electrocatalytic reduction of NO_3^- on palladium/copper electrodes. *J. Mol. Catal. A Chem.* **154**, 203–215 (2000).
25. Katsounaros, I., Ipsakis, D., Polatides, C. & Kyriacou, G. Efficient electrochemical reduction of nitrate to nitrogen on tin cathode at very high cathodic potentials. *Electrochim. Acta* **52**, 1329–1338 (2006).
26. Vorlop, K.-D. & Tacke, T. Erste Schritte auf dem Weg zur edelmetallkatalysierten nitrat- und nitrit-entfernung aus trinkwasser. *Chemie Ing. Tech.* **61**, 836–837 (1989).
27. Rozali, O. M. Electrochemical stability of Cu, Ni, Co, Pt and Ir metals sheet and their composite electrodes in potassium hydroxide solution. *Int. J. Electrochem. Sci* **7**, 8408–8419 (2012).
28. Wada, K., Hirata, T., Hosokawa, S., Iwamoto, S. & Inoue, M. Effect of supports on Pd-Cu bimetallic catalysts for nitrate and nitrite reduction in water. *Catal. Today* **185**, 81–87 (2012).

29. Milhano, C. & Pletcher, D. The electrodeposition and electrocatalytic properties of copper–palladium alloys. *J. Electroanal. Chem.* **64**, 24–30 (2008).
30. Yoshinaga, Y., Akita, T., Mikami, I. & Okuhara, T. Hydrogenation of nitrate in water to nitrogen over Pd–Cu supported on active carbon. *J. Catal.* **207**, 37–45 (2002).
31. Piao, S., Kayama, Y., Nakano, Y., Nakata, K., Yoshinaga, Y. & Shimazu, K. Nitrate reduction on tin-modified rhodium, ruthenium, and iridium electrodes. *J. Electroanal. Chem.* **629**, 110–116 (2009).
32. Rodríguez, R., Pfaff, C., Melo, L. & Betancourt, P. Characterization and catalytic performance of a bimetallic Pt–Sn/HZSM-5 catalyst used in denitratation of drinking water. *Catal. Today* **107–108**, 100–105 (2005).
33. Mattarozzi, L., Cattarin, S. Comisso, N., Gerierro, P., Misiani, M., Vázquez-Gómez, L. & Verlato, E. Electrochemical reduction of nitrate and nitrite in alkaline media at CuNi alloy electrodes. *Electrochim. Acta* **89**, 488–496 (2013).
34. Dima, G. E., Rosca, V. & Koper, M. T. M. Role of germanium in promoting the electrocatalytic reduction of nitrate on platinum: An FTIR and DEMS study. *J. Electroanal. Chem.* **599**, 167–176 (2007).
35. Figueiredo, M. C., Souza-Garcia, J., Climent, V. & Feliu, J. M. Nitrate reduction on Pt (1 1 1) surfaces modified by Bi adatoms. *Electrochem. commun.* **11**, 1760–1763 (2009).
36. Magalon, A., Fedor, J. G., Walburger, A. & Weiner, J. H. Molybdenum enzymes in bacteria and their maturation. *Coord. Chem. Rev.* **255**, 1159–1178 (2011).
37. Anderson, L. J., Richardson, D. J. & Butt, J. N. Catalytic protein film voltammetry from a respiratory nitrate reductase provides evidence for complex electrochemical modulation of enzyme activity. *Biochemistry* **40**, 11294–11307 (2001).
38. Gates, A. J., Richardson, D. J. & Butt, J. N. Voltammetric characterization of the aerobic energy-dissipating nitrate reductase of paracoccus pantotrophus: exploring the activity of a redox-balancing enzyme as a function of electrochemical potential. *Biochem. J.* **409**, 159–168 (2008).
39. Majumdar, A., Pal, K. & Sarkar, S. Necessity of fine tuning in Mo(iv) bis(dithiolene) complexes to warrant nitrate reduction. *Dalt. Trans.* **11**, 1927–1938 (2009).
40. Pletcher, D. & Milhano, C. *The electrochemistry and electrochemical technology of nitrate*. (Springer Science, 2009).
41. Taniguchi, I., Nakashima, N., Matsushita, K. & Yasukouchi, K. Electrocatalytic reduction of nitrate and nitrite to hydroxylamine and ammonia using metal cyclams. *J. Electroanal. Chem.* **224**, 199–209 (1987).
42. Chebotareva, N. & Nyokong, T. Metallophthalocyanine catalysed electroreduction of nitrate and nitrite ions in alkaline media. **27**, 975–981 (1996).
43. Pope, M. T. & Müller, A. Polyoxometalate chemistry. *Angew. Chemie Int. Ed.* **30**, 34–48 (1991).
44. Berzelius, J. J. Beitrag zur naheren kenntnifs des molybdans. *Ann. Phys.* **82**, 369–392 (1826).
45. Keggin, J. F. Structure and formula of 12-phosphotungstic acid. *Proc. R. Soc. A* **144**. 75–100 (1934).
46. Müller, A., Krickemeyer, E., Meyer, J., Bogge, H., Peters, F., Plass, W., Diemann, E., Dillinger, S., Nonnenbruch, F., Randerath, M. & Menke, C. $[Mo_{154}(NO)_{14}O_{420}(OH)_{28}(H_2O)_{70}]^{(25+-5)-}$: a water-soluble big wheel with more than 700 atoms and a repative molecular mass of about 24000. *Angew. Chemie Int. Ed.* **34**, 2122–2124 (1995).
47. Müller, A., Krickemeyer, E., Bögge, H., Schmidtmann, M. & Peters, F. Organizational forms of matter: an inorganic super fullerene and keplerate based on molybdenum oxide. *Angew. Chemie Int. Ed.* **37**, 3359–3363 (1998).
48. Müller, A., Beckmann, E., Bögge, H., Schmidtmann, M. & Dress, A. Inorganic chemistry goes protein size: a Mo_{368} nano-hedgehog initiating nanochemistry by symmetry breaking. *Angew. Chemie Int. Ed.* **41**, 1162–1167 (2002).
49. Sadakane, M. & Steckhan, E. Electrochemical properties of polyoxometalates as electrocatalysts. *Chem. Rev.* **98**, 219–238 (1998).
50. Proust, A. & Gouzerh, P. Functionalization of polyoxometalates: towards advanced applications in catalysis and materials science. *Chem. Commun.* **0**, 1837–1852 (2008).
51. Artero, V., Proust, A., Herson, P., Villain, F., Cartier dit Moulin, C. & Gouzerh, P. Synthesis and characterization of the first carbene derivative of a polyoxometalate. *J. Am. Chem. Soc* **125**, 11156–11157 (2003).
52. Mialane, P., Dolbecq, A., Rivière, E., Marrot, J. & Sécheresse, F. A polyoxometalate containing the $\{Ni_2N_3\}$ fragment: Ferromagnetic coupling in a Ni^{II} μ-1,1 azido complex with a large bridging angle. *Angew. Chemie Int. Ed.* **43**, 2274–2277 (2004).
53. Compain, J.-D., Deniard, P., Dessapt, R., Dolbecq, A., Oms, O., Sécheress, F., Marrota, J. & Mialane, P. Functionalized polyoxometalates with intrinsic photochromic properties and their association with spiropyran cations. *Chem. Commun.* **46**, 7733–7735 (2010).
54. Proust, A., Matt, B., Villanneau, R., Guillemot, G., Gouzerha, P. & Izzet, G. Functionalization and post-functionalization: a step towards polyoxometalate-based materials. *Chem. Soc. Rev.* **41**, 7605–7622 (2012).
55. Kozhevnikov, I. V. Sustainable heterogeneous acid catalysis by heteropoly acids. *J. Mol. Catal. A Chem.* **262**, 86–92 (2007).

56. Clemente-Juan, J. M., Coronado, E. & Gaita-Ariño, A. Magnetic polyoxometalates: from molecular magnetism to molecular spintronics and quantum computing. *Chem. Soc. Rev.* **41**, 7464 (2012).
57. Palii, A., Tsukerblat, B., Klokishner, S., Dunbar, K. R., Clemente-Juand, J. M. & Coronado, E. Beyond the spin model: exchange coupling in molecular magnets with unquenched orbital angular momentaw andrei. *Chem. Soc. Rev.* **40**, 3130–3156 (2011).
58. Borrás-Almenar, J. J., Clemente, J. M., Coronado, E. & Tsukerblat, B. S. Mixed-valence polyoxometalate clusters. I. Delocalization of electronic pairs in dodecanuclear heteropoly blues with Keggin structure. *Chem. Phys.* **195**, 1–15 (1995).
59. Borrás-Almenar, J. J., Clemente, J. M., Coronado, E. & Tsukerblat, B. S. Mixed-valence polyoxometalate clusters. II. Delocalization of electronic pairs in 18-site heteropoly blues with Wells-Dawson structure. *Chem. Phys.* **195**, 17–28 (1995).
60. Papaconstantinou, E. Photochemistry of polyoxometallates of molybdenum and tungsten and/or vanadium. *Chem. Soc. Rev.* **18**, 1–31 (1989).
61. Hiskia, A., Mylonas, A. & Papaconstantinou, E. Comparison of the photoredox properties of polyoxometallates and semiconducting particles. *Chem. Soc. Rev.* **30**, 62–69 (2001).
62. Azcarate, I., Huo, Z. H., Farha, R., Goldmann, M., Xu, H. L., Hasenknopf, B., Lacôte, E. & Ruhlmann, L. Generation of photocurrent by visible-light irradiation of conjugated dawson polyoxophosphovanadotungstate-porphyrin copolymers. *Chem. - A Eur. J.* **21**, 8271–8280 (2015).
63. Khenkin, A. M., Efremenko, I., Weiner, L., Martin, J. M. L. & Neumann, R. Photochemical reduction of carbon dioxide catalyzed by a ruthenium substituted polyoxometalate. *Chem. - A Eur. J.* **16**, 1356–1364 (2010).
64. Troupis, A., Hiskia, A. & Papaconstantinou, E. Synthesis of metal nanoparticles by using polyoxometalates as photocatalysts and stabilizers. *Angew. Chem., Int. Ed.* **41**, 1911–1914 (2002).
65. Costa-Coquelard, C., Schaming, D., Lampre, I. & Ruhlmann, L. Photocatalytic reduction of Ag_2SO_4 by the Dawson anion α-$[P_2W_{18}O_{62}]^{6-}$ and tetracobalt sandwich complexes. *Appl. Catal. B Environ.* **84**, 835–842 (2008).
66. Tausch-Treml, R., Henglein, A. & Lilie, J. Reactivity of silver atoms in aqueous solution II. a pulse radiolysis study. *Berichte der Bunsengesellschaft für Phys. Chemie* **82**, 1335–1343 (1978).
67. Wang, Y., Neyman, A., Arkhangelsky, E., Gitis, V., Meshi, L. & Weinstock, I. A. Self-assembly and structure of directly imaged inorganic-anion monolayers on a gold nanoparticle. *J Am Chem Soc* **131**, 17412–17422 (2009).
68. Troupis, A., Gkika, E., Hiskia, A. & Papaconstantinou, E. Photocatalytic reduction of metals using polyoxometalates: recovery of metals or synthesis of metal nanoparticles. *C. R. Chim.* **9**, 851–857 (2006).
69. Troupis, A., Hiskia, A. & Papaconstantinou, E. Selective photocatalytic reduction–recovery of palladium using polyoxometallates. *Appl. Catal. B Environ.* **52**, 41–48 (2004).
70. Rong, C. Y. & Pope, M. T. Lacunary polyoxometalate anions are acceptor ligands characterization of some tungstoruthenate heteropolyanions and their atom transfer reactivity. *J Am Chem Soc* **114**, 2932–2938 (1992).
71. Bart, J. C. & Anson, F. C. Coordination, electron transfer and catalytic chemistry of a ruthenium-substituted heteropolytungstate anion as revealed in its electrochemical behavior. *J. Electroanal. Chem.* **390**, 11–19 (1995).
72. S Sadakane, M. & Steckhan, E. Investigation of the manganese-substituted Keggin-heteropolyanion $K_6SiW_{11}O_{39}Mn(H_2O)$ by cyclic voltammetry and its application as oxidation catalyst. *J. Mol. Catal. A Chem.* **114**, 221–228 (1996).
73. El Moll, H., Rousseau, G., Dolbecq, A., Oms, O., Marrot, J., Haouas, M., Taulelle, F., Rivière, E., Wernsdorfer, W., Lachkar, D., Lacôte, E., Keita, B. & Mialane, P. Properties of a tunable multinuclear nickel polyoxotungstate platform. *Chem. - A Eur. J.* **19**, 6753–6765 (2013).
74. Tayebee, R. Epoxidation of some olefins with hydrogen peroxide catalyzed by heteropolyoxometalates. *Asian J. Chem.* **20**, 8–14 (2008).
75. Jameel, U., Zhu, M.-Q., Chen, X.-Z., Liu, Y. & Tong, Z.-F. Green epoxidation of cyclooctene with molecular oxygen over an ecofriendly heterogeneous polyoxometalate-gold catalyst $Au/BW_{11}/Al_2O_3$. *J. Zhejiang Univ. A* **17**, 1000–1012 (2016).
76. Cheng, L., Zhang, X., Xi, X., Liu, B. & Dong, S. Electrochemical behavior of the molybdotungstate heteropoly complex with neodymium, $K_{10}H_3[Nd(SiMo_7W_{40}O_{39})_2].xH_20$ in aqueous solution. *J. Electroanal. Chem.* **407**, 97–103 (1996)..
77. Toth, J. E., Melton, J. D., Cabelli, D., Bielski, B. H. J. & Anson, F. C. Electrochemistry and redox chemistry of $H_2OFe^{III}SiW_{11}O_{39}$ in the presence of H_20_2 and OH. *Inorg. Chem* **29**, 1952–1957 (1990).
78. Dong, S. & Liu, M. Electrochemical and electrocatalytic properties Dawson-type tungstophosphate anion of iron (III) -substituted. *J. Electroanal. Chem.* **372**, 95–100 (1994).
79. Girardi, M., Blanchard, S., Griveau, S., Simon, P., Fontecave, M., Bedioui, F. & Proust, A. Electro-assisted reduction of CO_2 to CO and formaldehyde by $(TOA)_6[SiW_{11}O_{39}Co(\_)]$ polyoxometalate. *Eur. J. Inorg. Chem.* **2015**, 3642–3648 (2015).

80. Rong, C. Y. & Anson, F. C. Spontaneous adsorption of heteropolytungstates and heteropolymolybdates on the surfaces of solid electrodes and the electrocatalytic activity of the adsorbed anions. *Inorganica Chim. Acta* **242**, 11–16 (1996).
81. Rong, C. Y. & Anson, F. C. Unusually strong adsorption of highly charged heteropolytungstate anions on mercury electrode surfaces. *Anal. Chem.* **66**, 3124–3130 (1994).
82. Keita, B., Belhouari, A., Nadjo, L. & Contant, R. Electrocatalysis by polyoxometalate I polymer systems: reduction of nitrite and nitric oxide. *J. Electroanal. Chem.* **381**, 243–250 (1995).
83. Xi, X. & Dong, S. Electrocatalytic reduction of nitrite using Dawson-type tungstodiphosphate anions in aqueous solutions, adsorbed on a glassy carbon electrode and doped in polypyrrole film. *J. Mol. Catal. A Chem. A* **114**, 257–265 (1996).
84. Zagórska, M., Kulszwicz-Bajer, I., Lukomska-Godzisz, E., Pron, A., Glowacki, I. & Ulanski, J. Lefrant, S. Modification of polyacetylene and polyalkylthiophene by doping with heteropolyanions. *Synth. Met.* **37**, 99–106 (1990).
85. Pham, M.-C., Moslih, J., Chauveau, F. & Lacaze, P.-C. *In situ* multiple internal reflection Fourier transform infrared spectroscopic (MIRFTIRS) study of the electrochemical immobilization of heteropolyanions in poly(1-naphthol) coated electrodes. *J. Appl. Electrochem.* **21**, 902–909 (1991).
86. Keïta, B. & Nadjo, L. Activation of electrode surfaces Application to the letrocatalysis of the hydrogen evolution reaction. *J. Electroanal. Chem. Interfacial Electrochem.* **191**, 441–448 (1985).
87. Savadogo, O. & Carrier, F. The hydrogen evolution reaction in basic medium on iron electrodeposited with heteropolyacids. *J. Appl. Electrochem.* **22**, 437–442 (1992).
88. Wang, S.-M., Liu, L., Chen, W.-L., Zhang, Z-M., Su, Z.-M. & Wang E.-B. A new electrodeposition approach for preparing polyoxometalates-based electrochromic smart windows. *J. Mater. Chem.* **1,** 216–220 (2013).
89. Yang, H., Li, J., Zhang, H., Lv, Y. & Gao, S. Facile synthesis of POM@MOF embedded in SBA-15 as a steady catalyst for the hydroxylation of benzene. *Microporous Mesoporous Mater.* **195**, 87–91 (2014).
90. Du, D.-Y., Qin, J.-S., Li, S.-L., Su, Z.-M. & Lan, Y.-Q. Recent advances in porous polyoxometalate-based metal–organic framework materials. *Chem. Soc. Rev. Chem. Soc. Rev* **43**, 4615–4632 (2014).
91. Dufaud, V. & Lefebvre, F. Inorganic hybrid materials with encapsulated polyoxometalates. *Materials (Basel).* **3**, 682–703 (2010).
92. Toth, J. E. & Anson, F. C. Electrocatalytic reduction of nitrite and nitric oxide to ammonia with iron-substituted polyoxotungstates. *J. Am. Chem. Soc.* **256**, 2444–2451 (1989).
93. Dong, S., Xi, X. & Tian, M. Study of the electrocatalytic reduction of nitrite with silicotungstic heteropolyanion. *J. Electroanal. Chem.* **385**, 227–233 (1995).
94. McCormac, T., Fabre, B. & Bidan, G. Part II. Role of pH and the transition metal for the electrocatalytic reduction of nitrite with transition metal substituted Dawson type heteropolyanions. *J. Electroanal. Chem.* **427**, 155–159 (1997).
95. Keita, B., Girard, F., Nadjo, L., Contant, R., Belghiche, R. & Abbessi, M. Cyclic voltammetric evidence of facilitation of the reduction of nitrite by the presence of molybdenum in Fe- or Cu-substituted heteropolytungstates. *J. Electroanal. Chem.* **508**, 70–80 (2001).
96. Shan, Y., Yang, G., Sun, Y., Pang, S., Gong, J., Su, Z. & Qu, L. ITO electrode modified by self-assembling multilayer film of polyoxometallate on poly(vinyl alcohol) nanofibers and its electrocatalytic behavior. *Electrochim. Acta* **53**, 569–574 (2007).
97. Liu, S., Volkmer, D. & Kurth, D. G. Smart polyoxometalate-based nitrogen monoxide sensors. *Anal. Chem.* **76**, 4579–4582 (2004).
98. Keita, B., Abdeljalil, E., Nadjo, L., Contant, R. & Belgiche, R. First examples of efficient participation of selected metal-ion-substituted heteropolyanions in electrocatalytic nitrate reduction. *Electrochem. commun.* **3**, 56–62 (2001).
99. Jabbour, D., Keita, B., Mbomekalle, I. M., Nadjo, L. & Kortz, U. Investigation of multi-nickel-substituted tungstophosphates and their stability and electrocatalytic properties in aqueous media. *Eur. J. Inorg. Chem.* **4**, 2036–2044 (2004).
100. Keita, B., Martyr, I., Nadjo, L. & Contant, R. $[H_4AsW_{18}O_{62}]^{7-}$, A novel Dawson heteropolyanion and two of its sandwich-type derivatives: electrocatalytic properties towards nitrite and nitrate. *Electrochem. commun.* **3**, 267–273 (2001).
101. Ammam, M., Mbomekallea, I.-M., Keita, B., Nadjo, L., Anderson, T. M., Zhang, X., Hardcastle, K. I., Hill, C. L. & Fransaer, J. Electrochemical behavior and electrocatalytic properties towards hydrogen peroxide, dioxygen and nitrate of the polyanions $(Ni^{II}OH_2)_2(Fe^{III})_2(X_2W_{15}O_{56})_2^{14-}$ ($X = P^V$ or As^V): A comparative study. *J. Electroanal. Chem.* **647**, 97–102 (2010).
102. Bi, L.-H., Kortz, U., Nellutla, S., Stowe, A. C., Dalal, N. S., Keita, B. & Nadjo, L. Structure , electrochemistry , and magnetism of the iron (III) -substituted Keggin dimer. *Inorg. Chem.* **44**, 896–903 (2005).

103. Keita, B., de Oliveira, P., Nadjo, L. & Kortz, U. The ball-shaped heteropolytungstates $[[Sn(CH_3)_2(H_2O)]_{24}[Sn(CH_3)_2]_{12}(A\text{-}XW_9O_{34})_{12}]^{36-}$ (X=P, As): stability, redox and electrocatalytic properties in aqueous media. *Chem. - A Eur. J.* **13**, 5480–91 (2007).

104. Zhang, Z., Qi, Y., Qin, C., Li, Y., Wang, E.B., Wang, X., Su, Z. & Xu, L. Two multi-copper-containing heteropolyoxotungstates constructed from the lacunary keggin polyoxoanion and the high-nuclear spin cluster. *Inorg. Chem.* **46**, 8162–8169 (2007).

105. Mal, S. S., Bassil, B. S., Ibrahim, M., Nellutla, S., Tol, J., Dalal, N. S., Fernandez, J. A. Lopez, X., Poblet, J. M., Biboum, R. N., Keita, B. & Kortz. U. Wheel-shaped Cu_{20}-tungstophosphate $[Cu_{20}X(OH)_{24}(H_2O)_{12}(P_8W_{48}O_{184})]^{25-}$ ion (X = Cl, Br, I) and the role of the halide guest. *Inorg. Chem.* **48**, 11636–11645 (2009).

106. Imar, S., Maccato, C., Dickinson, C., Vagin, M. & Mccormac, T. Enhancement of nitrite and nitrate electrocatalytic reduction through the employment of self-assembled layers of nickel- and copper-substituted crown-type Heteropolyanions. *Langmuir* **31**, 2584–2592 (2015).

107. Bassil, B. S., Ibrahim, M., Mal, S. S., Suchopar, A., Biboum, R. N., Keita, B., Nadjo, L., Nellutla, S., van Tol, J., Dalal, N. S. & KortzCobalt, U. Manganese, nickel, and vanadium derivatives of the cyclic 48-tungsto-8-phosphate $[H_7P_8W_{48}O_{184}]^{33-}$. *Inorg. Chem.* **49**, 4949–4959 (2010).

Chapter II

Reduction of NO_x on Cu or Ag bulk electrode in the presence of polyoxometalates

Chapter II Reduction of NO_x on Cu or Ag bulk electrode in the presence of polyoxometalates

1 Introduction

Nitrate reduction at various metal electrodes has been widely studied in both acid and alkaline solutions. In these studies, nitrate reduction generally occurs at the same potential of hydrogen evolution. On coinage metal, Duca and co-workers[1] showed that the electrocatalytic activity for nitrate reduction in acidic medium decreases in the order Cu > Ag > Au. On these metals, kinetics suggests that the reduction of nitrate into nitrite is the rate-determining step of the reaction, while the final product depend on the mechanism of the nitrite reduction.[2] If using Ag or Au electrode, only a small reduction current during nitrate reduction is observed. The reduction starts at 0.75 V *vs.* RHE on Au electrode and at 0.15 V *vs.* RHE on Ag electrode while nitrate can be reduced on Cu electrode in 0.1 $mol \cdot L^{-1}$ $HClO_4$ at 0 V *vs.* RHE with a higher catalytic current than on other two metals.[1]

The amount of metal catalyst can be significantly reduced by using nanoparticles instead of bulk materials. However, the nanoparticles need to be protected by a capping agent to prevent their agglomeration which would resulting a decrease of the catalytic efficiency. In this respect, POMs are very promising compounds, since they can be used both as protecting ligand to stabilizer metal nanoparticles and also as co-catalyst for tandem processes since POMs are also active for the nitrate and nitrite reduction. Thus, the association of POMs with catalytic metallic nanoparticles may lead to enhance the catalytic properties and may allow to tune the reaction selectivity. It is well known that POMs are able to spontaneously adsorb on various electrode surfaces such as Au, Hg, Ag and carbon.[3,4,5] Among various kinds of POMs, Keggin-type POMs modified surface were the most widely investigated. Nadjo and his co-workers[4] have shown that $[SiW_{12}O_{40}]^{4-}$ adsorbs spontaneously on Au surface at pH 4 0.5 $mol \cdot L^{-1}$ $Na_2SO_4 + H_2SO_4$ in only 600 seconds with 10^{-4} $mol \cdot L^{-1}$ $[SiW_{12}O_{40}]^{4-}$ in solution. At potentials below -0.40 V *vs.* SCE (first W^{VI} reduction wave), the POM is reduced and desorbs from Au surface based on Electrochemical Quartz Crystal Microbalance (EQCM). Gewirth and his co-workers[5] have reported a strong interaction between $[SiW_{12}O_{40}]^{4-}$ and Ag surface, the formation of the adsorbed Ag-$SiW_{12}O_{40}{}^{4-}$ passivating the surface with negative potential cycling between -0.80 V and -0.50 V *vs.* Ag/AgCl. To the best of our knowledge, the interaction between $[SiW_{12}O_{40}]^{4-}$

and Cu bulk electrode has not been addressed. However, in most studies, the electrochemical response of the POM in the voltammetric current potential curves is not strongly affected after being adsorbed on electrode surface such as Au, Pt or GC.[6]

One of the aims of this thesis is to understand the influence of the presence of POM entities during the nitrate and nitrite reduction on Cu and Ag metal and to determine under which conditions a synergy between POM and metal can exist during these reactions.

In this chapter, we present some results of nitrate and nitrite reductions on Cu or Ag bulk electrode in the absence or in the presence of POMs in aqueous solution at various pH, in order to understand the role of the POM entity in the electrocatalytic reduction.

For this purpose, a Keggin-type POM $[SiW_{12}O_{40}]^{4-}$ has been chosen for its catalytic properties toward NO_2^- or HNO_2 reduction. Dong and his co-workers[7] have shown that $[SiW_{12}O_{40}]^{4-}$ possesses two one-electron redox waves followed by one two-electron redox wave in cyclic voltammogram from +0.10 V *vs.* Ag/AgCl in acidic medium. In the presence of $NaNO_2$, electrocatalytical reduction has been reported at the first reduction wave (at E = -0.20 V *vs.* Ag/AgCl at pH 2) or at the third wave (at E = -0.85 V *vs.* Ag/AgCl at pH ≈ 4). The nitrite reduction is then catalyzed in the presence of $[SiW_{12}O_{40}]^{4-}$. The details have been discussed in Chapter I page 34. It should be noted that the nitrous acid disproportionates slowly under pH = 3.39[8] according to:[9]

$$2HNO_2(aq) \rightleftarrows NO(aq) + NO_2(aq) + H_2O$$

Therefore, the measurements have to be completed rapidly.

2 Electrochemical properties of $[SiW_{12}O_{40}]^{4-}$ on Cu or Ag electrode

Electrochemical properties of $[SiW_{12}O_{40}]^{4-}$ in solution on Cu, Ag and Glassy Carbon (GC) bulk electrodes were studied by using cyclic voltammetry in two buffer solutions: 1 mol·L^{-1} $CH_3COOLi + CH_3COOH$ (pH 5) and 0.5 mol·L^{-1} $Na_2SO_4 + H_2SO_4$ (pH 1).

2.1 On GC bulk electrode

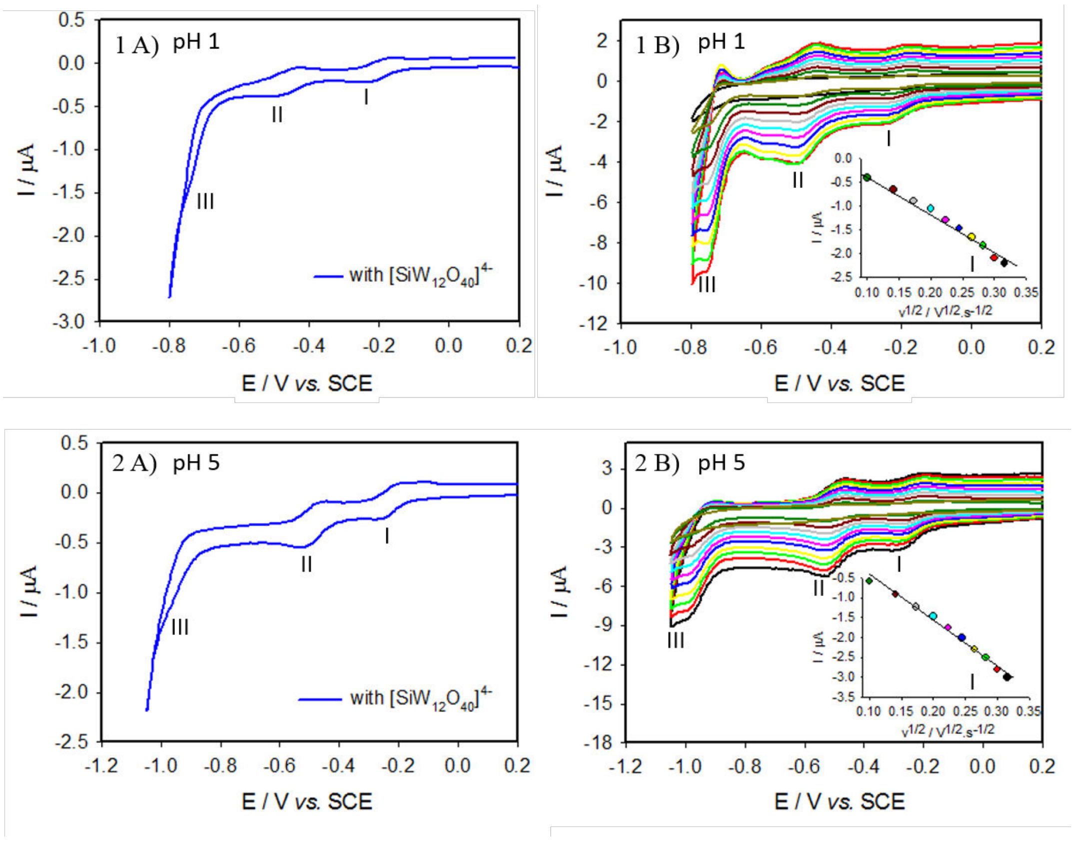

Figure II.1: *Top*: 1A) CV of 0.1 mmol·L^{-1} $[SiW_{12}O_{40}]^{4-}$ in pH 1 0.5 mol·L^{-1} Na_2SO_4 + H_2SO_4 solution on GC electrode, v = 2 mV·s^{-1}. 1B) Variation of scan rates from inner to outer curve: 10, 20, 30, 40, 50, 60, 70, 80, 90 and 100 mV s^{-1}. (Inset) variation of cathodic peak current intensity as a function of the scan rate. *Bottom*: 2A) CV of 0.1 mmol·L^{-1} $[SiW_{12}O_{40}]^{4-}$ in pH 5 1 mol·L^{-1} CH_3COOLi + CH_3COOH solution on GC electrode, v = 2 mV·s^{-1}. 2B) Variation of scan rates from inner to outer curve: 10, 20, 30, 40, 50, 60, 70, 80, 90 and 100 mV·s^{-1}. (Inset) variation of cathodic peak current intensity as a function of the scan rate.

Cyclic voltammgrams are displayed in Fig II.1. The range of potential is limited from 0.20 V to the end of the W^{VI} reduction waves. Three reduction peaks are observed in both pH 1 solution and pH 5 solution. The first cathodic peak currents have been shown proportional to the square root of the scan rate, indicating a diffusion-controlled process.[7,10] The first two peaks are reversible and independent of pH, while the third redox wave varies with the pH of the solution (-0.73 V at pH 1 and -0.95 V at pH 5), with a shift around 60 mV/pH unit. These results are coherent with the work of Dong.[7] The three redox processes can be described as:

$$SiW_{12}^{VI}O_{40}^{4-} + e^- \rightleftharpoons SiW_{11}^{VI}W^{V}O_{40}^{5-}$$

$$SiW_{11}^{VI}W^{V}O_{40}^{5-} + e^- \rightleftharpoons SiW_{10}^{VI}W_2^{V}O_{40}^{6-}$$

$$SiW_{10}^{VI}W_2^{V}O_{40}^{6-} + 2e^- + 2H^+ \rightleftharpoons H_2SiW_8^{VI}W_4^{V}O_{40}^{6-}$$

2.2 On Cu bulk electrode

The range of CV was limited anodically to -0.10 V *vs.* SCE (above which Cu oxidation occurs) and to the H_2 evolution potential on Cu (at -0.65 V *vs.* SCE at pH 1 and -0.90 V at pH 5).

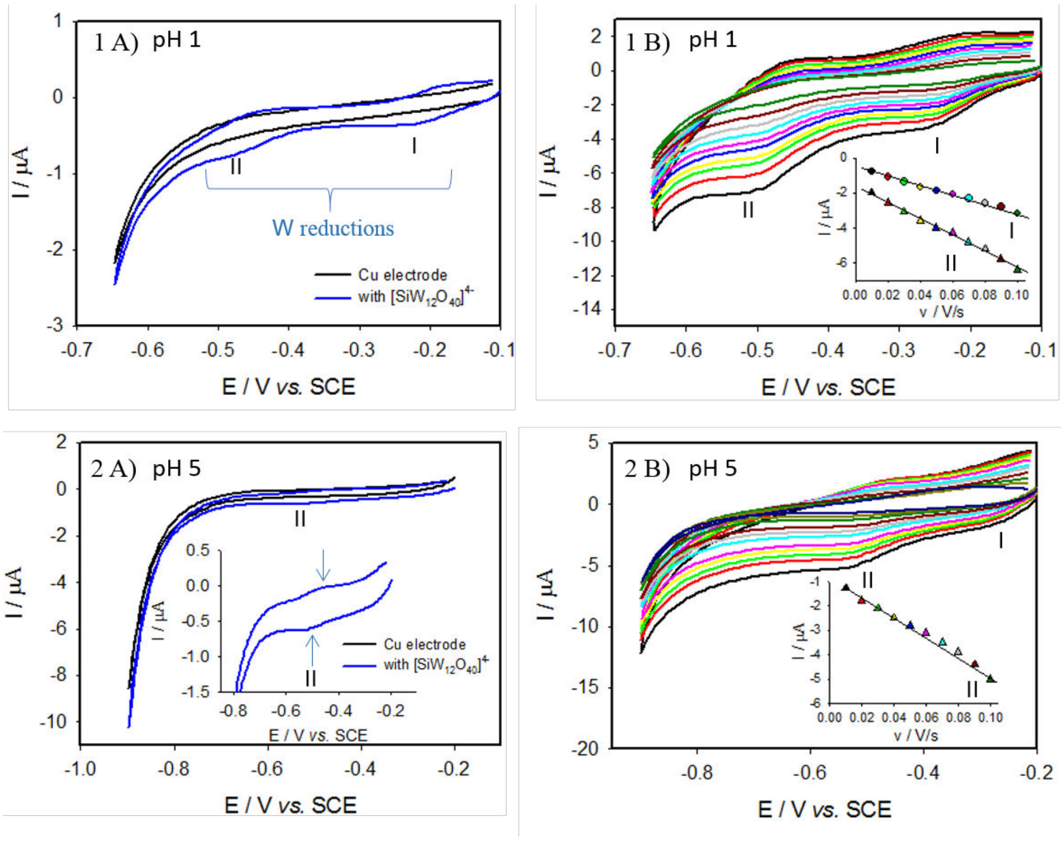

*Figure II.2: **Top**: 1A) CV of 0.1 mmol·L^{-1} $[SiW_{12}O_{40}]^{4-}$ in pH 1 0.5 mol·L^{-1} Na_2SO_4 + H_2SO_4 solution on Cu electrode, v = 2 mV·s^{-1}. 1B) Variation of scan rates from inner to outer curve: 10, 20, 30, 40, 50, 60, 70, 80, 90 and 100 mV·s^{-1}. (Inset) variation of cathodic peak current intensity as a function of the scan rate. **Bottom**: 2A) CV of 0.1 mmol·L^{-1} $[SiW_{12}O_{40}]^{4-}$ in pH 5 1 mol·L^{-1} CH_3COOLi + CH_3COOH solution on Cu electrode, v = 2 mV·s^{-1}. 2B) Variation of scan rates from inner to outer curve: 10, 20, 30, 40, 50, 60, 70, 80, 90 and 100 mV·s^{-1}. (Inset) variation of cathodic peak current intensity as a function of the scan rate.*

At pH 1, two quasi-reversible reduction peaks are observed at -0.22 V and -0.47 V *vs.* SCE (wave I and II), attributed to the redox processes of W centers (W^{VI}/W^{V} couples) as shown in Fig. II.2A. In contrast at pH 5, the first wave is difficult to define due to the significant redox peak of ion acetate on Cu electrode (see Fig. II.3) which conceals the first reduction wave of W^{VI}. However, this wave is detectable at higher scan rate (100 mV·s^{-1}). The second reduction wave is observed at -0.52 V (wave II, see Fig. II.2B). The cathodic current increases linearly with the scan rate suggesting that the POM detected is absorbed on electrode surface. This observation explains the reason that $[SiW_{12}O_{40}]^{4-}$ reduced at more positive potential on Cu bulk electrode than on GC electrode at pH 1.

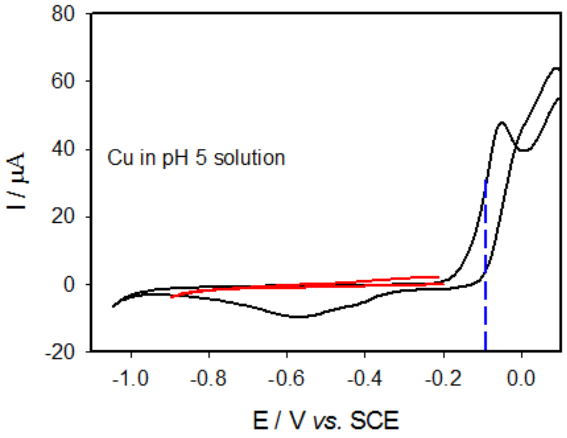

Figure II.3: CV of Cu bulk electrode in pH 5 1 mol·L^{-1} CH_3COOLi + CH_3COOH solution, v = 20 mV·s^{-1}. ***Black line****: the measurement is carried out at potential range of 0.10 V to -1.05 V.* ***Red line****: the measurement is carried out at potential range of -0.20 V to -0.9 V to avoid the reduction of ions acetate in solution on Cu electrode as well as the oxidation of the Cu.*

2.3 On Ag bulk electrode

The redox properties of the POM were also investigated on Ag electrode in range between -0.10 V and -0.65 V at pH 1 and between -0.10 V and -0.90 V at pH 5. In pH 1 solution, two quasi-reversible reduction peaks are observed at -0.23 V and -0.48 V corresponding to the reductions of $W^{VI/V}$ couple (see Fig. II.1A). It should be mentioned that the redox waves of the $[SiW_{12}O_{40}]^{4-}$ occurs nearly at the same potential on Ag and on Cu electrodes at pH 1. In contrast, at pH 5, the two reduction peaks were found at slightly lower potentials: -0.30 V and -0.56 V on Ag electrode *versus* ≈ -0.28 V and -0.52 V on Cu electrode (see Fig. II.2A). Since the cathodic peak current is proportional to the scan rate, the POM is assumed to be adsorbed on the Ag electrode in this potential range.

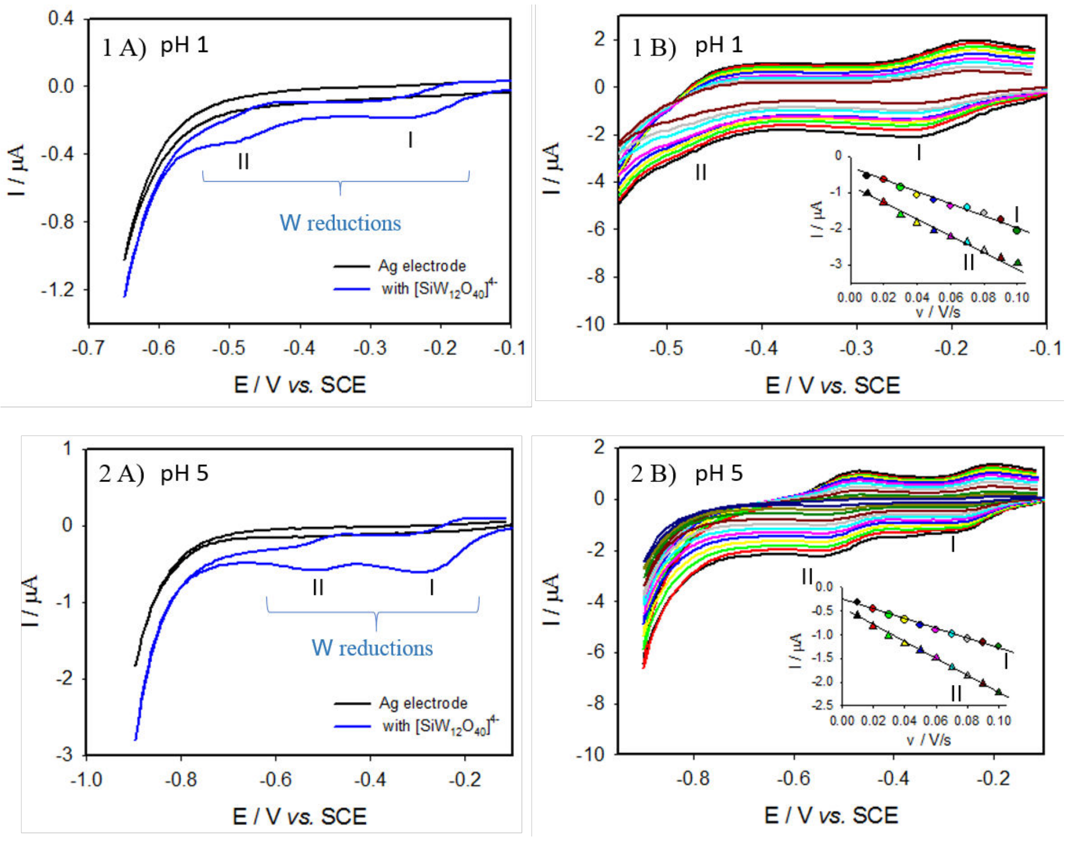

*Figure II.4: **Top**: 1A) CV of 0.1 mmol·L^{-1} $[SiW_{12}O_{40}]^{4-}$ in pH 1 0.5 mol·L^{-1} Na_2SO_4 + H_2SO_4 solution on Ag electrode, v = 2 mV·s^{-1}. 1B) Variation of scan rates from inner to outer curve: 10, 20, 30, 40, 50, 60, 70, 80, 90 and 100 mV·s^{-1}. (Inset) variation of cathodic peak current intensity as a function of the scan rate. **Bottom**: 2A) CV of 0.1 mmol·L^{-1} $[SiW_{12}O_{40}]^{4-}$ in pH 5 1 mol·L^{-1} CH_3COOLi + CH_3COOH solution on Ag electrode, v = 2 mV·s^{-1}. 2B) Variation of scan rates from inner to outer curve: 10, 20, 30, 40, 50, 60, 70, 80, 90 and 100 mV·s^{-1}. (Inset) variation of cathodic peak current intensity as a function of the scan rate.*

Reduction peak potentials of $[SiW_{12}O_{40}]^{4-}$ on GC, Cu and Ag are summarized in the Table II.1. In resume, at pH 1, the first two reductions were measured at similar potentials on Cu and Ag electrode. But these two reduction peaks shift approximately 30 mV to more negative potential on GC electrode. In contrast, in pH 5 solution, POM is reduced at more negative potential on Ag surface than on other two electrodes. The different redox potentials reflect a strong interaction between POM and metal surface which affects its electrochemical properties. The third reduction wave is observed only on GC electrode because GC electrode is less active for the hydrogen evolution reaction.

	E / V vs. SCE	wave I	wave II	wave III
pH 1	GC	-0.25	-0.50	-0.73
	Cu	-0.22	-0.47	-
	Ag	-0.23	-0.48	-
pH 5	GC	-0.27	-0.51	-0.95
	Cu	-0.28[a]	-0.52	-
	Ag	-0.30	-0.56	-

[a]: measured at 100 mV·s^{-1}

Table II.1: Reduction peak potentials measured from cyclic voltammograms of $[SiW_{12}O_{40}]^{4-}$ on GC, Cu and Ag electrodes in pH 1 0.5 mol·L^{-1} Na_2SO_4 + H_2SO_4 or in pH 5 1 mol·L^{-1} CH_3COOLi + CH_3COOH solutions, v = 2 mV·s^{-1}.

3 Reduction of NO_2^-/HNO_2 on Cu or Ag bulk electrode in the presence of $[SiW_{12}O_{40}]^{4-}$

3.1 Reduction of HNO_2 in pH 1 medium with or without $[SiW_{12}O_{40}]^{4-}$

Nitrite is protonated under pH =3.39,[8] therefore the main specie at pH 1 in aqueous solution is HNO_2.

The catalytic onset potential (measured at v = 2 mV·s^{-1}) is arbitrarily defined at the potential where the nitrite reduction $\Delta I = I_0 - I_{NOx} = 0.5$ µA (corresponding to 7.15 µA/cm^2 with electrode surface A = 0.07 cm^2), in the presence of 1 mmol·L^{-1} NO_x (mainly HNO_2). I_0 is defined as $I_{electrode}$ (when no POM is present in the system) (see Fig. II.5A) or $I_0 = I_{electrode+POM}$ when Keggin POM $[SiW_{12}O_{40}]^{4-}$ is present (see Fig. II.5B). This current value $\Delta I = 0.5$ µA allows to compare the catalytic performances of the different systems since it is low enough to determine the onset potential at which the catalytic reduction occurs without significant influence of the NO_x mass transport and high enough in comparison to the background current. Note that the onset potential of the reduction might depend on the NO_x concentration affecting the mass transport and the reaction order of NO_x was not determined. In the following, the onset potential will be determined at a concentration of 1 mmol·L^{-1} NO_x.

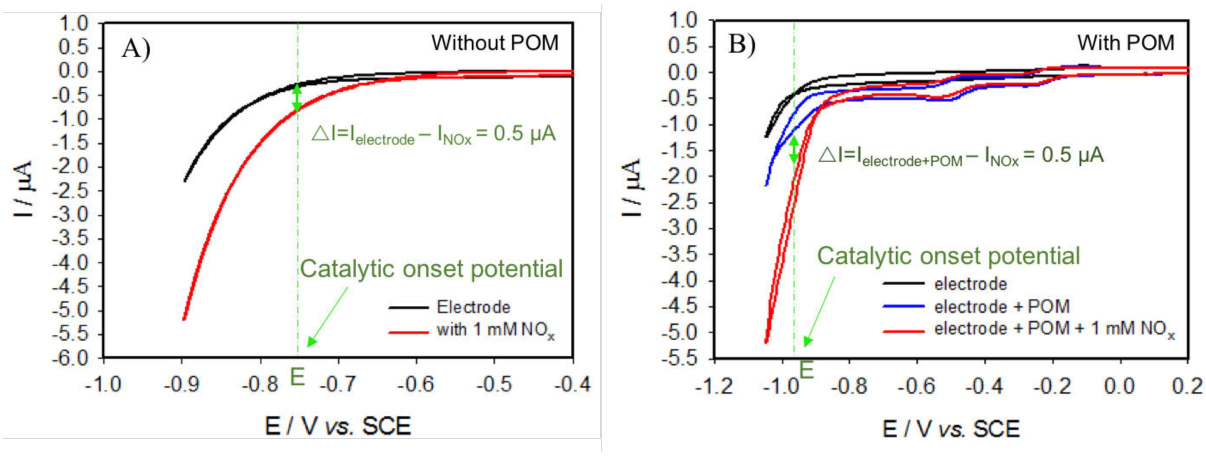

Figure II.5: Illustrations of measurement of catalytic onset potential in two situations: A) without POM in solution and B) in the presence of $H_4[SiW_{12}O_{40}]$ POM in solution.

3.1.1 On GC bulk electrode

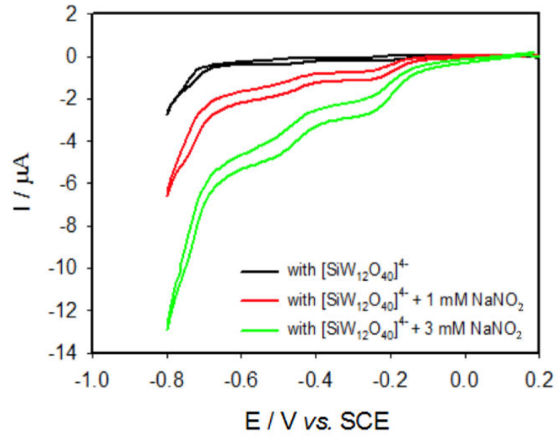

Figure II.6: Electrochemical reduction of HNO_2 in the presence of 0.1 $mmol \cdot L^{-1}$ $[SiW_{12}O_{40}]^{4-}$ on GC electrode in pH 1 0.5 $mol \cdot L^{-1}$ $Na_2SO_4 + H_2SO_4$, $v = 2\ mV \cdot s^{-1}$.

HNO_2 reduction on GC electrode with $[SiW_{12}O_{40}]^{4-}$ is shown in Fig II.6. In the absence of POM, the GC electrode is not active towards nitrite reduction. But in the presence of POM, the catalytic current starts from the first reduction wave of $W^{VI/V}$ while the catalytic onset potential is located at -0.21 V with $\Delta I = 0.5$ µA for a nitrite concentration 1 $mmol \cdot L^{-1}$. An augmentation of current is observed at all measured range especially at last two reduction waves of POMs. The current intensity increases with the concentration of HNO_2.

3.1.2 On Cu bulk electrode

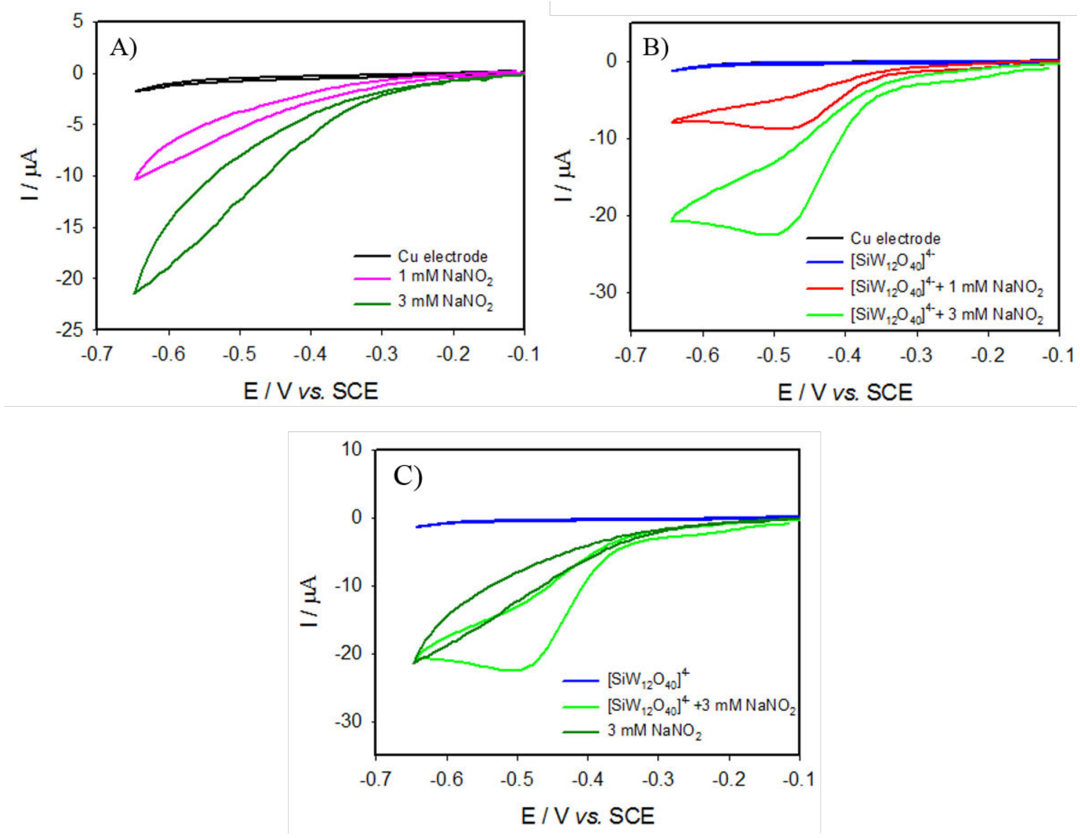

Figure II.7: A) Electrochemical reduction of HNO_2 on Cu electrode. B) Electrochemical reduction of HNO_2 in the presence of 0.1 mmol·L^{-1} $[SiW_{12}O_{40}]^{4-}$ on Cu electrode. C) Comparison of HNO_2 reduction with or without $[SiW_{12}O_{40}]^{4-}$ in solution. Buffer solution: pH 1 0.5 mol·L^{-1} Na_2SO_4 + H_2SO_4, v = 2 mV·s^{-1}.

The current potential curves obtained during the HNO_2 reduction on Cu electrodes at pH 1 are displayed in Fig. II.7A. A clear HNO_2 reduction current can be observed from -0.26 V, the current increasing linearly with the nitrite concentration. Duca and his co-workers[1] have observed a high catalytic current on Cu electrode during the entire range (from -0.30 V to 0.20 V *vs*. RHE in 0.1 mol·L^{-1} $HClO_4$, 20 mV·s^{-1}), earlier than in our measurement.

A general mechanism for the nitrite reduction at Cu cathode in acidic media could be summarized according to the published works:[11]

$$2HNO_2 \rightarrow NO_2 + (NO)_{ads} + H_2O$$

$$5H^+ + 5e^- \rightarrow 5(H)_{ads}$$

$$(NO)_{ads} + 5(H)_{ads} + H^+ \rightarrow NH_4^+ + H_2O$$

Interestingly, the shape of HNO_2 reduction current potential curves on Cu electrode is significantly affected in the presence of POM in solution. First, in the presence of 1 mmol·L^{-1}

$[SiW_{12}O_{40}]^{4-}$, a small enhancement of the reduction current can be observed at -0.19 V. In addition, a pronounced current peak emerging at -0.50 V *vs.* SCE (Fig. II.7B). The comparison of the current potential curves in Fig. II.7C reveals the enhancement by a factor 2 of the HNO_2 reduction current in the presence of the POM. This result suggests that the Cu and the Keggin POM can work in tandem for the HNO_2 reduction catalysis.

3.1.3 On Ag bulk electrode

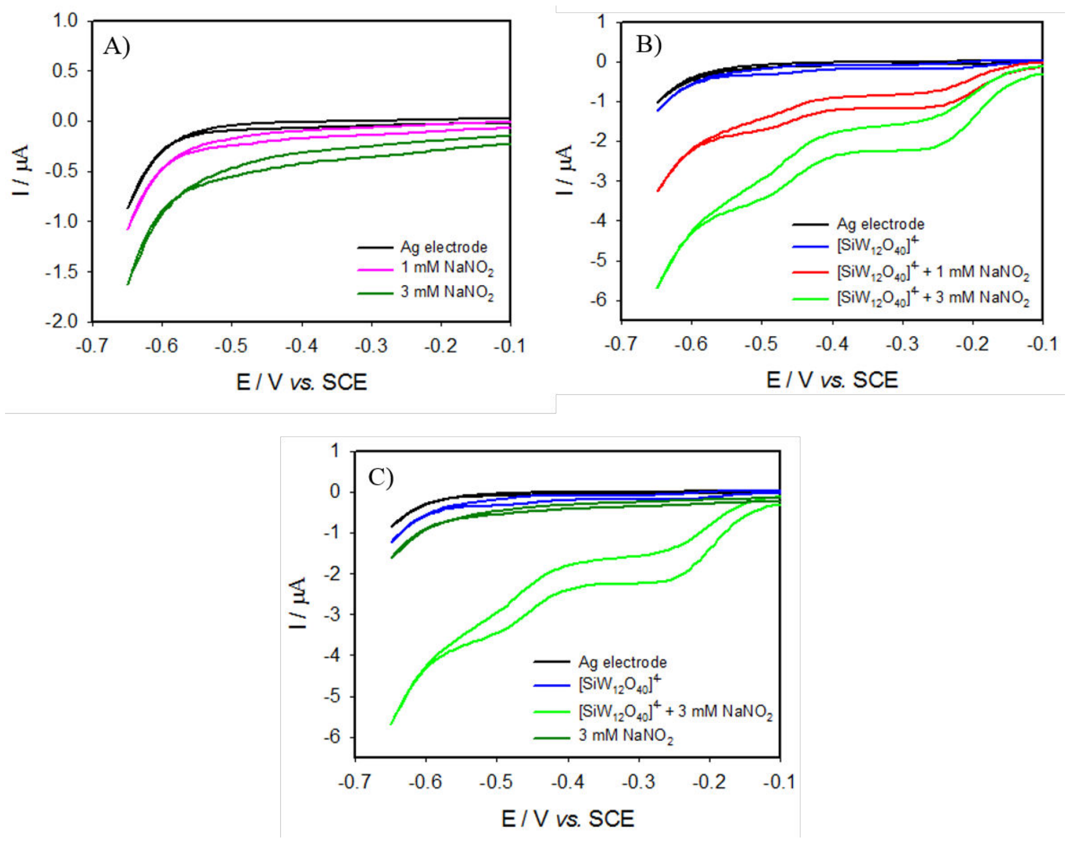

Figure II.8: A) Electrochemical reduction of HNO_2 on Ag electrode. B) Electrochemical reduction of HNO_2 in the presence of 1 $mmol \cdot L^{-1}$ $[SiW_{12}O_{40}]^{4-}$ on Ag electrode. C) Comparison of HNO_2 reduction with or without $[SiW_{12}O_{40}]^{4-}$ in solution. Buffer solution: pH 1 0.5 $mol \cdot L^{-1}$ $Na_2SO_4 + H_2SO_4$, $v = 2\ mV \cdot s^{-1}$.

On Ag electrode, a small reduction current of HNO_2 is observed in the potential range between -0.20 V and -0.60 V, similar to the results obtained by Duca and co-worker's work.[1] However, the increase of current is too small to determine the onset potential.

Interestingly in the presence of $[SiW_{12}O_{40}]^{4-}$, the HNO_2 reduction current is significantly increased. Two HNO_2 reduction waves at -0.25 V and -0.45 V *vs.* SCE can be clearly observed at the potential of the POM's redox waves. The catalytic onset potential is around -0.18 V for $\Delta I = 0.5$ μA.

3.2 Reduction of NO_2^- in pH 5 medium with or without $[SiW_{12}O_{40}]^{4-}$

3.2.1 On GC electrode

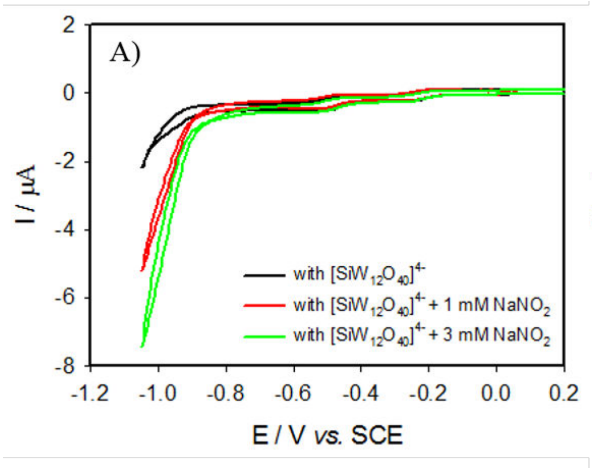

Figure II.9: A) Electrochemical reduction of NO_2^- in the presence of 0.1 mmol·L^{-1} $[SiW_{12}O_{40}]^{4-}$ on GC electrode. B) Magnification of A to highlight the onset of the catalysis. Buffer solution: pH 5 1 mol·L^{-1} CH_3COOLi + CH_3COOH, v = 2 mV·s^{-1}.

The current intensity decreases at pH 5 than that at pH 1. The catalysis occurs from -0.48 V at the second wave of $W^{VI/V}$ reduction in the presence of 3 mmol·L^{-1} $[SiW_{12}O_{40}]^{4-}$ (see Fig. II.9B). However, the nitrite reduction current is further enhanced at the $W^{VI/V}$ reduction wave involving proton transfer (the third wave). The following mechanism was suggested by Dong and his co-workers:[7]

$$SiW_{11}^{VI}W^{V}O_{40}^{5-} + NO_2^- + nH^+ \rightleftharpoons SiW_{12}^{VI}O_{40}^{4-} + \text{"}product(s)\text{"}$$

The condition $\Delta I = 0.5$ μA can be only reached at the third reduction wave around -0.94 V.

3.2.2 On Cu bulk electrode

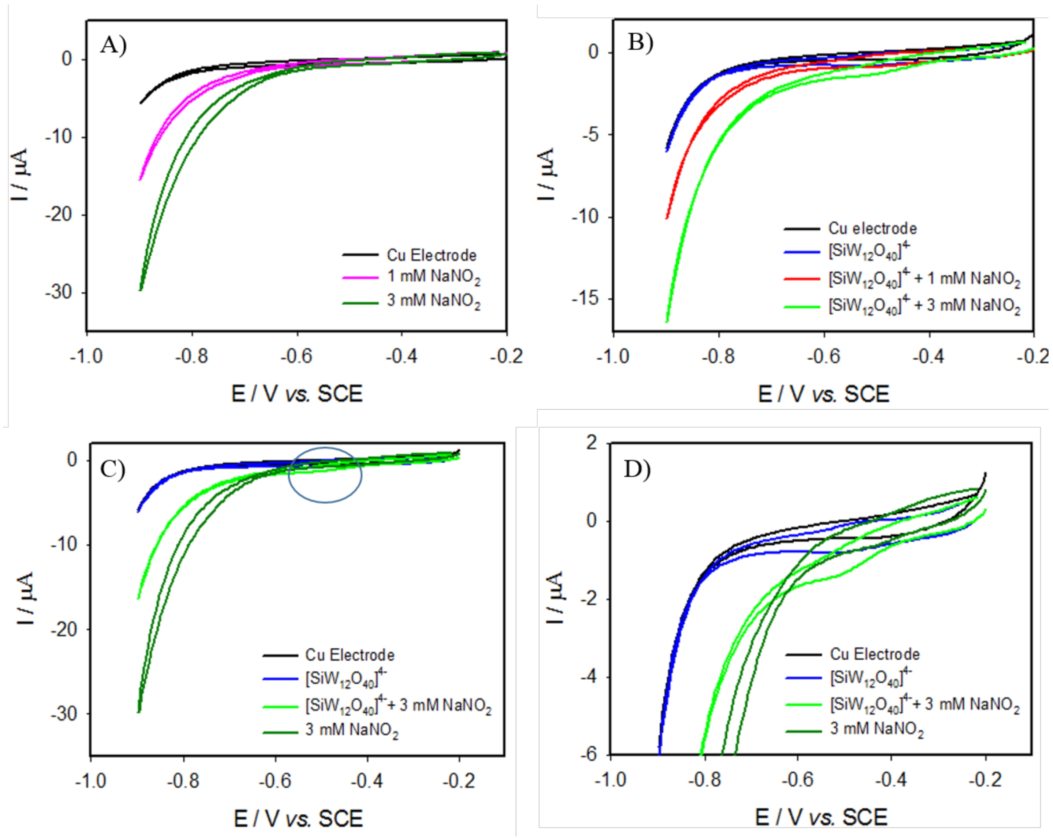

Figure II.10: A) Electrochemical reduction of NO_2^- *on Cu electrode. B) Electrochemical reduction of* NO_2^- *in the presence of 0.1 mmol·L*$^{-1}$ $[SiW_{12}O_{40}]^{4-}$ *on Cu electrode. C) Comparison of* NO_2^- *reduction with or without* $[SiW_{12}O_{40}]^{4-}$ *in solution. D) Magnification of C between -6 to 2 µA. Buffer solution: pH 5 1 mol·L*$^{-1}$ $CH_3COOLi + CH_3COOH$*, v = 2 mV.s*$^{-1}$*.*

The potential of NO_2^- reduction is shifted toward more negative potential when pH increases, the onset of the reduction being at -0.66 V on Cu electrode at pH 5 in the absence of POMs (Figure II.10A). According to previous works, the reduction of nitrite can be presented below:[12]

$$NO_2^- + 4H_2O + 4e^- \rightarrow NH_2OH + 5OH^-$$

Contrary to the pH 1 solution, in the presence of POMs, the NO_2^- reduction current on Cu electrode is enhanced only in a narrow potential region, around -0.48 V, close to the W^{VI} reduction (Fig. II.10D). At potential below -0.65 V, the NO_2^- reduction current is inhibited in the presence of POM in comparison to the reduction on Cu electrode alone. At this stage, the reasons for such inhibition are still unclear. One of the possible explanation is that the adsorbed POM hinders the access of the NO_2^- to the Cu surface. Since the current potential curves are almost independent on the mass transport, a Tafel analysis can be performed with a high concentration of NO_2^- (30 mmol·L^{-1}, in order to avoid the limitation by the material transport due to the presence of excess of nitrite). For this concentration, the nitrite reduction current on Cu is almost the same in the presence and in the absence of POM in a potential range between -0.45 V and -0.57 V and the Tafel slope is approximately of 305 mV/decade. However, below -0.57 V *vs.* SCE, the Tafel slope of the nitrite reduction on the Cu electrode in the presence of POM increases to ca. 370 mV/decade, while it is only of 200 mV/decade in the absence of POM in solution (see in Fig. II.11). This reveals that the interaction of the POM with the Cu surface is detrimental to the catalytic activity for 30 mmol·L^{-1} NO_2^- solution in this potential range since a higher overpotential has to be applied to obtain the same NO_2^- reduction current value.

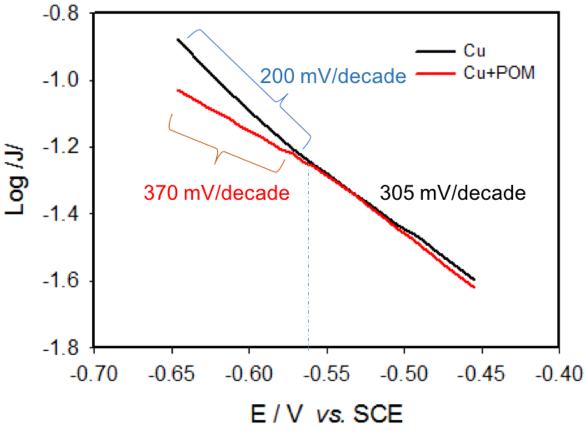

Figure II.11: Tafel plot for 30 mmol·L^{-1} NO_2^- reduction on Cu bulk electrode in pH 5 1 mol·L^{-1} CH_3COOLi + CH_3COOH, v = 2 mV.s^{-1}.

3.2.3 On Ag bulk electrode

Contrary to the results obtained in pH 1 medium, nitrite can only be reduced in the potential range where hydrogen evolution takes place on Ag surface at pH 5. The catalytic onset potential is defined at -0.83 V (see Fig. II.12A).

In the presence of POM in solution, a slightly higher reduction current is observed. This is not surprising since our results suggested that the reduction of $[SiW_{12}O_{40}]^{4-}$ is demonstrated difficult to reduce on Ag bulk electrode at pH 5. It has to note that the increase of current is too small for determining the onset potential of nitrite reduction in the presence of POM (see Fig. II.12B).

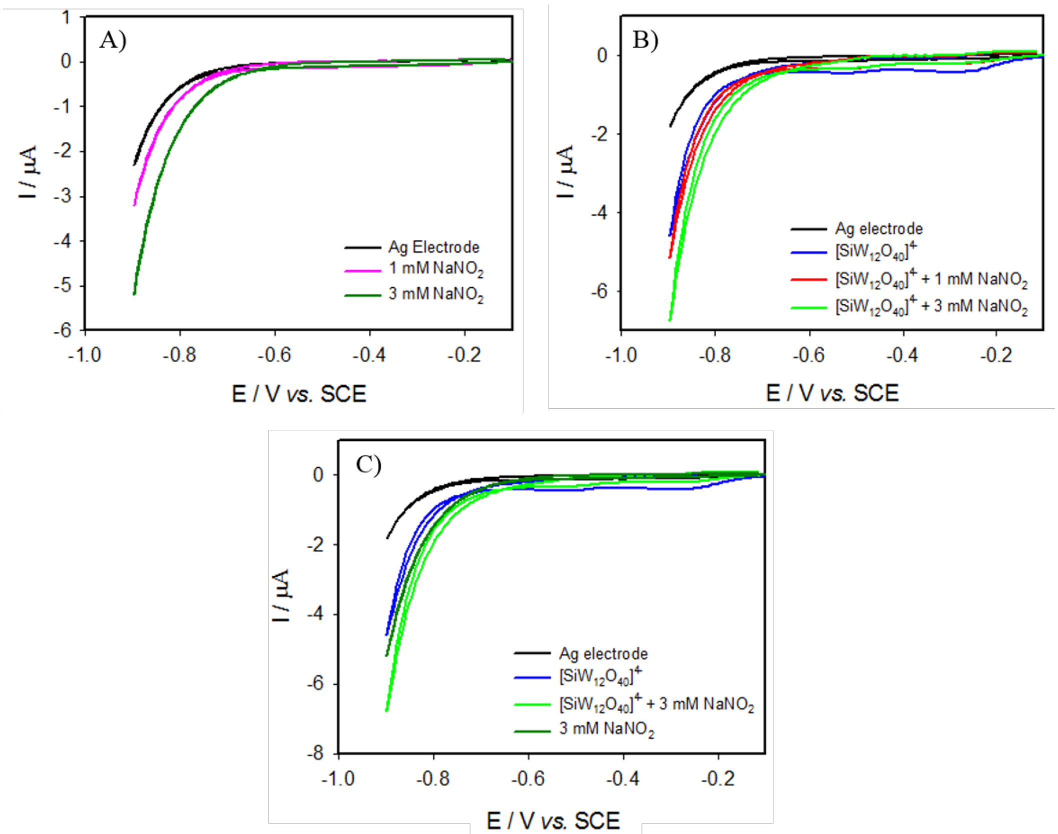

Figure II.12: A) Electrochemical reduction of NO_2^- on Ag electrode. B) Electrochemical reduction of NO_2^- in the presence of 0.1 mmol·L^{-1} $[SiW_{12}O_{40}]^{4-}$ on Ag electrode. C) Comparison of NO_2^- reduction with or without $[SiW_{12}O_{40}]^{4-}$ in solution. Buffer solution: pH 5 1 mol·L^{-1} $CH_3COOLi + CH_3COOH$, v = 2 mV·s^{-1}.

3.3 Comparison of catalytic onset potentials of nitrite (HNO_2 or NO_2^-) reduction on GC, Cu and Ag bulk electrodes

Electrode	POM	pH 1	pH 5
GC	without	no activity	no activity
GC	$[SiW_{12}O_{40}]^{4-}$	-0.21	-0.94
Cu	without	-0.26	-0.66
Cu	$[SiW_{12}O_{40}]^{4-}$	-0.19	-0.62
Ag	without	*	-0.83
Ag	$[SiW_{12}O_{40}]^{4-}$	-0.18	*

**catalytic onset potential undefined due to the small catalytic current*

Table II.2: Catalytic onset potentials of HNO_2 or NO_2^- reduction on different electrode surface in pH 1 0.5 mol·L^{-1} $Na_2SO_4 + H_2SO_4$ solution or in pH 5 1 mol·L^{-1} $CH_3COOLi + CH_3COOH$ solution.

Metal surfaces are generally more active towards nitrite reduction and copper bulk electrode is more active than silver bulk electrode in both solutions. In pH 1 solution, the catalytic onset potentials on Cu or Ag electrode advanced to nearly the same potential after adding POM showing a significant effect of POM towards nitrite reduction.

Nitrite ions are more difficult to be reduced in pH 5 solution than in pH 1 solution even in the absence of POMs. It might be related to the fact that most of catalytic reductions consume H^+ during reaction. At pH 5, silver has no considerable activity towards nitrite reduction before hydrogen evolution, while Cu keeps its reactivity. After adding POM, a small advance of potential is observed on Cu electrode.

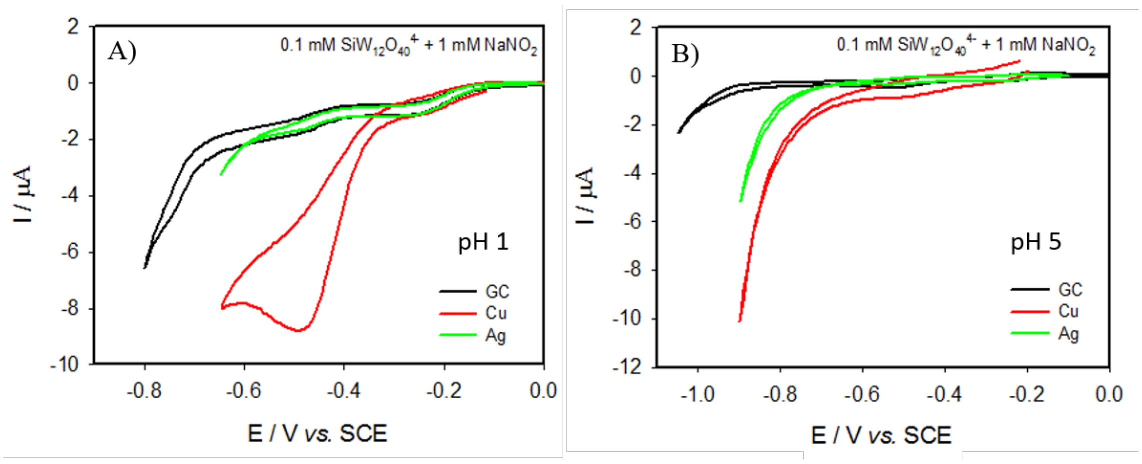

Figure II.13: Reduction of 1 mmol·L^{-1} NaNO$_2$ in the presence of 0.1 mmol·L^{-1} [SiW$_{12}$O$_{40}$]$^{4-}$ on GC, Cu and Ag electrodes, v = 2 mV·s^{-1}.

Nitrite reductions with 0.1 mmol·L^{-1} $[SiW_{12}O_{40}]^{4-}$ on GC, Cu and Ag electrodes in the presence of the same quantity of $NaNO_2$ (1 mmol·L^{-1}) have been studied and are shown in Fig. II.13. In pH 1 solution, a catalytic current of HNO_2 reduction is observed at the first wave of POM (-0.24 V). Interestingly, the reduction current occurs at the same potential (-0.24 V) and has the same value whatever the electrode, GC, Cu or Ag. This reveals that the catalysis is only due to the POM at this potential. In contrast, the catalytic current at the second reduction wave of the POM (ca. -0.47 V) is strongly affected by the nature of the electrode. While GC and Ag electrodes show the same catalytic properties in the presence of $[SiW_{12}O_{40}]^{4-}$, a large reduction peak is observed at -0.47 V on Cu bulk electrode confirming a synergy between the POM and Cu surface. Finally, in the presence of POM, the Ag electrode exhibits a better reduction current than the GC electrode only below -0.60 V.

At pH 5, a higher catalytic current is observed on metal surfaces after the second $W^{VI/V}$ reduction wave. The current intensity is two times higher on Cu electrode than on Ag electrode, which is better than GC in the presence of POM.

4 Reduction of NO_3^- in the presence of POM on Cu or Ag bulk electrode

4.1 Reduction of NO_3^- in pH 1 medium with or without $[SiW_{12}O_{40}]^{4-}$

4.1.1 On GC electrode

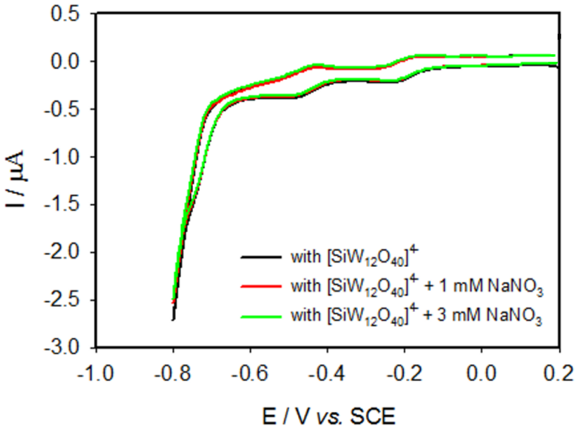

Figure II.14: Electrochemical reduction of NO_3^- in the presence of 0.1 mmol·L^{-1} $[SiW_{12}O_{40}]^{4-}$ on GC electrode. Buffer solution: pH 1 0.5 mol·L^{-1} Na_2SO_4 + H_2SO_4, v = 2 mV·s^{-1}.

Nitrate reduction on GC electrode in the presence of $[SiW_{12}O_{40}]^{4-}$ in pH 1 solution is shown in Fig. II.14. There is no change observed in the measured potential range showing no catalytic effect of the POM as well as the GC electrode.

4.1.2 On Cu bulk electrode

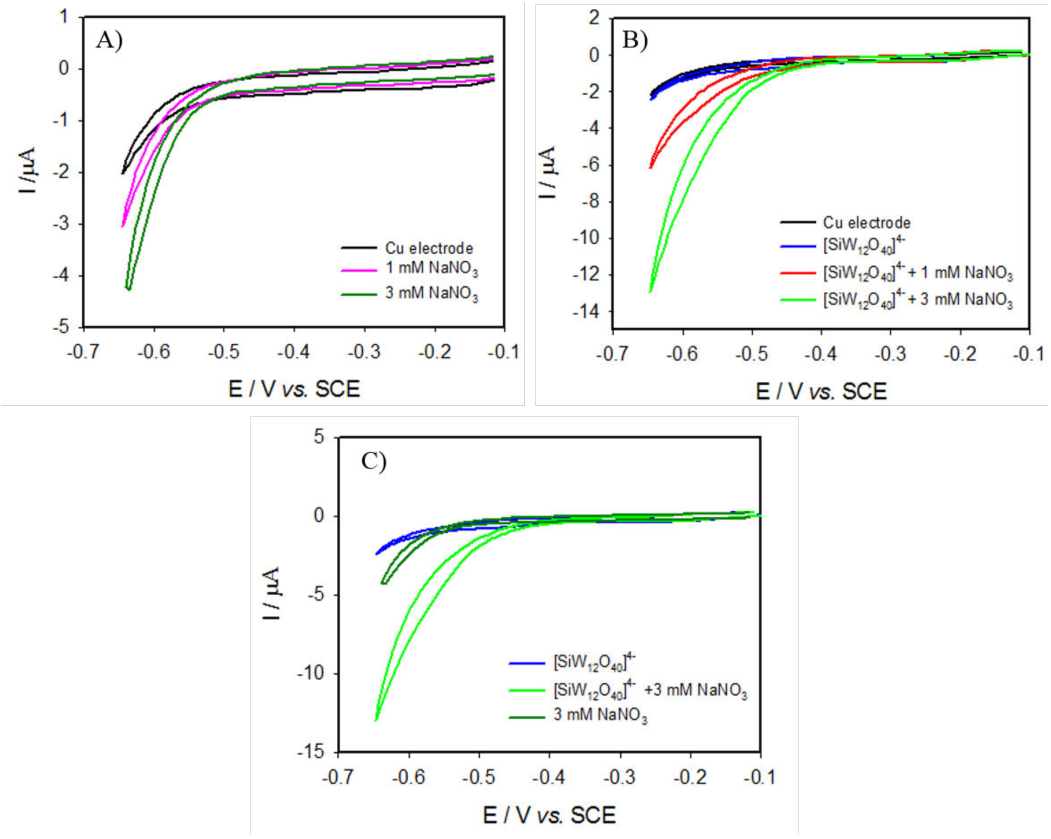

Figure II.15: A) Electrochemical reduction of NO_3^- on Cu electrode. B) Electrochemical reduction of NO_3^- in the presence of 0.1 mmol·L^{-1} $[SiW_{12}O_{40}]^{4-}$ on Cu electrode. C) Comparison of NO_3^- reduction with or without $[SiW_{12}O_{40}]^{4-}$ in solution. Buffer solution: pH 1 0.5 mol·L^{-1} $Na_2SO_4 + H_2SO_4$, v = 2 mV·s^{-1}.

On Cu electrode, the catalytic reduction of NO_3^- begins around -0.63 V, about 0.37 V more negative than that for nitrite reduction, in agreement with other published work.[13] However, Dima and co-workers reported an onset of the reduction at -0.10 V *vs.* SCE in 0.5 mol·L^{-1} H_2SO_4 with a higher NO_3^- concentration (0.1 mol·L^{-1}, at 20 mV·s^{-1}).[14] The difference in the onset potential can be attributed to the different concentrations of NO_3^- ions in the solution and nitrate reduction is also known to be sensitive to the state of Cu surface. The first step of reduction of NO_3^- in acidic media on Cu electrode is considerate as:[15]

$$NO_3^- + 2H^+ + 2e^- \rightarrow NO_2^- + H_2O$$

After adding $[SiW_{12}O_{40}]^{4-}$, the nitrate reduction catalytic wave is significantly shifted toward more positive potential with a higher intensity of current. Between -0.52 V to -0.42 V, Tafel plot confirmed a better activity with $[SiW_{12}O_{40}]^{4-}$ in solution, with a slope of 105 mV/decade. This reveals that the interaction of the $[SiW_{12}O_{40}]^{4-}$ with the Cu surface is helpful to the catalytic activity for 30 mmol·L^{-1} NO_2^- solution in this potential range since a lower overpotential has to be applied to obtain the same NO_2^- reduction current value measured in the absence of POM.

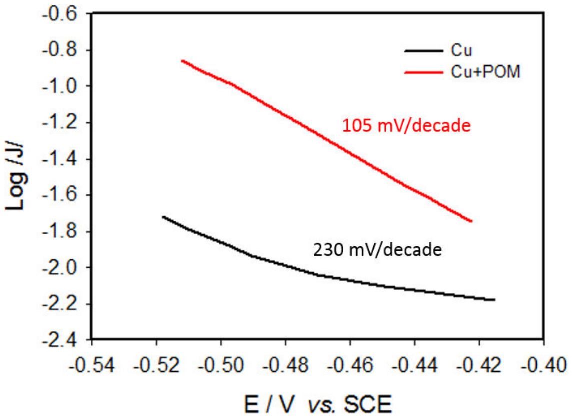

Figure II.16: Tafel plot for 30 mmol·L^{-1} NO_3^- reduction on Cu bulk electrode in pH 1 0.5 mol·L^{-1} Na_2SO_4 + H_2SO_4 solution, v = 2 mV·s^{-1}.

4.1.3 On Ag bulk electrode

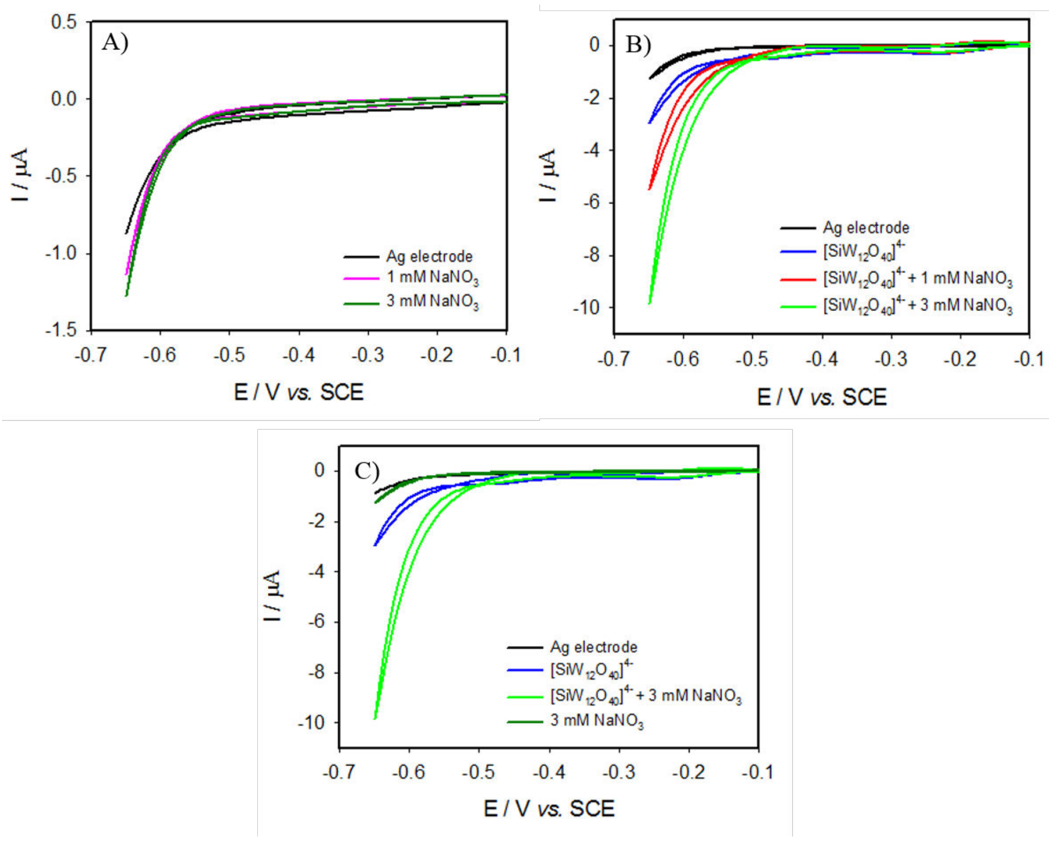

Figure II.17: A) Electrochemical reduction of NO_3^- on Ag electrode. B) Electrochemical reduction of NO_3^- in the presence of 0.1 mmol·L^{-1} $[SiW_{12}O_{40}]^{4-}$ on Ag electrode. C) Comparison of NO_3^- reduction with or without $[SiW_{12}O_{40}]^{4-}$ in solution. Buffer solution: pH 1 0.5 mol·L^{-1} Na_2SO_4 + H_2SO_4, v = 2 mV·s^{-1}.

On Ag electrode, the nitrate reduction activity is relatively low, a small increase of current being observed after -0.60 V (2 $mV \cdot s^{-1}$), superimposed with H_2 evolution. The onset finding is -0.30 V later than that observed by Dima and co-workers in 0.5 $mol \cdot L^{-1}$ H_2SO_4 + 0.1 $mol \cdot L^{-1}$ $NaNO_3$ at 20 $mV \cdot s^{-1}$.[14] With the presence of $[SiW_{12}O_{40}]^{4-}$, the catalysis advanced to -0.57 V and with a more significant current measured.

4.2 Reduction of NO_3^- in pH 5 medium with or without $[SiW_{12}O_{40}]^{4-}$

4.2.1 On GC bulk electrode

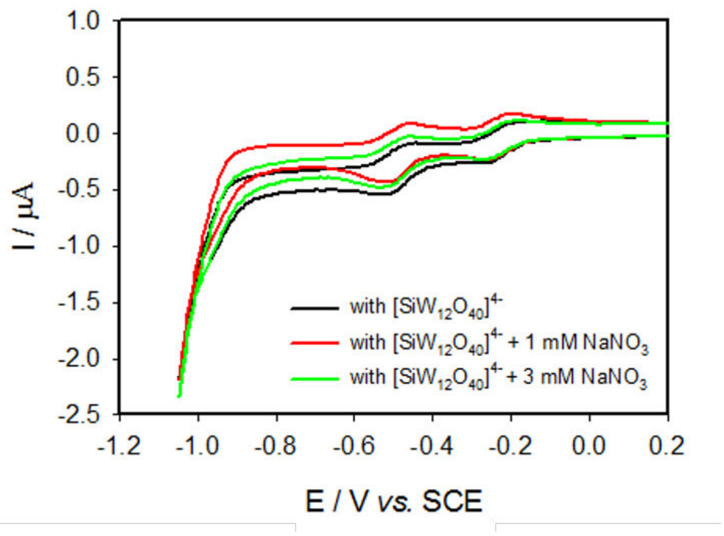

Figure II.18: Electrochemical reduction of NO_3^- in the presence of 0.1 $mmol \cdot L^{-1}$ $[SiW_{12}O_{40}]^{4-}$ on GC electrode. Buffer solution: pH 5 1 $mol \cdot L^{-1}$ $CH_3COOLi + CH_3COOH$, $v = 2\ mV \cdot s^{-1}$.

As in pH 1 solution, no catalytic current is observed on GC electrode in the presence of only 0.1 $mmol \cdot L^{-1}$ $[SiW_{12}O_{40}]^{4-}$, as shown in Fig. II.18.

4.2.2 On Cu bulk electrode

On Cu electrode at pH 5, the nitrate reduction starts at -0.74 V. The mechanism can be described as:

$$NO_3^- + H_2O + 2e^- \rightarrow NO_2^- + 2OH^-$$

In the presence of $[SiW_{12}O_{40}]^{4-}$, the reduction starts earlier at -0.70 V, a significant catalytic current increase is observed in the presence of POM. For this system, the Tafel analysis could not be performed because this reduction is superimposed with hydrogen reduction.

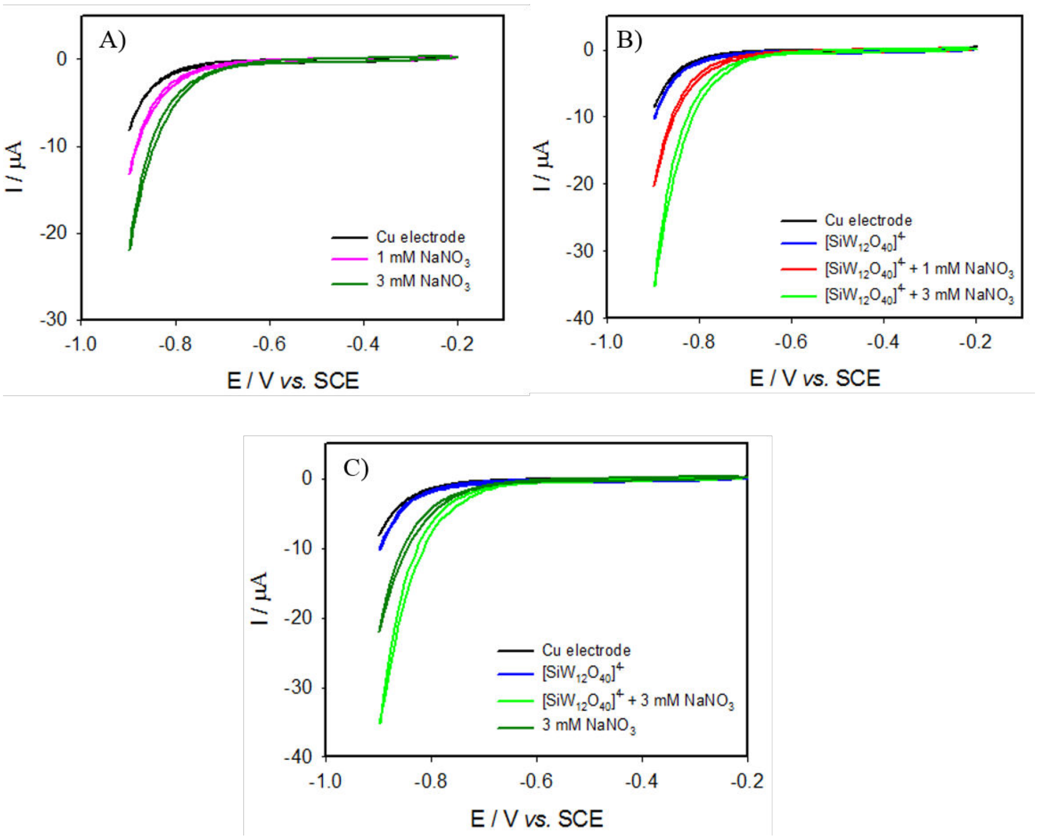

Figure II.19: A) Electrochemical reduction of NO_3^- on Cu electrode. B) Electrochemical reduction of NO_3^- in the presence of 0.1 $mmol \cdot L^{-1}$ $[SiW_{12}O_{40}]^{4-}$ on Cu electrode. C) Comparison of NO_3^- reduction with or without $[SiW_{12}O_{40}]^{4-}$ in solution. Buffer solution: pH 5 1 $mol \cdot L^{-1}$ $CH_3COOLi + CH_3COOH$, $v = 2\ mV \cdot s^{-1}$.

4.2.3 On Ag bulk electrode

As in the case of the Cu electrode, the nitrate reduction concomitant to the hydrogen evolution on Ag surface. After adding $[SiW_{12}O_{40}]^{4-}$, $W^{VI/V}$ reductions are well-defined but no catalytic effect is observed. Thus, there is no tandem catalysis between the POM and the silver electrode for the nitrate reduction at pH 5.

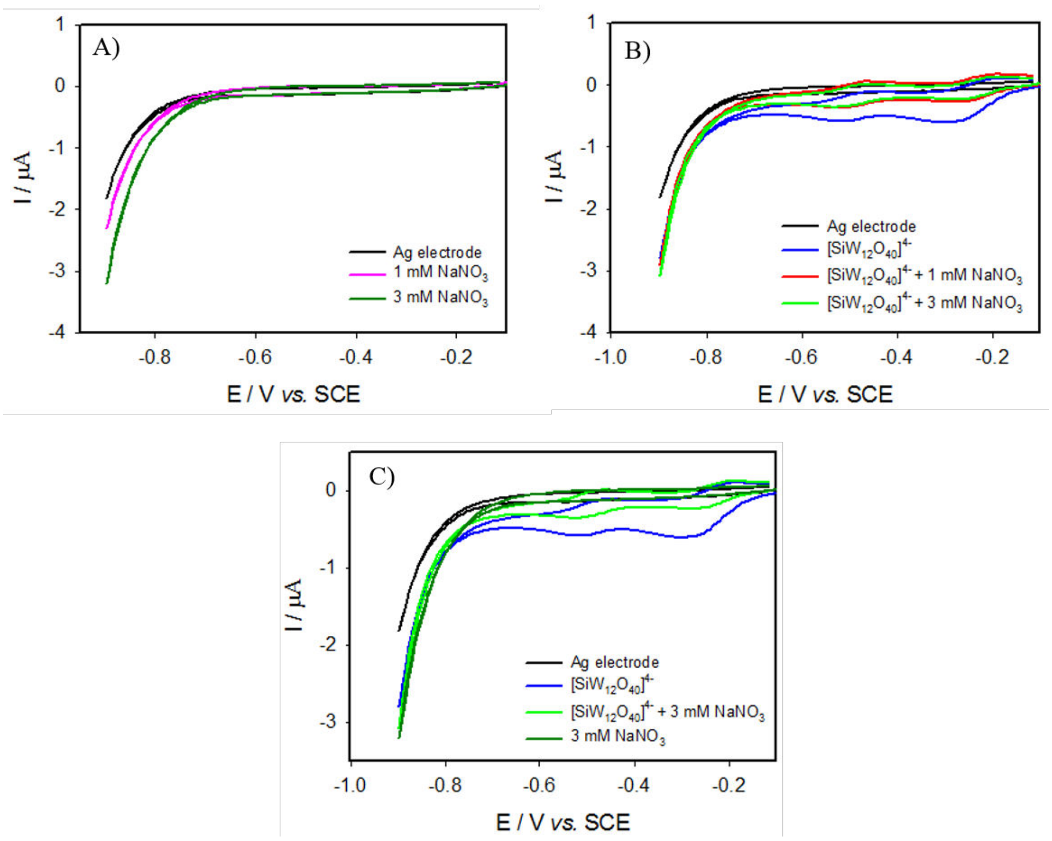

Figure II.20: A) Electrochemical reduction of NO_3^- on Ag electrode. B) Electrochemical reduction of NO_3^- in the presence of 0.1 mmol·L^{-1} $[SiW_{12}O_{40}]^{4-}$ on Ag electrode. C) Comparison of NO_3^- reduction with or without $[SiW_{12}O_{40}]^{4-}$ in solution. Buffer solution: pH 5 1 mol·L^{-1} CH_3COOLi + CH_3COOH, v = 2 mV·s^{-1}.

The catalytic onset potentials of NO_3^- reduction are summarized on table below:

Electrode	POM	pH 1	pH 5
Cu	without	-0.63	-0.74
Cu	$[SiW_{12}O_{40}]^{4-}$	-0.52	-0.70
Ag	without	*	-0.83
Ag	$[SiW_{12}O_{40}]^{4-}$	-0.57	no activity

**catalytic onset potential undefined due to the small catalytic current*

Table II.3: Catalytic onset potentials of NO_3^- reduction on different electrode surfaces, v = 2 mV·s^{-1}.

GC electrode and POM $[SiW_{12}O_{40}]^{4-}$ have no activity toward nitrate reduction. Hence, the presence of metal surface is a necessary condition for nitrate catalysis. In both solutions, nitrate is reduced at more positive potential on Cu electrode than on Ag electrode.

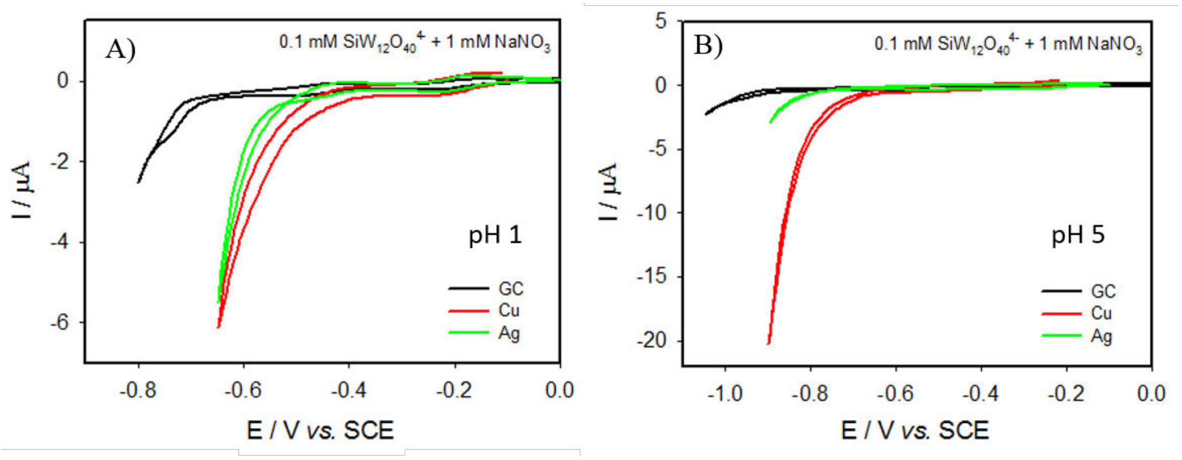

Figure II.21: Reduction of 1 mmol·L^{-1} $NaNO_3$ in the presence of 0.1 mmol·L^{-1} $[SiW_{12}O_{40}]^{4-}$ on GC, Cu and Ag electrodes, v = 2 mV·s^{-1}.

Nitrate reductions in the presence of 0.1 mmol·L^{-1} $[SiW_{12}O_{40}]^{4-}$ on GC, Cu and Ag electrodes in with the same quantity of $NaNO_3$ (1 mmol·L^{-1}) have been studied and are shown in Fig. II.21. In pH 1 solution, the catalytic current is observed between -0.45 V and -0.55 V and increases on Cu and Ag electrodes compared to GC. As for the nitrite reduction, the highest activity is obtained with Cu electrode.

Cu bulk electrode shows also the best activity in pH 5 solution, the catalytic current being five times higher than on Ag electrode.

5 Conclusion

In this chapter, the occurrence of a tandem catalysis between POM and silver or copper bulk electrodes was investigated for nitrite and nitrate reductions as a function of the pH of the solution. Based on electrochemical studies, POM $[SiW_{12}O_{40}]^{4-}$ are adsorbed on Cu and Ag surfaces even for as low as potential -0.50 V *vs.* SCE in pH 1 solution and in pH 5 solution. In contrast, the POM reduction is diffusion-controlled with GC electrode in this potential range. Hence the interactions between POM and electrode surfaces affect its electrochemical properties.

Clean GC electrode is not active for nitrite reduction, while catalytic reduction can be observed on both Cu and Ag bulk electrodes. Cu bulk electrode shows a better activity than Ag bulk electrode with smaller reaction overpotential and higher catalytic current especially at pH 1. A significant positive shift of the catalytic onset potentials and an increase of reduction currents are observed on these three bulk electrodes after adding POM $[SiW_{12}O_{40}]^{4-}$ into the solution. A synergy between Cu and POM is observed in the potential range between -0.40 V and -0.57 V *vs.* SCE in pH 1 solution.

In contrast, $[SiW_{12}O_{40}]^{4-}$ on GC electrode cannot catalyze the nitrate reduction, but the presence of POM in solution results in an increased activity of the Cu and Ag bulk electrodes. This is attributed to the occurrence of a tandem catalysis between the POM and the copper electrode which takes place at pH 1 and pH 5. However, the synergy in the catalysis between POM and silver electrode, could be evidenced only in pH 1. For all the systems investigated in this chapter, nitrate was found to be reduced at more negative potential than nitrite.

As POM has a positive effect on the NO_x reduction on GC, Cu and Ag electrodes in both pH 1 and pH 5 solutions, the preparation, characterization and catalytic properties of different types of POMs associated to Cu/Ag nanoparticles will be presented in the following chapters in order to understand the main factors influencing the efficiency of these catalysts for NO_x reduction.

References

1. Duca, M., Van Der Klugt, B. & Koper, M. T. M. Electrocatalytic reduction of nitrite on transition and coinage metals. *Electrochim. Acta* **68**, 32–43 (2012).
2. Duca, M. & Koper, M. T. M. Powering denitrification: the perspectives of electrocatalytic nitrate reduction. *Energy Environ. Sci.* **5**, 9726-9742 (2012).
3. Rong, C. & Anson, F. C. Spontaneous adsorption of heteropolytungstates and heteropolymolybdates on the surfaces of solid electrodes and the electrocatalytic activity of the adsorbed anions. *Inorganica Chim. Acta* **242**, 11–16 (1996).
4. Keita, B., Nadjo, L., Belanger, D., Wilde, C. P. & Hilaire, M. Electrochemical quartz crystal microbalance: evidence for the adsorption of heteropoly and isopoly anions on gold electrodes. *J. Electroanal. Chem.* **384**, 155–169 (1995).
5. Lee, L. & Gewirth, A. A. Electrochemical response of $H_4SiW_{12}O_{40}$ on Ag and Au electrodes. *J. Electroanal. Chem.* **522**, 11–20 (2002).
6. Sadakane, M. & Steckhan, E. Electrochemical properties of polyoxometalates as electrocatalysts. *Chem. Rev.* **98**, 219–238 (1998).
7. Dong, S., Xi, X. & Tian, M. Study of the electrocatalytic reduction of nitrite with silicotungstic heteropolyanion. *J. Electroanal. Chem.* **385**, 227–233 (1995).
8. Parkt, J.-Y. & Lee, Y.-N. Solubility and decomposition kinetics of nitrous acid in aqueous solution. *J . Phys. Chem* **92,** 6294–6302 (1988).
9. Ruhlmann, L. & Genet, G. Wells-Dawson-derived tetrametric complexes $\{K_{28}H_8[P_2W_{15}Ti_3O_{63.5}]_4\}$ electrochemical behaviour electrocatalytic reduction of nitrite and of nitritx oxide. *J. Electrocatal. Chem.* **568**, 315–321 (2004).
10. Keita, B., Lucas, T. & Nadjo, L. New aspects of the electrochemistry of heteropolyacids reduction currents as a probe of solvent-electrolyte interactions. *J. Electroanal Chem* **208***,* 343–356 (1986).
11. Gamboa, J. C. M., Peña, R. C., Paixão, T. R. L. C., Lima, A. S. & Bertotti, M. Activated copper cathodes as sensors for nitrite analysis. *Electroanalysis* **22**, 2627–2632 (2010).
12. Rosca, V., Duca, M., de Groot, M. T. & Koper, M. T. M. Nitrogen cycle electrocatalysis. *Chem. Rev.* **109**, 2209–44 (2009).
13. Bae, S., Stewart, K. L. & Gewirth, A. A. Nitrate adsorption and reduction on Cu (100) in acidic solution. *J Am Chem Soc* **129**, 10171–10180 (2007).
14. Dima, G. E., De Vooys, A. C. A. & Koper, M. T. M. Electrocatalytic reduction of nitrate at low concentration on coinage and transition-metal electrodes in acid solutions. *J. Electroanal. Chem.* **554–555**, 15–23 (2003).
15. De Vooys, A. C. A., Van Santen, R. A. & Van Veen, J. A. R. Electrocatalytic reduction of NO_3^- on palladium/copper electrodes. *J. Mol. Catal. A Chem.* **154**, 203–215 (2000).

Chapter III

Electrochemical and electrocatalytic properties of Cu-substituted polyoxometalate/alendronate

Chapter III Electrochemical and electrocatalytic properties of Cu-substituted polyoxometalate/alendronate

1 Introduction

In addition to the catalytic activity of metallic Cu electrode for the reduction of NO_x, it was found that Cu-substituted POMs possess also significant activity.

Non-substituted POMs such as $[SiW_{12}O_{40}]^{4-}$ are known to be active for nitrite reduction in acidic media as described in chapter II. In contrast, only few transition-metal-ion-substituted POM_S possess an activity for nitrate reduction. Most of them are Cu- or Ni-substituted POMs,[1,2] except for a few of Fe-substituted POMs. Ammam and his co-workers[3] have reported NO_3^- reduction by a Ni- and Fe-substituted sandwich-type POM $[Ni^{II}_2(Fe^{III})_2(P_2W_{15}O_{56})_2]^{14-}$ in pH 3 (0.5 $mol{\cdot}L^{-1}$ $Na_2SO_4 + H_2SO_4$) and pH 5 (1 $mol{\cdot}L^{-1}$ $CH_3COOLi + CH_3COOH$) solutions. The onset of the reduction takes place at the last reduction wave of the POMs (-0.85 V *vs.* SCE at pH 3 and -0.94 V *vs.* SCE at pH 5).[3] Keita and his co-workers have compared the catalytic activities of mono-substituted derivatives with its sandwich complex $[\{Cu(H_2O)\}_2Cu_2(H_4AsW_{15})_2]^{18-}$, which is the first example of a nitrate reduction on sandwich-type complex.[4] They concluded that the catalytic efficiency increases with the number of active metal centers in structure.[4] More details and other examples have been discussed in the Chapter I part 3. Among these results, Cu-substituted POMs possess the best reactivity towards nitrate reduction. Unfortunately, the mechanism as well as the product of the reduction remain unclear.

The elaboration of metal-substituted POMs functionalized by exogenous ligands may permit to adjust the properties of POM.[5] Alendronate (Ale=$[H_2O_3PC(C_3H_6NH_2(OH)PO_3H_2)]$) ligand-functionalized POMs have been demonstrated to be stable in water due to the chelating ability of the bisphosphonates (Bps) entities.[6] An alendronate Ni-substituted POM $Na_9[A\text{-}PW_9O_{34}]\cdot 7H_2O.Na_7K_7[\{(B\text{-}PW_9O_{34})Ni_3(OH)(H_2O)_2\text{-}O_3PC(O)C_3H_6NH_3)PO_3]\}_2Ni]\cdot 34H_2O$ was already reported being active towards nitrate reduction at pH 6 (1 $mol{\cdot}L^{-1}$ $CH_3COOLi + CH_3COOH$).[7]

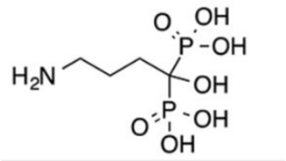

Alendronate (Ale)

In this chapter, the electrochemical and electrocatalytic properties of three Cu-substituted POMs have been investigated in order to identify the main factors which influence the activity. The electrochemical properties of Cu-substituted POMs in solution have been investigated by Cyclic Voltammetry (CV), potentiostatic coulometry and Electrochemical Quartz Crystal Microbalance (EQCM). The morphology of modified electrode has been studied by Atomic-Force Microscopy (AFM). The catalytic properties towards NO_x were studied in two different aqueous solutions of pH 5 (1 $mol\cdot L^{-1}$ $CH_3COOLi + CH_3COOH$) and pH 1 (0.5 $mol\cdot L^{-1}$ $Na_2SO_4 + H_2SO_4$) respectively.

The influence of the presence of Cu complex $[Cu_6(Ale)_4(H_2O)_4]^{4-}$ (CuAle) with ligand alendronate (Ale) grafted to CuPOMs entities will be explored. In this case, the catalysts are composed two types of Cu ions: one type of Cu is encapsulated in POMs units and the other Cu ions are coordinated by alendronate ligands. The properties of these three compounds are studied and compared with the corresponding CuPOMs as well as their catalytic properties towards NO_x.

2 Structure and characterization

2.1 Synthesis and structure of the CuPOMs

Six compounds have been investigated in this chapter (Fig. III.1). They were synthesized in collaboration with Prof. Pierre Mialane and DR. Anne Dolbecq, Institut Lavoisier, UMR 8180, Université Versailles Saint-Quentin en Yvelines.[8,9.]

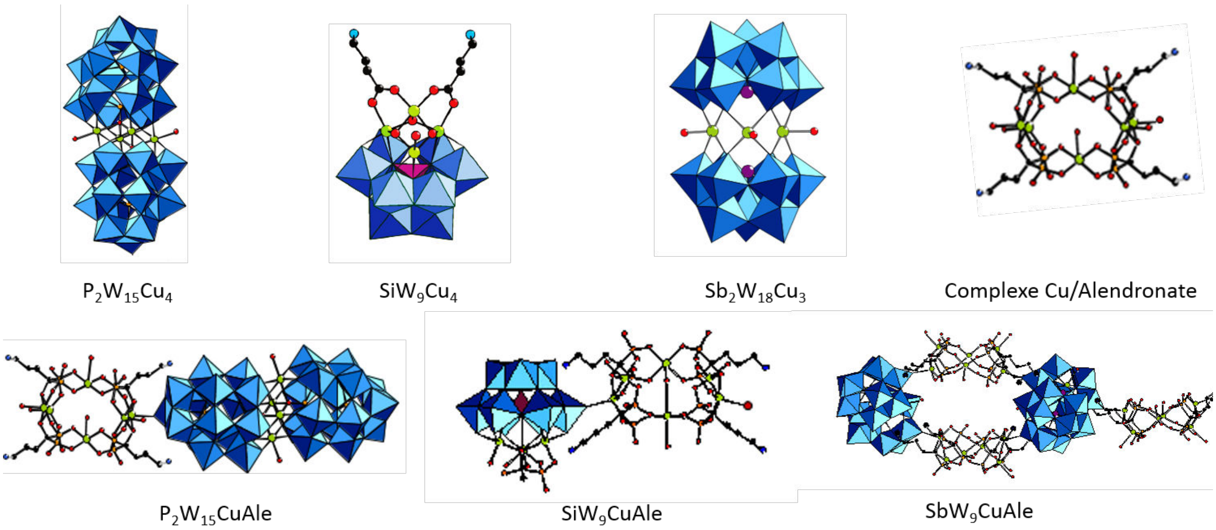

$P_2W_{15}Cu_4$ SiW_9Cu_4 $Sb_2W_{18}Cu_3$ Complexe Cu/Alendronate

$P_2W_{15}CuAle$ SiW_9CuAle SbW_9CuAle

Figure III.1: Representation of various structures of Cu-substituted polyoxometalates and Cu complex synthesized from the Cu ions and Alendronate ligand (Ale) (Reproduced from reference 8. Copyright (2017) American Chemical Society).

2.1.1 Synthesis

The three POMs units $Na_{10}[A\text{-}\alpha\text{-}SiW_9O_{34}]\cdot xH_2O$ (SiW_9),[10] $Na_{12}[\alpha\text{-}P_2W_{15}O_{56}]\cdot 24H_2O$ (P_2W_{15})[10] and $Na_9[\alpha\text{-}SbW_9O_{33}]\cdot 19.5H_2O$ (SbW_9)[11] are synthesized according to the reported procedures. More details concerning the synthesis and the characterization can be found in references 10 and 11.

To synthesize Cu-substituted POMs (CuPOMs): $Na_{16}[Cu_4(H_2O)_2(P_2W_{15}O_{56})_2]\cdot 50H_2O$ (**$P_2W_{15}Cu_4$**), $NaK_4[(A\text{-}\beta\text{-}SiW_9O_{34})Cu_4(OH)_3(H_2O)(H_3N(CH_2)_3COO)_2]_3\cdot 18H_2O$ (**SiW_9Cu_4**) and $K_{12}[(SbW_9O_{33})_2\{Cu(H_2O)\}_3]\cdot 41H_2O$ (**$Sb_2W_{18}Cu_3$**), the corresponding POM unit is mixed with a copper salt ($CuCl_2\cdot 2H_2O$) in water. The pH is adjusted to an interval between 7 to 8. The solution is boiled for 30 minutes. After cooling the solution to room temperature, potassium chloride is added to form a green precipitate. The powder is obtained by filtration and washed with water, ethanol, ether and then crystallized after redissolution in water at room temperature.

For CuPOM/Ale compounds, $Na_{12}[\{SiW_9O_{34}Cu_3(Ale)(H_2O)\}\{Cu_6(O_3PC(O)(C_3H_6NH_3)PO_3)_4(H_2O)_4\}]\cdot 50H_2O$ (**SiW_9CuAle**) and $Na_{20}[\{(P_2W_{15}O_{56})_2Cu_4(H_2O)_2\}\{Cu_6(O_3PC(O)(C_3H_6NH_3)PO_3)_4(H_2O)_4\}]\cdot 50H_2O$ (**$P_2W_{15}CuAle$**) are obtained by co-crystallization of the corresponding POM unit (SiW_9 and P_2W_{15} respectively), $CuCl_2$ and alendronic acid from a solution at pH 7.5. Green needle crystals are obtained after one week at room temperature.

To form $Na_8Li_{29}[\{(SbW_9O_{33})_2Cu_3(H_2O)_{2.5}Cl_{0.5}\}_2\{Cu_6(O_3PC(O)(C_3H_6NH_3)PO_3)_4(H_2O)_4\}_3]\text{-}163H_2O$ (**SbW_9CuAle**), SbW_9, $CuCl_2$ and alendronic acid are mixed in water at room temperature, the pH is adjusted to 8. NaCl is necessary to form a precipitate. After re-crystallization in a 1 $mol\cdot L^{-1}$ LiCl, green needle crystals are obtained after one week.

The samples collected are washed by ethanol and ether, then characterized by X-ray diffraction and infrared spectroscopy (IR), the results can be found in reference 8.

2.1.2 Structure

Cu complex $[Cu_6(Ale)_4(H_2O)_4]^{4-}$ (CuAle) contains two $\{Cu_2(Ale)_2(H_2O)_2\}$ pairs where all the Cu atoms are in square pyramidal distorted environment. These two pairs are connected by two Cu centers via eight O-P-O bridges leading to a cyclic hexanuclear species. The coordination of one Cu^{II} ion of each $\{Cu_2(Ale)_2(H_2O)_2\}$ pairs is completed by a terminal water molecular and the other one is connected to a terminal O=W oxygen atom of the $\{W_6\}$ crown of the POM entity.

In **SiW_9Cu_4**, a $\{Cu_4(OH)_3(H_2O)(H_3N(CH_2)_3COO)_2\}$ tetranuclear cluster covers the SiW_9 precursor, all the 3d centers are hexacoordinated and the fourth, apical Cu^{II} center is pentacoordinated because of the strong Jahn-Teller effect. Two amino acid are connected to POM and they are protonated in consonance with the pK_a value of primary amino groups.[9]

In **SiW_9CuAle**, the 3d metal cations fill the vacancies of the SiW_9 precursor, forming a pseudoisoscale triangle. Each Cu center is connecting to three O atoms of the silicotungstate ligand. An alendronate ligand covers the SiW_9Cu_3 fragment, connecting two copper ions via one O-P-O bridge. Each terminal O=W of the $\{W_6\}$ crown of the SiW_9Cu_3 is connected to one Cu atom of $\{Cu_2(Ale)_2(H_2O)_2\}$ pair, forming a -POM-$\{Cu_6\}$-POM-$\{Cu_6\}$- chain.

In **$Sb_2W_{18}Cu_3$**, three Cu atoms sandwiched between two SbW_9 units, which are connected by a O-W-O-W-O bridge. Similar to **SiW_9CuAle**, in **SbW_9CuAle,** two Cu centers of each $[Cu_6(Ale)_4(H_2O)_4]^{4-}$ cluster are connected to O=W of the $\{W_6\}$ crown of the POM, forming a -POM-$\{Cu_6\}$-POM-$\{Cu_6\}_2$-POM- chain. The POM/$[Cu_6(Ale)_4(H_2O)_4]^{4-}$ cluster ratio for **SiW_9CuAle** is 1:1 and 2:3 for **SbW_9CuAle**.

The third Cu-substituted POM **$P_2W_{15}Cu_4$** is described as a rhomb-like tetranuclear Cu cluster sandwiched between two sub units P_2W_{15}, followed by a $[Cu_6(Ale)_4(H_2O)_4]^{4-}$ complex. In the solid state, **$P_2W_{15}CuAle$** is formed by connecting **$P_2W_{15}Cu_4$** to $[Cu_6(Ale)_4(H_2O)_4]^{4-}$ cluster via O atoms which belongs to the $\{W_3\}$ of the Dawson units, forming a -POM-$\{Cu_6\}$-POM-$\{Cu_6\}$- one-dimensional chain. The POM/$[Cu_6(Ale)_4(H_2O)_4]^{4-}$ cluster ratio is 1:1.[8]

2.2 Magnetic properties

In the recent years, POMs are considered as good models for magnetic investigations.[5] Compared to other coordination compounds, POMs present some advantages: the preservation of integrity structure in the solid state, in solutions and on surfaces; the ability to accept various electrons while keeping their structure intact and the possibility of receiving magnetic ions or groups of magnetic ions, leading to the formation of magnetic molecules and large magnetic clusters.[5]

The magnetism of **SiW_9CuAle** and **SbW_9CuAle** were studied by Eric Rivière, Institut de Chimie Moléculaire et des Matériaux d'Orsay, University of Paris-sud. The magnetic measurements were performed on powder sample at room temperature.[8]

Both ferromagnetic and anti-ferromagnetic magnetic interactions are found in $[Cu_6(Ale)_4(H_2O)_4]^{4-}$ cluster. In **SbW_9CuAle**, two **$Sb_2W_{18}Cu_3$** units are considered as magnetically equivalent to the three $[Cu_6(Ale)_4(H_2O)_4]^{4-}$ clusters. The magnetic behavior of **SiW_9CuAle** shows a strong anti-ferromagnetic interaction because of the presence of SiW_9Cu_3 fragment.[8]

2.3 Cyclic voltammetry

Electrochemical measurement was carried out at room temperature under argon atmosphere. A three-electrode system was used with a glassy carbon (GC, Tokai Japan) electrode as the working electrode. A platinum wire was used as auxiliary electrode and the reference electrode was the saturated calomel electrode (SCE), which was electrically connected to the solution by a junction bridge filled with electrolyte. All reagents were used as purchased without further purification. The buffer solution was prepared from the following solutions of pH 1 (0.5 mol·L^{-1} $Na_2SO_4 + H_2SO_4$) and pH 5 (1 mol·L^{-1} $CH_3COOLi + CH_3COOH$).

In pH 1 solution, the high concentration of H^+ in the solution is profitable to the NO_x reduction which consumes protons. However, lacunary species of POMs are unstable in strongly acidic media. During the electrodeposition of Cu^0 on electrode surface, the POMs entities might be released in the solution or remains adsorbed on the electrode surface. The lacunary species are relatively stable in the solution at pH 5 and detectable by cyclic voltammetry.

For all compounds, the oxidation and reduction of the Cu species can be observed in the CVs. The case of **P_2W_{15}CuAle** is shown in Fig. III.2 as an example. In pH 1 solution, a large reduction wave is observed at -0.10 V, corresponds to the reduction of Cu^{II} to Cu^0 (waves I and II). The formation of Cu^0 continues below this potential during the cathodic and the anodic scans and Cu^0 re-oxidize at 0.01 V on the anodic scan. Several small redox waves are also observed between -0.20 V and -0.40 V. A magnification of the small waves is shown in the inset of Fig. III.2A. These waves are attributed to the reduction of W^{VI} to W^V of POMs. Hydrogen evolution is observed after -0.50 V, just after the second $W^{VI/V}$ reduction wave.

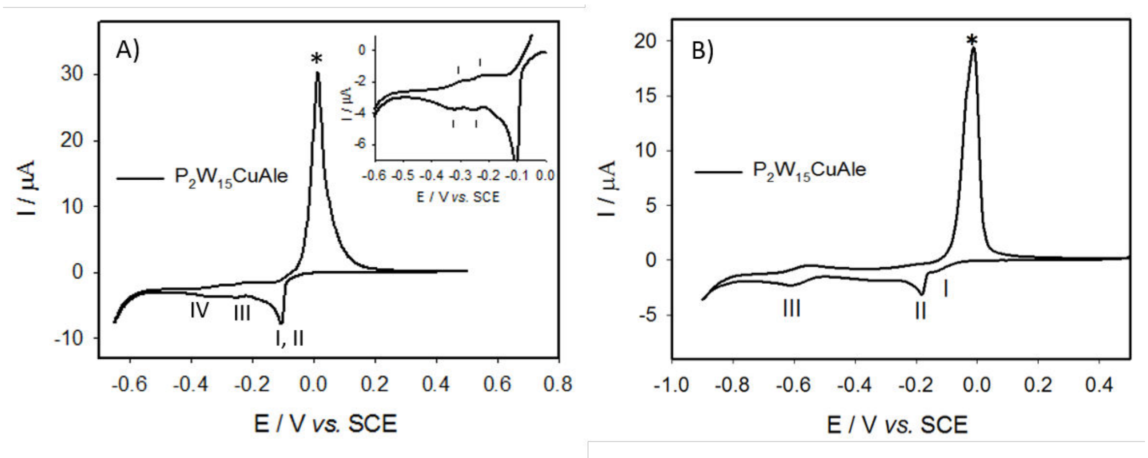

*Figure III.2: A) CV of 0.1 mmol·L^{-1} $P_2W_{15}CuAle$ in pH 1 0.5 mol·L^{-1} Na_2SO_4 + H_2SO_4 solution, v = 2 mV·s^{-1}. (Inset) Magnification of A to highlight the presence of the voltammetric characteristics of the POM. B) CV of 0.1 mmol·L^{-1} $P_2W_{15}CuAle$ in pH 5 1 mol·L^{-1} CH_3COOLi + CH_3COOH solution, v = 2 mV·s^{-1}. *: Reoxidation peak of the deposited Cu^0 on electrode surface.*

In pH 5 solution (Fig. III.2B), two reduction waves are observed during the reduction of Cu^{II} to Cu^0: $Cu^{II} + e^- \rightarrow Cu^I$ at -0.14 V followed by $Cu^I + e^- \rightarrow Cu^0$ at -0.18 V. The observation of these two waves suggests that the Cu^IPOM species might be stable in pH 5 aqueous solution. It should be mentioned that the presence of acetate in the buffer solution might play a role in the observation of these two waves since acetate ion can stabilize the Cu^I complex.[12] After the second reduction (wave II), Cu^0 is formed on the electrode surface. Therefore, the oxidation peak (*) at -0.02 V *vs.* SCE corresponds to the oxidation of Cu^0. The last reversible wave (waves III) is attributed to the redox process of the W centers (W^{VI}/W^V couple) at pH 5. Wave III is followed immediately by the proton reduction. In order to study better the first wave Cu^{II} to Cu^I, the potential scan was stopped just after this wave I as shown in Fig. III.3A. The first reduction wave (wave I) is reversible. Cathodic current shows a linear dependence to the square root of the scan rate $v^{1/2}$, which indicates that the current is limited by the diffusion of **$P_2W_{15}CuAle$** to the electrode surface (Fig. III.3B).

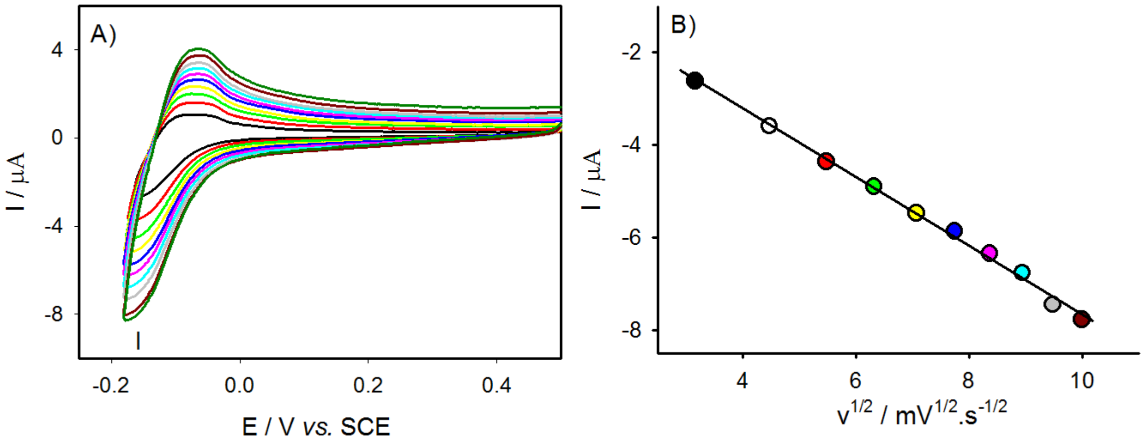

Figure III.3: A) Variation of scan rates of 0.1 mmol·L^{-1} $P_2W_{15}CuAle$ in pH 5 1 mol·L^{-1} CH_3COOLi + CH_3COOH solution (from inner to outer curve: 10, 20, 30, 40, 50, 60, 70, 80, 90, and 100 mV·s^{-1}). The potential reversal is fixed after Cu^{II} to Cu^{I} redox process. B) Variation of the cathodic peak current intensity as a function of the square root of the scan rate.

The CVs of other compounds are presented in appendix (Figs. S1 - S7).

The redox potentials of CuPOMs and CuPOMs/Ale compounds in pH 1 and in pH 5 solutions are listed in Table III.1 and Table III.2.

	Compounds	*	**I,II**	**III**	**IV**
		$Cu^{0/II}$	$Cu^{II/0}$	$W^{VI/V}$	
		Ep_a	Ep_c	$E_{1/2}$	$E_{1/2}$
pH 1	$P_2W_{15}CuAle$	0.01	-0.10	-0.24	-0.30
	$P_2W_{15}Cu_4$	0.02	-0.15	-0.24	-0.31
	SiW_9CuAle	0.00	-0.11	-0.52	
	SiW_9Cu_4	0.03	-0.15	-0.51	
	SbW_9CuAle	0.05	-0.09		
	$Sb_2W_{18}Cu_3$	0.03	-0.12	-0.44	
	$CuSO_4$	0.01	-0.17		

Table III.1: Reduction and re-oxidation peak potentials of each sample (0.1 mmol·L^{-1}) in pH 1 0.5 mol·L^{-1} Na_2SO_4 + H_2SO_4 solution. Reference electrode: SCE, v = 2 mV·s^{-1}.

	Compounds	*	**I**	**II**	**III**	**IV**
		$Cu^{0/II}$	$Cu^{II/I}$	$Cu^{I/0}$	$W^{VI/V}$	
		Ep_a	$E_{1/2}$	Ep_c	$E_{1/2}$	$E_{1/2}$
pH 5	$P_2W_{15}CuAle$	-0.02	-0.14	-0.18	-0.57	
	$P_2W_{15}Cu_4$	-0.02	-0.15	-0.26	-0.58	-0.80
	SiW_9CuAle	0.02	-0.11	-0.16		
	SiW_9Cu_4	0.00	-0.16	-0.26		-0.84
	SbW_9CuAle	0.03	-0.11	-0.16		
	$Sb_2W_{18}Cu_3$	-0.02	-0.13	-0.22	-0.59	-0.81
	$CuSO_4$	-0.02	-0.14	-0.24		

Table III.2: Reduction and re-oxidation peak potentials of each sample (0.1 mmol·L^{-1}) in pH 5 1 mol·L^{-1} $CH_3COOLi + CH_3COOH$ solution. Reference electrode: SCE, v = 2 mV·s^{-1}.

In pH 1 solution, the Cu^{II}POM reduction occurs at slightly higher potential that the one of **$CuSO_4$**, which might be tentatively attributed to the formation of an intermediate Cu^{I}POM species. It can be also noted that, Cu^{II} is reduced at more positive potential at pH 1 than at pH 5 with an anodic shift between 0 and 30 mV compared to the potential of the $Cu^{II/I}$ couple. The shift can be caused by the change of the buffer solution causing different junction potentials. Another possible explanation is the influence of the pK_a of the aqua Cu(II) center (Cu^{II}–OH_2) which can be easily deprotonated, giving the hydroxo forms Cu(II) centers (Cu^{II}–OH) when the pH increases which may affect slightly the redox potential.[13] At pH 1, the first redox wave of W (W^{VI}/W^{V} couple) is observed at nearly the same potential for **SiW_9CuAle**/**SiW_9Cu_4** or **$P_2W_{15}CuAle$**/**$P_2W_{15}Cu_4$**. In the case of **SbW_9CuAle**, the W^{VI}/W^{V} reversible waves are not observable, while one reduction wave is observed at -0.44 V for **$Sb_2W_{18}Cu_3$**.

In pH 5 solution, all compounds show similar redox behaviors with two successive reduction waves associated to the reduction of Cu^{II} to Cu^{I} and Cu^{I} to Cu^{0}. On the reverse potential scan, a large oxidation wave is observed, which corresponds to the re-oxidation of deposited Cu^{0}. For the first couple, Cu^{II}/Cu^{I}, the cathodic peak current is proportional to the square root of the scan rate, which indicates that the electrochemical processes are diffusion-controlled. The first redox wave of W (W^{VI}/W^{V} couple) in **$P_2W_{15}CuAle$** is observed at nearly the same potential as **$P_2W_{15}Cu_4$**. In the case of **SbW_9CuAle** and **SiW_9CuAle**, the W^{VI}/W^{V} reversible waves are not observable, while two ill-defined waves are observed at -0.59 V and -0.81 V for **$Sb_2W_{18}Cu_3$** and only one wave at -0.84 V for **SiW_9Cu_4**. Generally, Cu^{II} centers in CuPOM/Ale are reduced earlier than the ones encapsulated in CuPOM, indicating that Cu ions complexed by Ale ligands are easier to reduce.

In both solutions, W-centers in CuPOM/Ale are generally ill-defined or not detectable, due to the high sum of Cu ions led to more electron transferred. Hence, the reduction of W centers tends to be engulfed into the former Cu reduction.

2.4 Controlled-potential coulometry

Controlled-potential coulometry measurements were performed at a potential just below the peak potential of the second reduction process of Cu ($Cu^{I/0}$ couple, wave II) and after wave I (couple $Cu^{II/I}$) in order to evaluate the number of electron transferred per Cu^{II} species.

The illustration of a controlled-potential coulometric analysis is shown in Fig. III.4. Integration of the area, which is shown in pink, from t = 0 to t = t_e will give the total charge during the analysis.

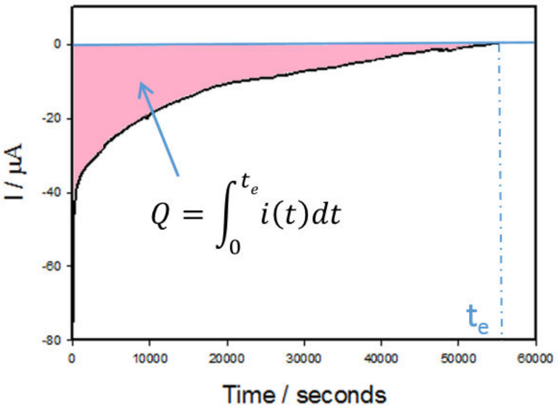

Figure III.4: Example of controlled-potential coulometry measurement. The black *curve is the measured current, the integrated area from t = 0 to t = t_e which is shown in pink, is the total charge. The background current is suppressed.*

The charge can also be calculated based on Faraday's law, which can be written as:

$$Q = n' \cdot (\frac{m}{M}) \cdot F$$

n': number of the electrons transferred, n' = 2n in which n is the sum of Cu ions in the structure

(2 being the number of exchanged electrons per Cu atom),

m: mass of the substance (g),

M: molar mass of the substance (g/mol),

F: Faraday constant (96485 C/mol).

The calculated charge and the measured charges of each substance are summarized in Table III.3. For an example, in the presence of 0.1 mmol·L^{-1} **P_2W_{15}CuAle**, 18.7 electrons per molecule are exchanged, which proves the reduction of all the ten Cu^{II} centers to Cu^0 (10×2e$^-$ per Cu^{II}). The presence of electrodeposited Cu^0 is also confirmed by the black deposit visible on the electrode surface. Similar results are observed for other compounds, indicating that all the Cu^{II} centers were reduced to Cu^0. The formation of the Cu^0 nanoparticles on the working electrode could be evidenced by AFM and EQCM, the results are presented in sections 2.5 and 2.6.

At the present stage, the characterization of the Cu^0 nanoparticles by other techniques, such as *in-situ* Transmission Electron Microscopy (*in-situ* TEM) and X-ray Photoelectron Spectroscopy (XPS), are also envisaged.

	Number of Cu(II) atoms	**Calculated Q (C)**	**Measured Q (C)**	**Number of electron (per molecule)**
P_2W_{15}CuAle	10	1.54	1.44	18.7
$P_2W_{15}Cu_4$	4	0.62	0.67	8.7
SiW_9CuAle	9	1.39	1.41	18.3
SiW_9Cu_4	4	0.62	0.63	8.2
SbW_9CuAle	24	3.71	3.80	49.3
$Sb_2W_{18}Cu_3$	3	0.46	0.48	6.2
$CuSO_4$	1	0.15	0.16	2.1

Table III.3: Controlled potential coulometry at the potential just below the peak potential of the second reduction process of Cu (after wave I and below wave II). The initial concentration is identical for each sample is 0.1 mmol·L^{-1} and the buffer solution is pH 5 1 mol·L^{-1} CH_3COOLi + CH_3COOH.

2.5 Atomic-Force Microscopy (AFM)

The morphology of deposited Cu^0 films are characterized by tapping mode AFM. The deposition is carried out from an acetate solution (pH 5) in absence of oxygen with different deposition times on ITO electrode.

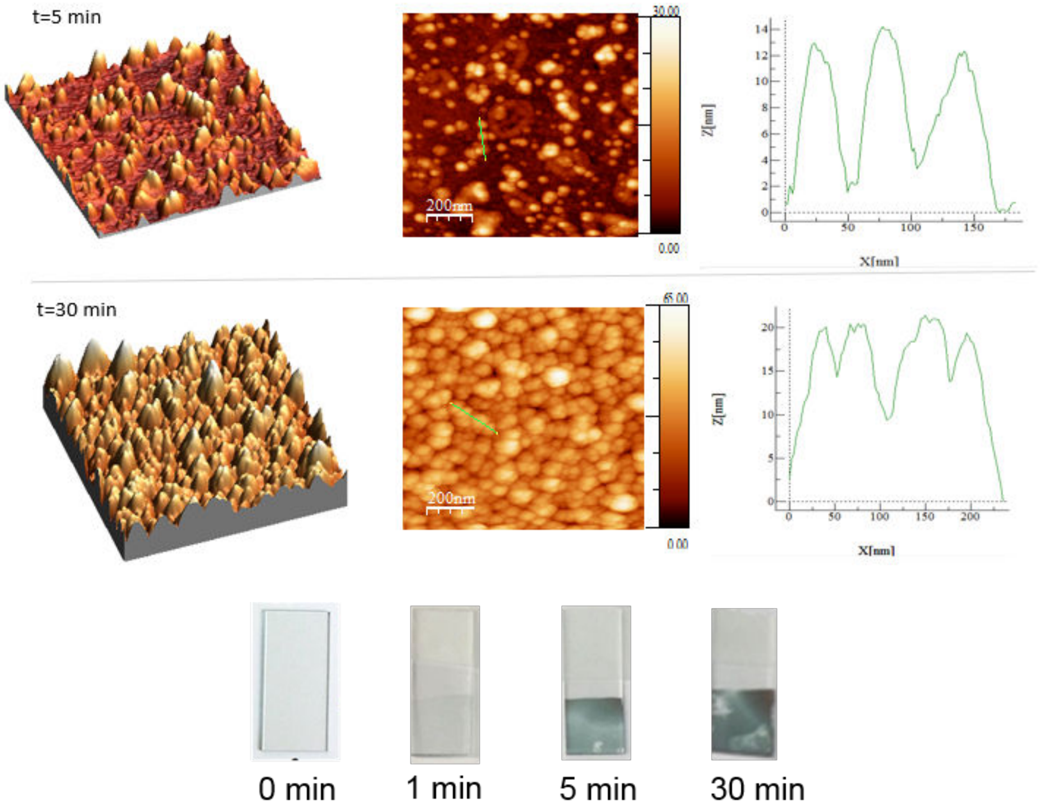

Figure III.5: (Top) Tapping mode AFM topography of 0.1 mmol·L^{-1} SiW$_9$CuAle obtained at potential -0.9 V vs. SCE with different deposition times: 5 minutes and 30 minutes. (Bottom) Photos of ITO electrode with different deposition times: clean ITO electrode (0 minute), 1, 5 and 30 minutes in the presence of 0.1 mmol·L^{-1} SiW$_9$CuAle. Buffer solution: pH 5 1 mol·L^{-1} CH$_3$COOLi + CH$_3$COOH solution.

After a 5-minutes deposition in **SiW$_9$CuAle** containing solution, particles with an average diameter of 50 nm and a height of 12 nm appear on the ITO electrode. The rms surface roughness of the film is 4.7 nm for 1 μm^2 area. The film grows with deposition time. After 30 minutes, the film gets thicker and the particles are more compact. The diameter does not change but the height increases to 20 nm. The rms surface roughness of the film increases to 7.8 nm for 1 μm^2 area.

Similar morphologies are obtained for other CuPOMs and CuPOMs/Ale compounds, but with an average diameter of 50 - 100 nm. The deposited film formed from **CuSO$_4$** was not studied in this work. According to the published works, the size of deposited Cu^0 from **CuSO$_4$** is 450 - 600 nm, much larger compared to the size of deposited Cu^0 particles from whatever Cu-substituted POM in this work.[1]

The photos of ITO electrode with different deposition times are shown in Fig. III.5, a change of color is observed and the colors becomes darker with deposition time.

2.6 Electrochemical Quartz Crystal Microbalance (EQCM)

The results of Electrochemical Quartz Crystal Microbalance (EQCM) studies were obtained in pH 5 1 mol·L^{-1} CH_3COOLi + CH_3COOH solution. The working electrode is an EQCM resonator which is carbon deposited on a 9.08 MHz AT-cut quartz crystal (A = 0.2 cm^2). An Ag wire is used as a reference electrode. The counter electrode is a platinum wire.

The cyclic voltammograms obtained by using this EQCM resonator as working electrode are qualitatively similar with that obtained on a glassy carbon electrode, except for **$Sb_2W_{18}Cu_3$** and **$CuSO_4$**, for which the two Cu reduction waves are not well distinguished as shown in Fig. III.6. The mass increases, provoked by the Cu and POM deposition on the electrode, is associated to the decrease of the frequency, allowing to determine precisely the potential below which the formation of Cu nanoparticles occurs (see. Table III.4). This decrease of the frequency is detected just at the second reduction wave (couple $Cu^{I/0}$) while no deposition is observed at the first wave (couple $Cu^{II/I}$), showing that even at the slow scan rate of 2 mV·s^{-1}, no disproportionation of Cu^I given Cu^0 and Cu^{II} occurs during the cathodic scan.

On the reverse scan, the oxidation Cu^0 leads to an abrupt decrease of the mass. Generally, the mass starts to decrease (with the increase of the frequency) at -0.30 V where Cu oxidation starts. The large oxidation wave is observed between -0.20 V to 0.00 V during re-oxidation scan, characterizing the surface-adsorbed species.

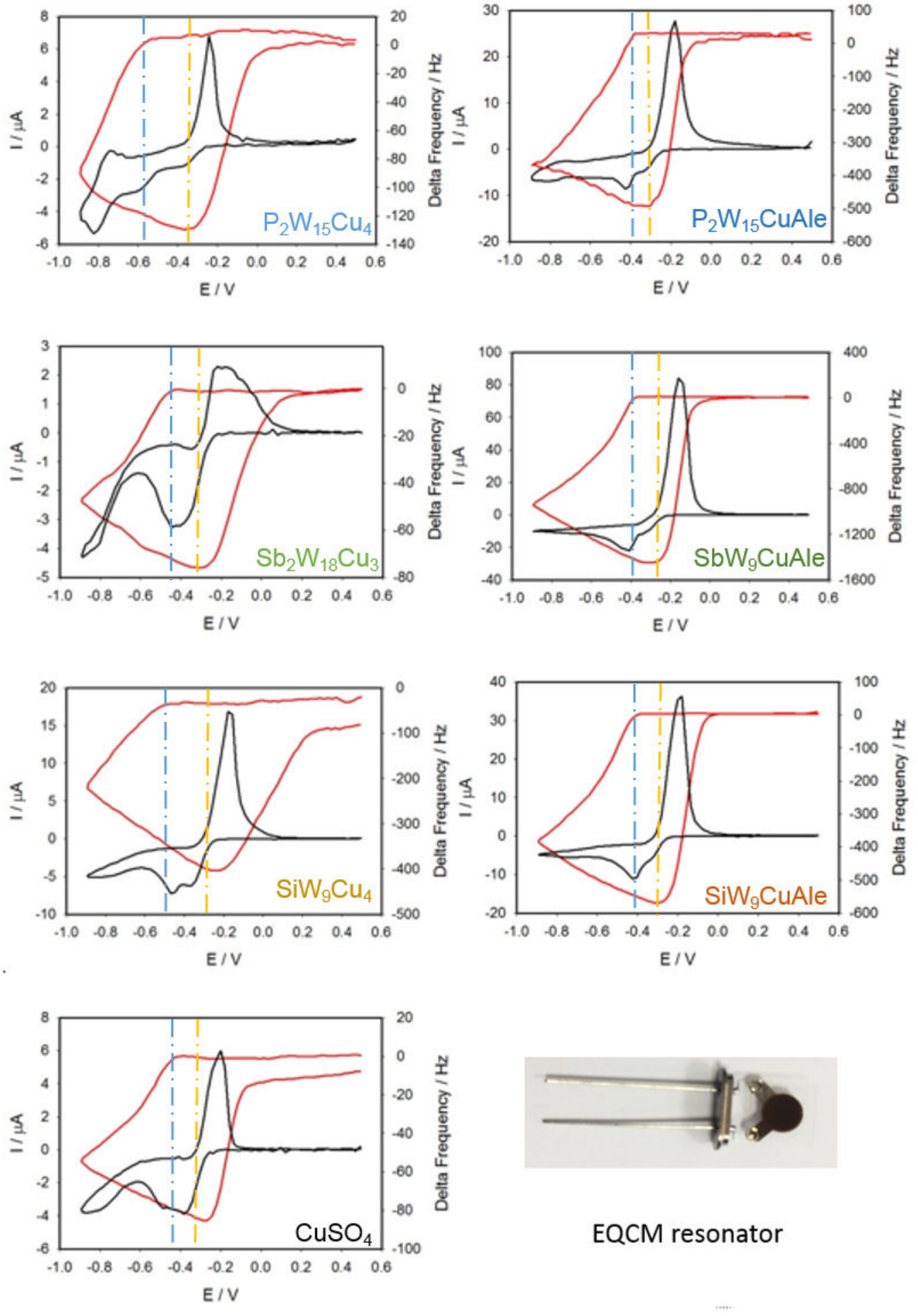

Figure III.6: Cyclic voltammetry (black curve) and electrochemical quartz crystal microbalance (EQCM; red curve) measurements for 0.1 mmol·L^{-1} samples in pH 5 1 mol·L^{-1} CH_3COOLi + CH_3COOH solution. v = 2 mV·s^{-1}. Blue line: the onset potential of the deposition of Cu nanoparticles (E_{onset}). Orange line: the end of the Cu nanoparticles deposition at revers scan (E_{end}).

In the case of **$CuSO_4$** and of the compounds **$P_2W_{15}CuAle$**, **SiW_9CuAle** and **SbW_9CuAle**, the deposition of Cu begins before -0.4 V (at the wave II), while for Cu-substituted POMs (**$P_2W_{15}Cu_4$**, **SiW_9Cu_4**, **$Sb_2W_{18}Cu_3$**), the onsets are 0.04 to 0.18 V later than the corresponding

CuPOM/Ale (see E_{onset} Table. III.4). The formation of electrodeposited Cu nanoparticles seems to be easier in the presence of alendronate (Ale) than with POM alone. Finally, it should be noted that for all investigated compounds, the Cu deposition process monitored by cyclic voltammetry and EQCM continues during the positive going scan and ends at a potential value slightly higher than the one of the onset during the cathodic scan (see E_{end} Table. III.4). This suggests that the onset potential value of the Cu nanoparticles formation is strongly influenced by the kinetics of formation of the Cu nuclei. It is also remarkable that the difference between the onset and the end potentials of the Cu deposition (see △E Table. III.4), is less pronounced when the alendronate ligand presented in the compounds which confirms the role of the CuAle on the nucleation kinetics on the glassy carbon surface.

	$P_2W_{15}CuAle$	$P_2W_{15}Cu_4$	SiW_9CuAle	SiW_9Cu_4	SbW_9CuAle	$Sb_2W_{18}Cu_3$	$CuSO_4$
E_{onset}	-0.37	-0.55	-0.37	-0.41	-0.37	-0.44	-0.40
E_{end}	-0.30	-0.35	-0.30	-0.28[a]	-0.28	-0.32	-0.32[a]
△E	0.07	0.20	0.07	0.13	0.09	0.12	0.08

Table III.4: Potentials of the beginning (E_{onset}) and the end (E_{end}) of the deposition of Cu nanoparticles for each POMs studied. $\triangle E = E_{end} - E_{onset}$ showing the difference between the onset and the end potentials of the Cu^0 deposition.

[a]: For most of the compounds, the potential at which EQCM frequency starts to increase during the anodic scan, corresponds to the onset of the Cu^0 oxidation current, except for $CuSO_4$ and SiW_9Cu_4 for which the onset of Cu^0 occurs simultaneously to an increase of the mass deposited on the electrode. Since the phenomena at the origin of this discrepancy are still unknown, E_{end} was determined using the onset potential of the Cu^0 oxidation current for these compounds.

The mass change (Δm) on electrode surface is calculated by the Sauerbrey's equation:

$$\Delta f = -2 f_0^2 \, \Delta m / \sqrt{\mu . \rho}$$

f_0: resonant frequency of the fundamental mode,

ρ: density of the crystal (2.684 g/cm^3),

A: area (0.2 cm^2),

μ: shear modulus of quartz (2.947×10^{11} $g/cm \cdot s^{-2}$).

The mass change during the Cu deposition (scan rate $\nu = 2$ $mV \cdot s^{-1}$, which corresponds to a deposition time of ca. 550 seconds) and the amount of Cu for each compound are plotted in Fig. III.7 using the same initial concentration. The smallest mass change is obtained with **$CuSO_4$** and **$Sb_2W_{18}Cu_3$** which is about 0.08 µg (0.4 $µg \cdot cm^{-2}$, with A = 0.2 cm^2) and the maximum is obtained for **SbW_9CuAle** with 1.58 µg (7.9 $µg \cdot cm^{-2}$, with A = 0.2 cm^2) due to the highest sum of Cu ions in structure. For others compounds, mass change increases with the number of Cu in structure except for the **SiW_9Cu_4** deposit which is ca. two times more than **$P_2W_{15}Cu_4$**, although both of them contain 4 Cu atoms in their structure. However, since the POM species adsorbed on the Cu nanoparticles contribute to the change of the mass, more quantitative interpretations might be taken with caution.

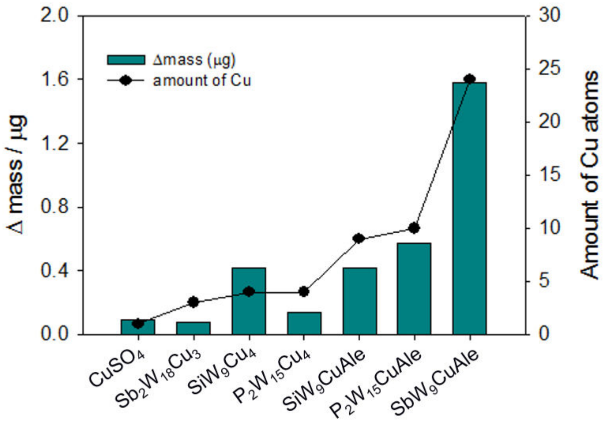

Figure III.7: Comparison of mass change in the presence of 0.1 mmol·L^{-1} sample in pH 5 1 mol·L^{-1} CH_3COOLi + CH_3COOH solution. v = 2 mV·s^{-1} (the deposition time is ca. 550 seconds) during EQCM measurement on a carbon deposited resonator (A = 0.2 cm^2) and the number of Cu atoms in structure.

3 Electrochemical reduction of NO_x by using CuPOMs

In this section, NO_x reduction is first studied with three Cu-substituted POMs (**$Sb_2W_{18}Cu_3$**, **$P_2W_{15}Cu_4$** and **SiW_9Cu_4**) in solution. Their activities are compared with the catalytic activity of **$CuSO_4$** in solution.

Cyclic voltammograms were collected between -0.90 V (before H^+ reduction) to 0.50 V (after the oxidation de NO_2^- to NO_3^-) on GC surface in a solution of pH 5 (1 mol·L^{-1} CH_3COOLi + CH_3COOH), and between -0.65 V to 0.50 V in pH 1 (0.5 mol·L^{-1} Na_2SO_4 + H_2SO_4). Thus, the reduction current observed above the hydrogen evolution potential can be attributed to the compounds studied or the nitrate and nitrite reduction processes.

For the sake of comparison, the onset potential of the catalytic reduction is defined at the potential where $\triangle I = I_{POM} - I_{NOx} - = 0.5$ µA for 1 mmol·L^{-1} NO_x presented in the solution (correspond to the parameter $\gamma = C_{NO_x^-}/C^{\circ}_{POM} = 10$). The electrocatalytic efficiencies are also compared by using kinetic current density $J_{kinetic}$ in µA·cm^{-2} ($J_{kinetic} = [(I_{(POM+NOx)} - I_{(POM)}) / A]$, where A = 0.07 cm^2) with a different values of parameter γ.

3.1 Electrochemical reduction of nitrite

3.1.1 In pH 1 solution

Nitrite is protonated below pH 3.39,[14] therefore the main species in aqueous solution is HNO_2 but as already discussed in Chapters I and II, it decomposes slowly in solution according to the reaction:[15]

$$2HNO_2(aq) \rightleftarrows NO(aq) + NO_2(aq) + H_2O$$

$NaNO_2$ reduction was first studied with 0.1 mmol·L^{-1} **$CuSO_4$** in pH 1 0.5 mol·L^{-1} Na_2SO_4 + H_2SO_4 solution (Fig. III.8A).

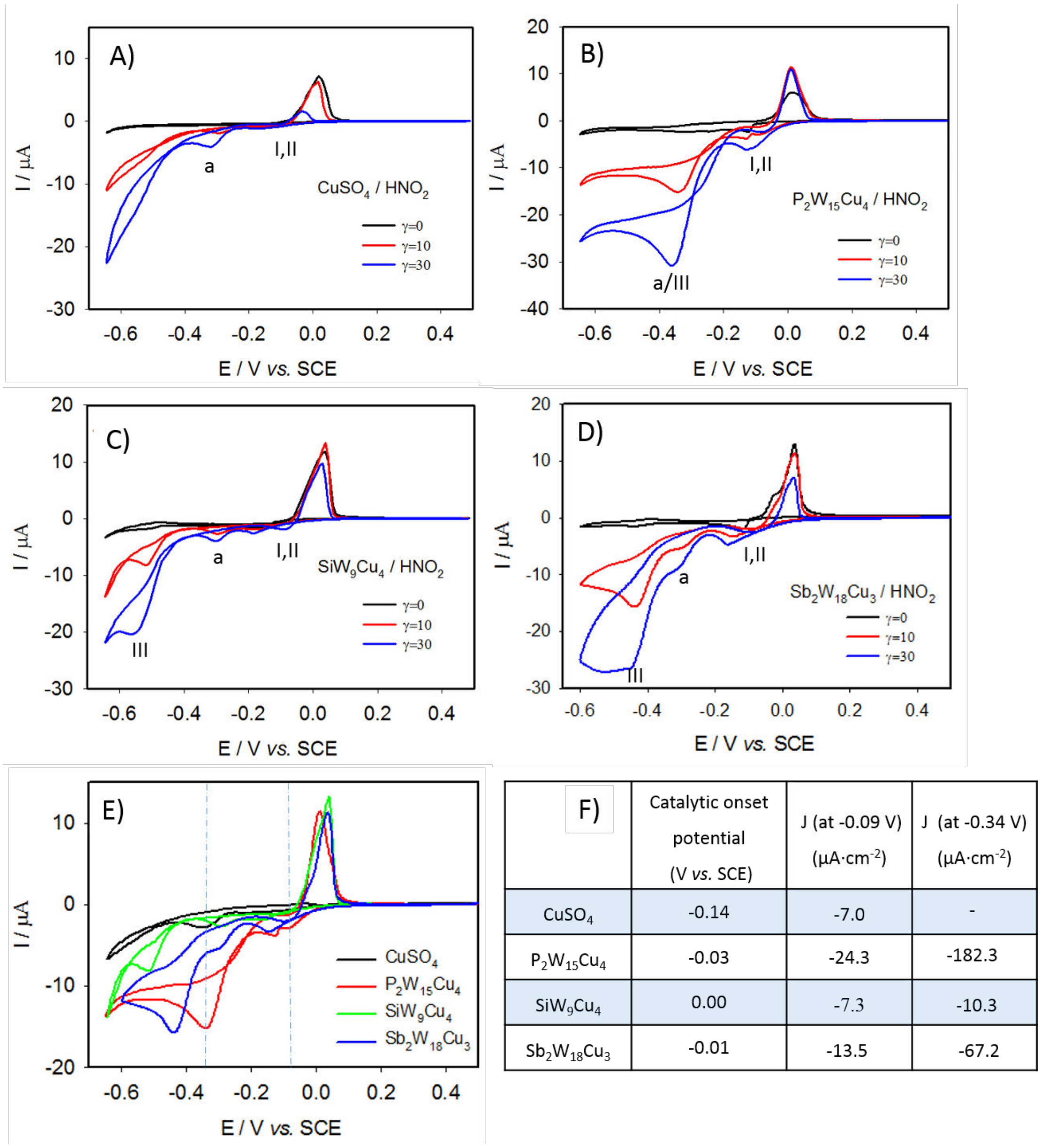

	Catalytic onset potential (V vs. SCE)	J (at -0.09 V) (µA·cm^{-2})	J (at -0.34 V) (µA·cm^{-2})
$CuSO_4$	-0.14	-7.0	-
$P_2W_{15}Cu_4$	-0.03	-24.3	-182.3
SiW_9Cu_4	0.00	-7.3	-10.3
$Sb_2W_{18}Cu_3$	-0.01	-13.5	-67.2

Figure III.8: Reduction of HNO_2 in the presence 0.1 mmol·L^{-1} (A) $CuSO_4$, (B) $P_2W_{15}Cu_4$, (C) SiW_9Cu_4 or (D) $Sb_2W_{18}Cu_3$. E) Comparison of 1 mmol·L^{-1} $NaNO_2$ reduction (equivalent to γ = 10) by different samples (0.1 mmol·L^{-1}). F) Catalytic onset potentials and kinetic current densities $J_{kinetic}(HNO_2)$ in µA·cm^{-2} calculated for 1 mmol·L^{-1} $NaNO_2$ (equivalent to γ = 10). Buffer solution pH 1 0.5 mol·L^{-1} Na_2SO_4 + H_2SO_4, v = 2 mV·s^{-1}. For the discussion of waves I, a, and III, see text.

In the presence of **$CuSO_4$** in pH 1 solution, a nitrite reduction current is observed especially below -0.14 V (waves I and II). An additional reduction wave is observed at -0.35 V (wave a) followed by the hydrogen evolution. In the literature, the wave a is attributed to the reduction of NO on Cu nanoparticles.[16]

In the presence of **$P_2W_{15}Cu_4$**, **SiW_9Cu_4** or **$Sb_2W_{18}Cu_3$,** an activity towards nitrite reduction is observed from the beginning of the Cu^{II} reduction around 0 V. This activity might be attributes to the Cu^{I} catalyze nitrite ions in solution. Even if the Cu^{I} state is not stable enough to give a clear signature in the CV, it might be reactive enough to react with HNO_2 and/or NO. When the potential decreases, the HNO_2 reduction current reaches a maximum and decreases after the formation of Cu^0 nanoparticles at -0.20 V. Interestingly, the HNO_2 reduction at wave I and wave II is followed by another wave (wave a) with higher current at the potential of the W^{VI}/W^{V} couple.

The nitrite reduction current increases by a factor three and two for **$P_2W_{15}Cu_4$** and **$Sb_2W_{18}Cu_3$** respectively, at potential of Cu^{II} reduction based on the calculated kinetic current densities for ($\gamma = 10$) (Fig. III.8F at -0.09 V). The catalytic activity for **SiW_9Cu_4** at this potential remains close to **$CuSO_4$**. For these three POMs, the catalytic current exhibits a maximum at -0.34 V, -0.51 V or -0.43 V (wave III), which is attributed to the POM diffusion limitation. In contrast, with the **$CuSO_4$** solutionn, no maximum is observed. It can be also noticed that a sharp current increase is obtained with **$P_2W_{15}Cu_4$** revealing relatively fast reduction kinetic while for **SiW_9Cu_4** and **$Sb_2W_{18}Cu_3$** (see Fig. III.8E), two reductions, wave a and wave III, can be separated because W^{VI} is reduced at more negative potential. The kinetic current density J calculated at -0.34 V for **$P_2W_{15}Cu_4$** is three times higher than that for **$Sb_2W_{18}Cu_3$** and 18 times higher than for **SiW_9Cu_4**.

Hence, in pH 1 solution, **$P_2W_{15}Cu_4$** shows the best catalytic activity towards nitrite reduction.

3.1.2 In pH 5 solution

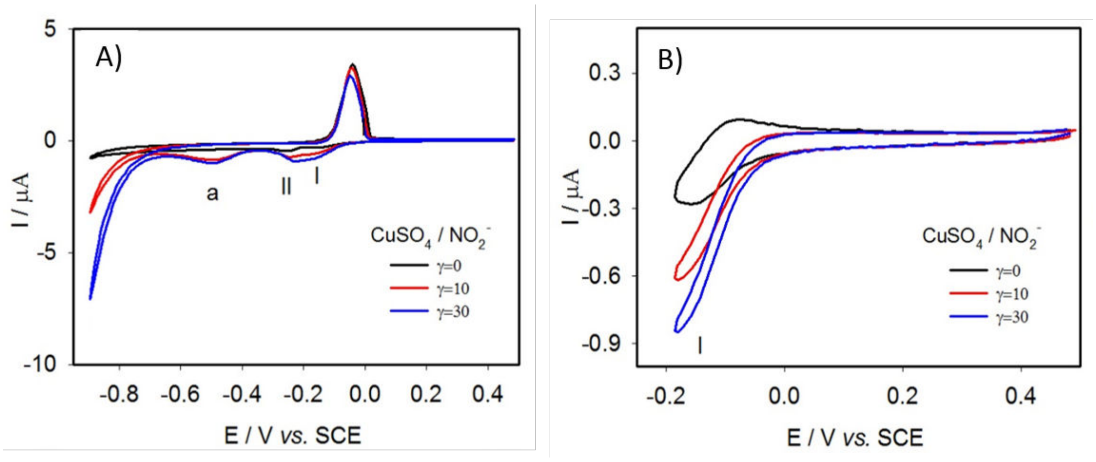

Figure III.9: A) Reduction of NO_2^- in the presence 0.1 mmol·L^{-1} $CuSO_4$. B) Nitrite reduction at $Cu^{II/I}$ reduction potential. Buffer solution: pH 5 1 mol·L^{-1} CH_3COOLi + CH_3COOH solution, v = 2 mV·s^{-1}.

In pH 5 solution, **$CuSO_4$** exhibits two consecutive waves at -0.14 V and -0.24 V *vs.* SCE, corresponding to the reductions Cu^{II} to Cu^{I} (wave I) and Cu^{I} to Cu^{0} (wave II) (Fig. III.9A). These two reduction waves are more distinguishable in pH 5 solution since the Cu^{I} species become more stable when the Cu ions are complexed by acetate ions which are used in the buffer solution. After the addition of $NaNO_2$, an increase of current intensity is observed at potential of Cu^{II}/Cu^{I} (see. Fig. III.9B), while no Cu^{0} nanoparticles form. This confirms the activity of the Cu^{I} species for the HNO_2/NO reduction.[17] As in pH 1 solution, further decrease of the potential leads to the Cu^{I} reduction into Cu^{0} nanoparticle, the current decreases to the same level than the one in the absence of NO_2^-. As in pH 1 solution, a NO reduction (wave a) is observed revealing the activity of Cu nanoparticles in this potential range. The reduction wave a is followed by a third reduction wave occurring simultaneously to the hydrogen evolution.

Cyclic voltammograms of NO_2^- reduction by **$P_2W_{15}Cu_4$**, **SiW_9Cu_4** and **$Sb_2W_{18}Cu_3$** are presented in Fig. III.10. Similar to the **$CuSO_4$** solution, a nitrite reduction current is observed at the potential of Cu^{II}/Cu^{I} reduction (wave I). Electrocatalysis of NO_2^- reduction by Cu^{II}/Cu^{I} redox process of each Cu-substituted POMs are presented in the left panel of Fig. III.10. No hint of Cu^{0} or Cu^{I} oxidation is observed during the reverse scan when the cathodic potential scan is stopped after Cu^{II}/Cu^{I} redox wave. This suggests that NO_2^- ions are able to re-oxidize electrochemically Cu^{I}POM complex and regenerate Cu^{II}POM. The current intensity increases with the quantity of nitrite ion added.

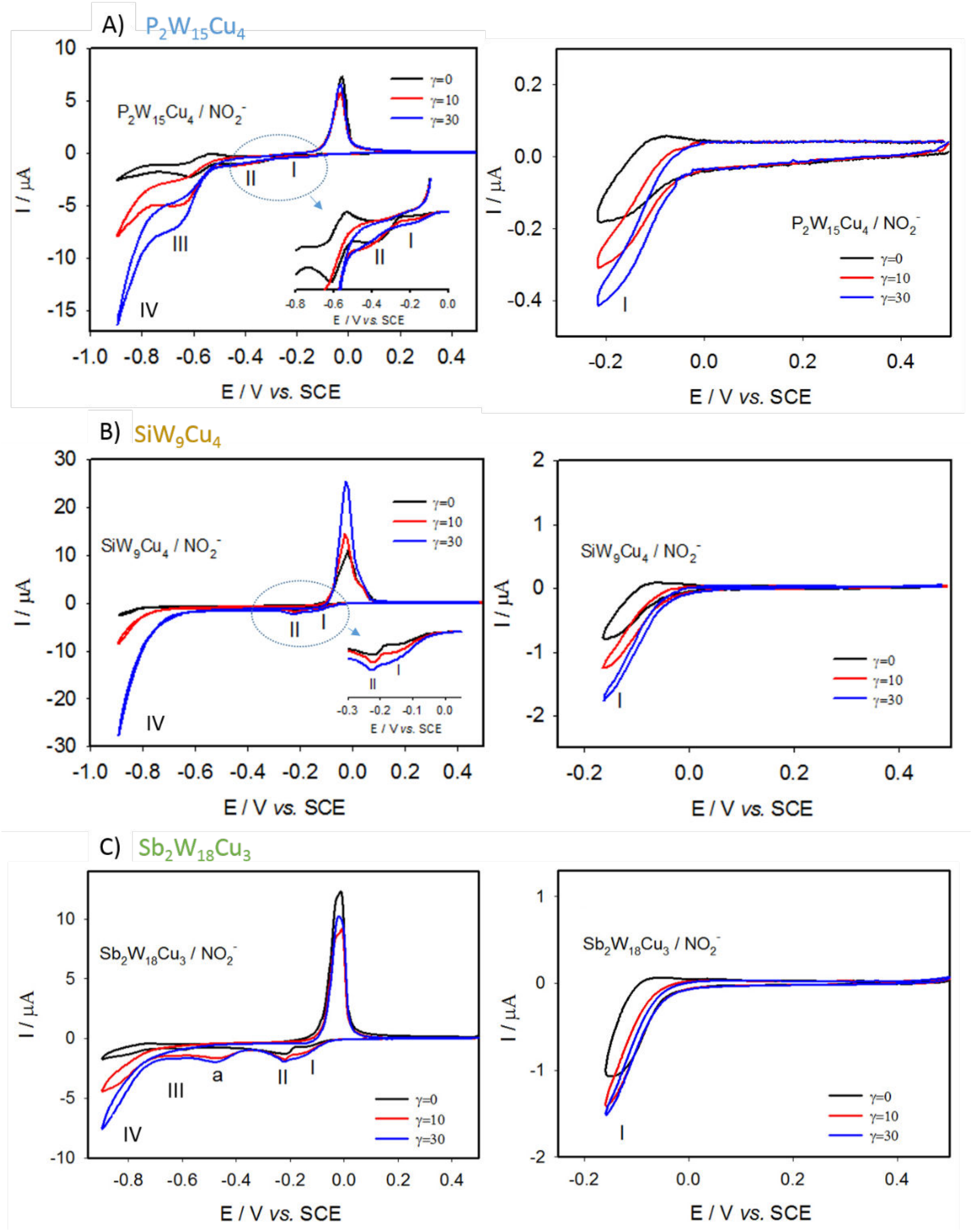

Figure III.10: (Left) Reduction of NO_2^- in the presence of 0.1 mmol·L^{-1} (A) $P_2W_{15}Cu_4$, (B) SiW_9Cu_4 or (C) $Sb_2W_{18}Cu_3$ (Right) nitrite reduction at $Cu^{II/I}$ reduction potential. Buffer solution: pH 5 1 mol·L^{-1} CH_3COOLi + CH_3COOH, v = 2 mV·s^{-1}.

With **$P_2W_{15}Cu_4$**, a significant reduction current is observed at potentials of $W^{VI/V}$ couple (waves III and IV) and in the same potential range as the hydrogen evolution. The reduction current at the wave III is about four times higher than at the one at the wave I (potential of $Cu^{II/I}$ redox transition). In the case of **SiW_9Cu_4**, the nitrite reduction occurs at -0.21 V and the catalytic current enhanced when the W is reduced at more negative potential of -0.84 V. This can attribute to the collective effect of nitrite reduction by $W^{VI/V}$ and the catalysis of nitrite reduction by Cu (peak IV in Fig. III.10B). The peak a observed with **$CuSO_4$** is also found with **$Sb_2W_{18}Cu_3$**

at -0.48 V. For **$Sb_2W_{18}Cu_3$**, this reduction is followed by catalytic wave at $W^{VI/V}$ redox potential (wave III) and at wave IV (Fig. III.10C).

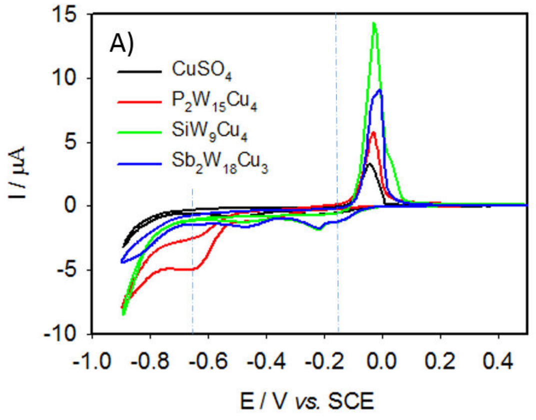

B)	Catalytic onset potential (V *vs.* SCE)	J (at -0.17 V) ($\mu A \cdot cm^{-2}$)	J (at -0.64 V) ($\mu A \cdot cm^{-2}$)
$CuSO_4$	-0.80	-3.99	-2.71
$P_2W_{15}Cu_4$	-0.54	-1.69	-38.01
SiW_9Cu_4	-0.21	-4.64	-19.47
$Sb_2W_{18}Cu_3$	-0.18	-4.83	-9.13

Figure III.11: A) Comparison of reduction of 1 mmol·L^{-1} $NaNO_2$ (equivalent to $\gamma = 10$) by different samples (0.1 mmol·L^{-1}). B) Catalytic onsetpotentials and kinetic current densities $J_{kinetic}(NO_2^-)$ in µA·cm^{-2} calculated for 1 mmol·L^{-1} $NaNO_2$ (equivalent to $\gamma = 10$). Buffer solution in pH 5 1 mol·L^{-1} CH_3COOLi + CH_3COOH, v = 2 mV·s^{-1}.

The comparison of these four compounds toward reduction of 1 mmol·L^{-1} NO_2^- (equivalent to $\gamma = 10$) is shown in Figure III.11A. **SiW_9Cu_4** and **$Sb_2W_{18}Cu_3$** show similar activity at wave I and II and their kinetic current densities are three times higher than **$P_2W_{15}Cu_4$** at -0.17 V (Fig. III.11B). The highest catalytic current is observed at W^{VI} reduction wave. **$P_2W_{15}Cu_4$** shows the best activity at -0.64 V with a kinetic current density $J_{kinetic}(NO_2^-)$ up to -38.01 µA·cm^{-2}.

3.2 Electrochemical reduction of nitrate

3.2.1 In pH 1 solution

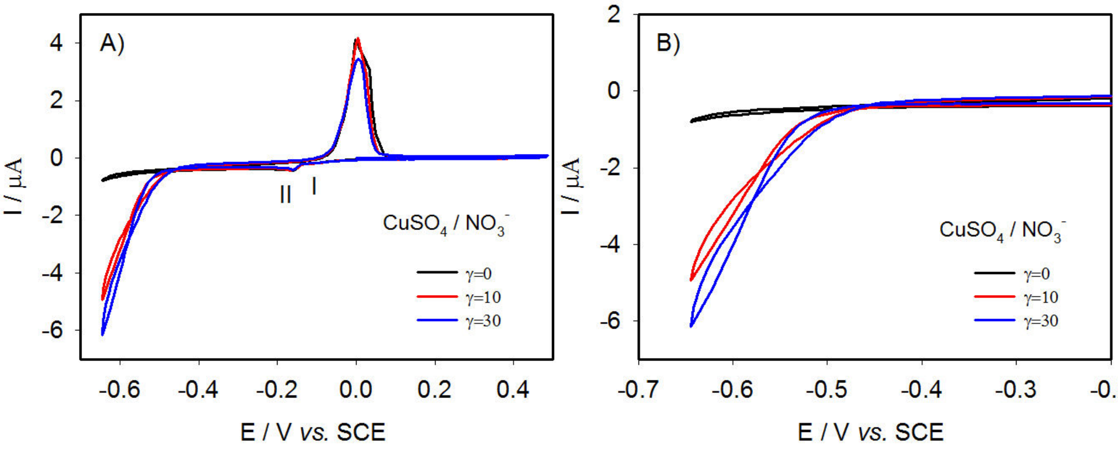

Figure III.12: A) Reduction of NO_3^- in the presence 0.1 mmol·L^{-1} $CuSO_4$. B) Magnification of A) between -0.65 V to -0.20 V. Buffer solution: pH 1 0.5 mol·L^{-1} Na_2SO_4 + H_2SO_4, v = 2 mV·s^{-1}.

Nitrate electrocatalytic reduction by 0.1 mmol·L^{-1} **$CuSO_4$** at pH 1 is shown in Fig. III.12. The catalytic current is observed below -0.52 V, showing that the application of a significant overpotential is necessary to reduce NO_3^- ions.

In the case of CuPOMs in solution (Fig. III.13), there is no significant activity for nitrate reduction at the potential of $Cu^{II/I}$ redox transition as observed with **$CuSO_4$**. The onset of the nitrate reduction is only observed after the reduction of $W^{VI/V}$ for **$P_2W_{15}Cu_4$** and **SiW_9Cu_4**, at -0.46 V and -0.55 V respectively, while **$Sb_2W_{18}Cu_3$** is not active towards nitrate reduction. However, Cu^0 nanoparticles are still formed. This indicates that the SbW_9 units inhibit the catalytic activity of Cu. One can hypothesize that the SbW_9 units are adsorbed on the Cu nanoparticles and block the access to the catalytic Cu sites.

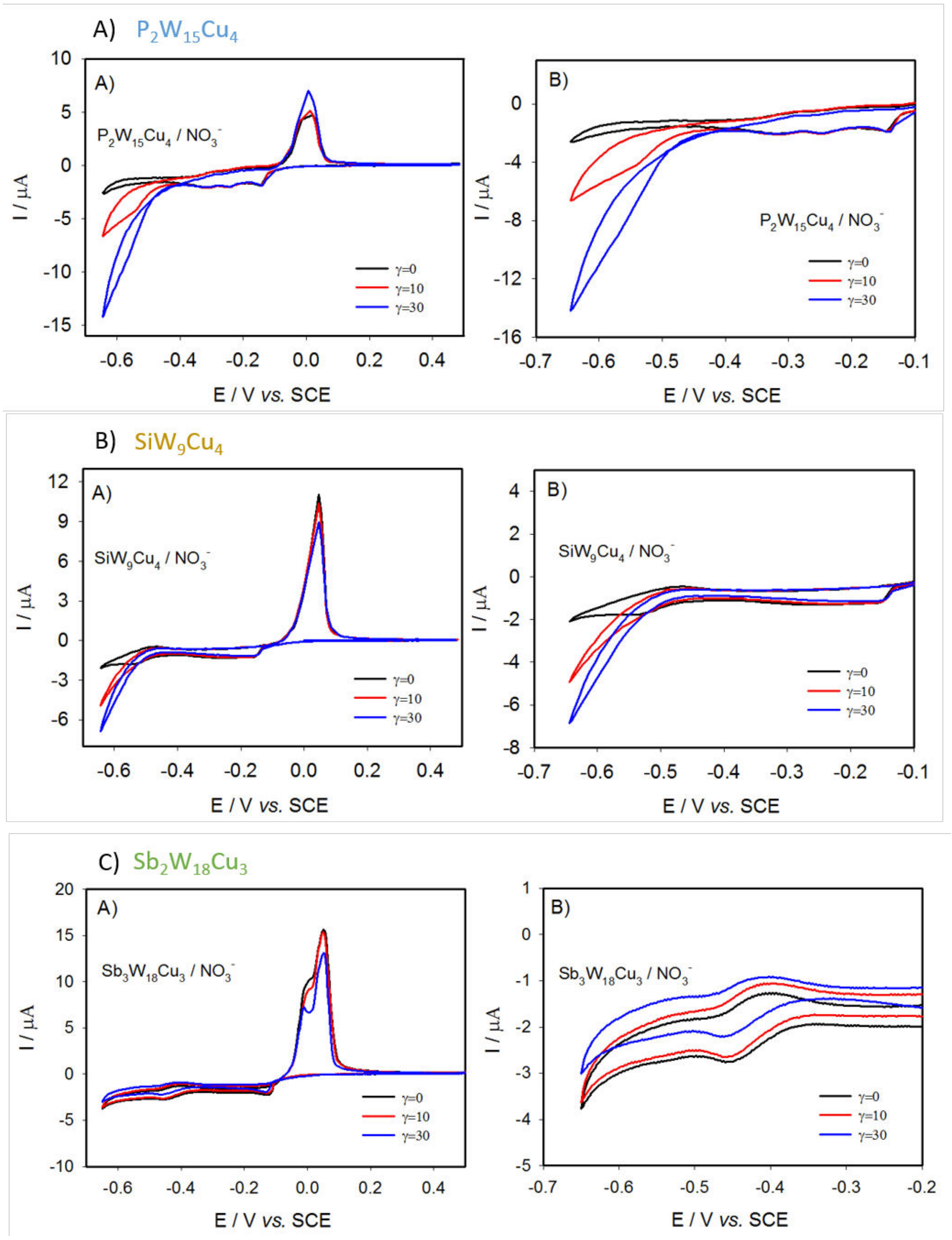

Figure III.13: (Left) Reduction of NO_3^- in presence of 0.1 mmol·L^{-1} (A) $P_2W_{15}Cu_4$, (B) SiW_9Cu_4 or (C) $Sb_2W_{18}Cu_3$ (Right) Magnification of nitrate reduction at the potential of reduced POM. Buffer solution: pH 1 0.5 mol·L^{-1} Na_2SO_4 + H_2SO_4, v = 2 mV·s^{-1}.

The catalytic onset potential of each compound and their kinetic currents calculated at -0.55 V (to avoid the hydrogen evolution) are presented in Table III. 5. The catalytic onset potential for **$P_2W_{15}Cu_4$** is -0.48 V, 0.06 V earlier than **SiW_9Cu_4** and 0.07 V earlier than **$CuSO_4$**. In addition, **$P_2W_{15}Cu_4$** possesses a better kinetic current density (-55.60 µA.cm^{-2}) than other two compounds.

	Catalytic onset potential (V *vs.* SCE)	J (-0.55 V) ($\mu A \cdot cm^{-2}$)
$CuSO_4$	-0.55	-14.16
$P_2W_{15}Cu_4$	-0.48	-55.60
SiW_9Cu_4	-0.54	-41.82
$Sb_2W_{18}Cu_3$	-	-

Table III.5: Catalytic onset potentials for nitrate reduction and kinetic current densities $J_{kinetic}(NO_3^-)$ in $\mu A \cdot cm^{-2}$ calculated at -0.55 V in pH 1 0.5 $mol \cdot L^{-1}$ $Na_2SO_4 + H_2SO_4$ solution, v = 2 $mV \cdot s^{-1}$.

3.2.2 In pH 5 solution

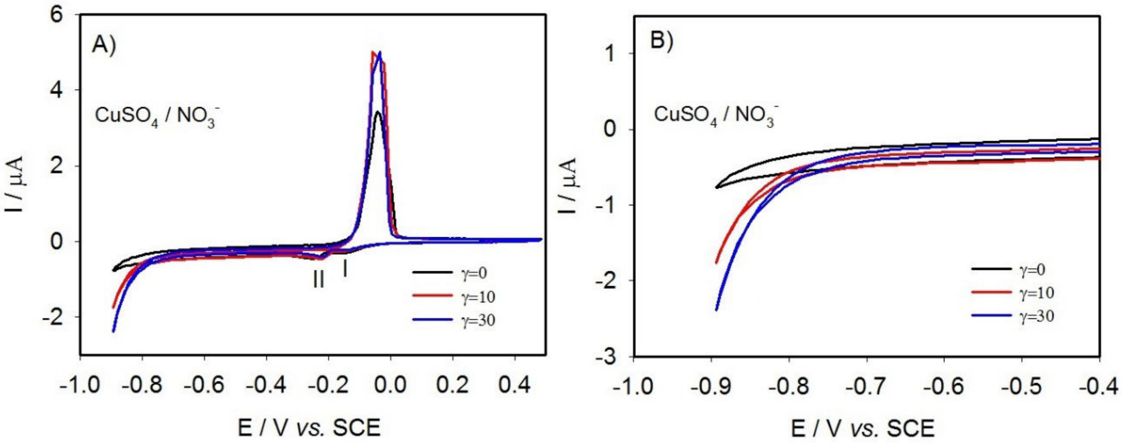

Figure III.14: A) Reduction of NO_3^- in the presence 0.1 $mmol \cdot L^{-1}$ $CuSO_4$. B) Magnification of A) between -0.90 V to -0.40 V. Buffer solution: pH 5 1 $mol \cdot L^{-1}$ $CH_3COOLi + CH_3COOH$, v = 2 $mV \cdot s^{-1}$.

Similar to at pH 1, the nitrate is reduced with 0.1 $mmol \cdot L^{-1}$ **$CuSO_4$** in pH 5 solution is observed when a high overpotential of -0.87 V is applied to the electrode.

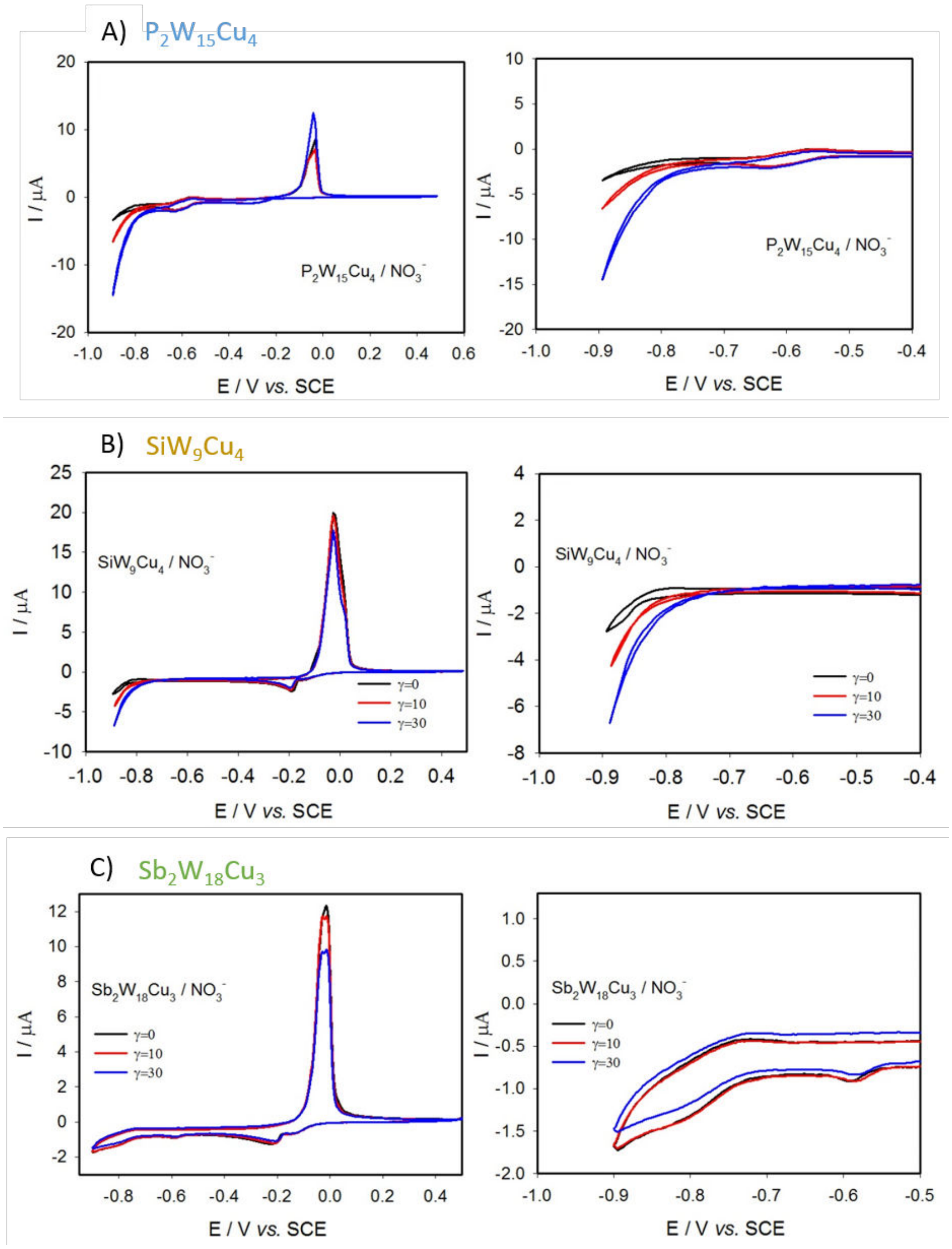

Figure III.15: Reduction of NO_3^- in the presence of 0.1 $mmol \cdot L^{-1}$ (A) $P_2W_{15}Cu_4$, (B) SiW_9Cu_4 or (C) $Sb_2W_{18}Cu_3$ in pH 5 1 $mol \cdot L^{-1}$ $CH_3COOLi + CH_3COOH$ solution, $v = 2\ mV \cdot s^{-1}$ (Right) Magnification of nitrate reduction at the potential of reduced POM.

For CuPOMs, the nitrate reduction is only observed after the reduction of $W^{VI/V}$ for **$P_2W_{15}Cu_4$** and **SiW_9Cu_4**, at -0.82 V and -0.83 V respectively (see. Fig. III.15A and Fig. III.15B). But with **$Sb_2W_{18}Cu_3$**, no increase is observed during the whole potential range under investigation (see. Fig. III.15C). This observation demonstrates again that the chemical nature of POMs entities adsorbed on the surface of the Cu^0 nanoparticles affects the electrocatalytic activity for the nitrate reduction on the Cu^0 nanoparticles.

	Catalytic onset potential (V *vs.* SCE)	J (-0.85 V) (µA·cm^{-2})
$CuSO_4$	-0.87	-4.61
$P_2W_{15}Cu_4$	-0.82	-44.78
SiW_9Cu_4	-0.83	-21.53
$Sb_2W_{18}Cu_3$	-	-

Table III.6: Catalytic onset potentials for nitrate reduction and kinetic current densities $J_{kinetic}(NO_3^-)$ in µA·cm^{-2} calculated at -0.85 V in pH 5 1 mol·L^{-1} CH_3COOLi + CH_3COOH solution, v = 2 mV·s^{-1}.

In pH 5 solution, the catalytic onset potentials of **$P_2W_{15}Cu_4$** and **SiW_9Cu_4** are close and 0.05 V earlier than that for **$CuSO_4$**. As in pH 1 solution, **$P_2W_{15}Cu_4$** possesses the best kinetic current density (-44.78 µA·cm^{-2}) which is around two times higher than **SiW_9Cu_4** and 10 times higher than **$CuSO_4$**.

Therefore, **$P_2W_{15}Cu_4$** shows the best activity towards nitrate and nitrite reduction in both pH 1 and pH 5 solutions.

3.2.3 Electrochemical reduction of nitrate on Cu electrode in presence of $P_2W_{15}Cu_4$ or $Sb_2W_{18}Cu_3$

As shown in sections 3.2.1 and 3.2.2, **$Sb_2W_{18}Cu_3$** is not active toward NO_3^- reduction on GC electrode, even though Cu nanoparticles are electrodeposited on the electrode. To confirm this observation, the electrocatalysis of NO_3^- reduction was studied on Cu bulk electrode in the presence of two different POMs in solution.

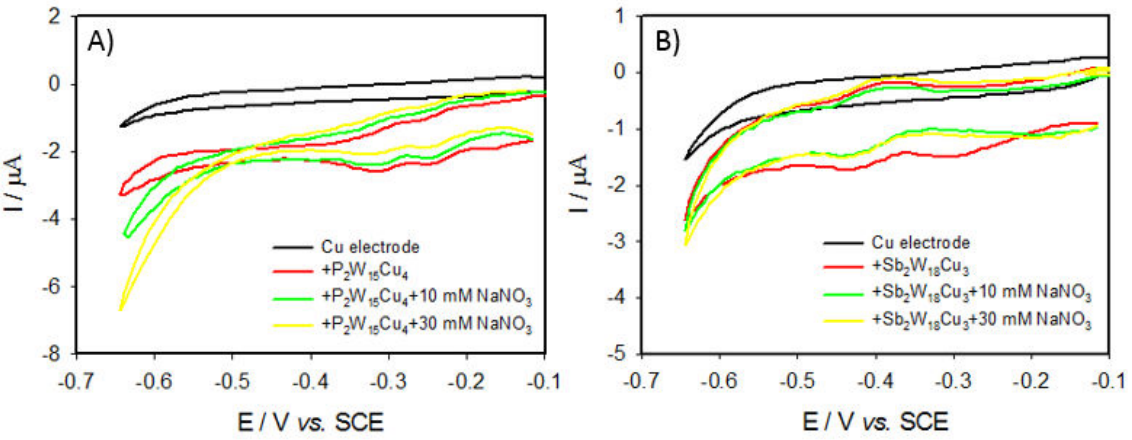

Figure III.16: Reduction of NO_3^- *in the presence of 0.1 mmol·L*$^{-1}$ *(A)* $P_2W_{15}Cu_4$ *or (B)* $Sb_2W_{18}Cu_3$ *on Cu bulk electrode in pH 5 1 mol·L*$^{-1}$ $CH_3COOLi + CH_3COOH$ *solution, v = 2 mV·s*$^{-1}$*.*

In the presence of $\mathbf{P_2W_{15}Cu_4}$ in solution, NO_3^- reduction occurs after the reduction of $W^{VI/V}$ around -0.48 V (Fig. III.16A) similar to the observation on GC electrode. However, in the presence of $\mathbf{Sb_2W_{18}Cu_3}$ (Fig. III.16B), no activity is observed. That confirms that adsorbed SbW_9 units can even block the access to the Cu bulk electrode surface.

4 Electrocatalytic reduction of NO_x on CuPOM/Ale

In this part, a complex of Cu coordinated by alendronate ligand (Ale) is added to CuPOMs presented in part 3. Three CuPOM/Ale compounds $\mathbf{SiW_9CuAle}$, $\mathbf{P_2W_{15}CuAle}$ and $\mathbf{SbW_9CuAle}$ were prepared and their electrocatalytic properties have been studied. The measurement conditions are the same as in the section 3.

4.1 Electrochemical reduction of NO_2^-/HNO_2

4.1.1 In pH 1 solution

Eletrocatalytic reduction of HNO_2 in presence of CuPOM/Ale is shown in Fig. III.17. The right panel is the comparison of the reduction scan of CuPOM/Ale and the corresponding CuPOM with 1 mmol·L^{-1} NO_2^- ($\gamma = 10$) in solution.

The catalytic current of NO_2^- reduction in the presence of these three CuPOM/Ale are found at similar potentials than the ones observed with the corresponding CuPOM without addition of complexes with Ale. Overall, the Cu^{II} reduction current is larger for CuPOM/Ale than for

CuPOM due to the higher number of Cu^{II} entities in the structure. In the case of **P_2W_{15}CuAle** and **SbW_9CuAle**, the reduction of Cu^{II} is spitted into two steps even in pH 1 solution suggesting that Cu^{I} state is more stable in CuPOM/Ale system than in CuPOM.

In the presence of **P_2W_{15}CuAle**, the current increase is observed at the waves I and II compared to **$P_2W_{15}Cu_4$**. A wider peak is obtained at wave III for **P_2W_{15}CuAle**, with a slightly shift of 37 mV towards more negative potential. However, the change in the maximal value of the catalytic current at wave III is relatively small, showing that the HNO_2 reduction of **P_2W_{15}CuAle** in this potential range is almost not affected by adding complex of CuAle entity. In contrast, for **SiW_9CuAle** and **SbW_9CuAle**, a significant increase of current is observed in the whole range of measured potential below the Cu^{II} reduction wave. The catalytic current is about two times higher with **SbW_9CuAle** than with **SiW_9CuAle**, which might be attributed to the higher number of Cu ions in the structure (24 Cu^{II} ions in **SbW_9CuAle** *versus* 9 Cu^{II} ions in **SiW_9CuAle**).

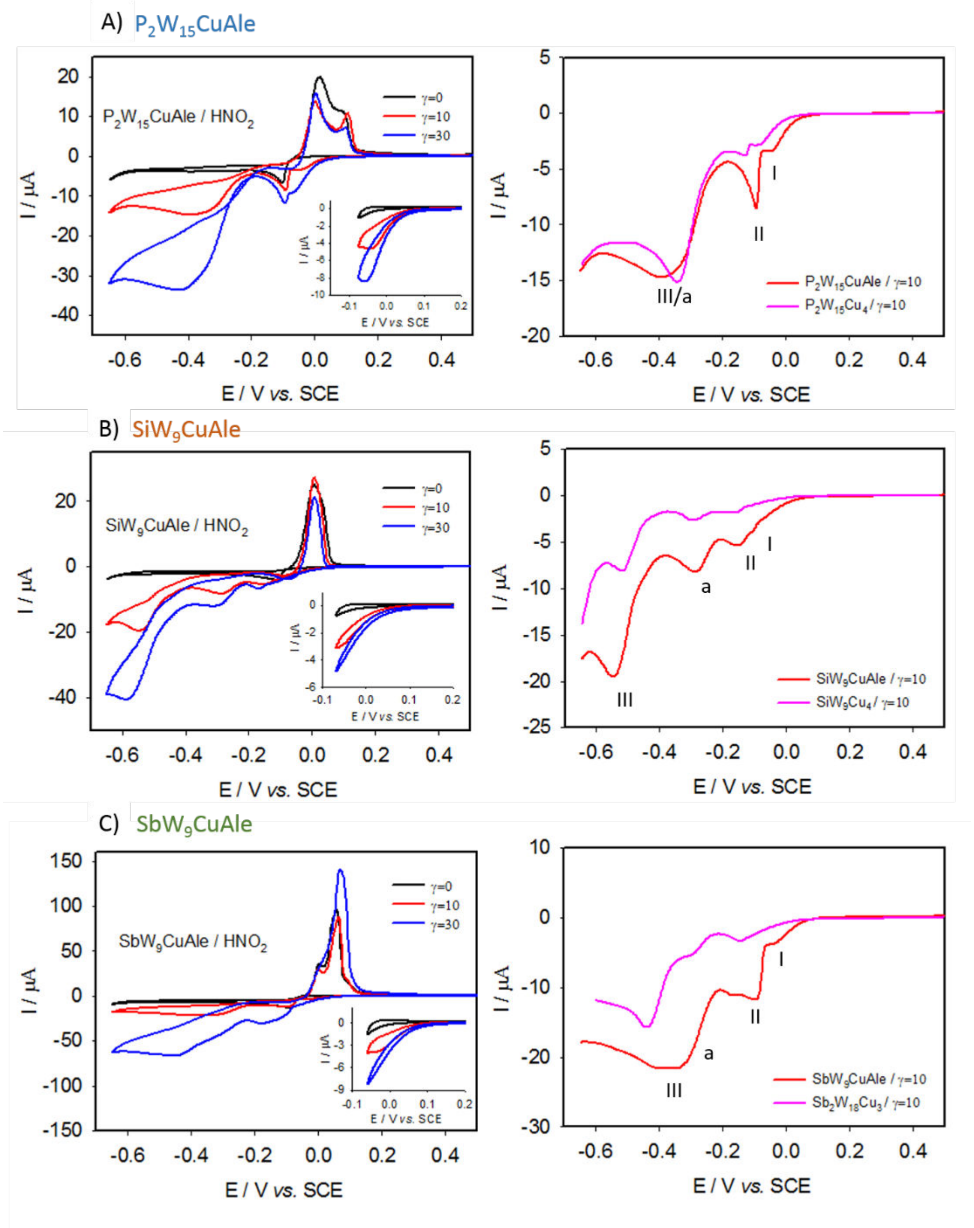

Figure III.17: (Left) Reduction of HNO_2 in the presence of 0.1 mmol·L^{-1} (A) $P_2W_{15}CuAle$, (B) SiW_9CuAle or (C) SbW_9CuAle. (Right) Reduction scans obtained for CuPOM/Ale (red curve) and the corresponding CuPOM (pink curve) after adding of 1 mmol·L^{-1} $NaNO_2$ (γ = 10). Buffer solution: pH 1 0.5 mol·L^{-1} Na_2SO_4 + H_2SO_4, v = 2 mV·s^{-1}.

The catalytic onset potentials of these CuPOM/Ale compounds are showed in Fig. III.18B. For **SiW_9CuAle**, the catalysis occurs at 0.03 V, earlier than other two compounds. However, **SbW_9CuAle** possesses the highest kinetic current at -0.09 V and -0.31 V, due to the higher sum of Cu ions present.

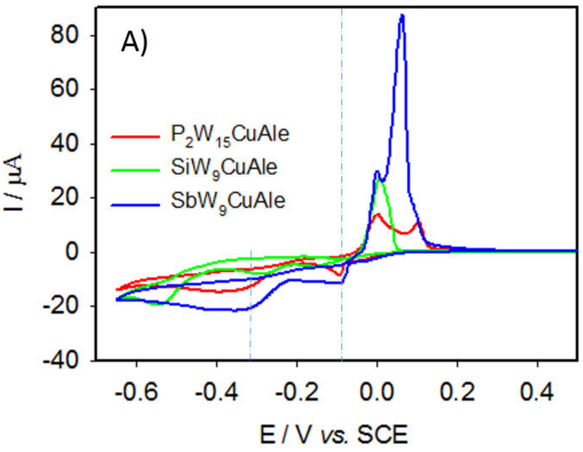

B)	Catalytic onset potential (V *vs.* SCE)	J (at -0.09 V) (µA·cm^{-2})	J (at -0.31 V) (µA·cm^{-2})
P_2W_{15}CuAle	0.05	-22.01	-144.11
SiW_9CuAle	0.03	-14.17	-73.98
SbW_9CuAle	0.07	-43.62	-201.96

Figure III.18: A) Comparison of 1 mmol·L^{-1} $NaNO_2$ (equivalent to γ = 10) reduction by 0.1 mmol·L^{-1} different CuPOM/Ale. B) Catalytic onset potentials and kinetic current densities $J_{kinetic}$(HNO_2) in µA·cm^{-2} calculated for 1 mmol·L^{-1} $NaNO_2$ (equivalent to γ = 10). Buffer solution in pH 1 0.5 mol·L^{-1} Na_2SO_4 + H_2SO_4, v = 2 mV·s^{-1}.

4.1.2 In pH 5 solution

Cyclic voltammograms of nitrite reductions by CuPOM/Ale in pH 5 solution are presented in Fig. III.19. An increase is observed at Cu reduction waves (waves I and II) in the presence of CuPOM/Ale comparing to the corresponding CuPOM. This increase is proportional to the increase of sum of Cu number in the structure (2 times for **P_2W_{15}CuAle** and **SiW_9CuAle** and about 7.5 times for **SbW_9CuAle** at wave I).

A significant increase is observed at wave IV (hydrogen evolution) with **P_2W_{15}CuAle** or **SbW_9CuAle** in solution, indicating that the electrodeposited Cu affects the reduction of nitrite occurring in the hydrogen evolution potential range.

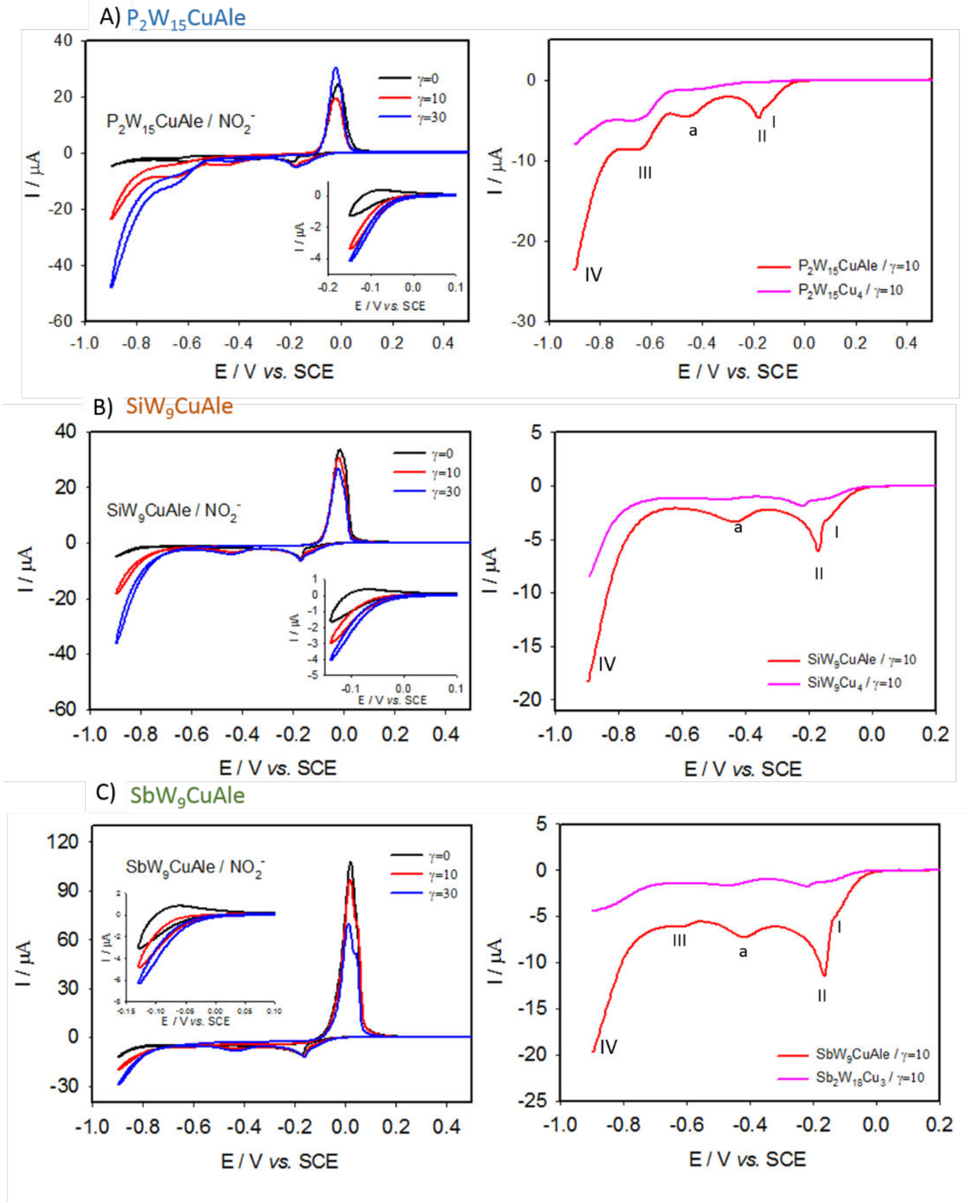

Figure III.19: (Left) Reduction of NO_2^- in the presence of 0.1 $mmol \cdot L^{-1}$ (A) $P_2W_{15}CuAle$, (B) SiW_9CuAle or (C) SbW_9CuAle. (Inset) Reduction of NO_2^- by $Cu^{II/I}$ couple. (Right) Negative scans obtained for CuPOM/Ale (red curve) and the corresponding CuPOM (pink curve) after adding of 1 $mmol \cdot L^{-1}$ NO_2^-. Buffer solution: pH 5 1 $mol \cdot L^{-1}$ $CH_3COOLi + CH_3COOH$, $v = 2\ mV \cdot s^{-1}$.

Reductions of 1 $mmol \cdot L^{-1}$ $NaNO_2$ in the presence of **$P_2W_{15}CuAle$**, **SiW_9CuAle** and **SbW_9CuAle** are presented in Figure III.20A. At potential of Cu reduction, the highest catalytic current is obtained in the presence of **SbW_9CuAle**. However, **$P_2W_{15}CuAle$** shows a better activity at the potential that W^{VI} is reduced (wave III). The catalytic onset potentials for these three compounds are close to each other. The kinetic current densities calculate at -0.14 V and -0.65 V are in agreement with the observations in voltammograms. The $J_{kinetic}$ at -0.14 V for **SbW_9CuAle** is -32.78 $\mu A \cdot cm^{-2}$ and at -0.65 V, the best kinetic current density is obtained with **$P_2W_{15}CuAle$** (-78.54 $\mu A \cdot cm^{-2}$).

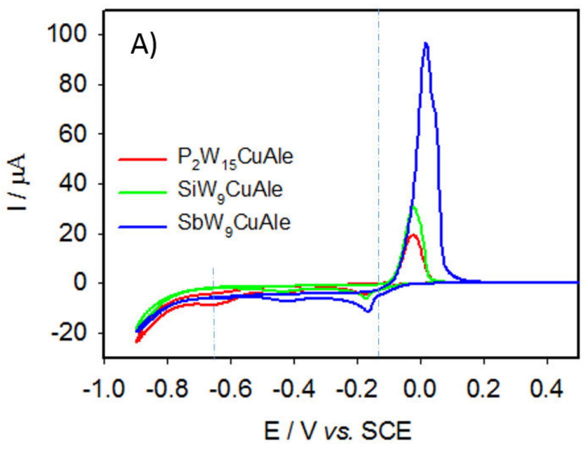

B)	Catalytic onset potential (V *vs.* SCE)	J (at -0.14 V) (µA·cm^{-2})	J (at -0.65 V) (µA·cm^{-2})
P_2W_{15}CuAle	-0.08	-29.18	-78.54
SiW_9CuAle	-0.08	-15.92	-11.46
SbW_9CuAle	-0.07	-32.78	-17.72

Figure III.20: A) Comparison of reduction of 1 mmol·L^{-1} $NaNO_2$ (equivalent to $\gamma = 10$) by different CuPOM/Ale (0.1 mmol·L^{-1}). B) Catalytic onset potentials and kinetic current densities $J_{kinetic}(NO_2^-)$ in µA·cm^{-2} calculated for 1 mmol·L^{-1} $NaNO_2$ (equivalent to $\gamma = 10$). Buffer solution in pH 5 1 mol·L^{-1} $CH_3COOLi + CH_3COOH$, $v = 2$ mV·s^{-1}.

4.2 Electrochemical reduction of NO_3^-

4.2.1 In pH 1 solution

A) P_2W_{15}CuAle

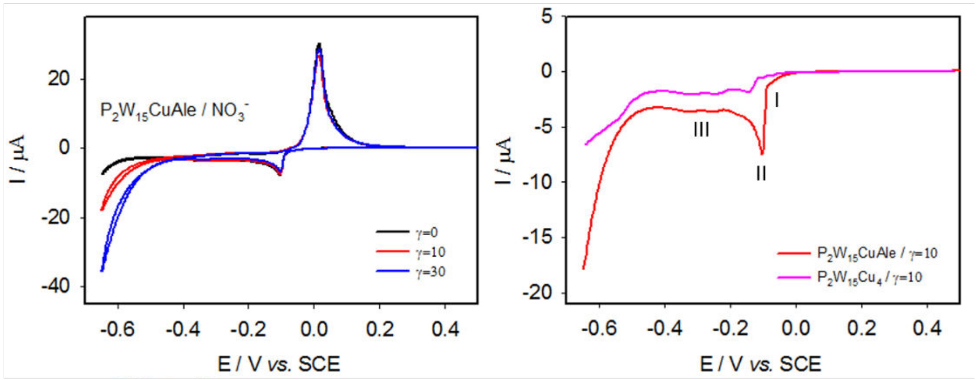

B) SiW_9CuAle

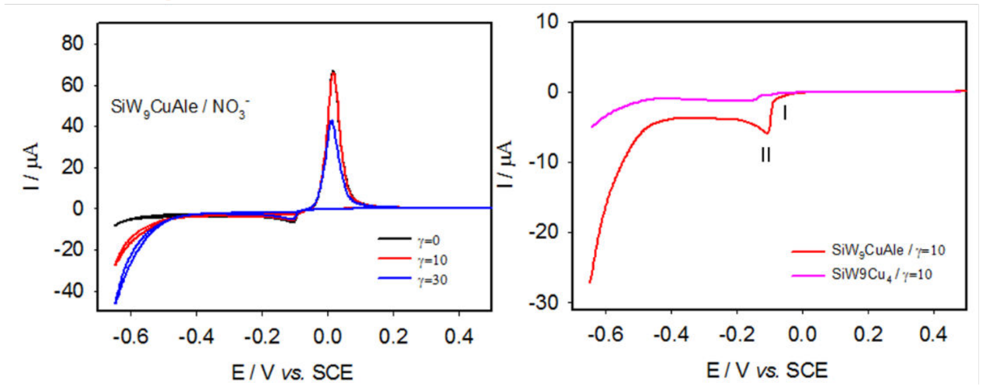

Figure III.21: (Left) Reduction of NO_3^- in the presence of 0.1 mmol·L^{-1} (A) P_2W_{15}CuAle or (B) SiW_9CuAle. (Right) Negative scans obtained for CuPOM/Ale (red curve) and the corresponding CuPOM (pink curve) after adding of 1 mmol·L^{-1} NO_3^-. Buffer solution: pH 1 0.5 mol·L^{-1} $Na_2SO_4 + H_2SO_4$ solution, $v = 2$ mV·s^{-1}.

The nitrate reduction occurs below -0.46 V with **$P_2W_{15}CuAle$** and -0.48 V with **SiW_9CuAle** (see. Table III.7). A positive shift of 0.02 V or 0.06 V is obtained after adding the complex CuAle to **$P_2W_{15}Cu_4$** or **SiW_9Cu_4** respectively. The current intensity measured at -0.65 V is three times higher with **$P_2W_{15}CuAle$** than for **$P_2W_{15}Cu_4$**, and five times higher with **SiW_9CuAle** compared to **SiW_9Cu_4**. The kinetic current density J calculated at -0.55 V for **$P_2W_{15}CuAle$** (-145.31 $\mu A\cdot cm^{-2}$) is a little higher than that for **SiW_9CuAle** (-119.66 $\mu A\cdot cm^{-2}$) and about six times higher than that for **$P_2W_{15}Cu_4$** (-55.60 $\mu A\cdot cm^{-2}$).

	Catalytic onset potential (V *vs.* SCE)	J ($\mu A\cdot cm^{-2}$) (at -0.55 V for $\gamma = 10$)
$P_2W_{15}CuAle$	-0.46	-145.31
SiW_9CuAle	-0.48	-119.66

Table III.7: Catalytic onset potentials for nitrate reduction and kinetic current densities $J_{kinetic}(NO_3^-)$ in $\mu A.cm^{-2}$ calculated at -0.55 V in pH 1 0.5 $mol\cdot L^{-1}$ $Na_2SO_4 + H_2SO_4$ solution, $v = 2\ mV\cdot s^{-1}$.

As for **$Sb_2W_{18}Cu_3$**, no activity towards nitrate reduction is observed with **SbW_9CuAle** with γ up to 200, which is in agreement with the hypothesis that SbW_9 can block the active Cu^0 surface (see. Appendix, Fig. S8).

4.2.2 In pH 5 solution

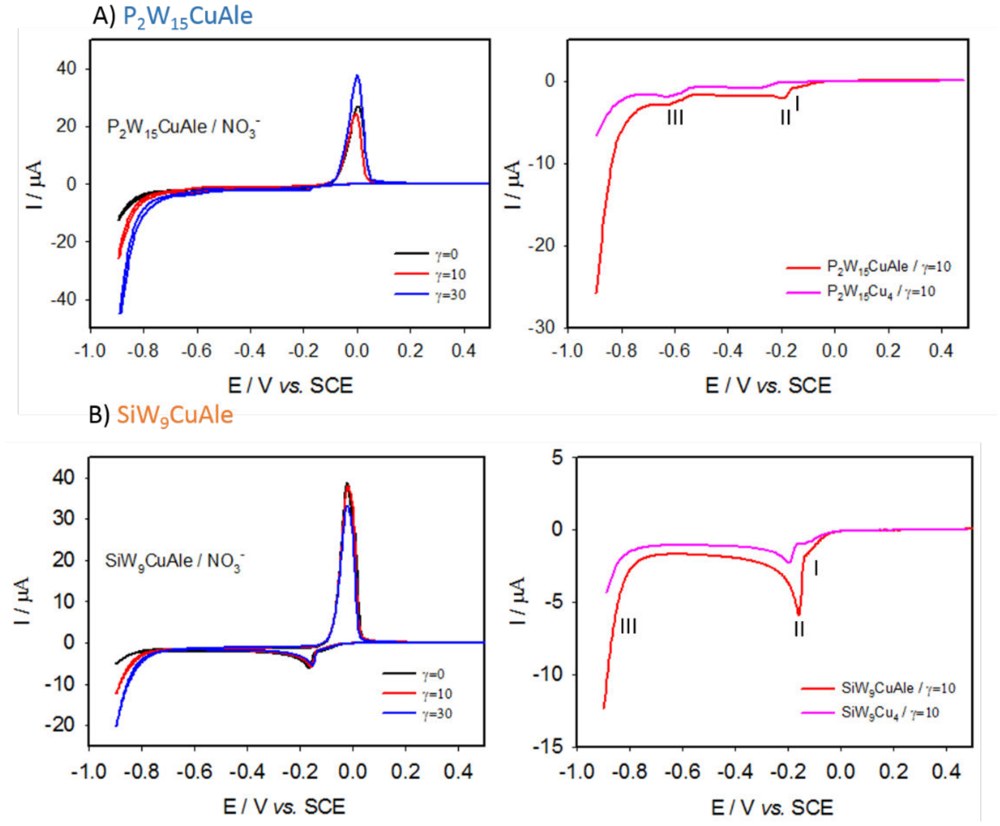

Figure III.22: (Left) Reduction of NO_3^- in the presence of 0.1 $mmol\cdot L^{-1}$ (A) $P_2W_{15}CuAle$ or (B) SiW_9CuAle. (Right) Negative scans obtained for CuPOM/Ale (red curve) and the corresponding CuPOM (pink curve) after adding of 1 $mmol\cdot L^{-1}$ NO_3^-. Buffer solution: pH 5 1 $mol\cdot L^{-1}$ CH_3COOLi + CH_3COOH solution, $v = 2$ $mV\cdot s^{-1}$.

The nitrate reduction current is observed in the hydrogen evolution potential region, negative than the wave III. In the case of **$P_2W_{15}CuAle$**, the reduction starts from -0.79 V, ca. 30 mV earlier than with **$P_2W_{15}Cu_4$** and 100 mV earlier than with **$CuSO_4$**. The current increases ca. 4 times when adding NO_3^- ($\gamma = 10$) at -0.90 V while the number of Cu increases 2.5 times. In the case of **SiW_9CuAle**, the nitrate reduction starts from -0.80 V, 30 mV earlier than **SiW_9Cu_4**. The catalytic current increases 3 times, less than with **$P_2W_{15}CuAle$**. As in pH 1 solution, **$P_2W_{15}CuAle$** possesses a better kinetic current density than **SiW_9CuAle** at -0.85 V for $\gamma = 10$ $NaNO_3$.

	Catalytic onset potential (V *vs.* SCE)	J (µA·cm^{-2}) (at -0.85 V for γ =10)
P_2W_{15}CuAle	-0.79	-43.08
SiW_9CuAle	-0.80	-39.03

Table III.8: Catalytic onset potentials for nitrate reduction and kinetic current densities $J_{kinetic}(NO_3^-)$ in µA·cm^{-2} calculated at -0.85 V in pH 5 1 mol·L^{-1} CH_3COOLi + CH_3COOH, v = 2 mV·s^{-1}.

In conclusion, among these three CuPOM/Ale, **SbW_9CuAle** possesses the best kinetic current density for the reduction of 1 mmol·L^{-1} $NaNO_2$ (γ = 10) in solution, due to the high sum of Cu ions present in the structure. For nitrate reduction, **P_2W_{15}CuAle** is considerate as the best catalyst in both pH 1 and pH 5 solution and its overpotential is smaller than that for **$P_2W_{15}Cu_4$** with a higher kinetic current density.

5 Influence of pH during nitrite reduction

As shown in part 4, all the CuPOM and CuPOM/Ale are good catalysts towards nitrite reduction, while **P_2W_{15}CuAle** is the best in the solution containing 1 mmol·L^{-1} $NaNO_2$ (equivalent to γ = 10) at pH 1 and at pH 5. In this part, the investigation of a better pH condition for nitrite reduction by using **P_2W_{15}CuAle** at pH 1, 2, 3 and 5 is presented.

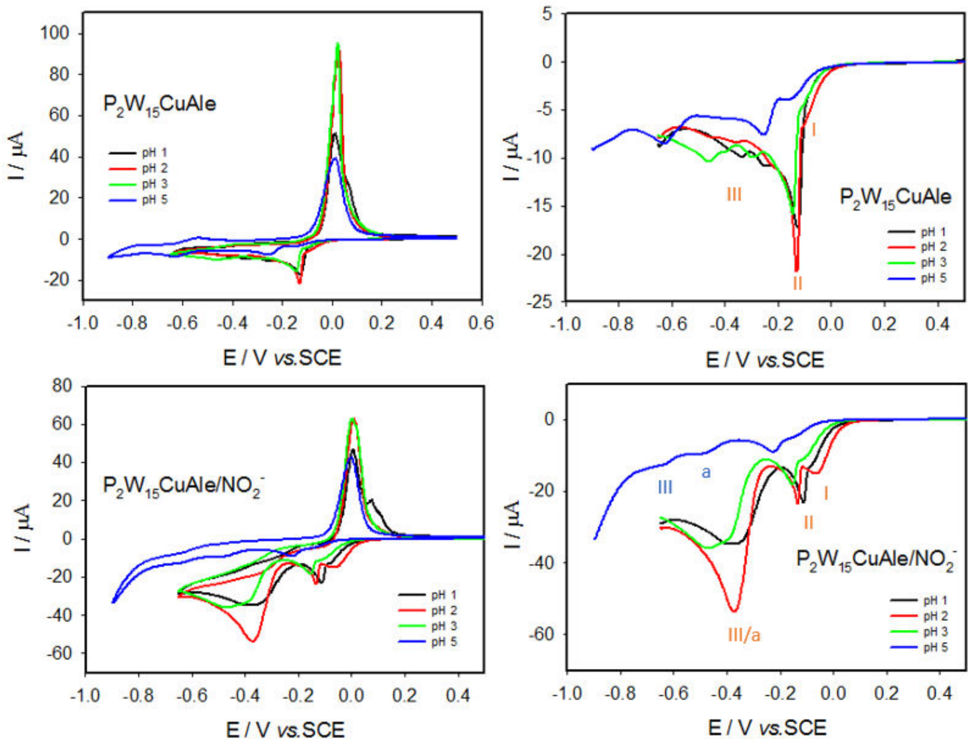

Figure III.23： CV (upper) and nitrite reduction (bottom) in the presence of 0.1 mmol·L^{-1} $P_2W_{15}CuAle$ as a function of pH: pH 1(0.5 mol·L^{-1} Na_2SO_4 + H_2SO_4), pH 2 and 3 (0.5 mol·L^{-1} NaH_2PO_4 + H_3PO_4) or pH 5 (1 mol·L^{-1} CH_3COOLi + CH_3COOH). The concentration of $NaNO_2$ is 3 mol·L^{-1} equivalent to γ = 30. v = 2 mV·s^{-1}.

At pH 1, 2 and 3, the overall shape of the Cu redox peaks is only slightly affected by the pH value. The reduction of $Cu^{II/I}$ and $Cu^{I/0}$ are found to occur around -0.07 V and -0.10 V, while the reduction of $W^{VI/V}$ is affected by the pH (-0.20 V to -0.40 V for pH 1, -0.21 V to -0.48 V for pH 2 and -0.25 V to -0.60 V for pH 3). In contrast, the $Cu^{II/I}$, $Cu^{I/0}$ and $W^{VI/V}$ reduction currents are smaller in pH 5 than in more acidic mediums and the peaks positions shift to more negative potentials. This indicates that the reduction of **$P_2W_{15}CuAle$** is strongly affected by the nature of acetate ions and the pH of the solution. After adding $NaNO_2$ in solution, the best activity is obtained in pH 2 solution both for the wave I and wave III (red line in Fig. III.23). A composite cathodic wave around -0.39 V comes from the wave III and wave a in acidic solution (pH 1, 2 and 3).

6 Sensing property for nitrate reduction

In most of published work, NO_x reduction is only used as a classical test of electrocatalytic properties of polyoxometalates.[18,19] Here, the range of detection will be established with the aim to explore the applicability to electrochemical sensors. In our experimental condition,

$P_2W_{15}CuAle$ shows the best activity toward nitrate reduction. Hence, **$P_2W_{15}CuAle$** is chosen as the example.

The catalytic current is graphed as a function of the nitrate concentration in solution shown in Fig. III.24. Generally, current increases with the quantity of nitrate added in pH 1 and pH 5 solutions, until reaching a plateau, probably due to the limitation by the catalyst turnover frequency (Fig. III.24A).

A linear range is observed for **$P_2W_{15}CuAle$** in both pH 1 and pH 5 solutions. The range at pH 1 (0 to 20 mmol·L^{-1}) is wider than in pH 5 solution (0 to 10 mmol·L^{-1}) as shown in Fig. III.24B.

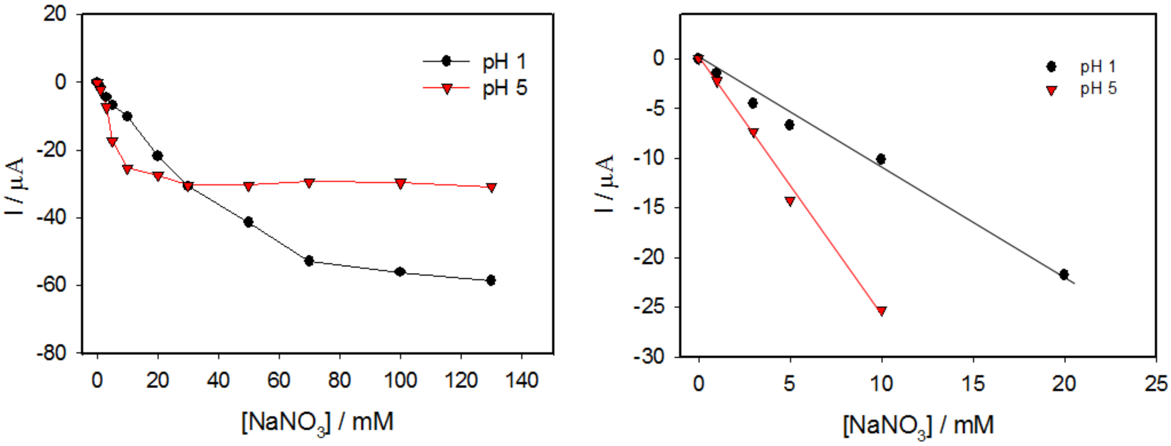

*Figure III.24: Sensing properties of **$P_2W_{15}CuAle$** towards nitrate reduction in pH 1 0.5 mol·L^{-1} Na_2SO_4 + H_2SO_4 solution or in pH 5 1 mol·L^{-1} CH_3COOLi + CH_3COOH solution. The current is measured at -0.55 V at pH 1 and at -0.85 V at pH 5.*

7 Conclusion

In this chapter, six Cu-substituted compounds have been examined by different techniques and their catalytic properties towards nitrite and nitrate reduction were studied in two different buffer solutions.

The electrochemical properties were studied in pH 1 (0.5 mol·L^{-1} $Na_2SO_4 + H_2SO_4$) and in pH 5 (1 mol·L^{-1} $CH_3COOLi + CH_3COOH$) solutions. The reduction and oxidation of Cu ions can be observed for all the compounds. Usually, Cu^{I} complex were better stabilized in pH 5 solution due to the presence of acetate ions. All the Cu^{II} centers were reduced as demonstrated by the controlled potential coulometry performed at a potential setted just below the Cu$^{II/0}$ reduction. The formed Cu^{0} nanoparticles are deposited on the electrode surface and their size/density increased with time. The quantity of material deposited on electrode was estimated by Electrochemical Quartz Crystal Microbalance (EQCM) where the deposited mass was found to increase with the number of Cu^{II} atoms in the structure. The onset potential of the formation of the Cu^{0} nanoparticles is slightly more positive for CuPOM/Ale compounds than for the corresponding CuPOM.

Their electrocatalytic properties have been studied in the presence of $NaNO_x$ (x = 2 or 3) into the solution. The analysis of the obtained current-potential curves demonstrated an efficient catalysis of nitrite and nitrate reduction concomitant to the reduction of CuPOM. The catalytic performances of the CuPOM species are improved compared to a simple Cu salt ($CuSO_4$) in solution or Cu bulk electrode. Two catalytic waves were observed in the case of the nitrite solution, the first one at the potential of Cu^{II} reduction and the second one at the W^{VI} reduction. In the case of nitrate reduction, only one catalytic reduction wave was observed after the reduction of W^{VI}. Interestingly, not every Cu-substituted POMs (**$P_2W_{15}Cu_4$**, **SiW_9Cu_4** and **$Sb_2W_{18}Cu_3$**) were found to be active toward nitrate reduction indicating that the formation of Cu^{0} nanoparticles and its catalytic properties can be modulated by the choice of POMs. **$P_2W_{15}Cu_4$** was the most active Cu-substituted POM for both nitrite and nitrate reduction under the experimental conditions that we have used.

After grafting an alendronate copper complex, namely $[Cu_6(Ale)_4(H_2O)_4]^{4-}$ to the Cu-substituted POMs, the catalytic properties were further ameliorated. A decrease of the overpotential and an increase in kinetic current density determined 1 mmol·L^{-1} NO_x (x = 2 or 3) solution were observed, showing that this Cu complex acted as a cofactor during the catalysis.

This improvement of the activity might be tentatively attributed to i) a better activity of the Cu^I species in the presence of alendronate and ii) to the formation of *in situ* Cu^0 nanoparticles by electroreduction at more anodic potential due to the presence of alendronate.

The catalytic properties were strongly influenced by the pH of the solution, the pH 2 being the best for nitrite reduction for **$P_2W_{15}CuAle$**. The ability of these catalysts to be used in a nitrate reduction sensor was also examined in the case of **$P_2W_{15}CuAle$**, which was found to be the most efficient catalyst. A linear dependence of the current on the nitrate concentration was obtained in the range of 0 to 20 $mmol \cdot L^{-1}$ in pH 1 solution while the linear concentration range 0 to 10 $mmol \cdot L^{-1}$ was narrower in pH 5 solution.

This work is still in progress, and further studies include the characterization of the CuPOM and CuPOM/Ale deposited electrode by using X-ray photoelectron spectroscopy (XPS). In addition, the formation of the reaction intermediates and products should be identified and their amount should be quantified by associating electrochemical method with other technique such as Differential Electrochemical Mass Spectroscopy (DEMS), Gas Chromatography (GC) and Fourier-Transformed Infrared Spectroscopy (FT-IR).

References

1. Keita, B., Abdeljalil, E., Nadjo, L., Contant, R. & Belghiche, R. Cooperativity of copper and molybdenum centers in polyoxometalate-based electrocatalysts : cyclic voltammetry, EQCM and AFM Characterization. *Langmuir* **22**, 10416–10425 (2006).
2. Jabbour, D., Keita, B., Mbomekalle, I. M., Nadjo, L. & Kortz, U. Investigation of multi-nickel-substituted tungstophosphates and their stability and electrocatalytic properties in aqueous media. *Eur. J. Inorg. Chem.* **4**, 2036–2044 (2004).
3. Ammam, M. Mbomekallea, I. M., Keita, B., Nadjo L., Anderson, T. M., Zhang X., Hardcastle K. I., Hill C. L. & Fransaer, J. Electrochemical behavior and electrocatalytic properties towards hydrogen peroxide, dioxygen and nitrate of the polyanions $[Ni^{II}OH_2)_2(Fe^{III})_2(X_2W_{15}O_{56})_2]^{14-}$ (X = P^V or As^V): A comparative study. *J. Electroanal. Chem.* **647**, 97–102 (2010).
4. Keita, B., Martyr, I., Nadjo, L. & Contant, R. $[H_4AsW_{18}O_{62}]^{7-}$, A novel Dawson heteropolyanion and two of its sandwich-type derivatives: electrocatalytic properties towards nitrite and nitrate. *Electrochem. commun.* **3**, 267–273 (2001).
5. Clemente-Juan, J. M., Coronado, E. & Gaita-Ariño, A. Magnetic polyoxometalates: from molecular magnetism to molecular spintronics and quantum computing. *Chem. Soc. Rev.* **41**, 7464 (2012).
6. El Moll, H., Dolbecq, A., Marrot, J., Rousseau, G., Haouas, M., Taulelle, F., Rogez, G., Rousseau, G., Keita, B. & Pierre Mialane. A stable hybrid bisphosphonate polyoxometalate single-molecule magnet. *Chem. - A Eur. J.* **18**, 3845–3849 (2012).
7. El Moll, H., Rousseau, G., Dolbecq, A., Oms, O., Marrot, J., Haouas, M., Taulelle, F., Rivière, E., Wernsdorfer, W., Lachkar, D., Lacôte, E., Keita, B. & Pierre Mialane. Properties of a tunable multinuclear nickel polyoxotungstate platform. *Chem. - A Eur. J.* **19**, 6753–6765 (2013).
8. Oms, O., Yang, S., Salomon, W., Marrot, J., Dolbecq, A., Rivière, E., Bonnefont, A., Ruhlmann, L., & Pierre Mialane. Heteroanionic materials based on copper clusters, bisphosphonates, and polyoxometalates: magnetic properties and comparative electrocatalytic NO_x reduction studies. *Inorg. Chem.* **55**, 1551–1561 (2016).
9. Rousseau, G., Oms, O., Dolbecq, A., Marrot, J. & Mialane, P. Route for the elaboration of functionalized hybrid 3d-substituted trivacant keggin anions. *Inorg. Chem.* **50**, 7376–7378 (2011).
10. Becker, G., Helmut, S., Gudrun, U., Werner, U., Manfred, R., Wolfgang, R. & Uwe-Josef, V. I*norganic Syntheses*. (John wiley & Sons 2007).
11. Bosing, M., Loose, I., Pohlmann, H. & Krebs, B. New strategies for the generation of large heteropolymetalate clusters: The beta-B-SbW_9 fragment as a multifunctional unit. *Chem. Eur. J.* **3**, 1232–1237 (1997).
12. Rorabacher, Davide, B. & Schroeder, R. R. Electrochemistry of copper. (Encyclopedia of Electrochemistry, 2007).
13. Ruhlmann, L., Nadjo, L., Canny, J. & Contant, R. Di- and tetranuclear dawson-derived sandwich complexes : synthesis, spectroscopic characterization, and electrochemical behavior. *Eur. J. Inorg. Chem.* **2002**, 975–986 (2002).
14. Parkt, J.-Y. & Lee, Y.-N. Solubility and decomposition kinetics of nitrous acid in aqueous solution. *J . Phys. Chem.* **92**, 6294–6302 (1988).
15. Pal, M. & Ganesan, V. Effect of silver nanoelectrode ensembles on the electrocatalytic reduction of NO_2^- by zinc phthalocyanine. *Electrochim. Acta.* **55**, 4071–4077 (2010).
16. De Vooys, A. C. A., Van Santen, R. A. & Van Veen, J. A. R. Electrocatalytic reduction of NO_3^- on palladium/copper electrodes. *J. Mol. Catal. A Chem.* **154**, 203–215 (2000).
17. Burg, A., Lozinsky, E., Cohen, H. & Meyerstein, D. Mechanism of reduction of the nitrite ion by Cu^I complexes. *Eur. J. Inorg. Chem.* 3675–3680 (2004)
18. Zhang, Z., Qi, Y., Qin, C., Li, Y., Wang, E., Wang, X., Su, Z. & Xu, L. Two multi-copper-containing heteropolyoxotungstates constructed from the lacunary keggin polyoxoanion and the high-nuclear spin cluster. *Inorg. Chem.* **46**, 8162–8169 (2007).
19. Keita, B., de Oliveira, P., Nadjo, L. & Kortz, U. The ball-shaped heteropolytungstates $[[Sn(CH_3)_2(H_2O)]_{24}[Sn(CH_3)_2]_{12}(A\text{-}XW_9O_{34})_{12}]^{36-}$ (X=P, As): stability, redox and electrocatalytic properties in aqueous media. *Chem. - A Eur. J.* **13**, 5480–91 (2007).

Chapter IV

POMs-stabilized Ag nanoparticles for NO_x reduction

Chapter IV POMs-stabilized Ag nanoparticles for NO_x reduction

1 Introduction

Besides copper, silver exhibits also a significant catalytic activity for nitrate reduction.[1] The nitrate reduction is observed from 0.10 V *vs.* RHE in 0.5 mol·L^{-1} H_2SO_4 solution.[2] The nitrate reduction current can be increased by using silver nanoparticles rather than bulk electrodes, due to the increase of the roughness factor of the electrode.[3] In this chapter, we are focusing on nitrate and nitrite reduction by AgNPs.

There is a large number of methods to prepare Ag nanoparticles. Among them, the most commons techniques are:[4]

- **Physical process**: the energies such as thermal, ac power, arc discharge are used to produce AgNPs in powder form. The physical approach allows to produce large quantities of AgNPs samples in a single process. However, the cost for the equipment should be considered.[3]

- **Chemical method**: this method has been mostly used for preparing AgNPs. Three components: metal precursors, reducing agents and stabilizing agents are critical in chemical process. Monodispersed and uniform AgNPs can be obtained by adjusting the reaction parameters such as pH of solution, reaction agents ($NaBH_4$, ethylene glycol, glucose), stabilizing agents (poly(vinyl acetate) (PVA), polyvinylpyrrolidone (PVP), sodium oleate) as well as the temperature.[5] However, the presence of the stabilizing agent can affect the catalytic activity of the silver particles.

- **Biological process**: bacteria, fungi, plants are used as reducing and stabilizing agents. This is a low cost technique and forms small size nanoparticles (2 to 11 nm). However, it is difficult to produce large quantity of AgNPs by using this method.[4]

- **Photocatalytical process**: a direct photo-reduction process of silver salt in the presence of reducing agent and stabilizing agent under illumination. Various advantages of this method have been reported such as clean process and controllable formation of nanoparticles by spectroscopy.[4]

- **Electrodeposition process**: a potential difference is applied to an electrode (such as metal, carbon, or semiconductor) and an electrolyte interface, which results in electron transfer between the electrode and ionic species in the electrolyte and the leads to the deposition of atoms of the species onto the electrode surface.[4]

- **Sonochemistry**: this techniques allows to prepare metallic nanoparticles by applying powerful ultrasound radiation (20 KHz – 10 MHz) generating different kind of reactive radicals, which is able to reduce the metallic ions.[6]

- **Radiolysis**: in this case, the radicals reacting with the metallic ions are generated by gamma radiation using for instance the ^{60}Co source.[7]

To increase the roughness factor of the electrode, the particles should to be nanosized, but also well dispersed to prevent their agglomeration. Polyoxometalates (POMs) are interesting compounds for the photochemical formation of AgNPs since the POMs can act as the reducing agent (under UV illumination) and also as the stabilizing agent which can protect nanoparticle from agglomeration.

Formation of Ag nanoparticles (AgNPs) is prepared by using photochemically reduced POM such as $[SiW_{12}O_{40}]^{4-}$, $[PW_{12}O_{40}]^{3-}$ and $[P_2Mo_{18}O_{62}]^{6-}$ at natural pH.[8,9] In the presence of the electron donor such as propan-2-ol, the photochemically reduced POMs are produced by illumination in the O-M charge transfer band (near visible and UV region).[8] Indeed, the excited POMs are strong oxidants which is able to capture electrons from electron donors. In this system, POMs serve as photocatalysts, reducing agents and stabilizers simultaneously, since the obtained metal colloids are stable against aggregation. A one-step synthesis using Mo^{V}-Mo^{VI} mixed-valence POMs in water has also reported.[10] The shapes and sizes of AgNPs can be modulated by using different POMs and the initial concentration of silver salt. To the best of our knowledge, this is the first time that Ag@POM nanoparticles prepared by this method are used towards nitrate reduction.

In this chapter, $[SiW_{12}O_{40}]^{4-}$ type polyoxometalate is chosen for preparing AgNPs due to their ability to reduce and stabilize nanoparticles, as well as their catalytic properties towards nitrite reduction.

2 Synthesis of Ag nanoparticles

2.1 Photocatalytic reduction of silver ions

A solution of $[SiW_{12}O_{40}]^{4-}$ (3.5×10^{-4} mol·L^{-1}) is mixed with Ag_2SO_4 (1.0×10^{-4} mol·L^{-1}), 0.5 mol·L^{-1} propan-2-ol is added into solution as the electron donor. Deaerated solution is obtained by argon bubbling before illumination for more than 30 minutes. Irradiation was performed by a 300 W Xe arc lamp equipped with a water cell filter to absorb the near-IR radiation. UV-vis absorption spectra were recorded during the illumination to follow the reduction reaction.

The mechanism of photo-reduction of Ag^+ by POM is described in Chapter I page 27.

The formation of the Ag nanoparticles is followed by the UV-visible spectroscopy. The UV-visible spectrum measured before illumination is displayed in Fig. IV.1A. The absorption band in the UV region (below 370 nm) is due to the POM. Once the illumination begins, a well-known plasmon absorption band of silver nanoparticles around 407 nm is obtained after 6 minutes and the color of the solution changes to yellow which characterizes the formation of Ag nanoparticles.[5] The plasmon band stems from the excitation of collective oscillation mode of the electrons in the particles. Based on the published work,[5] a plasmon band at 400 nm generally corresponds to AgNPs with sphere form (blue line in Fig. IV.1A). Mukherji and his co-workers[11] have synthesized a series of AgNPs and associated the nanoparticles size with UV-vis extinction spectras, the peaks at 406 nm and 411 nm wavelengths correspond to the average sizes of 20 nm and 30 nm respectively. In our case, by increasing the illumination time to 20 minutes, the solution color changes to blue and a wide band between 600 nm to 800 nm (blue line in Fig. IV.1A) is observed which can be attributed to the d-d transitions and tungsten-to-tungsten charge transfer (W^{5+}-W^{6+} CT) which is the signature of the formation of reduced POM. The name of this band is also called intervalence band. After 30 minutes under illumination, the UV-visible spectra do not evolve anymore indicating the end of the reaction and the total reduction of Ag^+ as well as the POM in solution. When oxygen comes into the solution by opening the cell in air (red line in Fig. IV.1A), the second absorption band (intervalence band) disappears indicating the re-oxidation of reduced POM. The absorbance of the band at 400 nm decreases only slightly suggesting that the silver nanoparticles formed during the photo-reduction are stable in air.

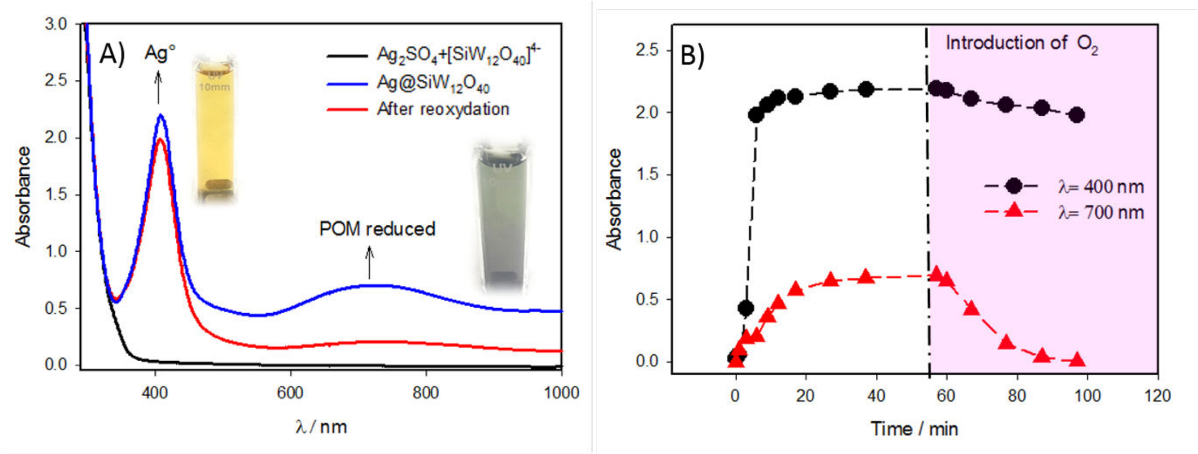

Figure IV.1: A) UV-visible absorption spectra of a solution containing $[SiW_{12}O_{40}]^{4-}$ (3.5×10^{-4} mol·L^{-1}), Ag_2SO_4 (1×10^{-4} mol·L^{-1}) and propan-2-ol (0.5 mol·L^{-1}) before (−), after (−) 50 minutes of illumination and after reoxydation in air (−). B) Measured absorbance bands at 400 nm and 700 nm as a function of illumination time.

2.2 Effect of the POM concentration on the silver nanoparticle formation

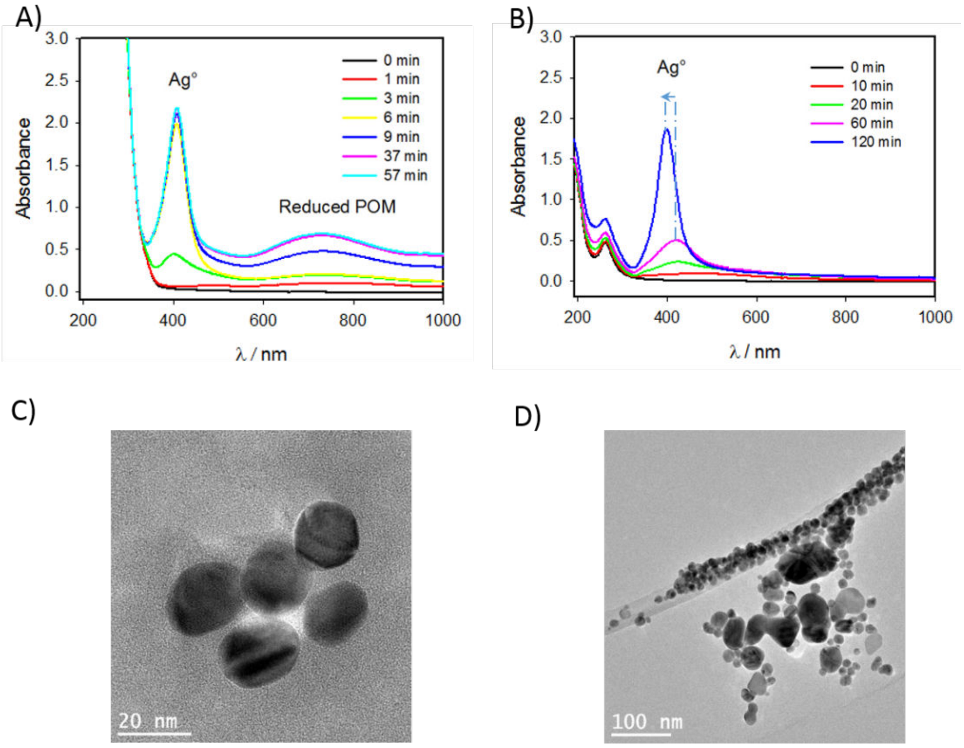

*Figure IV.2: UV-visible absorption spectra and TEM micrographics of: **synthesis a)** a deaerated solution of $[SiW_{12}O_{40}]^{4-}$ (3.5×10^{-4} mol·L^{-1}), Ag_2SO_4 (1×10^{-4} mol·L^{-1}) and propan-2-ol (0.5 mol·L^{-1}) under illumination (A and C); **synthesis b)** a deaerated solution of $[SiW_{12}O_{40}]^{4-}$ (8.4×10^{-6} mol·L^{-1}), Ag_2SO_4 (1×10^{-4} mol·L^{-1}) and propan-2-ol (0.5 mol·L^{-1}) (B and D).*

The influence of the concentration of POMs on the Ag nanoparticles formation was tested. Two different synthesis conditions have been compared: **synthesis a)** $[SiW_{12}O_{40}]^{4-}$ (3.5×10^{-4} mol·L^{-1}) mixed with Ag_2SO_4 (1×10^{-4} mol·L^{-1}) and **synthesis b)** $[SiW_{12}O_{40}]^{4-}$ (8.4×10^{-6} mol·L^{-1}) mixed with Ag_2SO_4 (1×10^{-4} mol·L^{-1}). In both solutions, 0.5 mol·L^{-1} propan-2-ol was added as the electron donor.

The UV-vis spectra using the **synthesis a** is shown in Fig. IV.2A, the plasmon band of Ag^0 is observed at 400 nm after the formation of reduced POM. The reaction of the silver reduction completes over 6 minutes. Representative TEM micrograph confirms the formation of spherical Ag nanoparticles with a diameter around 20 nm, in agreement with reported study.[11] The higher POM concentration leads to the fast formation of monodispersed AgNPs with uniform size distribution.[12]

By decreasing 40 times the concentration of POM (**synthesis b**), Ag^+ is in large excess, the formation of AgNPs becomes slower, ca. 120 minutes (Fig. IV.2B). However, the reduced POM absorption band (intervalence band) could not be observed in this system even after more than 24 hours under illumination (not show). During the AgNP formation, the initial band is large and around 430 nm. By increasing illumination time, the plasmon band shifts to 405 nm and the peak becomes narrower and more symmetrical. It can be explained by the fact that AgNPs formed at the beginning are heterogeneous with various forms due to the slower reaction rate, the nanoparticles becoming more homogeneous with prolonged illumination time. Representative TEM micrograph shows the trend of aggregation of AgNPs due to the lower POMs concentration in solution, which could not adsorb on the silver surface to protect nanoparticles. It is noticeable that POMs remain intact during the reaction as suggested by the stability of the absorbance band at 270 nm which corresponds to the oxidized form of Keggin-structure POMs. Similar band have been reported by Troupis and his co-workers.[8] This band is not observed in conditions of **synthesis a** only because to the higher POM concentration leading to the saturation in UV-vis spectra.

The POMs adsorbed on silver nanoparticles cannot be observed directly in the TEM micrographs shown in Fig. IV.2C and Fig. IV.2D. However, using Energy-Dispersive X-ray spectroscopy (EDX), the presence of the elements Ag, W, Si could be evidence suggesting the presence of POM on nanoparticles surfaces (see Fig. IV.3).

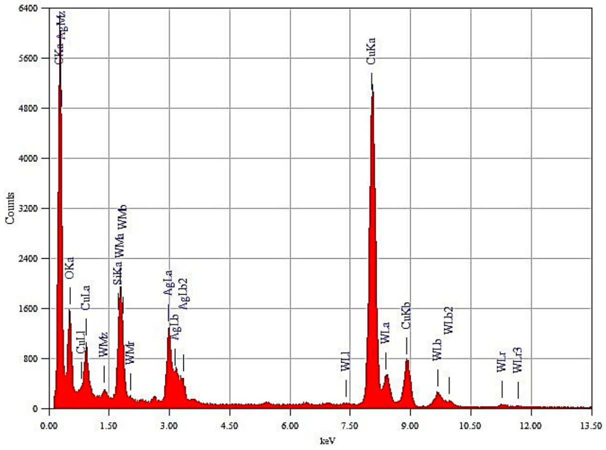

Figure IV.3: EDX analysis of $Ag@SiW_{12}O_{40}$ obtained from a solution contains $[SiW_{12}O_{40}]^{4-}$ (3.5×10^{-4} $mol\cdot L^{-1}$), Ag_2SO_4 (1×10^{-4} $mol\cdot L^{-1}$) and propan-2-ol (0.5 $mol\cdot L^{-1}$) under illumination. The Cu signals are due to the cupper grid used.

2.3 Stability of the silver nanoparticles

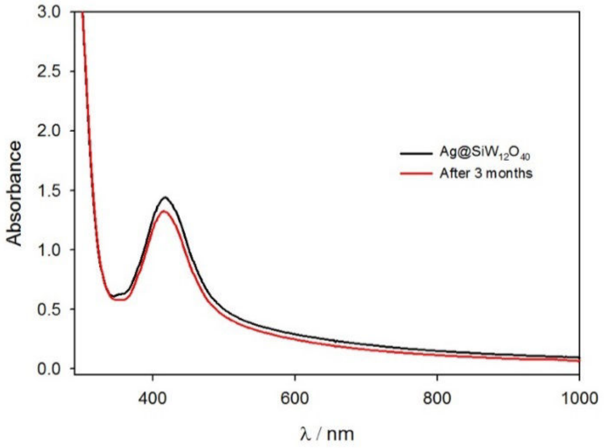

Figure IV.4: UV-vis spectra of formed $Ag@SiW_{12}O_{40}$ nanoparticles solution right after the illumination (black line) and after 3 months (red line).

The stability of formed $Ag@SiW_{12}O_{40}$ nanoparticles in solution was monitored by UV-vis spectroscopy after 3 months. The plasmon band of AgNPs remains at the same wavelength while only a slight intensity decrease is observed. This indicates that the formed POM-stabilized Ag nanoparticles are stable at least for 3 months.

3 Preparation of the Ag@POM modified GC electrode

To investigate the electrocatalytic properties of the Ag@$SiW_{12}O_{40}$ nanoparticles, they have to be deposited on a glassy carbon (GC) surface which will serve as current collector.

3.1 Experimental procedure for the thin film catalyst layer preparation

The modified electrode is prepared by successively dropping 5 µL Ag@$SiW_{12}O_{40}$ solution on GC electrode surface and drying in air. The deposition can be repeated until the desiring amount is reached. The dropping of small solution volume at different locations of the GC surface and the fast evaporation of the solvent allow to obtain homogeneous Ag@$SiW_{12}O_{40}$ distribution on the GC surface. At the end of the deposition, 2 µL 5wt. % Nafion solution is added to the film to improve its stability (Fig. IV.5).

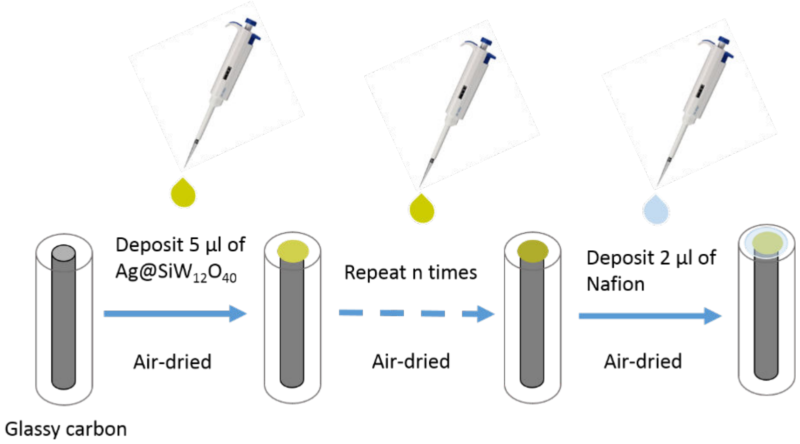

Figure IV.5: Schema of successively dropping method to deposit Ag@$SiW_{12}O_{40}$ solution on a glassy carbon (GC) electrode.

3.2 Characterization by cyclic voltammetry

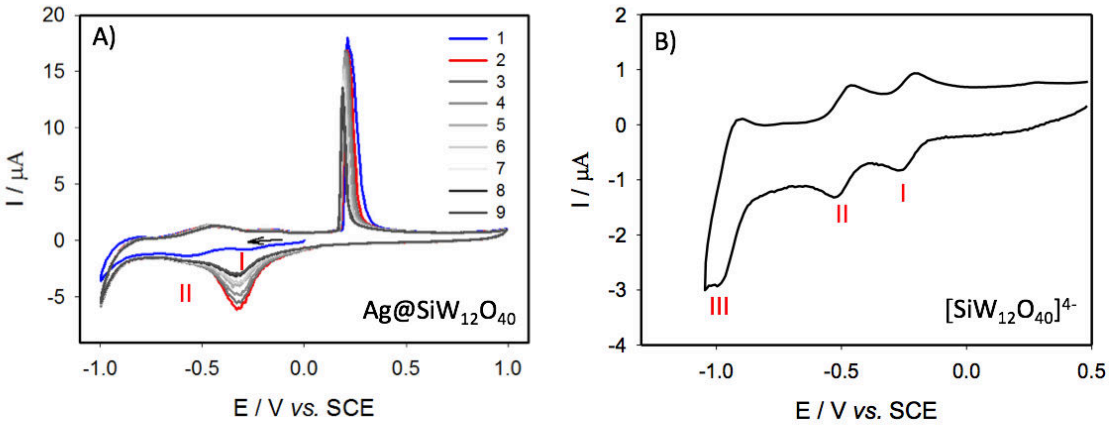

Figure IV.6: A) CV of 20 µL Ag@$SiW_{12}O_{40}$ modified on GC electrode; B) CV of 0.1 mmol·L^{-1} $[SiW_{12}O_{40}]^{4-}$ in solution. Buffer solution: pH 5 1 mol·L^{-1} CH_3COOLi + CH_3COOH, v = 20 mV·s^{-1}.

The electrochemical properties of the modified electrode were investigated by cyclic voltammetry in pH 5 1 mol·L^{-1} CH_3COOLi + CH_3COOH solution. The first scan starts from 0 V and sweeps to negative potential. Two reduction waves are observed at -0.26 V (peak I) and -0.53 V (peak II) which are similar to the ones of $[SiW_{12}O_{40}]^{4-}$ measured in solution, at -0.25 V and -0.50 V respectively (Fig. IV.6B). At reverse scan, a pronounced peak at 0.25 V is attributed to the oxidation of Ag^0 to Ag^+ (anodic redissolution peak). Hence, at the second cycle, an additional wave at -0.31 V appears corresponding to the reduction of Ag^+**.** The intensity of the redox peaks of $Ag^{I/0}$ decreases with the number of scan is attributed to the release of Ag^+ ions to the solution and cannot be reduced over the time scale of the potential scan. The peak III at -0.93 V of the POM is not well-defined in Ag@$SiW_{12}O_{40}$ because part of the redox peak is obscured by the hydrogen evolution.

3.3 Investigation of the formation of the catalyst layer through Quartz Crystal Microbalance (QCM)

A mass variation (△m) due to the deposition of the catalyst layer on electrode surface can be estimated by using Quartz Crystal Microbalance (QCM) by measuring the change of frequency of a quartz crystal resonator. The resonator is a thin quartz crystal sandwiched between two electrodes (carbon, ITO or metals) submitted to an alternating electric field across the crystal, generating vibrational motion of the crystal at its resonance frequency. This resonance frequency is sensitive to the mass change at the surface of the crystal or of the electrodes, hence, we can use one side of the resonator as a working electrode and simultaneously measure the mass variation of the electrode.[13]

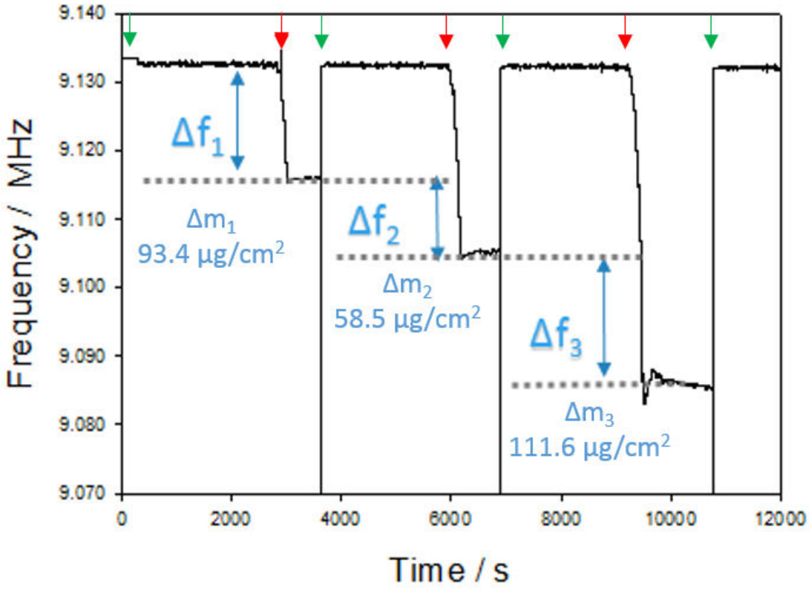

Figure IV.7: Frequency response of QCM sensor after three times 5 µL Ag@$SiW_{12}O_{40}$ deposition onto a carbon QCM resonator. Green arrow: the moment that the solution was dropped onto the dry quartz resonator. Red arrow: the moment that the electrode gets completely dry.

Typical resonance frequency evolution during the Ag@$SiW_{12}O_{40}$ catalyst deposition onto a carbon coved QCM resonator is displayed in Fig. IV.7. To obtain this curve, 5 µL of Ag@$SiW_{12}O_{40}$ solution prepared following the procedure described in paragraph 2.1, is deposited on a carbon covered QCM resonator (A = 0.2 cm^2) at a frequency of 9.08 MHz AT-cut (see Fig. IV.7). The green arrows indicate the different times when the solution was dropped onto the dry quartz resonator. The dropping results in first an abrupt decrease of the frequency that manifests itself by the vertical lines in Fig. IV.7 at 3800, 7000 and 10700 s. After the abrupt decrease, the resonance frequency of the resonator covered by the solution increases and stabilizes at a value of ca. 9.133 MHz. Then the electrode is allowed to dry in air. The deposition of the Ag@$SiW_{12}O_{40}$ nanoparticles on the carbon surface occurs suddenly during the drying step and manifest itself by an abrupt resonance frequency decrease (see the red arrows in Fig. IV.7).

The mass change due to the deposition Ag@$SiW_{12}O_{40}$ nanoparticles on resonator surface is calculated by using the Sauerbrey's equation: $\Delta f = -2f_0^2 \Delta m/\sqrt{\mu.\rho}$. Typically, a mass change between 58.5 to 111.6 µg·cm^{-2} at each 5 µL deposition is obtained. This corresponds to a concentration of ca. 2.80 to 4.42 g·L^{-1} for Ag@$SiW_{12}O_{40}$ nanoparticles solution prepared. From the Fig. IV.7, it can be seen that the resonance frequency reaches almost its initial value each time that 5 µL of $Ag@SiW_{12}O_{40}$ solution is dropped. This suggests that most of the $Ag@SiW_{12}O_{40}$ nanoparticles are removed from the electrode surface in contact of water. To improve the fixation of the nanoparticles on the surface, 2 µL of 5 wt. % Nafion solution has to be added on the surface at the end of the deposition process. This is discussed in the next paragraph.

3.4 Influence of Nafion on the electrochemical properties

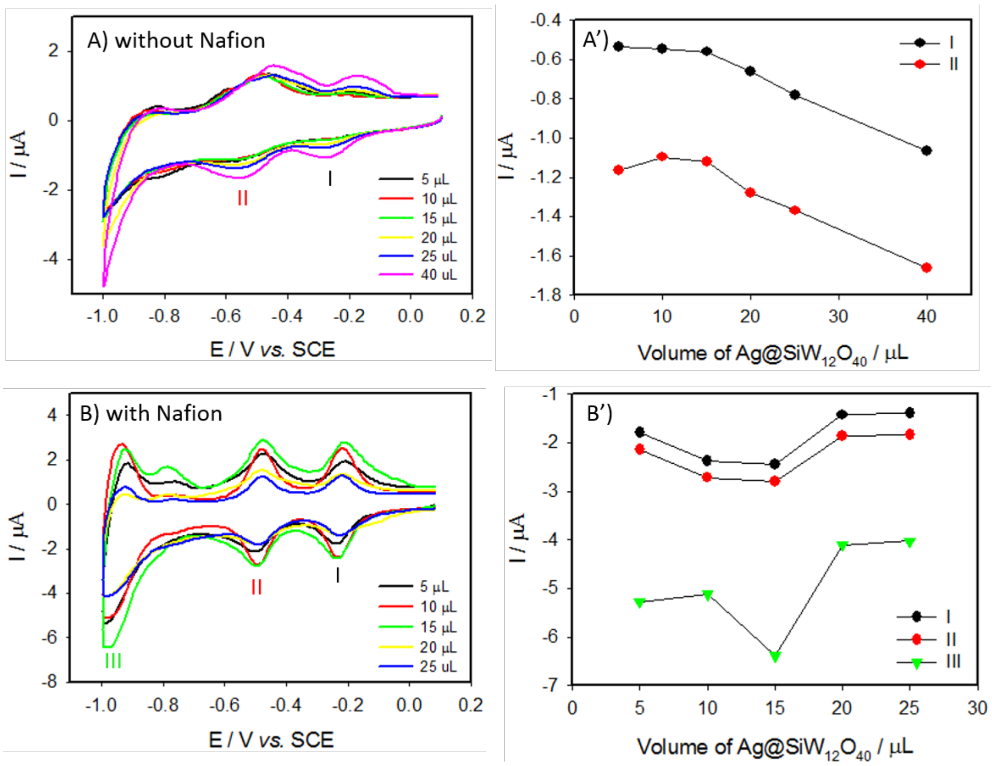

Figure IV.8: Influence of the quantity of $Ag@SiW_{12}O_{40}$ deposited on GC electrode without Nafion (A and A') and in the presence of 2 µL 5wt. % Nafion at the end of deposition (B and B'). Buffer solution: pH 5 1 mol·L^{-1} CH_3COOLi + CH_3COOH, v = 20 mV·s^{-1}.

The quantity of $Ag@SiW_{12}O_{40}$ deposited on electrode could be also monitored by cyclic voltammetry. The potential range is limited between 0.10 V to -1.00 V to avoid the oxidation of Ag^0 nanoparticles as well as the hydrogen evolution. When the CV is measured just after deposition on electrode surface (Fig. IV.8A), two redox peaks are observed at -0.27 V (peak I) and -0.56 V (peak II), but the intensity of current increases only after adding 15 µL $Ag@SiW_{12}O_{40}$ onto the surface (Fig. IV.8A'). However, the films take off from the glassy carbon surface right after the first CV cycle (Fig. IV.9A). Hence, Nafion is added to stabilize the film.

After addition of 2 µL Nafion, three well-defined waves are observed (Fig. IV.8B). The redox waves are more symmetrical and ΔE_p (peak to peak separation) gets smaller than in the absence of Nafion. Surprisingly, the current associated to the POM redox processes doesn't increase with the number of deposition cycle. This suggests that only small fractions of the particles are electrically connected to the glassy carbon current collector. As a better stability is obtained with Nafion (Fig. IV.9B), in following study, a system of 15 µL $Ag@SiW_{12}O_{40}$ + 2 µL Nafion is used to study its catalytic property towards NO_x reduction.

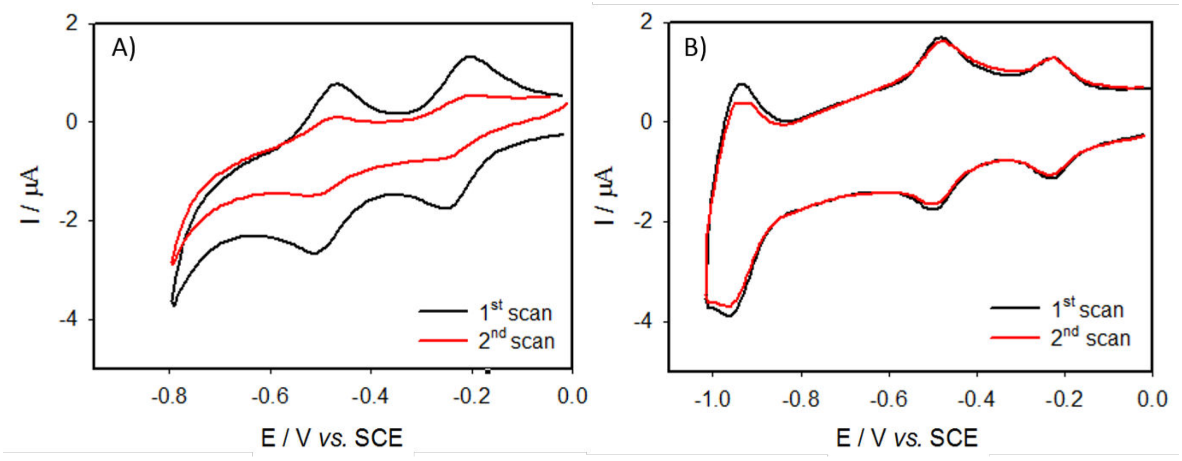

Figure IV.9: The first two scans of $Ag@SiW_{12}O_{40}$ *(A) and* $Ag@SiW_{12}O_{40}$*+2µL 5wt. % Nafion (B) modified glassy carbon electrode in pH 5 1 mol·L*$^{-1}$ CH_3COOLi + CH_3COOH *solution, v = 20 mV·s*$^{-1}$.

4 Electrocatalytic nitrite reduction by $[SiW_{12}O_{40}]^{4-}$ and $Ag@SiW_{12}O_{40}$

For these systems, the catalytic onset potential was defined as the potential where $\Delta I = I_{POM} - I_{POM+NOx-} = 1$ µA for 1 mmol·L^{-1} $NaNO_2$ added in solution. Note that the △I value chosen is higher than the one used with the CuPOM catalysts which was 0.5 µA (see chapter III, sections 3 and 4). Indeed, the background currents of the $Ag@SiW_{12}O_{40}$ modified GC electrodes are significantly increased compared to the unmodified GC electrode and higher △I value have to be chosen for a reliable determination of the onset potential of the reduction.

4.1 Nitrite reduction by POM $[SiW_{12}O_{40}]^{4-}$

First, we examined the catalytic property of $[SiW_{12}O_{40}]^{4-}$ in different pH solutions. The potential window for the investigation is chosen between 0.50 V and the potential just below the third reduction wave of POM.

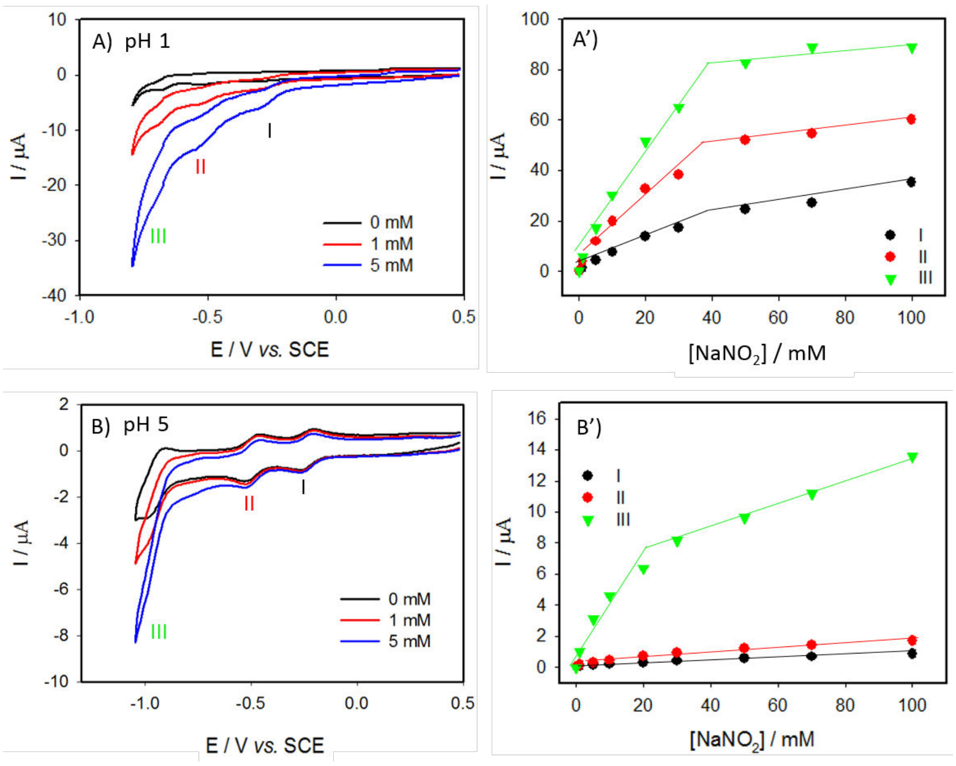

Figure IV.10: $NaNO_2$ reduction in the presence of 0.1 mmol·L^{-1} $[SiW_{12}O_{40}]^{4-}$ in pH 1 (A and A') and pH 5 (B and B') solutions. Concentrations of the nitrite are: 0, 1 and 5 mmol·L^{-1} (A and B) and between 0 to 100 mmol·L^{-1} (A' and B'). Buffer solutions: pH 1 0.5 mol·L^{-1} Na_2SO_4 + H_2SO_4 and pH 5 1 mol·L^{-1} CH_3COOLi + CH_3COOH, v = 20 mV·s^{-1}.

In pH 1 solution (Fig. IV.10A and Fig. IV.10A'), nitrite reduction current is observed from the first reduction wave and increases with the quantity of $NaNO_2$ added in solution. The catalytic onset potential is at -0.31 V. Catalytic current increases linearly for the three reduction waves from 0 mmol·L^{-1} to 40 mmol·L^{-1} and reaches the limiting current due to the rate-determining step of the reaction.

In pH 5 solution (Fig. IV.10B and Fig. IV.10B'), the catalysis begins after the second reduction wave (-0.85 V) and the current increases especially at the third wave. It has been noted that, the current intensity is smaller than at pH 1. No clear upper limit is observed in range of 0 mol·L^{-1} to 100 mol·L^{-1} $NaNO_2$.

4.2 Nitrite reduction by Ag@$SiW_{12}O_{40}$

The catalytic property of Ag@$SiW_{12}O_{40}$ towards nitrite reduction is studied in the same buffer solutions as for the $[SiW_{12}O_{40}]^{4-}$. The potential range was defined after 0 V to prevent the oxidation of Ag^0 and just after the end of the third reduction wave of the POM, before the hydrogen evolution. It needs to note that in the film of Ag@$SiW_{12}O_{40}$, the presence of free POM $[SiW_{12}O_{40}]^{4-}$ cannot be excluded because the dialysis was not performed.

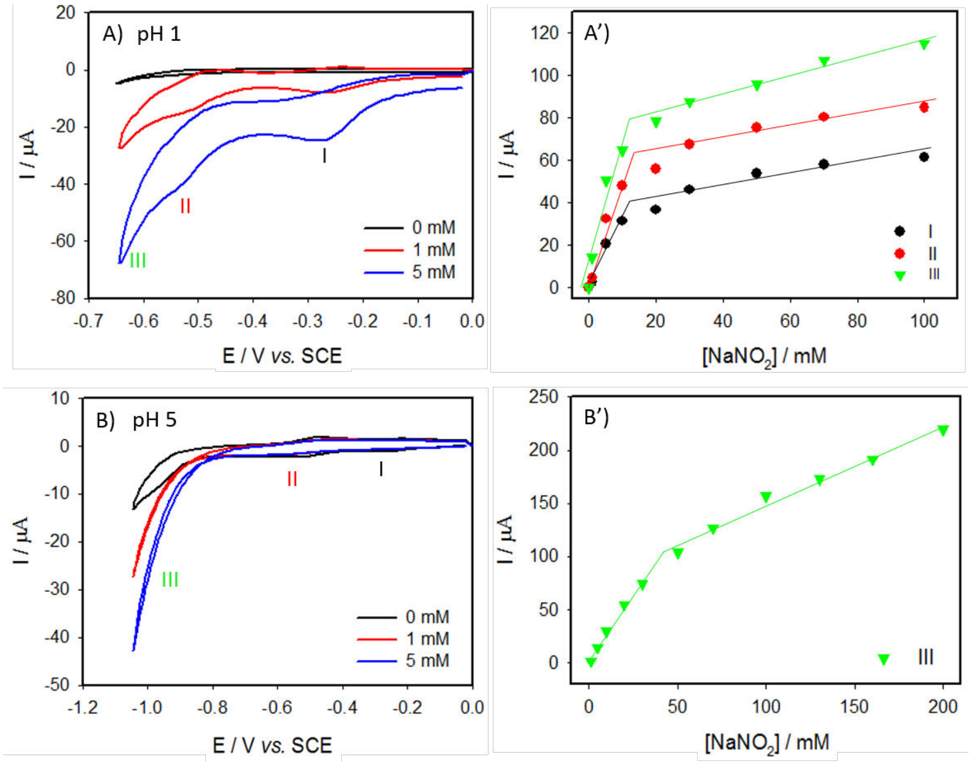

Figure IV.11: Nitrite reduction with 15 µL Ag@$SiW_{12}O_{40}$ + 2 µL Nafion modified electrode in pH 1 (A and A') and in pH 5 (B and B') solutions. Concentrations of the nitrite are 0, 1 and 5 mmol·L^{-1} (A and B), between 0 to 100 mmol·L^{-1} (A') and between 0 to 200 mmol·L^{-1} (B'). Buffer solutions: pH 1 0.5 mol·L^{-1} Na_2SO_4 + H_2SO_4 and pH 5 1 mol·L^{-1} CH_3COOLi + CH_3COOH, v = 20 mV·s^{-1}. The third reduction wave of W (wave III) is measured at -0.60 V at pH 1 and at -0.94 V at pH 5.

In pH 1 solution, nitrite reduction is observed before the anodic potential limit (0 V) in agreement with the catalytic properties of Ag towards nitrite reduction in pH 1 solution.[14] The current increases in the whole range of potential measured especially at three $W^{VI/V}$ reduction waves. This result demonstrates that adding POM to Ag nanoparticles leads to a significant enhancement of the catalytic current. The current increases rapidly with $NaNO_2$ concentration until 10 - 20 mmol·L^{-1} and then the growth rate slow down reaching the limiting current. It should be also mentioned that a higher limiting current can be obtained with the Ag@$SiW_{12}O_{40}$ than with the POM alone revealing the presence of a tandem catalysis (see Fig. IV.12A where $[SiW_{12}O_{40}]^{4-}$ is in solution and Ag@$SiW_{12}O_{40}$ modified on electrode surface with 5 mmol·L^{-1} $NaNO_2$ in solution are compared in the same graph). At pH 1, an important gain at potential is observed and a higher current intensity is observed since the departure with Ag@$SiW_{12}O_{40}$. The current intensity is about two times higher than with $[SiW_{12}O_{40}]^{4-}$ in solution.

In pH 5 solution, the nitrite reduction begins at -0.83 V, the third reduction wave of the POM, almost at same potential with $[SiW_{12}O_{40}]^{4-}$ in solution. However, if the reduction potential is not affected by the presence of the Ag^0 nanoparticles, the current intensity is much higher (about 5 times) than with $[SiW_{12}O_{40}]^{4-}$ alone for the same $NaNO_2$ concentration (see Fig.IV.12B). The current increases rapidly until 50 mmol·L^{-1} $NaNO_2$ and then the rate is slow down (see Fig.IV.11B').

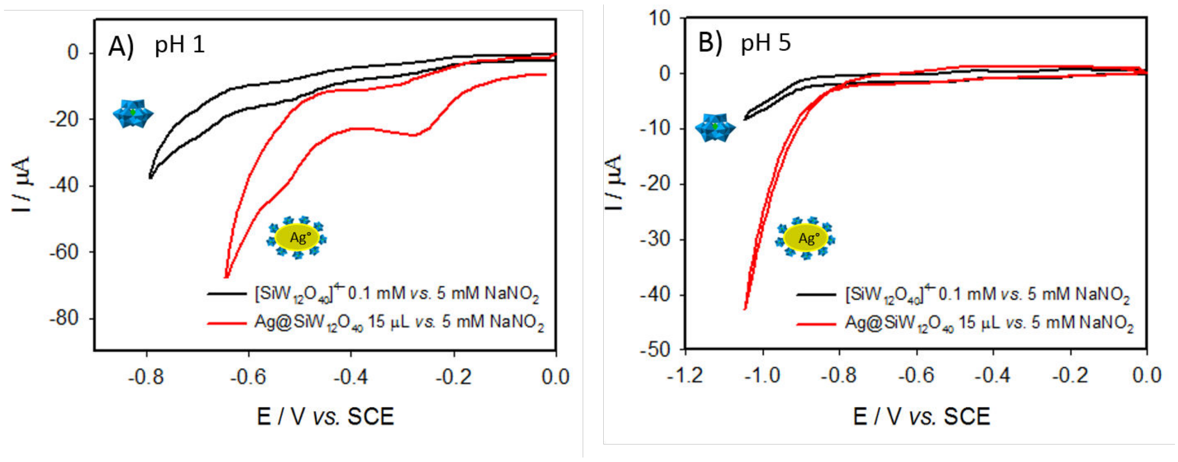

Figure IV.12: Comparison of $Ag@SiW_{12}O_{40}$ and $[SiW_{12}O_{40}]^{4-}$ towards nitrite reduction in pH 1 (A) and in pH 5 (B). Buffer solutions: pH 1 0.5 mol·L^{-1} $Na_2SO_4 + H_2SO_4$ and pH 5 1 mol·L^{-1} $CH_3COOLi + CH_3COOH$, v = 20 mV·s^{-1}.

The potential cycling study in a solution containing 200 mmol·L^{-1} $NaNO_2$ is shown in Fig. IV.13. The catalytic current remains noticeable after 750 scans. The decrease of current may be due to the disproportionation of nitrite over the time:

$$2HNO_2(aq) \rightleftarrows NO(aq) + NO_2(aq) + H_2O$$

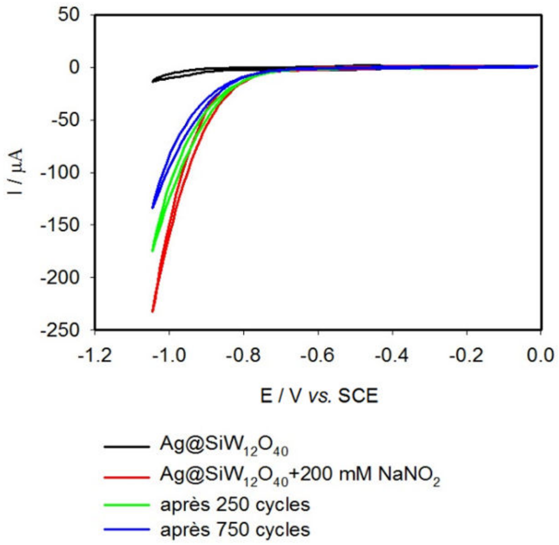

Figure IV. 13: Stability of 15 µL $Ag@SiW_{12}O_{40}$ +2 µL Nafion by sweep successively with 200 mmol·L^{-1} $NaNO_2$ in pH 5 1 mol·L^{-1} $CH_3COOLi + CH_3COOH$. v = 20 mV·s^{-1}.

5 Electrocatalytic nitrate reduction by Ag@$SiW_{12}O_{40}$

The catalytic properties toward nitrate reduction were studied in the same conditions than for nitrite reduction. The POM $[SiW_{12}O_{40}]^{4-}$ alone cannot catalyze the nitrate as shown before in the Chapter II sections 4.1 and 4.2.

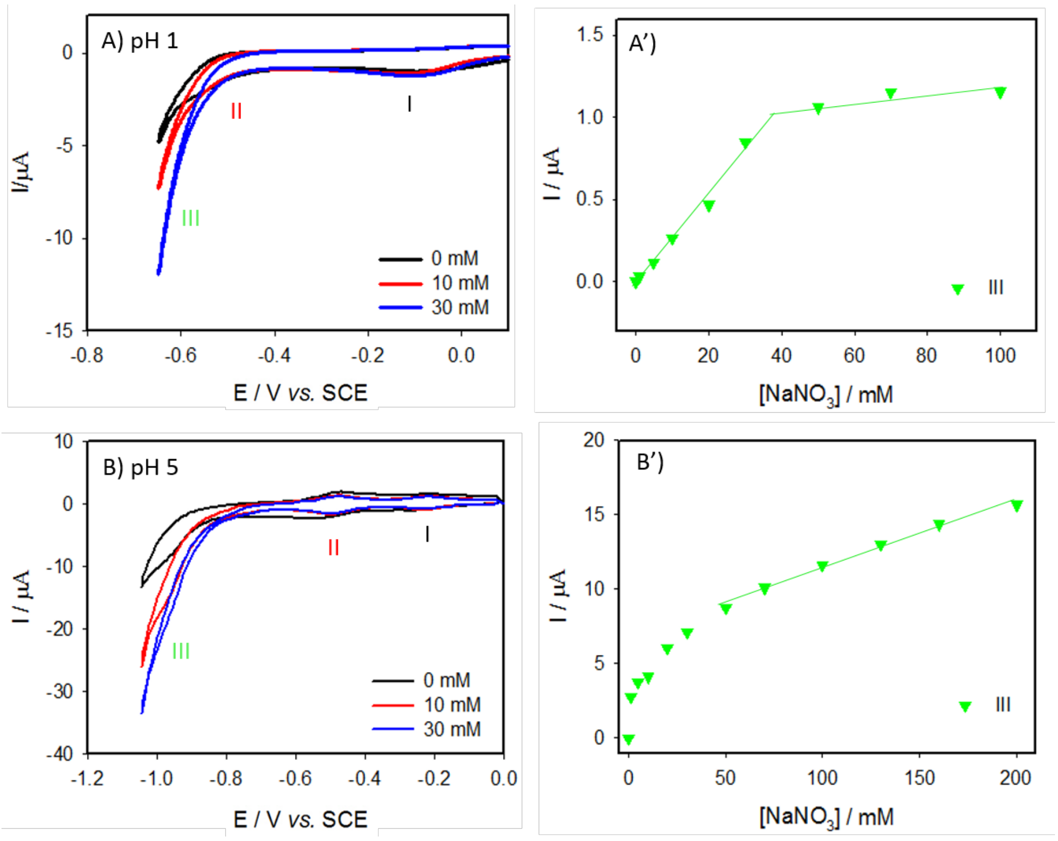

Figure IV.14: Nitrate reduction by 15 µL Ag@$SiW_{12}O_{40}$ +2 µL Nafion modified electrode in solution pH 1 (A and A') and in pH 5 (B and B'). Concentrations of the nitrate are: 0, 10 and 30 mmol·L^{-1} (A and C), between 0 to 100 mmol·L^{-1} (A') and between 0 to 200 mmol·L^{-1} (B') Buffer solution pH 1 0.5 mol·L^{-1} Na_2SO_4 + H_2SO_4 and pH 5 1 mol·L^{-1} CH_3COOLi + CH_3COOH, v = 20 mV·s^{-1}. The third reduction wave of W (wave III) is measured at -0.65 V at pH 1 and at -0.95 V at pH 5.

The nitrate reduction can be only observed below -0.52 V in pH 1 solution. However, the onset potential is difficult to define because of the small increase of current (Fig. IV.14A). In pH 5 solution, the onset point is at -0.91 V, about -0.08 V more cathodic than nitrite reduction. A linear trend is obtained between 50 mmol·L^{-1} to 200 mmol·L^{-1}, a nitrate sensor based on the Ag@$SiW_{12}O_{40}$ system can be expected working in this range. Reported Ag-based electrochemical nitrate sensor are generally used between 0-20 mmol·L^{-1}.[15,16,17,18] Our system may be used as complement for higher nitrate concentration solution.

An example of Ag-based nitrate sensor is shown in Fig. IV.15, Atmeh and his co-workers[18] have reported a nitrate sensor based on electrodeposited Ag nanoparticles and polypyrrole (PPy) modified carbon electrode. A linear concentration dependence is observed between 1 and 10 $mmol \cdot L^{-1}$.

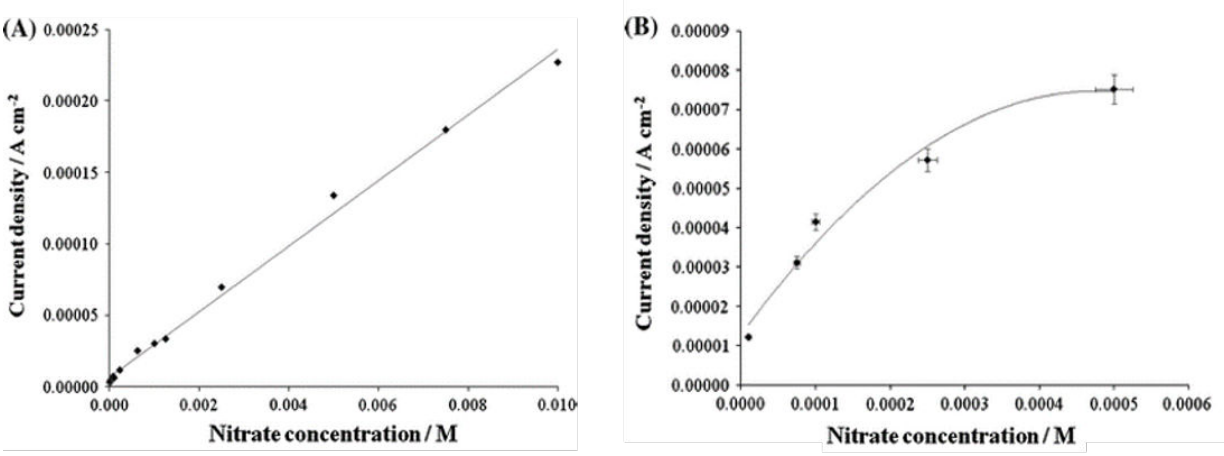

Figure IV.15: Peak current dependence on nitrate concentration range of 1-10000 µM of PPy/Ag. A) The entire concentration range B) the lower concentration range 1-500 $\mu mol \cdot L^{-1}$. Buffer solution: 0.1 $mol \cdot L^{-1}$ Na_2SO_4, reference electrode: SCE, $v = 20\ mV \cdot s^{-1}$. Peak current is measured at -1.42 V. (Reprinted from reference 16).

The catalytic onset potentials of $Ag@SiW_{12}O_{40}$ and $[SiW_{12}O_{40}]^{4-}$ towards nitrite and nitrate reduction are summarized in Table IV.1.

	pH	1	5
$[SiW_{12}O_{40}]^{4-}$	nitrite	-0.31	-0.85
$Ag@SiW_{12}O_{40}$	nitrite	>0	-0.83
	nitrate	*	-0.91

**: catalytic current too small to determine the catalytic potential*

Table IV.1: Catalytic onset potentials of NO_x reduction in pH 1 0.5 $mol \cdot L^{-1}$ Na_2SO_4 + H_2SO_4 solution and in pH 5 1 $mol \cdot L^{-1}$ CH_3COOLi + CH_3COOH solution, $v = 20\ mV \cdot s^{-1}$.

To conclude, the presence of AgNPs in the system can advance the catalytic reduction in pH 1 solution and it make the system active towards nitrate reduction at pH 5.

Fig. IV.16 shows nitrate reduction by three different systems: on Ag electrode (black line), on the Ag electrode with presence of 0.1 $mmol \cdot L^{-1}$ $[SiW_{12}O_{40}]^{4-}$ (red line) or on $Ag@SiW_{12}O_{40}$ modified GC electrode (green line). The presence of POMs onto the AgNP surface can prevent Ag^0 from the hydrogen evolution, hence a larger potential range can be applied to the $Ag@SiW_{12}O_{40}$ system. As shown in Chapter II, $[SiW_{12}O_{40}]^{4-}$ added directly in the solution, blocks the Ag surface from nitrate ions. Here, we demonstrate that $Ag@SiW_{12}O_{40}$ is a better catalyst than Ag electrode alone where a significant increase of reduction current is observed.

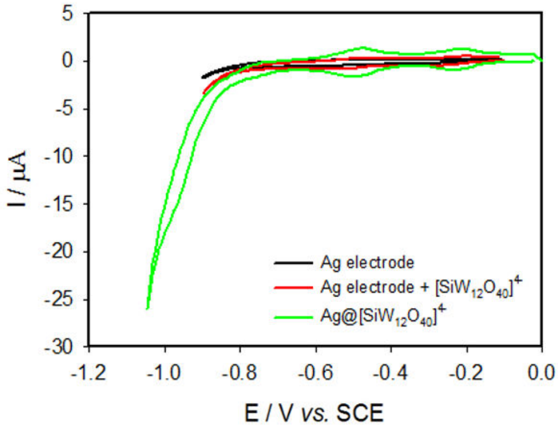

Figure IV.16: Reduction of 10 mmol·L^{-1} $NaNO_3$ on Ag electrode (black line), on the Ag electrode with presence of 0.1 mmol·L^{-1} $[SiW_{12}O_{40}]^{4-}$ (red line) or on $Ag@SiW_{12}O_{40}$ modified GC electrode (green line) in pH 5 solution 1 mol·L^{-1} CH_3COOLi + CH_3COOH, v = 20 mV·s^{-1}.

6. Conclusion

In this chapter, $[SiW_{12}O_{40}]^{4-}$-stabilized AgNPs are prepared by photoreduction method. The formed nanoparticles are stable for several months. When the concentration of $[SiW_{12}O_{40}]^{4-}$ is large enough, the formation of the AgNPs occurs within few minutes yielding spherical nanoparticles with uniform size distribution (ca. 20 nm). The preparation of modified electrodes by simply dropping $Ag@SiW_{12}O_{40}$ on glassy carbon electrode did not allow to obtain stable catalytic layers enabling further electrochemical study. Hence, Nafion was added at the end of deposition to stabilize the catalyst layer.

Electrochemical reduction of NO_x^- (NO_3^- and HNO_2 / NO_2^-) was studied in pH 1 and pH 5 solutions. For nitrite reduction, AgNPs and $[SiW_{12}O_{40}]^{4-}$ catalyst act in tandem in pH 1 solution resulting in a significant improvement of the reduction current. In contrast, at pH 5, nitrite is reduced at almost the same potential than $[SiW_{12}O_{40}]^{4-}$ and $Ag@SiW_{12}O_{40}$. In both conditions, current intensity is higher with $Ag@SiW_{12}O_{40}$ than with $[SiW_{12}O_{40}]^{4-}$ alone. $Ag@SiW_{12}O_{40}$ film keeps its catalytic property at least after 750 cycling. Only $Ag@SiW_{12}O_{40}$ is active for nitrate reduction, showing the presence of the silver is a necessary condition for nitrate reduction. The catalytic current of nitrate reduction is smaller than the one of nitrite reduction. Finally, it is worth mentioning that the catalytic performances towards nitrate reduction obtained with Ag@$SiW_{12}O_{40}$ modified GC electrode are improved compared to the ones obtained with the Ag bulk electrode alone, or in the presence of POM in solution.

However, this work might be completed with further studies:

- The centrifugation of the Ag@$SiW_{12}O_{40}$ solution at high rotation speed might allow to separate the the Ag@$SiW_{12}O_{40}$ nanoparticles from free POM not adsorbed on the silver. Other method will be the purification and the removal of free $[SiW_{12}O_{40}]^{4-}$ by dialysis using dialysis bag.
- Use of carbon nanotubes and/or graphene to support the $[SiW_{12}O_{40}]^{4-}$ or the Ag@$SiW_{12}O_{40}$ nanoparticles in order to improve the distribution of the catalyst on the electrode surface.
- The type of POMs might be varied in order to explore its influence on the Ag@POM NPs properties such as their size.
- The quantity of Nafion added on the catalyst layer in order to immobilize the catalyst might be optimized to improve the catalytic efficiency. Low amount of Nafion might not be sufficient to prevent the detachment of the silver nanoparticles, while excess of Nafion might hinder the access of the NO_x to the catalytic sites.
- The Ag@POM nanoparticles might be encapsulated within an electropolymerized polypyrrole (PPy) or polythiophene thin in order to improve the stability of the catalyst film;
- By associating porphyrin with the formed Ag@POM nanoparticles, the photosensitization of the Ag@POM catalyst might lead to interesting photoelectrocatalytic properties.

References

1. Dima, G. E., De Vooys, A. C. A. & Koper, M. T. M. Electrocatalytic reduction of nitrate at low concentration on coinage and transition-metal electrodes in acid solutions. *J. Electroanal. Chem.* **554–555**, 15–23 (2003).
2. Duca, M., Van Der Klugt, B. & Koper, M. T. M. Electrocatalytic reduction of nitrite on transition and coinage metals. *Electrochim. Acta* **68**, 32–43 (2012).
3. El-nour, K. M. M. A., Al-warthan, A. & Ammar, R. A. A. Synthesis and applications of silver nanoparticles. *Arab. J. Chem.* **3**, 135–140 (2010).
4. Tran, Q. H., Nguyen, V. Q. & Le, A. T. Silver nanoparticles : synthesis , properties , toxicology , applications and perspectives. *Adv. Nat. Sci. Nanosci. Nanotechnol.* **4**, 1–20 (2013).
5. Lu, X., Rycenga, M., Skrabalak, S. E., Wiley, B. & Xia, Y. Chemical synthesis of novel plasmonic nanoparticles. *Annu. Rev. Phys. Chem.* **60**, 167–194 (2009).
6. Gedanken, A. Using sonochemistry for the fabrication of nanomaterials. *Ultrason. Sonochem.* **11**, 47–55 (2004).
7. Tausch-Treml, R., Henglein, A. & Lilie, J. Reactivity of silver atoms in aqueous solution II. a pulse radiolysis study. *Berichte der Bunsengesellschaft für Phys. Chemie* **82**, 1335–1343 (1978).
8. Troupis, A., Hiskia, A. & Papaconstantinou, E. Synthesis of metal nanoparticles by using polyoxometalates as photocatalysts and stabilizers. *Angew. Chem., Int. Ed.* **41**, 1911–1914 (2002).
9. Kishore, P. S., Viswanathan, B. & Varadarajan, T. K. Synthesis and characterization of metal nanoparticle embedded conducting polymer-polyoxometalate composites. *Nanoscale Res. Lett.* **3**, 14–20 (2008).
10. Zhang, G., Keita, B., Dolbecq, A., Mialane, P., Sécheresse, F., Miserque, F. & Nadjo. L. Green chemistry-type one-step synthesis of silver nanostructures based on Mo^V –Mo^{VI} mixed-valence polyoxometalates. *Chem. Mater.* **19**, 5821–5823 (2007).
11. Agnihotri, S., Mukherji, S. & Mukherji, S. Size-controlled silver nanoparticles synthesized over the range 5–100 nm using the same protocol and their antibacterial efficacy. *RSC Adv.* **4**, 3974–3983 (2014).
12. Tang, Y. & Cheng, W. Key parameters governing metallic nanoparticle electrocatalysis. *Nanoscale* **7**, 16151–16164 (2015).
13. Buttry, D. a & Ward, M. D. Measurement of interfacial processes at electrode surfaces with the electrochemical quartz crystal microbalance. *Chem. Rev.* **92,** 1355–1379 (1992).
14. Zhang, X. L., Xing, J. X. & Jin, F. Electrocatalytic study at silver/polypyrrole nanowires composite modified electrodes. *Asian J. Chem.* **22**, 755–760 (2010).
15. Bonyani, M., Mirzaei, A., Leonardi, S. G., Bonavita, A. & Neri, G. Electrochemical properties of Ag@iron oxide nanocomposite for application as nitrate sensor. *Electroanalysis* **27**, 2654–2662 (2015).
16. Fajerwerg, K. Ynam, V., Chaudret, B., Garçon, V., Thouron, D. & Comtat, M.. An original nitrate sensor based on silver nanoparticles electrodeposited on a gold electrode. *Electrochem. commun.* **12**, 1439–1441 (2010).
17. Kim, D., Goldberg, I. B. & Judy, J. W. Chronocoulometric determination of nitrate on silver electrode and sodium hydroxide electrolyte. *Analyst* **132**, 350–357 (2007).
18. Atmeh, M. & Alcock-Earley, B. E. A conducting polymer/Ag nanoparticle composite as a nitrate sensor. *J. Appl. Electrochem.* **41**, 1341–1347 (2011).

Chapter V

Immobilization of polyoxometalates in the metal organic framework (POM@MOF)

Chapter V Immobilization of polyoxometalates in the metal organic framework (POM@MOF)

1 Introduction

POMs have interesting catalytic properties in various applications. However, their disadvantages are low specific surface area, low stability under catalytic conditions and high solubility in aqueous solution. Hence, a stable catalyst which combines the catalytic activity of POMs and advantages of heterogeneous catalysts, which are easier recovery and recycling, attracts a lot of interests. Inserting POMs into the cavities of metal organic frameworks (MOFs)[1] constitutes a strategy to access to POM-based heterogeneous catalysts.[2]

Metal-Organic Frameworks (MOFs) are crystalline porous materials of which the structure is defined by metal ions or metallic clusters that are connected to bi- or multimodal organic linkers with strong interactions.[3] The microporous structure of MOFs provides the surface areas up to 5900 $m^2 \cdot g^{-1}$ and specific pore volumes up to 2 $cm^3 \cdot g^{-1}$ with various pore dimensions and topologies.[4] The presence of strong metal-ligand interactions confers the permanent porosity to the MOFs. It is possible to remove the solvent molecules, which is required in order to liberate the inner space of the material, without destroying the structure.[3] The feature of MOFs, such as their pore sizes, shapes, dimensionalities and chemical environment can be finely controlled for proposes of the specific applications.[5] Hence, the use of MOFs as a support of POM is considered as an interesting strategy to develop their applications in catalysis.

Several advantages can be obtained by inserting POM into the cavities of MOF: i) improve of the specific surface area of POM; ii) uniform dispersion of POM units in a MOF skeleton; iii) introduce magnetic POM into MOF can lead to the application as molecular quantum spintronic devices; iv) allow the selective catalysis as a function of size and easy recycling after catalytic reactions; v) easily recycling after catalytic reactions.[3,5,6]

POM@MOF materials can be prepared by different methods:

- MOFs are directly impregnated into POMs solution. However, this method is difficult due to the distinction between POMs and MOFs in size, charge, structural symmetry, solubility and pH stability. Only few MOFs such as MIL-101 (Material of Institut Lavoisier)[4], HKUST-1 (Hong Kong University of Science and Technology)[7] and NENU-11 (NENU: Northeast Normal University)[8] have been successfully loaded with POMs. The structures of these MOFs are shown in Fig. V.1.

- POMs are used as nodes or linkers which is connected to the metal-organic coordination moieties in order to form POM-based MOFs.[9] The disadvantage of this method is the occupation of oxygen atoms at POM surface by the metal-organic fragments, which might limit the catalytic properties of the POM units.

- POMs are used as templates, metal ions as nodes and the organic functional groups as linkers to compose POM@MOF hybrid compounds.[10] The disadvantage of these hybrid compounds is the cavity of MOFs might be fully occupied by POM units.

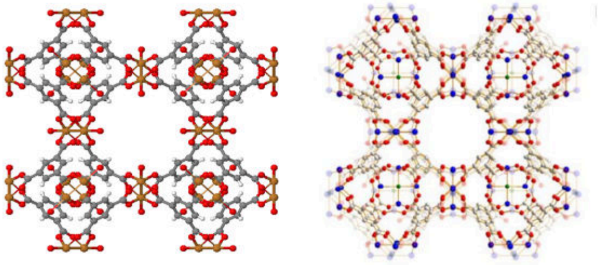

HKUST-1 NENU-11

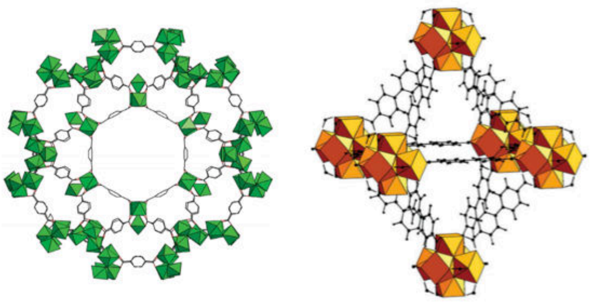

MIL-101 UiO-67

Figure V.1: Structures of different MOFs: HKUST-1, NENU-11, MIL-101 and UiO-67.(The structure of HKUST-1 is reprinted from reference 5 with the permission from John Wiley and Sons; NENU-11 is reprinted with the permission from reference 11, Copyright (2017) American Chemical Society; MIL-101 is reprinted from reference 12 with the permission from Royal Society of Chemistry; UiO-67 is reprinted from reference 13).

Hence, an adequate method to form POM@MOF materials while conserving the properties of POMs remains a challenge.

In this chapter, two systems of POM@MOF have been investigated. Firstly, three different POMs $[PW_{12}O_{40}]^{3-}$, $[PW_{11}O_{39}]^{7-}$ and $[P_2W_{18}O_{62}]^{6-}$ have been inserted to UiO-67 MOF (UiO for University of Oslo)[14]. The electrochemical properties of POM@MOF have been studied and compared to the corresponding POM. In the second part, POM $[Fe_4(FeW_9O_{39})_2(H_2O)_2]^{10-}$ (Fe_6W_{18}) has been inserted into three different supports: gelatin, MOFs MIL-101(Cr) and MOF UiO-67, the influence of these three supports on electrochemical properties of POM has been studied. The structures of these compounds will be presented in the following sections.

2 System of immobilized POMs into UiO-67

2.1 Synthesis method

The compounds have been synthetized by Prof. Pierre Mialane and DR. Anne Dolbecq, Institut Lavoisier, UMR 8180, Université de Versailles Saint-Quentin en Yvelines. A direct synthetic method was proposed for the first time:[13]

$ZrCl_4$ (116 mg, 0.5 mmol·L^{-1}), biphenyl-dicarboxylic acid (121 mg, 0.5 mmol·L^{-1}), benzoic acid (1.83 mg, 15 mmol·L^{-1}, 30 equivalents) and 1/6 equivalent of POM (0.0833 mmol·L^{-1} $[PW_{12}O_{40}]^{3-}$ (PW_{12}), $[PW_{11}O_{39}]^{7-}$ (PW_{11}) or $[P_2W_{18}O_{62}]^{6-}$ (P_2W_{18})) were dissolved in 10 mL dimethyformamide (DMF) in a polytetrafluoroethylene-lined stainless steel containers. Hydrochloride acid 37% (83 μL) was added into the solution. After a short stirring, the mixture was heating to 120 °C over one hour and kept at 120 °C for 24 hours. After that, the solution was cool down to room temperature. It should be noted that the monolaculary PW_{11} would react with Zr^{IV} ions and form $[Zr^{IV}(H_2O)_n(PW_{11}O_{39})]^{3-}$ (n = 2, 3) complex. The products obtained are insoluble microcrystalline materials, PW_{12}@UiO-67, $PW_{11}Zr$@UiO-67, P_2W_{18}@UiO-67, which were filtered and washed with DMF and acetone.

Prepared samples have characterized by Infrared spectra, elemental analysis, and solid nuclear magnetic resonance (NMR). These measurements confirmed that the introduction of POM into the synthetic medium does not disturb the formation of the MOF. N_2 sorption isotherms shows that the total pore volumes decrease from UiO-67 to POM@UiO-67 indicating the POMs are encapsulated in the cavities. However, a significant porosity is leaving for accessing the nitrogen. More information about the characterizations can be found in reference 13 (see Appendix).

2.2 Structure of POM@UiO-67

UiO is build up from $\{Zr^{IV}_6O_4(OH)_4\}$ oxocluster nodes and linear dicarboxlate linkers. In UiO-67, the inorganic octahedral Zr_6 units are connected to 12 other inorganic subunits through biphenyl dicarboxylate ligands which lead to a face-centred cubic (fcc) structure (a = 27.1 Å). Two types of cages are found in this MOF: super-tetrahedral (Ø ~ 11.5 Å) and super-octahedral (Ø ~ 18 Å) which is accessible through microporous triangle windows (Ø ~ 8 Å). Each super-octahedral cavity can encapsulate one Keggin- or Dawson-type POM.

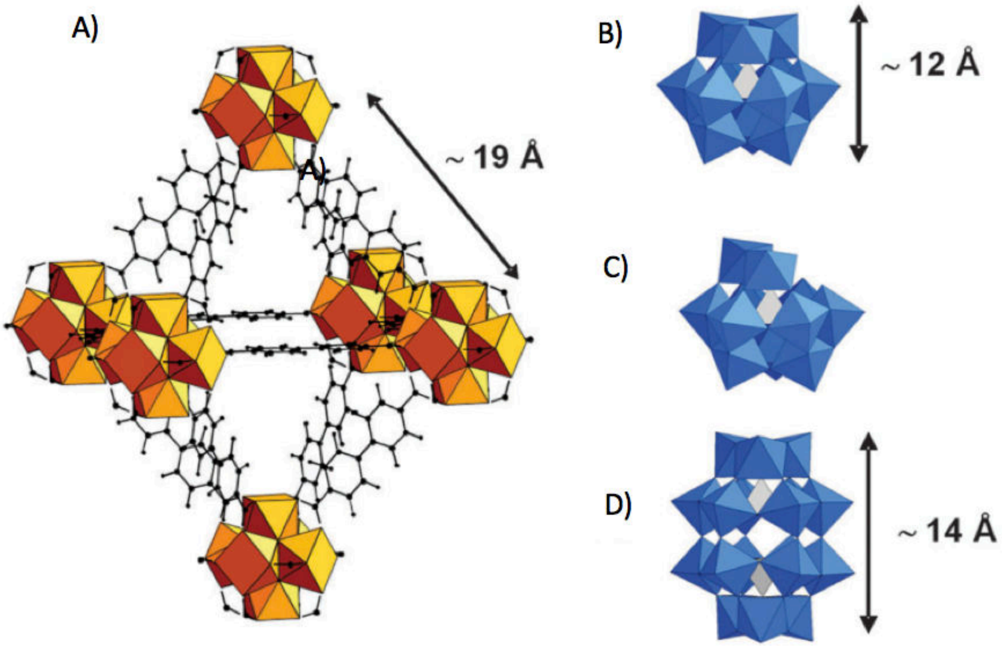

Figure V.2: Polyhedral representations of the octahedral cages of (A) UiO-67, (B) $[PW_{12}O_{40}]^{3-}$ (PW_{12}), (C) $[PW_{11}O_{39}]^{7-}$ (PW_{11}) and (D) $[P_2W_{18}O_{62}]^{6-}$ (P_2W_{18}) (Reprinted from reference 13).

2.3 Electrochemical properties

The electrochemical measurements were carried out at room temperature using a conventional three electrode set-up in pH 2.5 0.5 mol·L^{-1} Na_2SO_4 + H_2SO_4 buffer solution. For each POM, three systems have been investigated: POM alone, POM@UiO-67 and POM+UiO-67 by mechanical mixing method. The powder sample was immobilized on the surface of a basal plane of the Pyrolytic Graphite (PG) electrode.

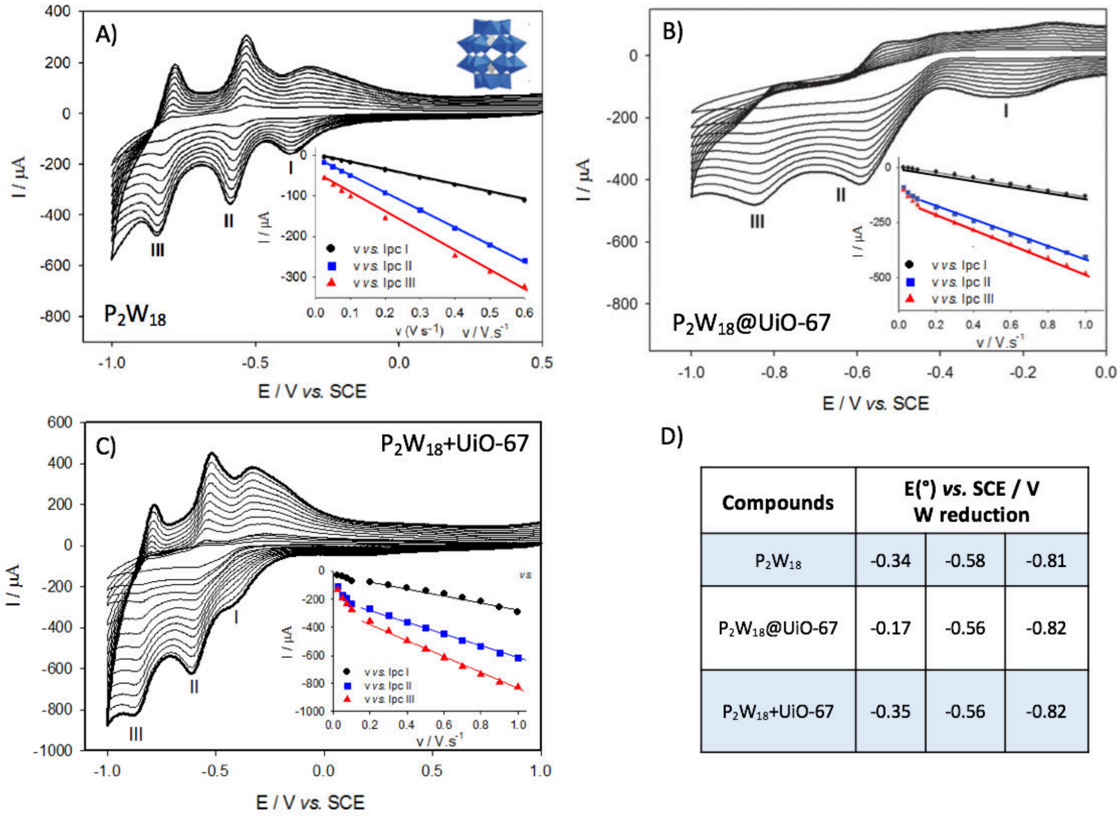

Compounds	E(°) vs. SCE / V W reduction		
P_2W_{18}	-0.34	-0.58	-0.81
P_2W_{18}@UiO-67	-0.17	-0.56	-0.82
P_2W_{18}+UiO-67	-0.35	-0.56	-0.82

Figure V.3: Cyclic voltammograms of (A) P_2W_{18}, (B) P_2W_{18}@UiO-67 and (C) P_2W_{18}+UiO-67 (mechanical mixing) immobilized on a PG electrode at different scan rate from 0.025 to 1.000 $V{\cdot}s^{-1}$. (Inset) plots of I_{pc} vs. v for reduction peaks. D) Reduction potentials of each composite immobilized on PG electrode. Buffer Solution: pH 2.5 0.5 $mol{\cdot}L^{-1}$ Na_2SO_4 + H_2SO_4.

$[P_2W_{18}O_{62}]^{6-}$ (P_2W_{18}) immobilized on PG electrode exhibits three successive waves at -0.34 V, -0.58 V and -0.81 V *vs.* SCE corresponding to the reductions of W^{VI} to W^{V} (Fig. V.3A). A simple mixture of P_2W_{18} with UiO-67 (mechanical mixing) did not lead to an evident change in voltammograms. Three reduction waves were found at similar potentials (Figs. V.3C-D). In the case of P_2W_{18}@UiO-67, a shift of 174 mV to more positive potential is observed at the first reduction wave while the last two waves are found at similar potentials as two other composites. Furthermore, the peak current intensities are proportional to the scan rate in the range of 0.1 – 1 $V{\cdot}s^{-1}$, as expect for the surface confined redox process. This behavior is in agreement with the immobilization of the POMs inside the cavities of the MOF. Similar observations are obtained with PW_{12} and PW_{12}@UiO-67 (see Appendix, Fig. S9). These results indicate that the saturated POMs are encapsulated inside the cages preserve their electrochemical properties.

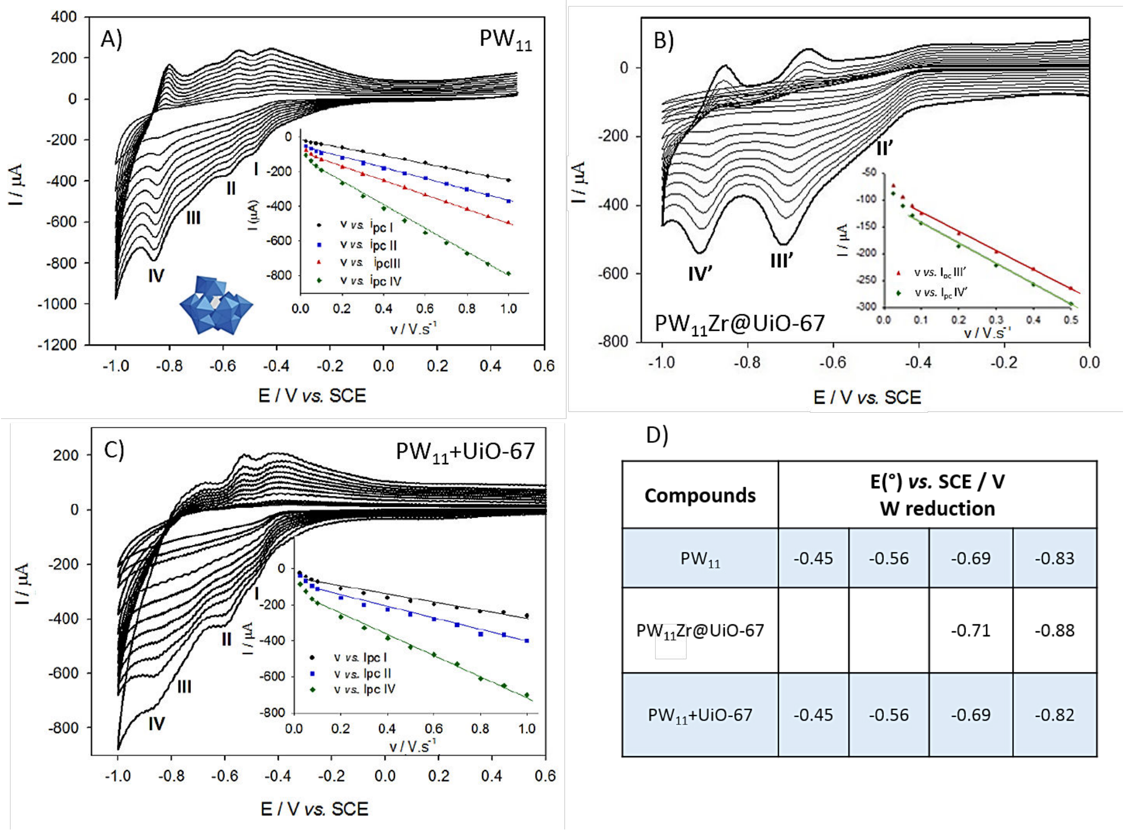

Compounds	E(°) *vs.* SCE / V W reduction			
PW_{11}	-0.45	-0.56	-0.69	-0.83
$PW_{11}Zr$@UiO-67			-0.71	-0.88
PW_{11}+UiO-67	-0.45	-0.56	-0.69	-0.82

Figure V.4: Cyclic voltammograms of (A) PW_{11}, (B) $PW_{11}Zr$@UiO-67 and (C) PW_{11}+UiO-67 (mechanical mixing) immobilized on a PG electrode at different scan rate from 0.025 to 1.000 $V{\cdot}s^{-1}$. (Inset) plots of I_{pc} vs. v for reduction peaks. D) Reduction potentials of each composite immobilized on PG electrode. Buffer Solution: pH 2.5 0.5 $mol{\cdot}L^{-1}$ Na_2SO_4 + H_2SO_4.

In the case of $[PW_{11}O_{39}]^{7-}$ (PW_{11}), four reduction waves are found at -0.45 V, -0.56 V, -0.69 V and -0.83 V *vs.* SCE corresponding to the W^{VI} reductions. As for the P_2W_{18}, mechanical mixed PW_{11} and UiO-67 did not change the electrochemical responds of POM. In contrast, the two first reductions waves are not observed in the presence of $PW_{11}Zr$@UiO-67, while only one wave around -0.47 V can be seen but difficult to determine the exact potential. After that, two reduction waves are obtained at -0.71 V and -0.88 V (waves III' and IV'). This difference can be attributed to the complexation of monolacunary PW_{11} with Zr^{IV} presents inside the UiO-67 MOF and the formation of $PW_{11}Zr$ complex encapsulated in UiO-67. Again, the peak current intensities vary linearly with the scan rate which indicate the $PW_{11}Zr$ is immobilized inside the MOF.

3 System of Fe_6W_{18} encapsulated in MIL-101(Cr) or in UiO-67

3.1 Synthesis method

These two POM@MOF are synthesized by Professor Pierre Mialane and DR. Anne Dolbecq, Institut Lavoisier, UMR 8180, Université de Versailles Saint-Quentin en Yvelines.[15]

$[Zr_6^{IV}O_4(OH)_4(C_{14}H_8O_4)_{5.5}][Fe_4^{III}(FeW_9O_{39})_2(H_2O)_2]_{0.1}(DMF)_{1.8}\cdot 17H_2O$ (**Fe_6W_{18}@UiO-67**) is prepared through the same synthesis approach described in the part 2.1. A mixture of the dioctadecyldimethylammonium ($DODA^+$, $(CH_3(CH_2)_{17})_2(CH_3)_2N^+$) salt of Fe_6W_{18}, zirconium tetrachloride, benzoic acid used as crystallization modular, concentrated HCl and biphenyl-4,4'-dicarboxylic acid was heated at 120 °C for 24 hours in dimethylformamide (DMF). The obtained solid was cool down to room temperature and then filter and washed with DMF, chloroform and dry acetone.

$[Cr^{III}_3(H_2O)_3O(O_2CC_6H_4CO_2)_3][(FeW_9O_{39})_2Fe_4(H_2O)_2]_{0.083}(NO_3)_{0.17}\cdot 30H_2O$ **(Fe_6W_{18}@MIL101-(Cr))** is prepared by impregnation method at room temperature.[16] $Na_6(TMA)_4[Fe_6W_{18}]\cdot 45H_2O$ and MIL-101(Cr) were mixed in water and then stirred for 24 hours at room temperature. The solid was collected by centrifugation, washed with water, ethanol and diethylether and then dried at 120°C for 24 hours.

Fe_6W_{18}@Gelatin is prepared by the complex coacervation-based procedure. Two solutions, one $Na_6(TMA)_4[Fe_6W_{18}].45\ H_2O$ (0.45g, 2.50 $mmol\cdot L^{-1}$) solution and one gelatin (10 wt%, 2.50 $mmol\cdot L^{-1}$ in water) solution, were prepared and their pH is adjusted to 3 with 1 $mol\cdot L^{-1}$ HCl solution. The solutions were heated to 40 °C and then 2.5 mL gelatin solution was added in to POM solution. An orange gel was quickly formed and was removed from the solution. The gel was dried for 2 hours and then dropped into liquid nitrogen to obtain the solid product.

The samples are characterized by IR spectra, X-ray, N_2 adsorption/desorption isotherms. The details can be found in reference 15. These characterizations indicate that POM are incorporate within the cavities and not adsorbed at the surface of the MOF and MOF preserve its integrity structure with the presence of POM.

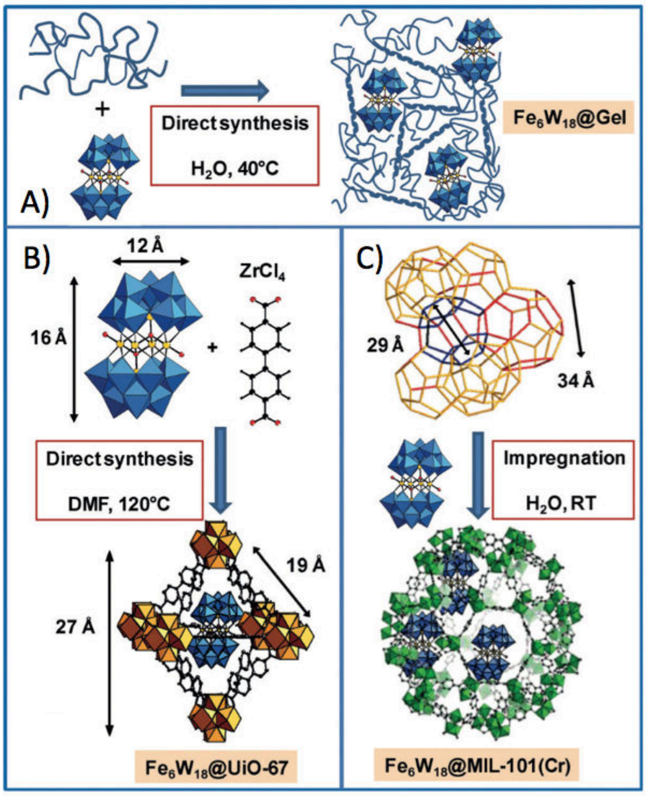

Figure V.5. Representations of POM $[Fe_4(FeW_9O_{39})_2(H_2O)_2]^{10-}$ *(*Fe_6W_{18}*), UiO-67, MIL-101(Cr), gelatin and the synthetic routes to the three composite materials A)* Fe_6W_{18}*@Gel, (B)* Fe_6W_{18}*@UiO-67 and C)* Fe_6W_{18}*@MIL-101(Cr). (Reprinted from reference 15 with the permission from John Wiley and Sons).*

3.2 Structure

Fe_6W_{18}@Gelatin: Fe_6W_{18} POMs are limited in a gelatin network consisted of coils and triple helices. The orange color of Fe_6W_{18}@Gelatin solid demonstrated the presence of the Fe_6W_{18} POMs. POMs are isolated by the long polymer chains of gelatin due to the electrostatic interactions.

Fe_6W_{18}@UiO-67: two types of cages were observed in the structure supertetrahedral (Ø ~ 11.5 Å) and superoctahedral (Ø ~ 18 Å) connected by triangular windows (Ø = 8 Å) as present in preview part. Only the octahedral cages can incorporate one Fe_6W_{18} unit for each, the tetrahedral cages are too small to receive a Fe_6W_{18} unit. The ratio of POM/UiO-67 is equal to 1:10.

Fe_6W_{18}@MIL-101(Cr): MIL-101(Cr) is built up from trimer of Cr^{III} octahedral linked by terephthalate anions, two types of mesocage (Ø = 29 and 34 Å) accessible through micropore windows ((Ø = 11 and 16 Å). The Fe_6W_{18} can be only incorporate in the largest cavities while the window for the smaller cages are too small to allow the penetration of such POM. A strong electrostatic POM-matrix interaction is obtained. The ratio of POM / MIL-101(Cr) is 1:12.

3.3 Electrochemical properties

The electrochemical property of Fe_6W_{18} POM is firstly studied in a pH 2.5 0.5 mol·L^{-1} Na_2SO_4 + H_2SO_4 (see. Fig. V.6). Six reduction waves were observed at -0.04 V, -0.18 V, -0.38 V, -0.53 V, -0.62 V and -0.68 V *vs.* SCE. The first three waves (a, b and c) correspond to the multi-step reductions of Fe^{III} centers ($Fe^{III/II}$ redox couple) and the last three waves (I, II and III) are attributed to the $W^{VI/V}$ redox couple, as reported in preview work.[17] The current intensities of peak c and peak I, for instance, are proportional to the square root of the scan rate which indicate a diffusion-controlled process of Fe_6W_{18} POM.

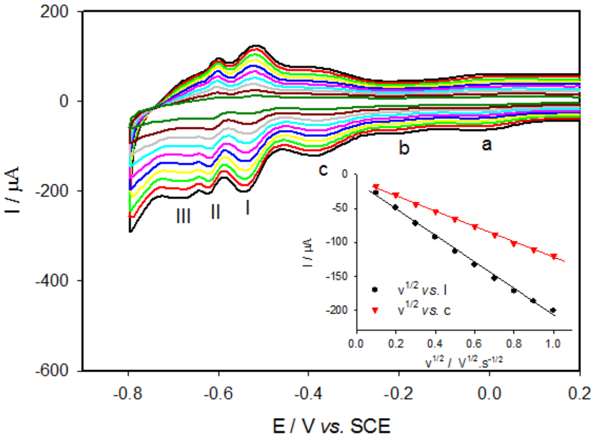

Figure V.6: Cyclic voltammograms of Fe_6W_{18} in pH 2.5 0.5 mol·L^{-1} Na_2SO_4 + H_2SO_4 solution at different scan rates from 0.1 to 1.0 V·s^{-1}. (Inset): plots of I_{pc} vs. $v^{1/2}$ for peak c ($Fe^{III/II}$ redox couple) and peak I ($W^{VI/V}$ redox couple).

The solid samples Fe_6W_{18}@MIL-101, Fe_6W_{18}@UiO-67 and Fe_6W_{18}@Gelatin were immobilized on a PG electrode surface, the measurement is carried out in a pH 2.5 0.5 mol·L^{-1} Na_2SO_4 + H_2SO_4 solution. It has to note that no electrochemical signal was detected for Fe_6W_{18}@Gelatin, probably due to the insulating character of gelatin.

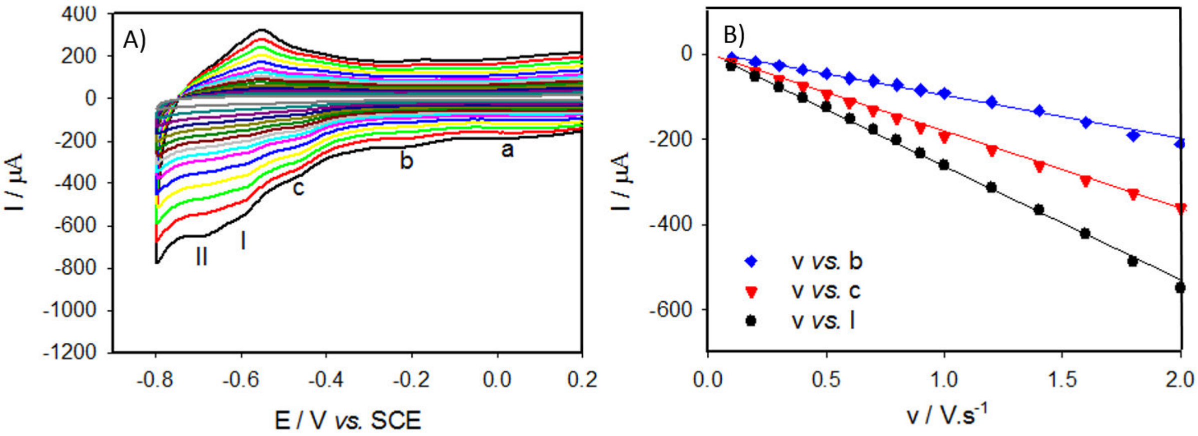

Figure V.7: Cyclic voltammograms of Fe_6W_{18}@UiO-67 immobilized on PG electrode in pH 2.5 0.5 mol·L^{-1} Na_2SO_4 + H_2SO_4 solution at different scan rates from 0.1 to 2.0 V·s^{-1}. (Inset): plots of I_{pc} vs. v for peaks b, c ($Fe^{III/II}$ redox couple) and peak I ($W^{VI/V}$ redox couple).

For Fe_6W_{18}@UiO-67 immobilized on PG electrode surface, cyclic voltammograms exhibit five successive waves at -0.02 V, -0.18 V, -0.44 V, -0.57 V and -0.65 V *vs.* SCE. The first three reduction waves (a, b and c for $Fe^{III/II}$ redox couple) are remained while for $W^{VI/V}$ reduction, two reduction waves are observed (I and II). The peak current intensities vary linearly with the scan rate in the range of 0.1 – 2.0 V·s^{-1}, which confirm the surface-confined redox process. The peak-to-peak separations (△E_p) calculated are between 0.00 and 0.02 V and the ratio i_{pa}/i_{pc} (i_{pa} *and* i_{pc} indicate anodic and cathodic peak current, respectively) is close to one. Consequently, this behavior is in agreement with the immobilization of the Fe_6W_{18} inside the cavities of the MOF.

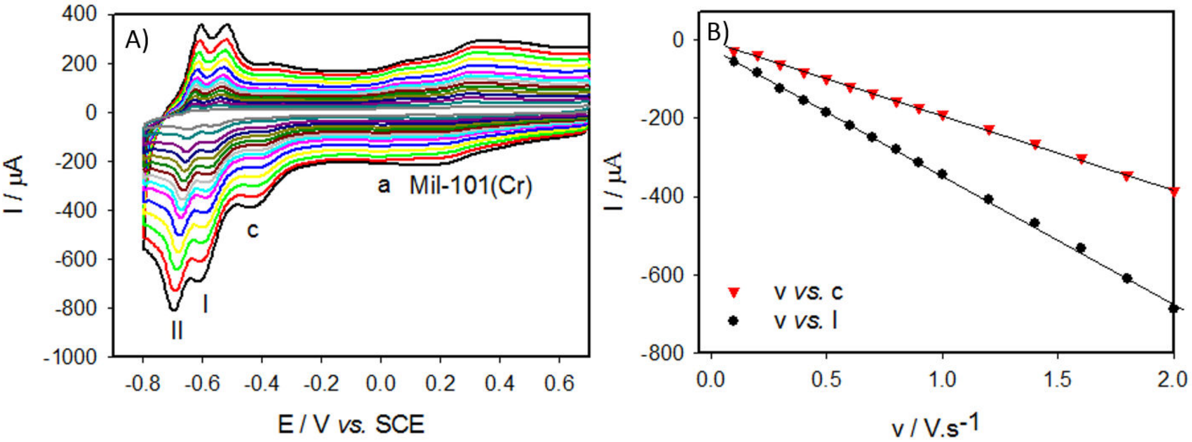

Figure V.8: Cyclic voltammograms of Fe_6W_{18}@MIL-101(Cr) immobilized on PG electrode in pH 2.5 0.5 mol·L^{-1} Na_2SO_4 + H_2SO_4 solution at different scan rates from 0.1 to 2.0 V·s^{-1}. (Inset): plots of I_{pc} vs. v for peak c ($Fe^{III/II}$ redox couple) and peak I ($W^{VI/V}$ redox couple).

In the case of Fe_6W_{18}@MIL-101(Cr) immobilized on PG electrode, two reduction waves of $W^{VI/V}$ are observed at -0.56 V and -0.65 V *vs.* SCE, similar to Fe_6W_{18}@UiO-67 (-0.57 V and -0.65 V). The reduction waves are better defined for Fe_6W_{18}@MIL-101(Cr) than for Fe_6W_{18}@UiO-67. For $Fe^{III/II}$ redox couple, the waves a and c retain (at -0.02 and -0.38 V respectively). It has to note that the second step of Fe reduction (wave b) is not detected which is due to the weak electrochemical signal. Compared to the Fe_6W_{18} POM, one additional well-defined pair of peaks at E_{pa} = 0.25 V and E_{pc} = 0.27 V is detected and attributed to the $Cr^{III/II}$ redox process, corresponding to the reduction of the MIL-101(Cr), in agreement to the preview work.[18]

The reduction potential of Fe_6W_{18} in solution, Fe_6W_{18}@MIL-101, Fe_6W_{18}@UiO-67 and Fe_6W_{18}@Gelatin immobilized at a PG electrode are summarized in Table V.1. The Fe_6W_{18} immobilized on PG electrode surface have also been tested. Unfortunately, the immobilized Fe_6W_{18} is not stable enough at electrode surface for the electrochemical measurement due to important desorption.

Compounds	**Fe reduction E(°) *vs.* SCE / V**			**W reduction E(°) *vs.* SCE / V**		
Fe_6W_{18}	-0.04	-0.17	-0.38	-0.53	-0.62	-0.68
Fe_6W_{18}@MIL-101(Cr)	-0.02	-[b]	-0.38	-0.58	-0.65	-[b]
Fe_6W_{18}@UiO-67	-0.02	-0.18	-0.44	-0.57	-0.65	-[b]
Fe_6W_{18}@Gelatin[a]	-	-	-	-	-	-

[a]: no signal measured. [b]: wave not observed

Table V.1: Reduction potentials of Fe_6W_{18} in solution, Fe_6W_{18}@MIL-101, Fe_6W_{18}@UiO-67 and Fe_6W_{18}@Gelatin immobilized at a PG electrode surface. Buffer solution: pH 2.5 0.5 mol·L^{-1} Na_2SO_4 + H_2SO_4, v=10 mV·s^{-1}.

3.4 Electrocatalytic properties toward nitrite reduction

A preliminary study of electrocatalysis of nitrite by immobilizing Fe_6W_{18}@MIL-101(Cr) or Fe_6W_{18}@UiO-67 on PG electrode is shown in Fig. V.9. The reduction current starts to increase at -0.20 V *vs.* SCE with both of these two POM@MOF and this potential corresponds to the second step of Fe^{III} reduction ($Fe^{III/II}$ redox couple). An enhancement of catalytic current is observed after -0.40 V *vs.* SCE, after the third reduction step of $Fe^{III/II}$ couple. However, the stability of this heterogeneous catalyst on electrode surface during the catalysis reduction remain as a challenge. Adding a layer of Nafion to the surface of catalyst could be contemplated.

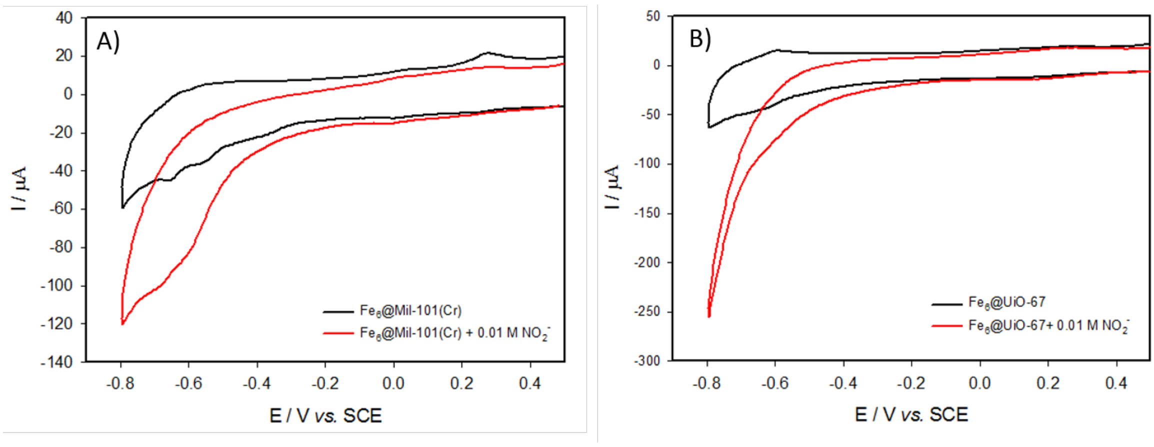

Figure V.9: reduction of 0.01 mol·L^{-1} $NaNO_2$ in the presence of (A) Fe_6W_{18}@MIL-101(Cr) or (B) Fe_6W_{18}@UiO-67 immobilized on PG electrode. Buffer solution: pH 2.5 0.5 mol·L^{-1} $Na_2SO_4 + H_2SO_4$, scan rate: v=10 mV·s^{-1}.

4 Conclusion

In this chapter, we have studied the electrochemical properties of POM encapsulated in the cavities of MOF. In the first system, insertion of different type of POMs into UiO-67 MOF, cyclic voltammetry studies have confirmed the direct formation of $PW_{11}Zr$ during the synthetic process and demonstrated that the saturated POMs are encapsulated inside the cages preserve their electrochemical properties. In the second part, we have shown that the Fe-substituted POM retain its electrochemical signals for $Fe^{III/II}$ redox couple and $W^{VI/V}$ redox couple after loading in the structure of two MOF. However, no electrocatalytic signal is detected for POM@Gelatin due to the insulating character of gelatin. We have also shown that Fe-substituted POM encapsulated in MOF is active for nitrite reduction, reveals a compelling direction to form POM-based heterogeneous catalysis toward NO_x reduction.

Still, significant challenges remain:

- Better matching of POMs with MOFs in terms of sizes, shapes, charges, etc., especially for specific catalysis application.
- Amelioration of electrocatalytic reaction's conditions such as pH, buffer solution, scan rate, according to the choice of MOF as well as POM.
- Better stabilizing the catalyst film on the electrode surface.
- Formation of a stable POM@MOF system for electrocatalytic reduction of nitrite and nitrate.

References

1. Wang, B. Special Issue of 'metal-organic frameworks'. *Chem. Soc. Rev.* **43**, 135 (2014).
2. Juan-Alcaniz, J., Gascon, J. & Kapteijn, F. Metal–organic frameworks as scaffolds for the encapsulation of active species: state of the art and future perspectives. *J. Mater. Chem.* **22**, 10102–10118 (2012).
3. Corma, A., Garcia, H. & Llabres, i. X. F. X. Engineering metal organic frameworks for heterogeneous catalysis. *Chem. Rev.* **110**, 4606–4655 (2010).
4. Férey, G. *et al.* A chromium terephthalate-based solid with unusually large pore volumes and surface area. *Science* **309**, 2040–2042 (2005).
5. Farrusseng, D., Aguado, S. & Pinel, C. Metal-organic frameworks: opportunities for catalysis. *Angew. Chemie - Int. Ed.* **48**, 7502–7513 (2009).
6. Hao, X.-L., Ma, Y.-Y., Zang, H.-Y., Wang, Y.-H., Li, Y.-G. & Wang, E.-B. A Polyoxometalate encapsulating cationic metal-organic framework as a heterogeneous catalyst for desulfurization. *Chem. - A Eur. J.* **21**, 3778–3784 (2015).
7. Liu, S., Sun, C., Ren, G., Wei, F., Chen, Y. & Su, Z. A sodalite-Type porous metal-organic framework with polyoxometalate templates adsorption and decomposition of dimethyl methylphosphophate. *J Am Chem Soc* **133**, 4178–4181 (2011).
8. Sun, C.-Y., Liu, S.-X., Liang, D.-D., Shao, K.-Z., Re, Y.-H. & Su, Z.-M. Highly stable catalysts based on a microporous metal organic framework and polyoxometalates. *J Am Chem Soc* **131**, 1883–1888 (2009).
9. Nohra, B., El Moll, H., Rodriguez, A., Mialane, P., Marrot, J., Mellot-Draznieks, C., O'Keeffe, M., Ngo Biboum, R., Lemaire, J., Keita, B., Nadjo, L. & Dolbecq, A. Polyoxometalate-based metal organic frameworks (POMOFs): structural trends, energetics, and high electrocatalytic efficiency for hydrogen evolution reaction. *J. Am. Chem. Soc.* **133**, 13363–13374 (2011).
10. Wei, M., He, C., Hua, W., Duan, C., Li, S., & Meng, Q. A large protonated water cluster in a 3D Metal - organic framework. *J Am Chem Soc* **128**, 13318–13319 (2006).
11. Ma, F., Liu, S., Sun, C., Liang, D., Ren, G, Wei, F., Chen, Y. & Su, Z. A porous sodalite-type metal-organic frameworks with polyoxometalate templates : adsorption and decomposition of dimethyl methylphosphonate. *J Am Chem Soc* **133**, 4178–4187 (2011).
12. Lo, S.-H.*, Raja, D.-S., Chen, C.-W., Kang, Y.-H., Chen, J.-J. & Lin, C-H.* Waste polyethylene terephthalate (PET) material as sustainable precursor for the synthesis of nanoporous MOFs, MIL-47, MIL-53(Cr, Al, Ga) and MIL-101(Cr). *Dalt. Trans.* **45**, 9565–9573 (2016).
13. Salomon, W. Roch-Marchal, C., Mialane, P., Rouschmeyer, P., Serre, C., Haouas, M., Taulelle, F., Yang, S., Ruhlmann L. & Dolbecq, A. Immobilization of polyoxometalates in the Zr-based metal organic framework UiO-67. *Chem. Commun.* **51**, 2972–2975 (2015).
14. Vermoortele, F., Ameloot, R., Vimont, A., Serre, C. & De Vos, D. An amino-modified Zr-terephthalate metal–organic framework as an acid–base catalyst for cross-aldol condensationw. *Chem. Commun* **47**, 1521–1523 (2011).
15. Salomon, W., Lan, Y. L., Rerière, E., Yang, S., Roch-Marchal, C., Dolbecq, A., Simonnet-Jégat, C., Steunou, N., Leclerc-Laronze, N., Ruhlmann, L., Mallah, T., Wernsdorfer, W. & Mialane, P. Single-molecule magnet behavior of individual polyoxometalate molecules incorporated within biopolymer or metal-organic framework matrices. *Chem. - A Eur. J.* **22**, 6564–6574 (2016).
16. Bromberg, L., Diao, Y., Wu, H., Speakman, S. a. & Hatton, T. A. chromium(III) terephthalate metal organic framework (MIL-101): HF-free synthesis, structure, polyxometalate composites and catalytic properties. *Chem. Mater.* **24**, 1664–1675 (2012).
17. Giusti, A., Charron, G., Mazerat, S., Compain, J. D., Mialane. P., Dolbecq. A., Rivière., E., Wernsdorfer, W., Bibouni, R. N., Keita, B., Nadjo, L., Filoramo, A., Bourgoin, J.-P. & Mallah, T. Magnetic bistability of individual single-molecule magnets grafted on single-wall carbon nanotubes. *Angew. Chemie - Int. Ed.* **48**, 4949–4952 (2009).
18. Fernandes, D. M., Barbosa, A. D. S., Balula, S. S., Cunha-silva, L. & Freire, C. Novel composite material polyoxovanadate@MIL-101(Cr): A highly efficient electrocatalyst for ascorbic acid oxidation. *ACS Appl. Mater. Interfaces* **5**, 13382–13390 (2013).

General Conclusion

General Conclusion

The objective of the present thesis was to investigate the electrocatalytic performances of hybrid materials associating polyoxometalates (POMs) with Cu or Ag nanoparticles for the nitrate and nitrite reductions, and try to find out the factors which influence the catalytic reduction.

First, we have investigated the nitrite and nitrate reduction in the presence of POM $[SiW_{12}O_{40}]^{4-}$ on silver or copper bulk electrodes in Chapter II. In agreement with the literature, Cu and Ag bulk electrodes alone are active toward nitrite reduction in both pH 1 and pH 5 solutions, while the glassy carbon (GC) electrode was found to be rather inactive. The catalytic properties of Cu or Ag bulk electrodes in the presence of this POM have been investigated in aqueous solutions of various pH and compared to the ones of the Cu and Ag electrodes in the absence of POM as well as the ones of the POM on glassy carbon electrode. Based on electrochemical studied, POM $[SiW_{12}O_{40}]^{4-}$ are adsorbed on Cu and Ag surfaces even for as low as potential -0.50 V *vs.* SCE in pH 1 solution and in pH 5 solution. In contrast, POMs redox properties are diffusion controlled when using a GC electrode. Hence the interactions between POM and electrode surfaces affect its electrochemical properties. In the presence of POM in solution, the catalytic onset potential is positively shifted and the catalytic current increases especially at potentials that POM reduced. Interestingly, a synergy between Cu and POM is observed in the potential range between -0.40 V and -0.57 V *vs.* SCE in pH 1 solution. In the case of nitrate reduction, POM $[SiW_{12}O_{40}]^{4-}$ is not active with a glassy carbon working electrode but an enhanced activity is observed on Cu and Ag electrodes. As POM shows a positive effect for the NO_x^- (NO_3^- and NO_2^-/HNO_2) reduction on Cu and Ag bulk electrodes, we have investigated the NO_x reduction in the presence of POM-protected Cu nanoparticles or POM-protected Ag nanoparticles.

In Chapter III, two groups of compounds have been examined. The first group is three Cu-substituted POMs (CuPOMs) **$P_2W_{15}Cu_4$**, **SiW_9Cu_4**, **$Sb_2W_{18}Cu_3$**. In the second group, an alendronate copper complex (CuAle) $[Cu_6(Ale)_4(H_2O)_4]^{4-}$ has been grafted to the above compounds to form CuPOM/Ale **P_2W_{15}CuAle**, **SiW_9CuAle** and **SbW_9CuAle** respectively. For these six compounds, all the Cu^{II} ions in the structure were reduced to form Cu^0 nanoparticles during the reduction of CuPOMs, the POMs species being probably adsorbed at the copper nanoparticles' surface. The size and density of Cu^0 nanoparticles deposited on the glassy carbon electrode increase with the deposition time. The mass of CuPOM electrodeposited has been calculated based on EQCM measurements and was found to increase with the number of Cu ions in the structure. The electrocatalytic reductions of NO_x have been studied first with CuPOMs. An efficient catalysis toward nitrite reduction was observed for all the samples and the catalytic performance of CuPOMs species were found to be better than a simple Cu salt ($CuSO_4$) or Cu electrode alone. Two catalytic waves were observed during the electrocatalytic reduction of nitrite ions, the first one was found at the potential of Cu^{II} reduction and the second one was at the W^{VI} reduction. In the case of nitrate, only one catalytic reduction wave was observed after the formation of Cu^0 nanoparticles and after the reduction of W^{VI}, which indicates the nitrate catalysis is due to the collaboration between the Cu nanoparticles and POM units. Interestingly, no catalytic performance was observed in the presence of **$Sb_2W_{18}Cu_3$**, even though the Cu nanoparticles were still formed during the reduction. This absence of catalytic current was attributed to the blocking of the Cu surface by the adsorbed POM. Hence, the choice of POM is very important for nitrate reduction.

After grafting copper alendronate CuAle complex to the presented CuPOMs, the catalytic properties were ameliorated in both pH 1 and pH 5 solutions. A decrease of the overpotential and an increase of catalytic current were observed showing CuAle complex acted as a cofactor during the catalysis. This improvement might be attributes to the better stabilization of Cu^I species in the presence of Ale ligand and also to the earlier formation of the Cu nanoparticles.

Among these six compounds, **$P_2W_{15}CuAle$** has been demonstrated as the most active catalyst towards nitrate and nitrite reduction. We have also investigated the influence of pH of the solution with this compound and pH 2 being the best for nitrite reduction. A nitrate sensor can be build using **$P_2W_{15}CuAle$** as electrocatalyst, a linear dependence range of 0 to 20 $mmol \cdot L^{-1}$ in pH 1 solution and a narrower range of 0 to 10 $mmol \cdot L^{-1}$ was found at pH 5.

In Chapter IV, Ag nanoparticles prepared by photocatalytic reduction of silver ion in catalysed by the POMs $[SiW_{12}O_{40}]^{4-}$ under illumination were immobilized on GC electrode. By adjusting the concentration of POMs, spherical silver nanoparticles with uniform size distribution (ca. 20 nm) can be obtained in few minutes. The mass concentration of $Ag@SiW_{12}O_{40}$ nanoparticles solution was estimated based on EQCM measurements (ca. 2.80 to 4.42 $g \cdot L^{-1}$). The formed $Ag@SiW_{12}O_{40}$ nanoparticles were stable in solution for more than three months based on their signature in UV-visible spectra. $Ag@SiW_{12}O_{40}$ nanoparticles were dropped on electrode surface to form the catalyst films. A layer of Nafion added at the end of deposition can better fix the catalyst film. Electrochemical reduction of NO_x^- (NO_3^- and HNO_2/NO_2^-) was studied. We have demonstrated that AgNPs and $[SiW_{12}O_{40}]^{4-}$ act in tandem in pH 1 solution resulting in a significant improvement of the reduction current. In pH 5 solution, a smaller improvement was observed but the Ag@$SiW_{12}O_{40}$ nanoparticles films were still active in $NaNO_2$ solution after 750 potential cycles between 0 V and -1.05 V *vs.* SCE and at a scan rate of 20 mV s^{-1}. In contrast to $[SiW_{12}O_{40}]^{4-}$ alone, Ag@$SiW_{12}O_{40}$ is active for nitrate reduction, showing that the presence of silver is necessary to catalyse nitrate reduction. In addition, Ag@$SiW_{12}O_{40}$ nanoparticles films have been demonstrated to be more active than using Ag bulk electrode no matter the $[SiW_{12}O_{40}]^{4-}$ is present or not. A nitrate sensor can be expected in the concentration range of 50 $mmol \cdot L^{-1}$ to 200 $mmol \cdot L^{-1}$ which may complete the published studies.

Finally, in Chapter V, we have shown that POMs encapsulated in the MOFs (UiO-67 or MIL-101) conserve their electrochemical properties after being immobilized on electrode surface. No response was detected for POM@gelatin due to the insulating character of gelatin. A preliminary study was also presented, in which Fe-substituted POM were still active toward nitrite reduction after being encapsulated in MOFs. The catalytic current was observed at the potential that Fe^{III} reduced and enhanced at the W^{VI} reduction waves. This observation may reveal a new direction to form POM-based heterogeneous catalysis toward NO_x catalysis.

Continuation of this work includes the characterization of the POM-protected nanoparticles by using X-ray photoelectron spectroscopy (XPS), *in-situ* Transmission Electron Microscopy (*in-situ* TEM), etc. The identification of the products and their amount should be quantified by Differential Electrochemical Mass Spectroscopy (DEMS), Gas Chromatography (GC) and Fourier-Transformed Infrared Spectroscopy (FT-IR).

More particularly, in the system of CuPOMs, the complexe CuAle should be investigated independent in order to better understand the influence of chemical environment of Cu ions. For the Ag@POM and POM@MOF systems, the choice of POM can be varied to find out the best matching candidates and the experimental condition should be modified in order to adapt to the catalyst. Furthermore, the catalyst film should be better fix on electrode surface by varying the quantity of the Nafion quantity or by embedding the catalyst in a polymer matrix.

Appendix

Appendix

Reagent and apparatus

Regent

$NaNO_3$, extra pure	Merck KGaA	N° CAS : 7631-99-4
$NaNO_2$, extra pure	Merck KGaA	N° CAS : 7632-00-0
propan-2-ol, 99.8%	Fluka	N° CAS : 67-63-0
Ag_2SO_4, ≥ 99.9%	Sigma-Aldrich	N° CAS : 10294-26-5
$CH_3COOLi\cdot 2H_2O$, ≥ 97%	Sigma-Aldrich	N° CAS : 6108-17-4
CH_3COOH, ≥ 99.7%	Sigma-Aldrich	N° CAS : 64-19-7
H_2SO_4, 96%	Merck KGaA	N° CAS : 7604-93-9
Na_2SO_4, extra pure	Acros organics	N° CAS :7757-82-6
Nafion, 5%wt.	Sigma-Aldrich	N° CAS :31175-20-9
$CuSO_4$ anhydrous	Sigma-Aldrich	N° CAS :7758-98-7

Electrochemistry Voltammetric and electroreduction have been performed with a standard three-electrode system using a PARSTAT 2273 potentiate. Glass carbon (GC) electrode, single-side coated indium-tin-oxide (ITO, SOLEMS, 25-35 Ω/cm^{-2}) electrodes, or pyrolytic graphite (PG) disk electrode have been used as working electrode. A platinum wire has been used as an auxiliary electrode. The reference electrode was a saturated calomel electrode (SCE). It was electrically connected to the solution by a junction bridge filled with the electrolyte.

Electrochemical quartz crystal measurement A QCA-922 (SEIKO EG&G instrument) system combined with Versa STAT 3 was used for simultaneous quartz crystal measurement and cyclic voltammetric measurements. The electrochemical cell was assembled in a glove box using an carbon AT-cut quartz crystal resonator (mirror finished, resonant frequency: 9.08 MHz ± 50 kHz, $A = 0.2\ cm^2$, SEIKO EG&G., LTD) as working electrode, a platinum wire as counter electrode, and a Ag/AgCl wire as a quasi-reference electrode.

UV–visible spectroscopic measurements UV–vis absorption spectra have been recorded on an Agilent 8453 spectrophotometer with A 300 W Xe arc lamp equipped with a water cell filter to absorb the near-IR radiation.

Atomic force micrographs (AFM) measurement. AFM have been conducted directly on the ITO surfaces using a Dimension 3100 (Veeco) in the tapping mode under ambient conditions. Silicon cantilevers (Veeco probes) with a spring constant of 300 N/m and a resonance frequency in the range of 120–139 kHz have been used. The scanning rate was 1.0 Hz.

Chapter III Electrochemical and electrocatalytic properties of Cu-substituted polyoxometalate/alendronate

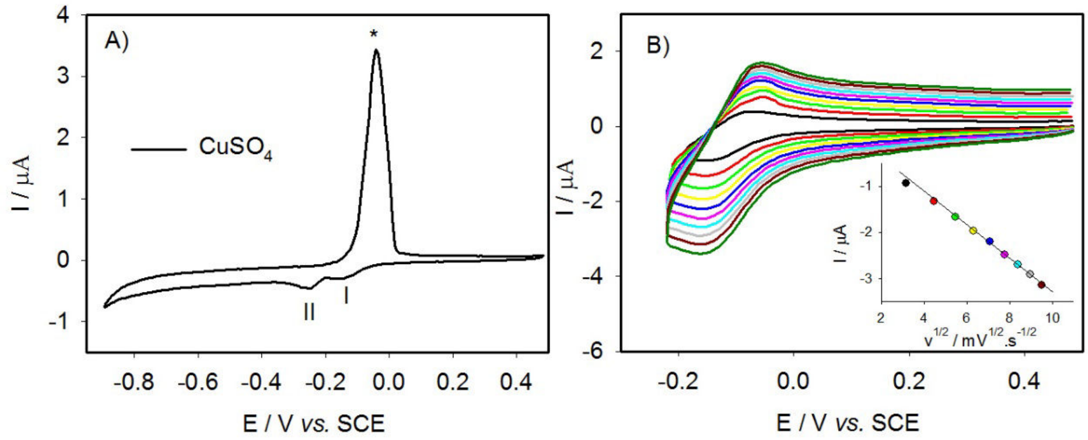

Figure S1: A) CV of 0.1 mmol·L^{-1} CuSO$_4$ in pH 5 1 mol·L^{-1} CH$_3$COOLi + CH$_3$COOH solution, v = 2 mV·s^{-1}. B) Variation of scan rates of 0.1 mmol·L^{-1} CuSO$_4$ in pH 5 1 mol·L^{-1} CH$_3$COOLi + CH$_3$COOH solution (from inner to outer curve: 10, 20, 30, 40, 50, 60, 70, 80, 90, and 100 mV·s^{-1}). The potential reversal is fixed after Cu^{II} to Cu^{I} redox process. (Inset) Variation of the cathodic peak current intensity as a function of the square root of the scan rate.

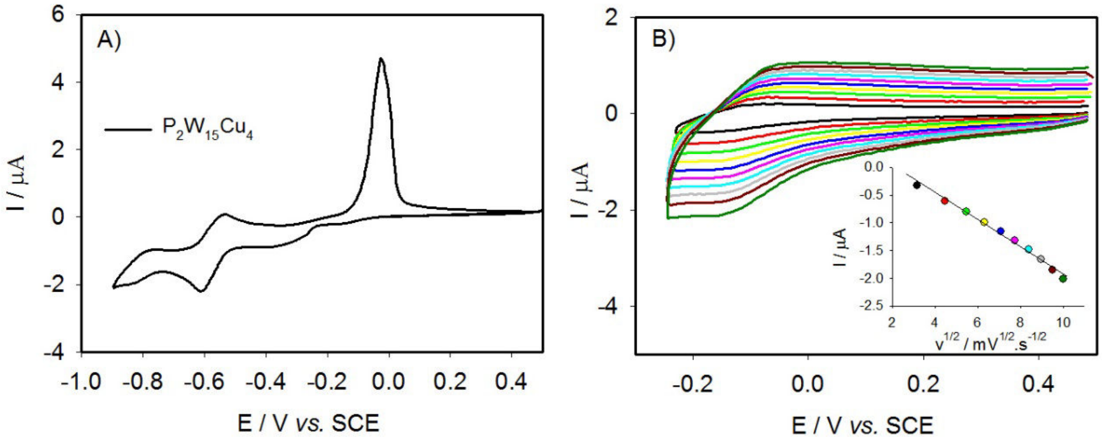

Figure S2: A) CV of 0.1 mmol·L^{-1} P$_2$W$_{15}$Cu$_4$ in pH 5 1 mol·L^{-1} CH$_3$COOLi + CH$_3$COOH solution, v = 2 mV·s^{-1}. B) Variation of scan rates of 0.1 mmol·L^{-1} P$_2$W$_{15}$Cu$_4$ in pH 5 1 mol·L^{-1} CH$_3$COOLi + CH$_3$COOH solution (from inner to outer curve: 10, 20, 30, 40, 50, 60, 70, 80, 90, and 100 mV·s^{-1}). The potential reversal is fixed after Cu^{II} to Cu^{I} redox process. (Inset) Variation of the cathodic peak current intensity as a function of the square root of the scan rate.

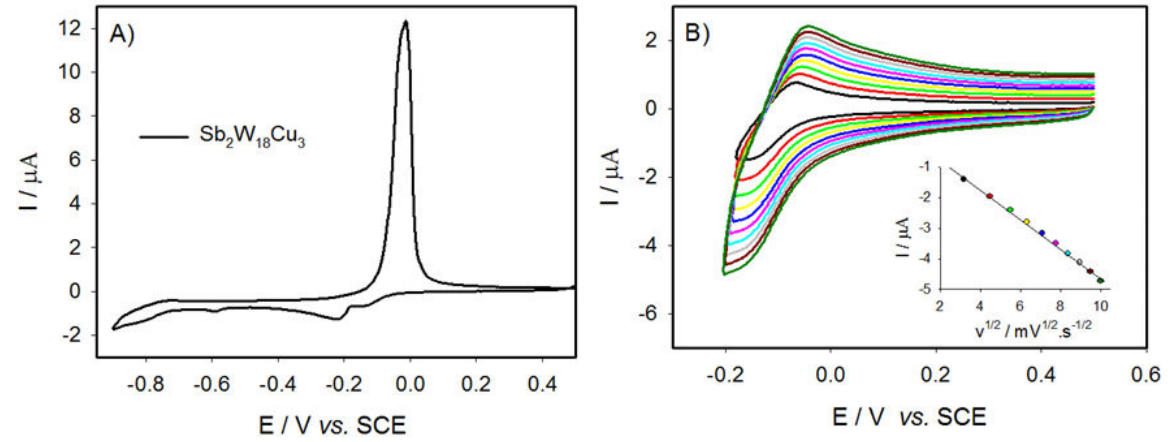

Figure S3: A) CV of 0.1 mmol·L^{-1} $Sb_2W_{18}Cu_3$ in pH 5 1 mol·L^{-1} CH_3COOLi + CH_3COOH solution, v = 2 mV·s^{-1}. B) Variation of scan rates of 0.1 mmol·L^{-1} $Sb_2W_{18}Cu_3$ in pH 5 1 mol·L^{-1} CH_3COOLi +CH_3COOH solution (from inner to outer curve: 10, 20, 30, 40, 50, 60, 70, 80, 90, and 100 mV·s^{-1}). The potential reversal is fixed after Cu^{II} to Cu^{I} redox process. (Inset) Variation of the cathodic peak current intensity as a function of the square root of the scan rate.

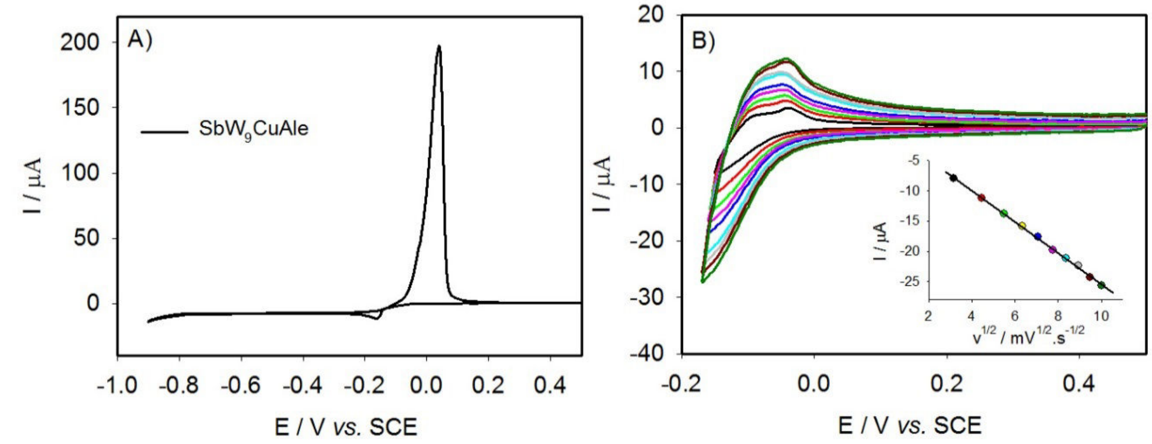

Figure S4: A) CV of 0.1 mmol·L-1 SbW9CuAle in pH 5 1 mol·L-1 CH3COOLi + CH3COOH solution, v = 2 mV·s-1. B) Variation of scan rates of 0.1 mmol·L-1 SbW9CuAle in pH 5 1 mol·L-1 CH3COOLi +CH3COOH solution (from inner to outer curve: 10, 20, 30, 40, 50, 60, 70, 80, 90, and 100 mV·s-1). The potential reversal is fixed after CuII to CuI redox process. (Inset) Variation of the cathodic peak current intensity as a function of the square root of the scan rate.

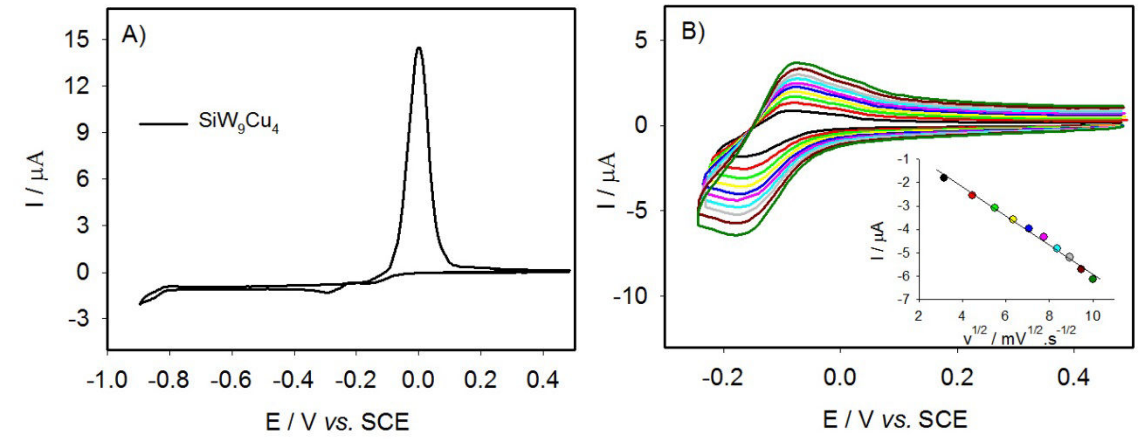

Figure S5: A) CV of 0.1 mmol·L^{-1} SiW$_9$Cu$_4$ in pH 5 1 mol·L^{-1} CH$_3$COOLi + CH$_3$COOH solution, v = 2 mV·s^{-1}. B) Variation of scan rates of 0.1 mmol·L^{-1} SiW$_9$Cu$_4$ in pH 5 1 mol·L^{-1} CH$_3$COOLi +CH$_3$COOH solution (from inner to outer curve: 10, 20, 30, 40, 50, 60, 70, 80, 90, and 100 mV·s^{-1}). The potential reversal is fixed after Cu^{II} to Cu^{I} redox process. (Inset) Variation of the cathodic peak current intensity as a function of the square root of the scan rate.

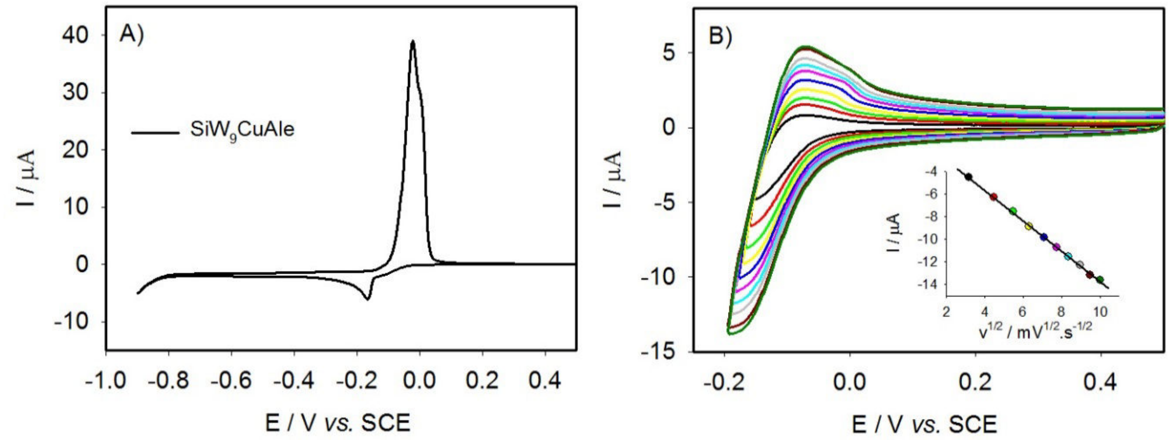

Figure S6: A) CV of 0.1 mmol·L^{-1} SiW$_9$CuAle in pH 5 1 mol·L^{-1} CH$_3$COOLi + CH$_3$COOH solution, v = 2 mV·s^{-1}. B) Variation of scan rates of 0.1 mmol·L^{-1} SiW$_9$CuAle in pH 5 1 mol·L^{-1} CH$_3$COOLi + CH$_3$COOH solution (from inner to outer curve: 10, 20, 30, 40, 50, 60, 70, 80, 90, and 100 mV·s^{-1}). The potential reversal is fixed after Cu^{II} to Cu^{I} redox process. (Inset) Variation of the cathodic peak current intensity as a function of the square root of the scan rate.

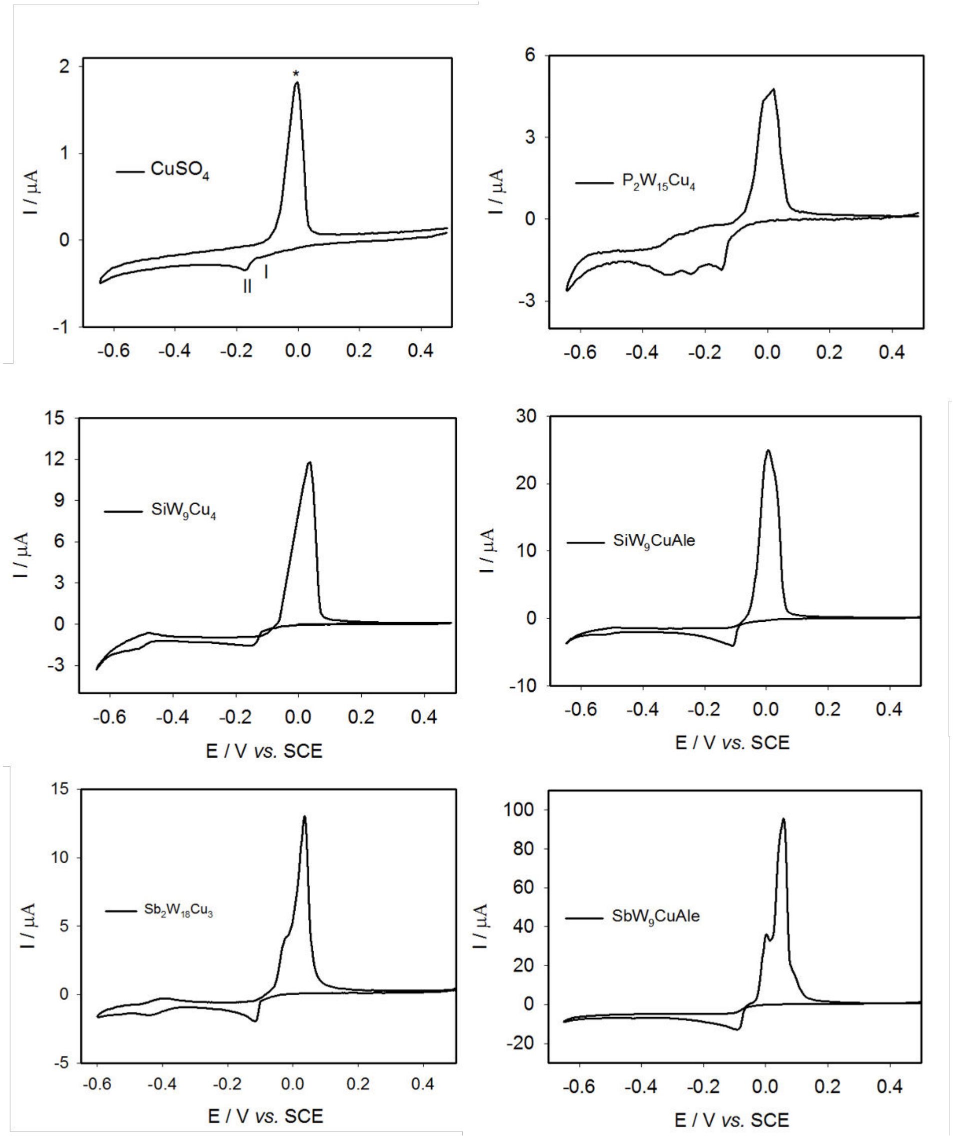

Figure S7: CV of 0.1 mmol·L^{-1} samples in pH 1 0.5 mol·L^{-1} Na_2SO_4 + H_2SO_4 solution, v = 2 mV·s^{-1}.

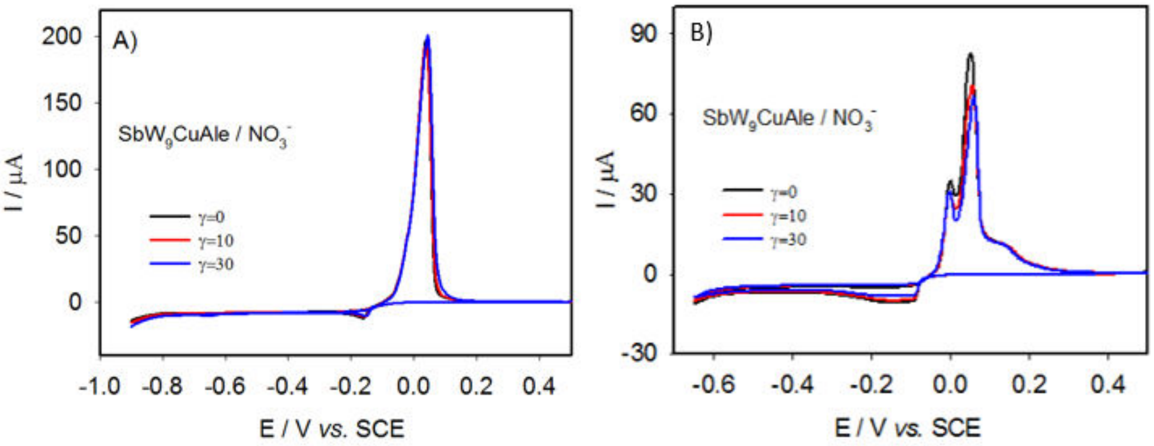

Figure S8: Reduction of NO_3^- in presence of 0.1 mmol·L^{-1} SbW_9CuAle in pH 5 1 mol·L^{-1} CH_3COOLi + CH_3COOH (A) or in pH 10.5 mol·L^{-1} Na_2SO_4 + H_2SO_4 (B), v = 2 mV·s^{-1}.

Chapter V Immobilization of polyoxometalates in the metal organic framework (POM@MOF)

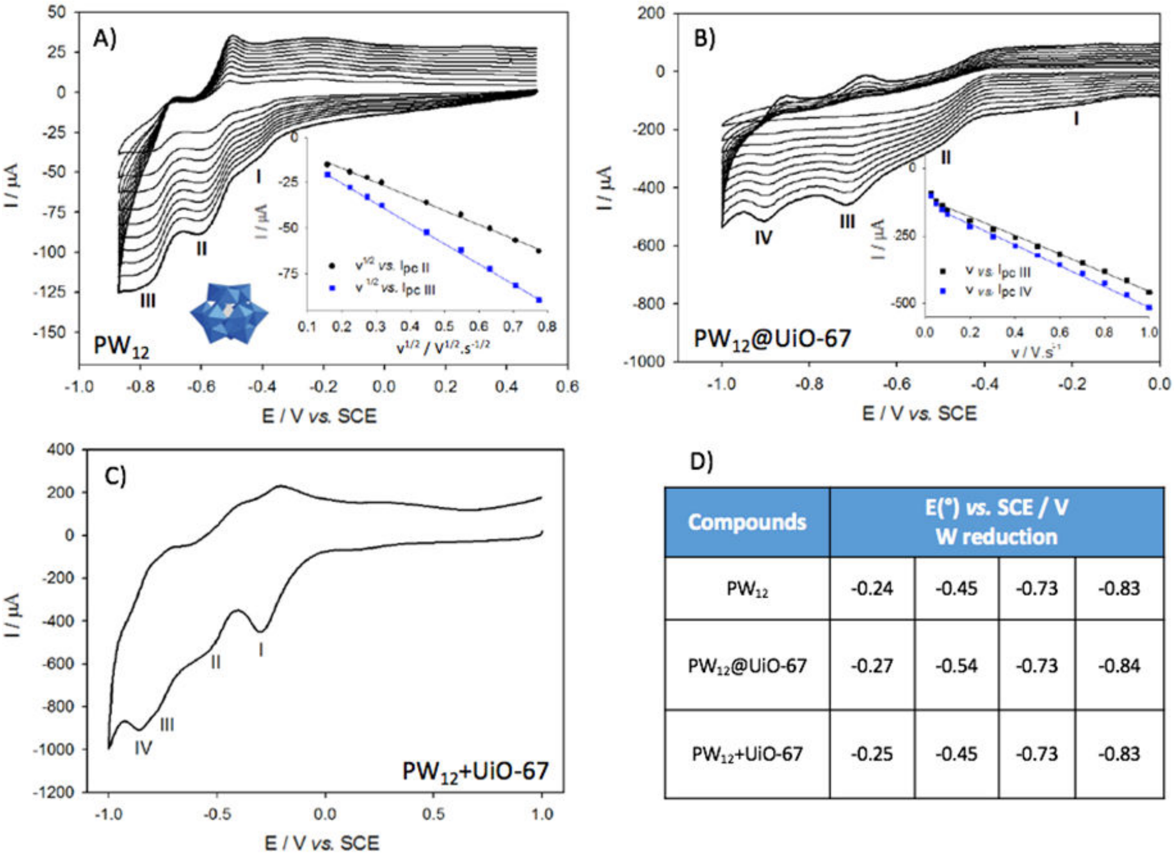

Compounds	E(°) vs. SCE / V W reduction			
PW$_{12}$	-0.24	-0.45	-0.73	-0.83
PW$_{12}$@UiO-67	-0.27	-0.54	-0.73	-0.84
PW$_{12}$+UiO-67	-0.25	-0.45	-0.73	-0.83

Figure S9: Cyclic voltammograms of (A) PW$_{12}$, (B) PW$_{12}$@UiO-67 and (C) PW$_{12}$+UiO-67 (mechanical mixing) immobilized on a PG electrode at different scan rate from 0.025 to 1.000 V·s^{-1}. (Inset) plots of I$_{pc}$ vs. v$^{1/2}$ (A) and I$_{pc}$ vs. v (B) for reduction peaks. D) Reduction potentials for each composite immobilized on PG electrode. Buffer solution : pH 2.5 0.5 mol·L^{-1} Na$_2$SO$_4$ + H$_2$SO$_4$.

Inorganic Chemistry
Article
pubs.acs.org/IC

Heteroanionic Materials Based on Copper Clusters, Bisphosphonates, and Polyoxometalates: Magnetic Properties and Comparative Electrocatalytic NO_x Reduction Studies

Olivier Oms,[†,⊥] Shu Yang,[§,⊥] William Salomon,[†] Jérôme Marrot,[†] Anne Dolbecq,[†] Eric Rivière,[‡] Antoine Bonnefont,[§] Laurent Ruhlmann,[*,§] and Pierre Mialane[*,†]

[†]Institut Lavoisier de Versailles, UMR 8180, Université de Versailles Saint-Quentin en Yvelines, Université Paris-Saclay, 45 Avenue des Etats-Unis, 78035 Versailles cedex, France

[‡]Institut de Chimie Moléculaire et des Matériaux d'Orsay, UMR 8182, CNRS, Univ. Paris-Sud, Université Paris-Saclay, 91405 Orsay cedex, France

[§]Institut de Chimie, Laboratoire d'Electrochimie et de Chimie Physique du Corps Solide, UMR CNRS 7177, Université de Strasbourg, 4 rue Blaise Pascal, CS 90032, 67081 Strasbourg cedex, France

S *Supporting Information*

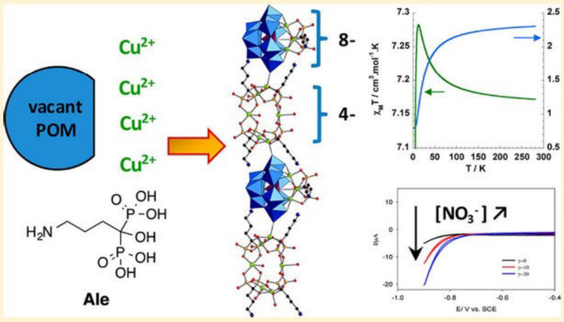

ABSTRACT: Three compounds associating for the first time polyoxotungstates, bisphosphonates, and copper ions were structurally characterized. They consist in heteropolyanionic monodimensional materials where $[Cu_6(Ale)_4(H_2O)_4]^{4-}$ (Ale = alendronate = $[O_3PC(O)(C_3H_6NH_3)PO_3]^{4-}$) complexes alternate with polyoxometalate (POM) units. In $Na_{12}[\{SiW_9O_{34}Cu_3(Ale)(H_2O)\}\{Cu_6(Ale)_4(H_2O)_4\}]\cdot 50H_2O$ (**SiW$_9$CuAle**), the polyoxometalate core consists in a $\{SiW_9Cu_3\}$ monomer capped by a pentacoordinated Ale ligand, while sandwich-type Keggin $\{(SbW_9O_{33})_2Cu_3(H_2O)_{2.5}Cl_{0.5}\}$ and Dawson $\{(P_2W_{15}O_{56})_2Cu_4(H_2O)_2\}$ complexes are found in $Na_8Li_{29}[\{(SbW_9O_{33})_2Cu_3(H_2O)_{2.5}Cl_{0.5}\}_2\{Cu_6(Ale)_4(H_2O)_4\}_3]\cdot 163H_2O$ (**SbW$_9$CuAle**) and $Na_{20}[\{(P_2W_{15}O_{56})_2Cu_4(H_2O)_2\}\{Cu_6(Ale)_4(H_2O)_4\}]\cdot 50H_2O$ (**P$_2$W$_{15}$CuAle**), respectively. A comparative magnetic study of the **SiW$_9$CuAle** and **SbW$_9$CuAle** compounds enabled full quantification of the Cu^{II} superexchange interactions both for the POM and non-POM subunits, evidencing that, while the paramagnetic centers are anti-ferromagnetically coupled in the polyoxometalate units, both anti-ferromagnetic and ferromagnetic interactions coexist in the $\{Cu_6(Ale)_4(H_2O)_4\}$ cluster. All the studied compounds present a good efficiency upon the reduction of HNO_2 or NO_2^-, the POM acting as a catalyst. However, it has been found that **SbW$_9$CuAle** is inactive toward the reduction of nitrates, highlighting that both the $\{(SbW_9O_{33})_2Cu_3\}$ unit and the $\{Cu_6(Ale)_4(H_2O)_4\}$ cluster do not act as electrocatalysts for this reaction. In contrast, **SiW$_9$CuAle** and **P$_2$W$_{15}$CuAle** have shown a significant activity upon the reduction of NO_3^- and thus both at pH 1 and pH 5, evidencing that the chemical nature of the polyoxometalate is a crucial parameter even if it acts as precatalyst. Moreover, comparison of the activities of **P$_2$W$_{15}$CuAle** and $[(P_2W_{15}O_{56})_2Cu_4(H_2O)_2]^{16-}$ evidenced that if the $[Cu_6(Ale)_4(H_2O)_4]^{4-}$ cluster does not act as electrocatalyst, it acts as a cofactor, significantly enhancing the catalytic efficiency of the active POM.

■ INTRODUCTION

Among polyoxometalates (POMs),[1] polyoxotungstates (POTs) and especially the Dawson- or Keggin-type POT derivatives occupy a specific place, as they represent perfect candidates for the multistep elaboration of POM-based materials. In particular, starting from well-known vacant polyoxotungstate precursors[2] able to incorporate from one to 20 3d centers, a vast family of 3d-incorporating inorganic compounds with a tremendous variety of compositions and structures has been obtained.[3] Organic–inorganic hybrid 3d metal-POTs have also been isolated using a large range of secondary oxygen ((poly) carboxylate)[4] and nitrogen (ethylenediamine, (poly)pyridine, azide,...)[5] containing ligands. As they represent a class of well-insulated complexes of controlled nuclearity and topology, these inorganic or hybrid materials constitute ideal models for magnetic investigations.[6] Moreover, these last years, several POM compounds behaving as single-molecule magnets have been characterized.[7] 3d-containing polyoxotungstates have also been widely investigated for their catalytic and electrocatalytic properties.[8] For example, the ability of the $[Co^{II}_4(H_2O)_2(PW_9O_{34})_2]^{10-}$ complex to act as a robust water oxidation catalyst has been demonstrated.[9] The epoxidation of alkenes by Zn^{II}, Fe^{III}, or Ni^{II}/Fe^{III} POTs has also been studied.[10] Besides,

Received: October 23, 2015
Published: February 4, 2016

DOI: 10.1021/acs.inorgchem.5b02456
Inorg. Chem. 2016, 55, 1551−1561

Table 1. Crystallographic Data for SiW$_9$CuAle, SbW$_9$CuAle, and P$_2$W$_{15}$CuAle

	SiW$_9$CuAle	SbW$_9$CuAle	P$_2$W$_{15}$CuAle
empirical formula	$SiW_9O_{120}Cu_9$ $C_{20}H_{147}N_5P_{10}Na_{12}$	$Sb_4W_{36}Cu_{24}P_{24}C_{48}$ $N_{12}H_{468}ClNa_8Li_{29}O_{396}$	$P_{12}W_{30}Cu_{10}C_{16}H_{148}N_4$ $O_{196}Na_{20}$
formula weight, *g*	5218.4	17 346.2	10 515.4
crystal system	monoclinic	triclinic	monoclinic
space group	$P2_1/c$	$P\bar{1}$	$P2_1/c$
a/Å	23.3560(8)	22.384(3)	32.256(3)
b/Å	22.4995(8)	32.340(4)	28.454(3)
c /Å	28.2725(9)	34.221(4)	27.131(2)
α/°	90	75.951(4)	90
β/°	99.6330(17)	78.016(5)	93.400(4)
γ / °	90	78.695(5)	90
V/Å^3	14647.7(9)	23229(5)	24857(9)
Z	4	2	4
T/K	200	200	200
ρ_{calc}/g cm^{-3}	2.370	2.304	2.654
μ/mm^{-1}	8.577	10.359	14.838
data/parameters	42833/1636	82318/4165	43911/2165
R_{int}	0.0984	0.0954	0.1015
GOF	1.072	1.031	1.037
R (>2σ(I))	$R_1{}^a = 0.0827$ $wR_2{}^b = 0.1890$	$R_1{}^a = 0.0918$ $wR_2{}^b = 0.2469$	$R_1{}^a = 0.0806$ $wR_2{}^b = 0.2163$

$^aR_1 = \frac{\sum |F_o| - |F_c|}{\sum |F_c|}$ $^bwR_2 = \sqrt{\frac{\sum w(F_o{}^2 - F_c{}^2)^2}{\sum w(F_o{}^2)^2}}$

the electrocatalytic activity of these materials has been investigated, focusing mainly on the NO$_x$ reduction. Especially, a huge number of 3d-POTs have been found to reduce nitrites electrochemically.[11] In contrast, much less-substituted POTs have been found to be active toward nitrate electroreduction. In short, it has been found that some POTs incorporating Cu^{II}[12] or Fe^{III}[13] centers can be highly active for the reduction of NO$_3^-$. More recently, it has been shown that a POT incorporating Ni^{II} centers and bisphosphonate (BP) ligands is also able to efficiently reduce nitrate into nitrogen.[14] Herein we report on a series of BP/POT/Cu^{II} compounds. The reactivity of three different vacant POTs ([A-α-SiW$_9$O$_{34}$]$^{10-}$, [α-SbW$_9$O$_{33}$]$^{9-}$, and [α-P$_2$W$_{15}$O$_{56}$]$^{12-}$, respectively) with the [O$_3$PC(OH)(C$_3$H$_6$NH$_2$)PO$_3$]$^{4-}$ alendronate ligand (Ale) and Cu^{II} ions was intensely investigated, and three new compounds were structurally characterized. Surprisingly, they all contain chains built of two anionic fragments where POM units—the POM being purely inorganic or incorporating the alendronate ligand—and copper/alendronate multinuclear clusters alternate. The magnetic properties of two of these compounds were thoroughly studied, allowing quantifying the magnetic exchange interactions both within the POM complexes and the copper/alendronate entities. The abilities of these three compounds to electrochemically reduce nitrites and nitrates were evaluated and compared, highlighting that the nature of the POM plays a crucial role in the electrocatalytic activity even if these materials can act as pre-electrocatalysts since the reduction of the nitrate ions occurs at a potential lower than the one of the Cu(II/I) reduction. Also, the ability of the copper/alendronate entity to act as a cofactor is discussed.

■ EXPERIMENTAL SECTION

Synthesis. All reagents were purchased and used without further purification except alendronic acid H$_4$[O$_3$PC(OH)(C$_3$H$_6$NH$_2$)PO$_3$] (**Ale**),[15] K$_{12}$[(SbW$_9$O$_{33}$)$_2${Cu(H$_2$O)}$_3$]·41H$_2$O (**Sb$_2$W$_{18}$Cu$_3$**),[16] Na$_{10}$[A-α-SiW$_9$O$_{34}$]·xH$_2$O (**SiW$_9$**),[2] Na$_{12}$[α-P$_2$W$_{15}$O$_{56}$]·24H$_2$O (**P$_2$W$_{15}$**),[2] and Na$_9$[α-SbW$_9$O$_{33}$]·19.5H$_2$O (**SbW$_9$**),[17] which were synthesized according to reported procedures.

Preparation of Na$_{12}$[{SiW$_9$O$_{34}$Cu$_3$(Ale)(H$_2$O)}{Cu$_6$(O$_3$PC(O)(C$_3$H$_6$NH$_3$)PO$_3$)$_4$(H$_2$O)$_4$}]·50H$_2$O (**SiW$_9$CuAle**): Na$_{10}$[α-SiW$_9$O$_{34}$]·nH$_2$O (500 mg, 1.78 × 10^{-4} mol (n = 20)) and CuCl$_2$·2H$_2$O (121 mg, 7.09 × 10^{-4} mol) were dissolved in 10 mL of water, and the pH was adjusted to 7.5 with 1 M NaOH. Then, alendronic acid (93 mg, 3.73 × 10^{-4} mol) was added, and the pH was readjusted to 7.5 with 1 M NaOH. The solution is stirred for 2 h at room temperature and let slowly evaporate. After one week, green needle crystals suitable for X-ray diffraction studies are collected and washed with ethanol and ether (m = 250 mg; yield = 64% based on Ale). Anal. Calcd (found) for SiW$_9$O$_{120}$Cu$_9$C$_{20}$H$_{147}$N$_5$P$_{10}$Na$_{12}$ (MW = 5218.4 g·mol^{-1}): W 31.71 (29.72), Cu 10.96 (11.06), P 5.93 (5.89), Na 5.29 (5.44), C 4.60 (4.64), H 2.84 (2.51), N 1.34 (1.18). IR (ν/cm^{-1}): 1626 (m), 1511 (m), 1472 (m), 1395 (w), 1109 (m), 1054 (s), 1115 (m), 980 (m), 967 (m), 950 (m), 930 (m), 911 (m), 878 (s), 804 (s), 671 (s), 559 (s), 509 (s).

Preparation of Na$_8$Li$_{29}$[{(SbW$_9$O$_{33}$)$_2$Cu$_3$(H$_2$O)$_{2.5}$Cl$_{0.5}$}$_2$-{Cu$_6$(O$_3$PC(O)(C$_3$H$_6$NH$_3$)PO$_3$)$_4$(H$_2$O)$_4$}$_3$]·163 H$_2$O (**SbW$_9$CuAle**): Na$_9$[α-SbW$_9$O$_{33}$]·19.5H$_2$O (570 mg, 2 × 10^{-4} mol) and alendronic acid (80 mg, 3.21 × 10^{-4} mol) are dissolved in 10 mL of water. Then, CuCl$_2$·2H$_2$O (108 mg, 6.33 × 10^{-4} mol) is added, and the pH is adjusted to 8 with 1 M NaOH. The solution is stirred for 1 h at room temperature. The addition of 750 mg of NaCl leads to the precipitation of a green powder, which is redissolved in 20 mL of 1 M LiCl. After one week, green needle crystals suitable for X-ray diffraction studies are collected and washed with ethanol and ether (m = 200 mg; yield = 43% based on Cu). Anal. Calcd (found) for Sb$_4$W$_{36}$Cu$_{24}$P$_{24}$C$_{48}$N$_{12}$H$_{444}$ClNa$_8$Li$_{29}$O$_{396}$ (MW = 17 322.5 g·mol^{-1}): W 38.21 (37.30), Cu 8.80 (8.82), P 4.29 (4.32), C 3.33 (3.41), H 2.58 (2.19), N 0.97 (0.93), Na 1.06 (1.00), Li 1.16 (1.13). IR (ν/cm^{-1}): 1625 (m), 1493 (m), 1396 (w), 1115 (m), 1049 (s), 932 (s), 864 (s), 682 (s), 566 (s), 505 (s).

Preparation of Na$_{20}$[{(P$_2$W$_{15}$O$_{56}$)$_2$Cu$_4$(H$_2$O)$_2$}{Cu$_6$(O$_3$PC(O)(C$_3$H$_6$NH$_3$)PO$_3$)$_4$(H$_2$O)$_4$}]·50H$_2$O (**P$_2$W$_{15}$CuAle**): CuCl$_2$·2H$_2$O (60 mg, 4.46 × 10^{-4} mol) and alendronic acid (45 mg, 1.80 × 10^{-4} mol) are dissolved in 20 mL of water. Then, Na$_{12}$[α-P$_2$W$_{15}$O$_{56}$]·24H$_2$O (750 mg, 1.74 × 10^{-4} mol) is added as a solid, and the pH is adjusted to 7 with 1 M NaOH. The solution is stirred for 2 h at room temperature. Finally, NaCl (40 mg) is added, and the solution is left to crystallize. After two weeks, green rod crystals suitable for X-ray diffraction studies are collected and washed with ethanol and ether (m = 152 mg; yield = 32% based on Ale). Anal. Calcd (found) for

DOI: 10.1021/acs.inorgchem.5b02456
Inorg. Chem. 2016, 55, 1551−1561

$P_{12}W_{30}Cu_{10}C_{16}H_{148}N_4O_{196}Na_{20}$ (MW = 10 515.4 g·mol^{-1}): P 3.53 (3.67), W 52.45 (50.07), Cu 6.04 (6.05), C 1.83 (2.10), H 1.42 (1.74), N 0.53 (0.53), Na 4.37 (4.28). IR (ν/cm^{-1}): 1622 (m), 1494 (m), 1395 (w), 1118 (m), 1081 (s), 1051 (s), 1015 (m), 933 (s), 877 (s), 727 (s), 687 (s), 577 (s), 558 (s).

Physical Measurements. Elemental analyses of the solids were performed by the "Service de microanalyses ICSN CNRS", in Gif sur Yvette (France), and by the "Service d'Analyse du CNRS", in Vernaison (France). FT-IR spectra were recorded in the 4000−400 cm^{-1} range on a Nicolet 30 ATR 6700 FT spectrometer. Single-crystal X-ray intensity data collections were performed with a Bruker Nonius X8 APEX 2 diffractometer equipped with a CCD bidimensional detector using Mo Kα monochromatized radiation (λ = 0.710 73 Å). The absorption corrections were based on multiple and symmetry-equivalent reflections in the data sets using the SADABS program[18] based on the method of Blessing.[19] The structures were solved by direct methods and refined by full-matrix least-squares using the SHELX-TL package.[20] In the three reported structures, there is a discrepancy between the formulas determined by elemental analysis and that deduced from the crystallographic atom list because of the difficulty in locating all the disordered water molecules and alkali ions. Disordered water molecules and counterions were thus refined with partial occupancy factors. The hydrogen atoms were theoretically located on the basis of the conformation of the supporting atoms. The crystallographic data are gathered in Table 1. CCDC numbers: 1431904 (**SiW₉CuAle**), 1431905 (**SbW₉CuAle**), and 1431906 (**P₂W₁₅CuAle**).

Magnetic Measurements. Magnetic measurements on powder were performed with a Quantum Design SQUID Magnetometer with an applied field of 1000 G using powder samples pressed in pellets to avoid preferential orientation of the crystallites. The independence of the susceptibility value with regard to the applied field was checked at room temperature. The susceptibility data were corrected from the diamagnetic contributions as deduced by using Pascal's constant tables. The susceptibility times temperature as a function of temperature curves were simulated using MAGPACK.[21]

Electrochemistry. The solutions were deaerated thoroughly for at least 30 min with pure argon and kept under a positive pressure of this gas during experiments. Electrochemical measurements were performed on a PARSTAT 2273 potentiostat at room temperature under argon atmosphere. A three-electrode system was used with a glassy carbon (GC, Tokai Japan) electrode as a working electrode, a platinum wire as auxiliary electrode, and the reference electrode was the saturated calomel electrode, which was electrically connected to the solution by a junction bridge filled with electrolyte. The buffer solutions were prepared from the following solution, 1 mol·L^{-1} CH_3COOLi + CH_3COOH (pH 5) and 0.5 mol L^{-1} Na_2SO_4 + H_2SO_4 (pH 1).

■ RESULTS AND DISCUSSION

Synthesis and Structures of SiW₉CuAle, SbW₉CuAle, and P₂W₁₅CuAle.

$Na_{12}[\{SiW_9O_{34}Cu_3(Ale)(H_2O)\}\{Cu_6(Ale)_4(H_2O)_4\}]\cdot 50H_2O$ (**SiW₉CuAle**) can be obtained in good yield (64%) in water (pH = 7.5) at room temperature from the reaction of $[A\text{-}\alpha\text{-}SiW_9O_{34}]^{10-}$, $CuCl_2$, and alendronate. **SiW₉CuAle** results from the cocrystallization of two distinct polyanionic units, the polyoxometalate/copper/alendronate $[SiW_9O_{34}Cu_3(Ale)(H_2O)]^{8-}$ complex (Figure 1a) and the copper/alendronate $[Cu_6(Ale)_4(H_2O)_4]^{4-}$ cluster (Figure 1b). In **SiW₉CuAle**, all the alendronate ligands are tetraanionic, the global charge of the compound being compensated by 12 sodium cations. In the $\{SiW_9O_{34}Cu_3(Ale)(H_2O)\}$ POM, the 3d metal cations fill the vacancies of the $\{SiW_9\}$ precursor, the three Cu^{II} ions forming a pseudoisosceles triangle ($d_{Cu\cdots Cu}$ = 3.67 and 3.84−3.85 Å, respectively). Each paramagnetic center is connected to three oxygen atoms of the silicotungstate ligand, and an alendronate ligand caps the $\{SiW_9Cu_3\}$ fragment, connecting two copper ions of two edges of the triangle via one O−P−O bridge, respectively. In the third edge, the d^9 centers are directly connected via the deprotonated alkoxo group of the Ale ligand and via a long O−P−C−P−O bridge. All the 2p orbitals of the Ale bridging oxygen atoms are directed toward the Cu^{II} $d_{x^2-y^2}$ magnetic orbitals. We can note that, while the $[SiW_9O_{37}\{Cu(H_2O)\}_3]^{10-}$ species has been postulated,[22] it has not been possible so far to isolate this monomeric complex. However, several $\{SiW_9\}$/Cu^{II} compounds have been characterized, including one monomeric $\{SiW_9Cu_4\}$ hybrid compound,[4f] four dimeric $\{(SiW_9)_2Cu_n\}$ (n = 5,[23] 6,[24] or 8[25]) species, and a tetrameric $\{(SiW_9)_4Cu_{14}\}$ complex.[26]

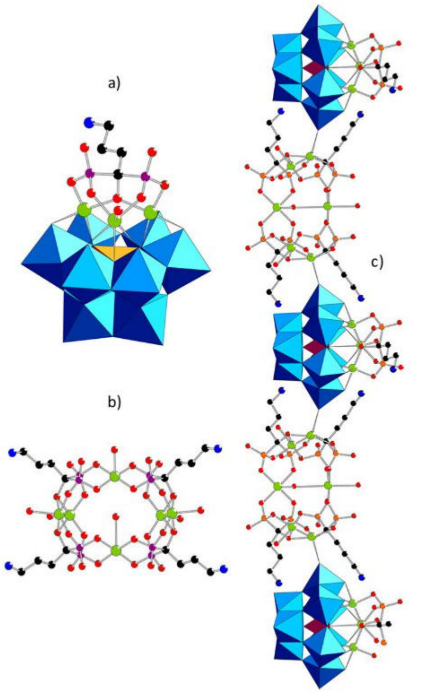

Figure 1. Ball-and-stick representations of (a) the monomeric $\{SiW_9O_{34}Cu_3(Ale)(H_2O)\}$ Keggin building unit found in **SiW₉CuAle**; (b) the $\{Cu_6(Ale)_4(H_2O)_4\}$ unit common to **SiW₉CuAle**, **SbW₉CuAle**, and **P₂W₁₅CuAle**, and (c) the 1D structure of $[\{SiW_9O_{34}Cu_3(Ale)(H_2O)\}\{Cu_6(Ale)_4(H_2O)_4\}]^{12-}$. Blue octahedra, WO_6; purple tetrahedra, SiO_4; green spheres, Cu; orange spheres, P; black spheres, C; blue spheres, N; red spheres, O. Hydrogen atoms were omitted for clarity.

Focusing now on the $[Cu_6(Ale)_4(H_2O)_4]^{4-}$ complex, it is observed that this unit contains two $\{Cu_2(Ale)_2(H_2O)_2\}$ pairs where all the copper atoms are in square pyramidal distorted environment. The basal planes of the copper ions are each made of two bridging alkoxo ligands ($d_{Cu\cdots O}$ = 1.93−1.99 Å, Cu−O−Cu = 88.8−90.1°) and two P−O oxygen atoms ($d_{Cu\cdots O}$ = 1.93−1.95 Å). These pairs are connected by two copper centers via eight O−P−O bridges, affording a cyclic hexanuclear species. Again, all the bridging oxygen atoms reside in the xy planes. While the coordination sphere of one Cu^{II} ion of each $\{Cu_2(Ale)_2(H_2O)_2\}$ pair is completed by a terminal water molecule ($d_{Cu\cdots O}$ = 2.36−2.37 Å), the other one is connected to a terminal O═W oxygen atom ($d_{Cu\cdots O}$ = 2.29−2.34 Å) of the $\{W_6\}$ crown of the $[SiW_9O_{34}Cu_3(Ale)(H_2O)]^{8-}$ moiety, affording a -POM-$\{Cu_6\}$-POM-$\{Cu_6\}$- infinite molecular wire (Figure 1c). Notice that only one pure alendronate/copper cluster has been previously fully characterized,[27] and its structure is completely different from that of the $[Cu_6(Ale)_4(H_2O)_4]^{4-}$ one found in **SiW$_9$CuAle**. Indeed, in the neutral dinuclear $[Cu_2(Ale)_4(H_2O)_2]$ complex previously reported, the copper centers are connected by two Ale ligands via two O−P−O and two O−P−C−P−O bridges, all the alkoxo groups of the Ale ligands remaining protonated. This can be explained considering the much lower pH (pH = 2) of the reacting media compared to the one fixed for the synthesis of **SiW$_9$CuAle** (pH = 7.5). The IR spectrum of **SiW$_9$CuAle** shows intense O−P−O symmetric and asymmetric stretching bands in the 1000−1200 cm^{-1} region. Above 1200 cm^{-1}, the bands related to the organic backbone are observed, while the intense bands due to the W═O and W−O vibrations are observed below 1000 cm^{-1}. **SiW$_9$CuAle** is soluble in water. It can be recovered after dissolution by addition of NaCl, the obtained product possessing exactly the same IR spectrum as the pristine one, strongly suggesting that both the $\{SiW_9O_{34}Cu_3(Ale)(H_2O)\}$ and the $\{Cu_6(Ale)_4(H_2O)_4\}$ fragments are stable in solution.

$Na_8Li_{29}[\{(SbW_9O_{33})_2Cu_3(H_2O)_{2.5}Cl_{0.5}\}_2\{Cu_6(Ale)_4(H_2O)_4\}_3]\cdot 163H_2O$ (**SbW$_9$CuAle**) was obtained by mixing $[\alpha\text{-}SbW_9O_{33}]^{9-}$, $CuCl_2$, and Ale in water (room temperature, pH = 8). Addition of NaCl afforded a precipitate, which can be recrystallized in a 1 M LiCl aqueous solution, leading to a mixed Na/Li salt. In **SbW$_9$CuAle**, one $[(SbW_9O_{33})_2Cu_3(H_2O)_2Cl]^{13-}$ unit and one $[(SbW_9O_{33})_2Cu_3(H_2O)_3]^{12-}$ POM unit (Figure S1) cocrystallize with three crystallographically independent $[Cu_6(Ale)_4(H_2O)_4]^{4-}$ complexes analogous to that found in **SiW$_9$CuAle**. The $\{Sb^{III}{}_2W_{18}Cu_3\}$ POM cluster has been previously described[16] and consists in three Cu^{II} centers sandwiched between two $\{Sb^{III}W_9\}$ units and connected via long O−W−O−W−O bridges ($d_{Cu\cdots Cu}$ = 4.72−4.84 Å). As for the **SiW$_9$CuAle** compound, two copper centers of each $[Cu_6(Ale)_4(H_2O)_4]^{4-}$ cluster are connected to O═W oxygen atoms ($d_{Cu\cdots O}$ = 2.17−2.31 Å) of the $\{W_6\}$ crown of the POM. However, in opposition to **SiW$_9$CuAle**, in **SbW$_9$CuAle**, the anionic units form a -POM-$\{Cu_6\}$-POM-$\{Cu_6\}_2$-POM-$\{Cu_6\}$-POM-$\{Cu_6\}_2$- chain (Figure 2a), with a POM/$[Cu_6(Ale)_4(H_2O)_4]^{4-}$ ratio of 2:3 compared to 1:1 in **SiW$_9$CuAle**.

The third compound $Na_{20}[\{(P_2W_{15}O_{56})_2Cu_4(H_2O)_2\}\{Cu_6(Ale)_4(H_2O)_4\}]\cdot 50H_2O$ (**P$_2$W$_{15}$CuAle**) was synthesized in conditions similar to those used for **SiW$_9$CuAle** but replacing the $\{SiW_9\}$ precursor with the $\{P_2W_{15}\}$ one. **P$_2$W$_{15}$CuAle** is made of the $[(P_2W_{15}O_{56})_2Cu_4(H_2O)_2]^{16-}$ POM, which can be described as a rhomb-like tetranuclear Cu^{II} cluster sandwiched between two $\{P_2W_{15}\}$ units,[28] and the $[Cu_6(Ale)_4(H_2O)_4]^{4-}$ complex. In the solid state, $[(P_2W_{15}O_{56})_2Cu_4(H_2O)_2]^{16-}$ clusters alternate with $[Cu_6(Ale)_4(H_2O)_4]^{4-}$ units, forming a -POM-$\{Cu_6\}$-POM-$\{Cu_6\}$- one-dimensional (1D) material (Figure 2b), the $[Cu_6(Ale)_4(H_2O)_4]^{4-}$ complexes and the POMs being connected via oxygen atoms belonging to the $\{W_3\}$ caps of the Dawson units ($d_{Cu\cdots O}$ = 2.21−2.23 Å). Finally, all known attempts to isolate separately the POM and the $\{Cu_6Ale_4\}$ clusters by adding various counter-cations to an aqueous solution of **SbW$_9$CuAle** have failed, a combination of the two anionic species exhibiting an IR spectrum strictly analogous to that of **SbW$_9$CuAle** being systematically obtained.

Magnetic Properties. The magnetic properties of **SbW$_9$CuAle** and **SiW$_9$CuAle** were investigated, and the $\chi_M T$ product versus T curves of powdered samples of these compounds are represented in Figures 3a and 4a, respectively. For **SbW$_9$CuAle,** $\chi_M T$ continuously decreases from 300 K ($\chi_M T$ = 10.98 cm^3·mol^{-1}·K, the $\chi_M T$ value calculated for 24 noninteracting Cu^{II} centers being 10.89 cm^3·mol^{-1}·K assuming g = 2.2) to 2 K ($\chi_M T$ = 6.82 cm^3·mol^{-1}·K), indicating that overall weak anti-ferromagnetic interactions are predominant. In contrast, the $\chi_M T = f(T)$ curve related to **SiW$_9$CuAle** is characteristic of overall strong anti-ferromagnetic interactions, $\chi_M T$ decreasing from 300 K ($\chi_M T$ = 3.57 cm^3·mol^{-1}·K, the $\chi_M T$ value calculated for nine non-interacting Cu^{II} centers being 4.08 cm^3 mol^{-1} K assuming g = 2.2) to 20 K ($\chi_M T$ = 3.20 cm^3·mol^{-1}·K). At low temperature, the $\chi_M T$ product increases from 20 to 4 K ($\chi_M T$ = 3.38 cm^3·mol^{-1}·K), highlighting the presence of weak ferromagnetic interactions. Finally, $\chi_M T$ decreases from 4 to 2 K ($\chi_M T$ = 3.30 cm^3·mol^{-1}·K).

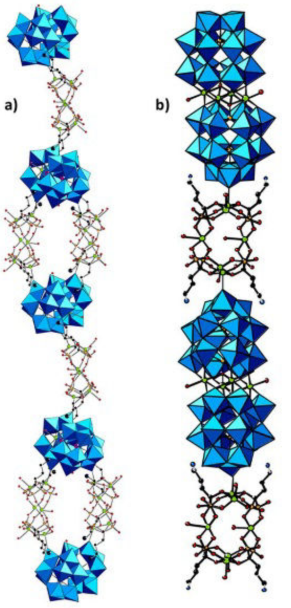

Figure 2. Ball-and-stick representations of the 1D structures of (a) $[\{(SbW_9O_{33})_2Cu_3(H_2O)_{2.5}Cl_{0.5}\}_2\{Cu_6(Ale)_4(H_2O)_4\}_3]^{37-}$ (**SbW$_9$CuAle**) and (b) $[\{(P_2W_{15}O_{56})_2Cu_4(H_2O)_2\}\{Cu_6(Ale)_4(H_2O)_4\}]^{20-}$ (**P$_2$W$_{15}$CuAle**). Blue octahedra, WO$_6$; purple spheres, Sb; green spheres, Cu; orange spheres, P; black spheres, C; blue spheres, N; red spheres, O.

The quantification of the magnetic exchange interactions in **SbW$_9$CuAle** and **SiW$_9$CuAle** is not an easy task considering that for these materials the measured $\chi_M T$ products are the resultant of the contributions of trinuclear POM units and hexanuclear $\{Cu_6Ale_4\}$ BP complexes. Moreover, **SbW$_9$CuAle** is made of three crystallographically independent $\{Cu_6Ale_4\}$ fragments and two crystallographically independent POM units (see above). Nevertheless, attempts to fit the data were effectuated.

Starting with **SbW$_9$CuAle**, it has been considered that (i) the two POMs and the three $\{Cu_6Ale_4\}$ units constituting this material are magnetically equivalent, respectively, and (ii) the $\{Cu_6Ale_4\}$ and the $\{(SbW_9)_2Cu_3\}$ units are magnetically isolated. Also, in the $\{(SbW_9)_2Cu_3\}$ fragment, it was assumed that the copper centers form an equilateral triangle. Besides, a two-J model was used for the modelization of the $\{Cu_6Ale_4\}$

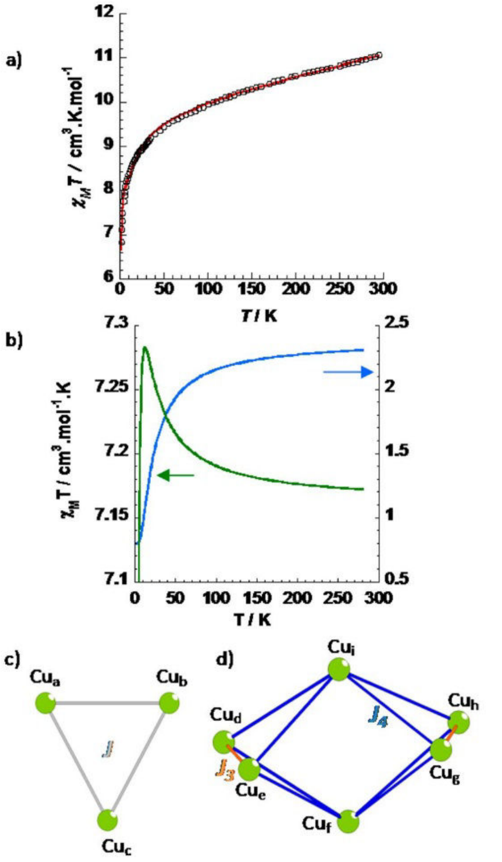

Figure 3. (a) Thermal behavior of $\chi_M T$ for **SbW$_9$CuAle** at 1000 Oe in the 2–300 K range. The solid red line above the experimental data is the theoretical curve derived from the Hamiltonian 1 (see text); (b) deconvolution of the theoretical thermal behavior of $\chi_M T$ for **SbW$_9$CuAle** highlighting the contributions of the POM (blue) and $\{Cu_6Ale_4\}$ (green) fragments; (c) the coupling scheme used for modelizing the magnetic behavior of the $\{(SbW_9O_{33})_2Cu_3\}$ units in **SbW$_9$CuAle**; (d) the coupling scheme used for modeling the magnetic behavior of the $\{Cu_6(Ale)_4(H_2O)_4\}$ units in **SbW$_9$CuAle** and **SiW$_9$CuAle**.

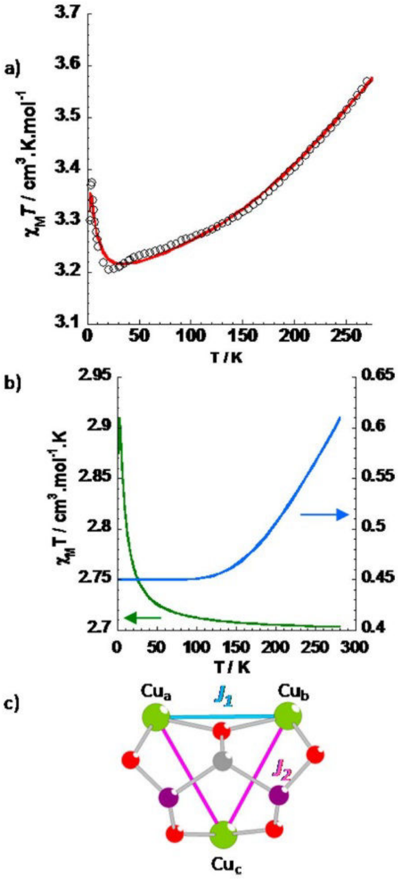

Figure 4. (a) Thermal behavior of $\chi_M T$ for **SiW$_9$CuAle** at 1000 Oe in the 2–300 K range. The solid red line above the experimental data is the theoretical curve derived from the Hamiltonian 2 (see text); (b) deconvolution of the theoretical thermal behavior of $\chi_M T$ for **SiW$_9$CuAle** highlighting the contributions of the POM (blue) and $\{Cu_6Ale_4\}$ (green) fragments. (c) The coupling scheme used for modelizing the magnetic behavior of the $\{SiW_9O_{34}Cu_3(Ale)(H_2O)\}$ unit in **SiW$_9$CuAle**.

complex. This led to the coupling schemes represented in Figure 3c,d, which correspond to the following Hamiltonian:

$$\begin{aligned}\hat{H}(1) = &-2J(\hat{S}_{Cua}\hat{S}_{Cub} + \hat{S}_{Cub}\hat{S}_{Cuc} + \hat{S}_{Cuc}\hat{S}_{Cua}) \\ &- 2J_3(\hat{S}_{Cud}\hat{S}_{Cue} + \hat{S}_{Cug}\hat{S}_{Cuh}) \\ &- 2J_4(\hat{S}_{Cue}\hat{S}_{Cuf} + \hat{S}_{Cud}\hat{S}_{Cuf} + \hat{S}_{Cuf}\hat{S}_{Cug} + \hat{S}_{Cuf}\hat{S}_{Cuh} \\ &+ \hat{S}_{Cug}\hat{S}_{Cui} + \hat{S}_{Cuh}\hat{S}_{Cui} + \hat{S}_{Cui}\hat{S}_{Cud} + \hat{S}_{Cui}\hat{S}_{Cue})\end{aligned} \qquad (1)$$

A good fit to the experimental $\chi_M T$ data in the 300–2 K temperature range has been obtained for $J = -6.80$ cm^{-1}, $J_3 = +2.40$ cm^{-1}, and $J_4 = -0.37$ cm^{-1} (TIP = 231×10^{-6} cm^3·mol^{-1} per Cu^{II} center (TIP stands for temperature-independent paramagnetism), g = 2.06, and R = 3.3×10^{-5}).[29] The calculated $|J|$ value is slightly higher than those previously determined for pure $\{(XW_9)_2Cu_3\}$ (X = As, Sb, Ge) POM species.[30] This can be due to the approximations mentioned above. In particular, in **SbW$_9$CuAle**, the intramolecular Cu···Cu distances are in the 4.72–4.84 Å range, while the shortest Cu···Cu distances between the copper ions of the $\{(SbW_9)_2Cu_3\}$ and those of the $\{Cu_6Ale_4\}$ units are of 5.52 Å. These relatively short intermolecular copper–copper distances can induce weak interactions, which were not taken into account in our model.

Focusing now on the $\{Cu_6Ale_4\}$ cluster, it is found that both ferromagnetic and anti-ferromagnetic magnetic interactions coexist in this fragment. It is well-known that, while several parameters affect the amplitude of the magnetic interactions in $\{Cu(OX)_2Cu\}$ (X = H, CH$_3$, Ph···) dimers with $d_{x^2-y^2}$ copper orbitals directed toward the bridging ligands, the major factor controlling the exchange coupling is the Cu–O(X)–Cu θ bridging angle. In OH-bridged complexes, based both on experimental results[31] or theoretical calculations,[32] a linear correlation between J and θ has been proposed, with a crossover point at $\theta \approx 97.5°$ below which the magnetic behavior changes from antiferromagnetic to ferromagnetic coupling. In contrast, for OPh-bridged complexes a crossover point has been theoretically predicted at $\theta \approx 77.5°$,[33] highlighting the huge importance of the X substituent borne by the oxygen atom. In the $\{Cu_6Ale_4\}$ cluster, the Cu_d and Cu_e and the Cu_h and Cu_g centers are dibridged by oxygen atoms of {P−C(O)−P} BP groups, respectively. Such magnetic core has not been previously reported. However, it can be mentioned that the $\{Cu-O(CP_2)-Cu\}$ fragment is characterized by θ angles in the 87.8−90.6° range. Such very low bridging angles must highly favor ferromagnetic interactions. Also, the two connected $\{CuO_4\}$ fragments are not planar, with a dihedral angle of 65.2−66.9°, thus reducing the overlap of the magnetic orbitals of the copper centers via the p-orbitals of the bridging oxygens. Both these factors explain the sign of the $J_3 = +2.40$ cm^{-1} constant determined.[34] Finally, weak anti-ferromagnetic interactions ($J_4 = -0.37$ cm^{-1}) were found between the copper centers connected by {O−P−O} bridges. The energy diagram deduced from the J_3 and J_4 values indicate that the ground state characterizing $\{Cu_6Ale_4\}$ is a triplet, with an $S = 0$ first excited state very close in energy and located at 0.74 cm^{-1}. The magnetic behavior of **SiW_9CuAle** was interpreted considering the POM $\{SiW_9Cu_3\}$ fragment and the $\{Cu_6Ale_4\}$ cluster as magnetically isolated. In $\{SiW_9Cu_3\}$, the copper centers form an isosceles triangle, necessitating the introduction of an additive exchange parameter compared to the model used for the $\{SbW_9Cu_3\}$ magnetic unit. The coupling scheme associated with **SiW_9CuAle** is represented in Figures 3d and 4c and leads to the following Hamiltonian:

$$\begin{aligned}\hat{H}(2) = & -2J_1\hat{S}_{Cua}\hat{S}_{Cub} - 2J_2(\hat{S}_{Cub}\hat{S}_{Cuc} + \hat{S}_{Cuc}\hat{S}_{Cua}) \\ & - 2J_3(\hat{S}_{Cud}\hat{S}_{Cue} + \hat{S}_{Cug}\hat{S}_{Cuh}) \\ & - 2J_4(\hat{S}_{Cue}\hat{S}_{Cuf} + \hat{S}_{Cud}\hat{S}_{Cuf} + \hat{S}_{Cuf}\hat{S}_{Cug} + \hat{S}_{Cuf}\hat{S}_{Cuh} \\ & + \hat{S}_{Cug}\hat{S}_{Cui} + \hat{S}_{Cuh}\hat{S}_{Cui} + \hat{S}_{Cui}\hat{S}_{Cud} + \hat{S}_{Cui}\hat{S}_{Cue})\end{aligned} \tag{2}$$

The best fit to the experimental $\chi_M T$ data in the 300−2 K temperature range was obtained for $J_1 = -255$ cm^{-1}, $J_2 = -55.0$ cm^{-1}, $J_3 = +1.56$ cm^{-1}, and $J_4 = -0.11$ cm^{-1} (TIP = 110×10^{-6} cm^3·mol^{-1} per Cu^{II} center, $g = 2.19$, and $R = 8.6 \times 10^{-6}$).[29] Considering the $\{SiW_9Cu_3\}$ fragment, the $d_{x^2-y^2}$ orbitals of the Cu_a and Cu_b atoms interact via the p-orbital of the deprotonated O(C) atom of the BP ligand, with a low dihedral angle of 12.1° and a large θ Cu−O−Cu bridging angle of 134.1°. This leads to a strong anti-ferromagnetic interaction ($J_1 = -255$ cm^{-1}), slightly higher than those found for the few previously reported single alkoxo-bridged Cu^{II} dimers. For example, a coupling constant of −191.5 cm^{-1} was found for the $[Cu_2(bdmap)(acac)(NH_3)]^{2+}$ (bdmap = 1,3-bis(dimethylamino)-2-propanolato; acac = acetylacetonate) complex (θ = 135.8°).[35] However, in **SiW_9CuAle**, the copper centers are bridged by an additional O−Si−O group. The coupling constant associated with the interactions involving the magnetic metal centers connected via O−P−O bridges is also negative but, as expected, weaker ($J_2 = -55.0$ cm^{-1}).

While the $\chi_M T$ behavior at high temperature is mainly due to the $\{SiW_9Cu_3\}$ unit, at lower temperature, the increase observed between 25 and 3 K is related to the ferromagnetic interactions between, respectively, the Cu_d and Cu_e and the Cu_h and Cu_g centers ($J_3 = +1.56$ cm^{-1}) belonging to the $\{Cu_6Ale_4\}$ fragment (Figure 4b). In contrast, we can note that, for **SbW_9CuAle**, the low-temperature $\chi_M T$ versus T behavior is due *both* to the $\{Cu_6Ale_4\}$ ($J_3 = +2.40$ cm^{-1} and $J_4 = -0.37$ cm^{-1}) and the $\{SbW_9Cu_3\}$ ($J = -6.80$ cm^{-1}) fragments. As a consequence, on the **SbW_9CuAle** $\chi_M T$ versus T plot, the ferromagnetic coupling in $\{Cu_6Ale_4\}$ is masked by the weak anti-ferromagnetic coupling in the $\{SbW_9Cu_3\}$ fragment; a deconvolution of the $\chi_M T$ versus T curve is thus needed for visualizing the ferromagnetic exchange in **SbW_9CuAle** (Figure 3b). In addition, for **SiW_9CuAle**, the $\chi_M T$ decrease below 3 K is correlated to the small anti-ferromagnetic interactions between the O−P−O bridged Cu^{II} ions of $\{Cu_6Ale_4\}$ ($J_4 = -0.11$ cm^{-1}). Importantly, we can note that the magnetic coupling constants characterizing the $\{Cu_6Ale_4\}$ unit and determined in **SbW_9CuAle** and **SiW_9CuAle** are in good agreement.

Electrochemistry. The redox potentials of **$P_2W_{15}CuAle$**, **SbW_9CuAle**, and **SiW_9CuAle** in a pH 5 and pH 1 medium are gathered in Table 2 and compared to that of the previously reported fully inorganic $[(SbW_9O_{33})_2\{Cu(H_2O)\}_3]^{12-}$ (**$Sb_2W_{18}Cu_3$**) POM[16] considered here as a reference.

Table 2. Reduction and Reoxidation Peak Potentials[a] Measured from Cyclic Voltammograms of $Sb_2W_{18}Cu_3$, SiW_9CuAle, SbW_9CuAle, and $P_2W_{15}CuAle$

	compounds	*	I	II	III	IV
		Cu 0/II	Cu II/I	Cu I/0	W VI/V	
		Ep_a	$E_{1/2}$	Ep_c	$E_{1/2}$	$E_{1/2}$
pH 5	$Sb_2W_{18}Cu_3$	−0.02	−0.13	−0.22	−0.59	−0.81
	SbW_9CuAle	0.03	−0.11	−0.16		
	SiW_9CuAle	0.02	−0.11	−0.16		
	$P_2W_{15}CuAle$	−0.02	−0.14	−0.18	−0.57	
	$P_2W_{15}Cu_4$	−0.02	−0.22	−0.34	−0.58	−0.80
pH 1	$Sb_2W_{18}Cu_3$	0.03	−0.06	−0.12	−0.44	
	SbW_9CuAle	0.05	−0.03	−0.09		
	SiW_9CuAle	0.00	−0.03	−0.11	−0.52	
	$P_2W_{15}CuAle$	0.01	−0.06	−0.10		
	$P_2W_{15}Cu_4$	0.01	−0.10	−0.12	−0.23	−0.31

[a] Potentials in volts vs SCE were obtained from cyclic voltammetry in pH 5 medium (1 M CH_3COOLi + CH_3COOH) or in pH 1 medium (0.5 M Na_2SO_4 + H_2SO_4 at pH 1). Scan rate = 2 mV s^{-1}. Working electrode: glassy carbon.

The cyclic voltammogram (CV) of **$P_2W_{15}CuAle$** in a pH 5 medium is shown in Figure 5A. In the potential domain explored, it consists of three waves with peak potentials located at −0.14, −0.18, and −0.57 V versus SCE, respectively. The last reversible wave, denoted III in Figure 5A, is attributed to the redox processes of the W centers (W^{VI}/W^{V} couple). To the reduction waves I and II is associated a single oxidation peak at −0.02 V versus SCE with a characteristic shape usually encountered for the oxidation of Cu^0 species.[24b]

The shapes and potential positions of the Cu^{II} reduction waves I and II are analogous to those already observed for Cu-substituted POMs.[36] This pattern features the two-step reduction of Cu^{II} to Cu^0 through Cu^I. The first reduction wave is reversible. Plot of the cathodic current (I_{pc}) versus the square root of the scan rate $v^{1/2}$ shows a linear dependence (inset of Figure 5B) showing that the current is limited by the diffusion of **$P_2W_{15}CuAle$** to the electrode surface as expected for a reversible process where the species is in solution. Controlled potential coulometry at a potential just below that of the peak potential of the second reduction process of **$P_2W_{15}CuAle$** (at −0.20 V vs SCE) indicates the exchange of 19 electrons per molecule, in agreement with the reduction of the

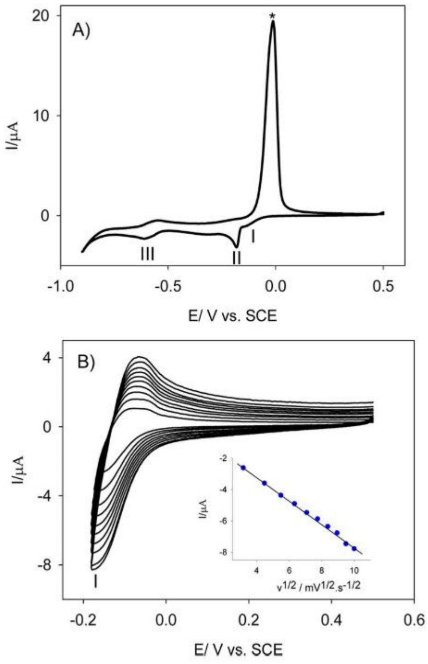

Figure 5. (A) CV of 0.1 mM **$P_2W_{15}CuAle$** in a pH 5 buffer solution (1 M CH_3COOLi + CH_3COOH). $\nu = 2$ mV·s^{-1}. (B) Variation of scan rates (from inner to outer curve): 10, 20, 30, 40, 50, 60, 70, 80, 90, and 100 mV s^{-1}. The potential reversal is fixed after the Cu^{II} to Cu^{I} redox process. (inset) Variation of the cathodic peak current intensity as a function of the square root of the scan rate. The working electrode was glassy carbon, and the reference electrode was the SCE. *Reoxidation peak of the deposited Cu^0 on electrode surface.

10 Cu^{II} centers in Cu^0. This is also confirmed by the black deposit visible on the electrode surface.

$Sb_2W_{18}Cu_3$, **SbW_9CuAle**, **SiW_9CuAle**, and **$P_2W_{15}Cu_4$** show at pH 5 (see Supporting Information, Figures S2−S5) similar redox behavior with two successive reduction waves associated with the reduction of Cu^{II} to Cu^{I} and the reduction of Cu^{I} to Cu^0. On potential reversal, a large oxidation current wave is observable, which displays the characteristic shape for the reoxidation of deposited Cu^0 on the electrode surface. Again for the first couple, Cu^{II}/Cu^{I}, the cathodic peak current (i_{pc}) is proportional to the square root of the scan rate, which indicates that the electrochemical processes are diffusion-controlled. For the **$P_2W_{15}Cu_4$** compound the first redox wave attributed to the W^{VI}/W^{V} couple is observed nearly at the same potential than for **$P_2W_{15}CuAle$** (Table 2). At variance, for **SbW_9CuAle** and **SiW_9CuAle**, the W^{VI}/W^{V} reversible waves III are not observable, while two ill-defined waves are observed at −0.59 and −0.81 V versus SCE for the parent compound **$Sb_2W_{18}Cu_3$**. Controlled potential coulometry at a potential just below the peak potential of the second reduction process for **$Sb_2W_{18}Cu_3$**, **SbW_9CuAle**, and **SiW_9CuAle** indicate that all the Cu^{II} centers are actually reduced with the exchange of 6.1, 48.2, and 18.2 electrons per molecule, respectively.

At pH 1 all the compounds present similar redox behavior with again two consecutive reduction waves related to the reduction of Cu^{II} to Cu^{I} and the reduction of Cu^{I} to Cu^0 (see Supporting Information, Figures S6−S10). In the reverse scan, a large reoxidation current wave is still noticeable. The only change is a small anodic shift of ca. 70−80 mV for the Cu^{II}/Cu^{I} couple and of ca. 50−100 mV for the Cu^{I}/Cu^0 couple, showing that these compounds are easier to reduce at lower pH. These small shifts may be due to the nature of the buffer used (1 M CH_3COOLi + CH_3COOH at pH 5 vs 0.5 M Na_2SO_4 + H_2SO_4 at pH 1). Another possible explanation is the influence of the pK_a of the aqua Cu(II) centers (Cu^{II}−OH_2) that can be easily deprotonated, giving the hydroxo forms Cu(II) centers (Cu^{II}−OH) when the pH increases as shown in previous work.[37]

Electrocatalysis of NO_x Reduction. Nitrate reduction was chosen to investigate the electrocatalytic capacities of each complex studied in this work. The nitrite reduction, NO_2^- being a possible chemical intermediate in the reduction of nitrate, has been studied.

Reduction of Nitrate. The CVs were measured as a function of the excess parameter γ ($\gamma = C_{NO_3^-}/C_{POM}$) with the same potential scan rate (2 mV·s^{-1}). As is apparent in Figure 6 at pH 5 for **$P_2W_{15}CuAle$**, the addition of even modest quantities of nitrate induced a large cathodic current enhancement starting at a potential below −0.75 V (only after the first W wave). These observations show an efficient reduction of nitrate by the reduced species of **$P_2W_{15}CuAle$**. In the explored potential domain, no reduction of nitrate could be detected on the glassy carbon electrode in the absence of polyoxometalate complexes (see Supporting Information, Figure S11). The relative electrocatalytic activities of the reported POMs can be determined calculating the kinetic current $J_{kinetic\ (NO_3^-)}$, using the following formula:

$$J_{kinetic(NO_3^-)} = (I_{POM+NO_3^-} - I_{POM})/S$$

where $I_{POM+NO_3^-}$ is the reduction current of the POM in the presence of nitrate, I_{POM} is the reduction current for the POM alone, and S is the geometrical surface of the electrode. In the

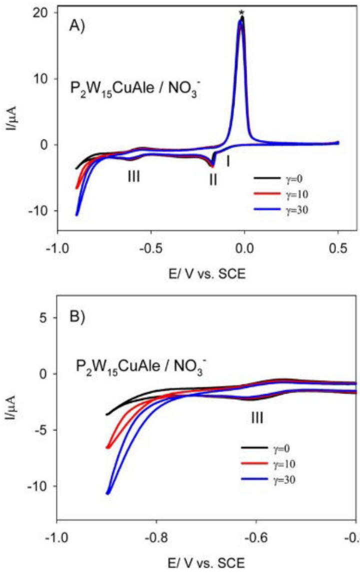

Figure 6. (A) Electrocatalysis of NO_3^- reduction in the presence of 0.1 mM **$P_2W_{15}CuAle$** in a pH 5 medium, $\nu = 2$ mV·s^{-1}. (B) Magnification of (A) to highlight the reduction of nitrate ions. *Reoxidation peak of the deposited Cu^0 on electrode surface.

current experiment, for $\mathbf{P_2W_{15}CuAle}$ and at pH 5, the $J_{\text{kinetic }(\text{NO}_3^-)}$ values measured at −0.90 V are −43.0 and −100.0 μA·cm^{-2} for excess parameters γ of 10 and 30, respectively. $\mathbf{SiW_9CuAle}$, in the same conditions, provides the $J_{\text{kinetic }(\text{NO}_3^-)}$ values of −99.2 and −209.6 μA·cm^{-2} for γ = 10 and 30, respectively (see Supporting Information, Table S1 and Figure S12).

For $\mathbf{P_2W_{15}Cu_4}$, using the same conditions at pH 5, the $J_{\text{kinetic }(\text{NO}_3^-)}$ values measured at −0.90 V are lower: −8.7 and −22.7 μA·cm^{-2} for excess parameters γ of 10 and 30, respectively (see Supporting Information, Table S1, Figures S13−S14). Similar electrocatalytic behaviors were previously published by Nadjo et al. for this compound.[38] It thus should be noticed that the $J_{\text{kinetic }(\text{NO}_3^-)}$ values obtained for $\mathbf{P_2W_{15}CuAle}$ are significantly higher than the ones obtained for the corresponding POM without the copper/alendronate complexes, which might be due to the higher number of Cu atoms in the $\mathbf{P_2W_{15}CuAle}$ compound (four in $\mathbf{P_2W_{15}Cu_4}$ versus 10 in $\mathbf{P_2W_{15}CuAle}$).

Surprisingly, the $\mathbf{Sb_2W_{18}Cu_3}$ and $\mathbf{SbW_9CuAle}$ compounds do not present significant cathodic enhancements upon the addition of nitrate in solution (see Supporting Information, Table S1 and Figures S15 and S16). So only the $\mathbf{P_2W_{15}CuAle}$, $\mathbf{P_2W_{15}Cu_4}$, and $\mathbf{SiW_9CuAle}$ compounds show an efficient reduction of nitrate but only after the first $\text{W}^{\text{VI}}/\text{W}^{\text{V}}$ reduction wave of the POM subunit, hence, after the reduction step II (couple $\text{Cu}^{\text{I}}/\text{Cu}^0$) corresponding to the copper deposition on the glassy carbon electrode. This suggests that the chemical nature of the POM entities adsorbed on the surface of the Cu^0 nanoparticles strongly affects the electrocatalytic activity for the reduction of nitrate on the Cu^0 nanoparticles.

Furthermore, it is worth pointing out that the catalytic current with Cu-containing POMs may not be due solely to the amount of deposited Cu^0 (which is higher for $\mathbf{SbW_9CuAle}$ than for $\mathbf{P_2W_{15}CuAle}$), but should also be influenced by the type of POM used. Thus, the electrocatalytic reduction of nitrate must be traced successively to the properties of the electrodeposited copper and to those of the reduced W centers.

At pH 1, $\mathbf{P_2W_{15}CuAle}$ gives the $J_{\text{kinetic }(\text{NO}_3^-)}$ values of −145.3 and −397.5 μA.cm^{-2} for γ = 10 and 30, respectively, showing an increase of current of the reduction of the nitrate at low pH (see Supporting Information, Figure S17). $\mathbf{SiW_9CuAle}$ under the same conditions provides the same behavior with $J_{\text{kinetic }(\text{NO}_3^-)}$ values of −276.5 and −537.0 μA.cm^{-2} for γ = 10 and 30, respectively, indicating an increase of more than 2 times the current for the reduction of nitrate for $\mathbf{SiW_9CuAle}$ at low pH (see Supporting Information, Table S1 and Figure S18). Again, $\mathbf{Sb_2W_{18}Cu_3}$ and $\mathbf{SbW_9CuAle}$ do not present a cathodic enhancement upon the addition of nitrate in solution at pH 1 (see Supporting Information, Table S1 and Figures S19 and S20).

Reduction of Nitrite. All the four complexes showed a good efficiency upon the reduction of nitrite. The results for $J_{\text{kinetic }(\text{HNO}_2/\text{NO}_2^-)}$ values are gathered for comparison in the Supporting Information (Table S1, Figures S21−S28). Figure 7 indicates that upon reduction, $\mathbf{P_2W_{15}CuAle}$ catalyzes the reduction of nitrite at pH 5.

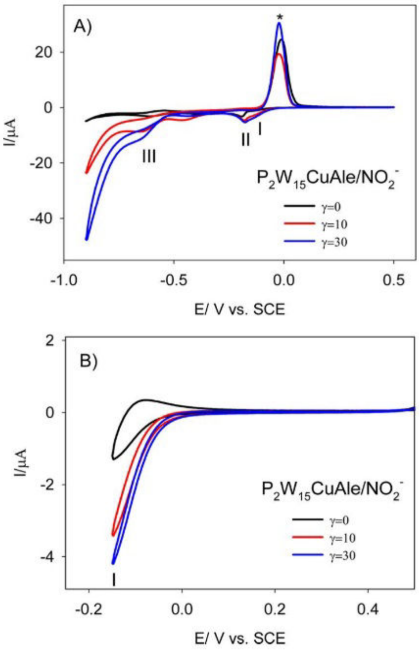

Figure 7. (A) Electrocatalysis of NO_2^- reduction in the presence of 0.1 mM $\mathbf{P_2W_{15}CuAle}$ in a pH 5 medium. ν = 2 mV·s^{-1}, the working electrode was GC, and the reference electrode was the SCE. (B) Electrocatalysis of NO_2^- reduction with reversal potential fixed after the $\text{Cu}^{2+}/\text{Cu}^+$ redox process. *Reoxidation peak of the deposited Cu^0 on electrode surface.

The electrocatalytic reduction of nitrite is found to occur just before the deposition of Cu^0 (wave II), after the first reversible wave corresponding to the $\text{Cu}^{\text{II}}/\text{Cu}^{\text{I}}$ reduction process (wave I). $J_{\text{kinetic }(\text{NO}_2^-)}$ measured at −0.15 V (peak I) and for γ = 10 and 30 were −30.3 and −40.7 μA·cm^{-2}, respectively (see Supporting Information, Table S1). In contrast, at this potential and in the same medium, no significant electrocatalytic activity toward the reduction of NO_3^- was detected. It is remarkable that in the presence of NO_2^-, a significant reduction current is obtained at the potential of the peak I, while no Cu^0 oxidation peak is obtained during the reversed anodic scan when the cathodic potential limit is set at −0.1 V versus SCE (Figure 8B). This shows that NO_2^- is able to reoxidize the electrochemically generated Cu^{I}POMAle species, leading to the regeneration of the Cu^{II}POMAle species, which seems to be stable when the potential is kept above −0.1 V versus SCE. It can be concluded that this POM is a good electrocatalyst for the reduction of nitrite in more acidic solution. We can note that at pH 1, the active species should be HNO_2 and/or NO. As a matter of fact, the equilibrium $\text{HNO}_2 + \text{H}_2\text{O} \leftrightarrows \text{H}_3\text{O}^+ + \text{NO}_2^-$ (pK_a = 3.3 at 18 °C) takes place. Also, even if HNO_2 disproportionates in a fairly acidic solution, with $3\text{HNO}_2 \rightarrow \text{H}_3\text{O}^+ + \text{NO}_3^- + 2\text{NO}$, the rate of this reaction is known to be low. $\mathbf{P_2W_{15}CuAle}$ at pH 1 presents the larger cathodic current enhancement (Figure 8) in a potential domain of first wave ($\text{Cu}^{\text{II}}/\text{Cu}^{\text{I}}$ couple) compared to $\mathbf{SiW_9CuAle}$, $\mathbf{SbW_9CuAle}$, and $\mathbf{P_2W_{15}Cu_4}$. The corresponding calculated $J_{\text{kinetic }(\text{HNO2})}$ for γ = 10 and 30 at −0.07 V versus SCE were −49.9 and −103.2 μA·cm^{-2}, respectively (see Supporting Information, Table S1).

In summary, the four complexes showed a good efficiency upon the reduction of nitrite, the efficiency being better at pH 1. A significant electrocatalytic activity could be measured already in a potential domain related to the first wave ($\text{Cu}^{\text{II}}/\text{Cu}^{\text{I}}$

DOI: 10.1021/acs.inorgchem.5b02456
Inorg. Chem. 2016, 55, 1551−1561

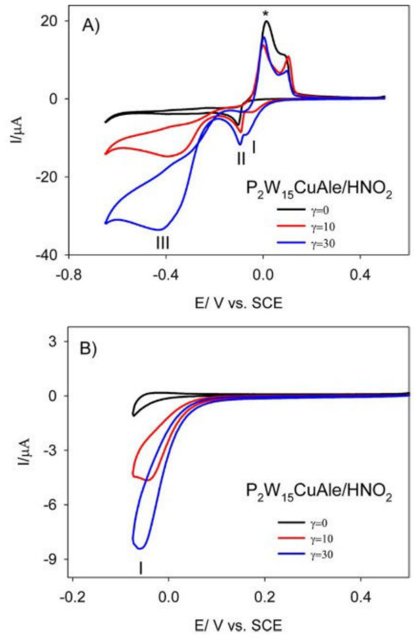

Figure 8. (A) Electrocatalysis of NO_2^- reduction in the presence of 0.1 mM **$P_2W_{15}CuAle$** in a pH 1 medium, $\nu = 2$ mV·s^{-1}, the working electrode was GC, and the reference electrode was SCE. (B) Electrocatalysis of NO_2^- reduction with reversal potential fixed after the Cu^{II}/Cu^{I} redox process. *Reoxidation peak of the deposited Cu^0 on electrode surface.

couple), suggesting that Cu^I was already able to reduce HNO_2/NO_2^-.

■ CONCLUSION

We have thus reported here the first materials associating polyoxotungstates, bisphosphonates, and copper ions. They consist in 1D compounds made of two adjacent anionic $[Cu_6(Ale)_4(H_2O)_4]^{4-}$ and POM units, with a $[Cu_6(Ale)_4(H_2O)_4]^{4-}$/POM ratio depending on the nature of the POM. In **SiW_9CuAle**, an alendronate ligand is directly connected to the $\{Cu_3\}$ fragment capping the POM unit. In contrast, no alendronate is grafted on the POM fragment in **SbW_9CuAle** and **$P_2W_{15}CuAle$**, these compounds being made of pure inorganic POMs connected to $[Cu_6(Ale)_4(H_2O)_4]^{4-}$ clusters. Combining the magnetic studies of **SiW_9CuAle** and **SbW_9CuAle**, it has been possible to evidence the coexistence of ferromagnetic and anti-ferromagnetic interactions in the $[Cu_6(Ale)_4(H_2O)_4]^{4-}$ unit, while strong anti-ferromagnetic interactions have been found in the $[SiW_9O_{34}Cu_3(Ale)(H_2O)]^{8-}$ fragment constituting **SiW_9CuAle**. The ability of the three reported compounds to electrocatalytically reduce nitrite and nitrate has been studied. All the studied compounds present a good efficiency upon the reduction of HNO_2 or NO_2^-. In contrast, it has been found that the purely inorganic complex **$Sb_2W_{18}Cu_3$** is inactive toward the reduction of nitrate, highlighting that the formation of a Cu^0 film at the electrode is not sufficient for electrocatalytically reducing NO_3^-. The **SbW_9CuAle** complex is also inactive toward nitrate reduction. As this compound is made of a $\{(SbW_9)_2Cu_3\}$ fragment, similar to that found in **$Sb_2W_{18}Cu_3$**, and $[Cu_6(Ale)_4(H_2O)_4]^{4-}$ units, this evidence that the copper/alendronate cluster is also inactive. In contrast, **SiW_9CuAle** and **$P_2W_{15}CuAle$** have shown a good efficiency as precatalysts upon the reduction of NO_3^- either at pH 1 or at pH 5, showing that the chemical nature of the POM is a crucial parameter for the catalytic reduction of nitrate by POM species. Interestingly, comparison of the activities of **$P_2W_{15}CuAle$** and $[(P_2W_{15}O_{56})_2Cu_4(H_2O)_2]^{16-}$ evidenced that if the $\{Cu_6(Ale)_4(H_2O)_4\}$ cluster does not act as an electrocatalyst, it acts as a cofactor, significantly enhancing the catalytic efficiency of the active POM. Moreover, it must be possible to introduce functional organic or inorganic fragments into the **SiW_9CuAle** POM by prefunctionalization of the bisphosphonate via its amino group, as previously shown for cobalt[38] and nickel[14] derivatives. In particular, the grafting of an anchoring organic group onto the bisphosphonate ligand constituting **SiW_9CuAle**, allowing to prepare covalently functionalized electrodes, is under study.

■ ASSOCIATED CONTENT

Ⓢ Supporting Information

The Supporting Information is available free of charge on the ACS Publications website at DOI: 10.1021/acs.inorgchem.5b02456.

CVs of **$P_2W_{15}CuAle$**, **$Sb_2W_{18}Cu_3$**, **SbW_9CuAle**, and **SiW_9CuAle** in a pH 5 and pH 1 medium. Table of the value of the catalytic efficiency CAT at different values of the excess parameter γ ($\gamma = C^0_{NO_3^-}/C^0_{POM}$ or $\gamma = C^0_{HNO_3}/C^0_{POM}$) in a pH 5 and pH 1 medium. (PDF)

X-ray crystallographic information. (CIF)

X-ray crystallographic information. (CIF)

■ AUTHOR INFORMATION

Corresponding Authors

*E-mail:lruhlmann@unistra.fr. (L.R.)
*E-mail: pierre.mialane@uvsq.fr. (P.M.)

Author Contributions

⊥These authors contributed equally to this work.

Notes

The authors declare no competing financial interest.

■ ACKNOWLEDGMENTS

This work was supported by the Ministère de l'Enseignement Supérieur et de la Recherche, the CNRS, the Univ. de Versailles Saint Quentin en Yvelines, the Univ. de Strasbourg, the Univ. Paris Sud, and a public grant overseen by the French National Research Agency (ANR) as part of the "Investissements d'Avenir" Program No. ANR-11-IDEX-0003-02 and the Labex CHARMMMAT ANR-11-LABX-0039. We also thank the Labex CSC of the Univ. of Strasbourg for financial support.

■ REFERENCES

(1) (a) Miras, H. N.; Yan, J.; Long, D.-L.; Cronin, L. *Chem. Soc. Rev.* **2012**, *41*, 7403. (b) Banerjee, A.; Bassil, B. S.; Röschenthaler, G.-V.; Kortz, U. *Chem. Soc. Rev.* **2012**, *41*, 7590. (c) Sartorel, A.; Bonchio, M.; Campagna, S.; Scandola, F. *Chem. Soc. Rev.* **2013**, *42*, 2262. (d) Lv, H.; Geletii, Y. V.; Zhao, C.; Vickers, J. W.; Zhu, G.; Luo, Z.; Song, J.; Lian, T.; Musaev, D. G.; Hill, C. L. *Chem. Soc. Rev.* **2012**, *41*, 7572. (e) Proust, A.; Matt, B.; Villanneau, R.; Guillemot, G.; Gouzerh, P.; Izzet, G. *Chem. Soc. Rev.* **2012**, *41*, 7605. (f) Reinoso, S. *Dalton Trans.* **2011**, *40*, 6610. (g) Du, D. Y.; Yan, L. K.; Su, Z.-M.; Li, S. L.; Lan, Y. Q.; Wang, E.-B. *Coord. Chem. Rev.* **2013**, *257*, 702.

(2) *Inorganic Syntheses;* Ginsberg, A. P., Ed.; John Wiley and Sons: New York, 1990; Vol. *27*.

(3) (a) Zheng, S.-T.; Yang, G.-Y. *Chem. Soc. Rev.* **2012**, *41*, 7623. (b) Oms, O.; Dolbecq, A.; Mialane, P. *Chem. Soc. Rev.* **2012**, *41*, 7497.

(4) (a) *Trends in Polyoxometalate Researchs;* Ruhlmann, L., Ed.; Nova Science Publishers: New York, 2015. (b) Godin, B.; Chen, Y.-G.; Vaissermann, J.; Ruhlmann, L.; Verdaguer, M.; Gouzerh, P. *Angew. Chem., Int. Ed.* **2005**, *44*, 3072. (c) Al-Oweini, R.; Bassil, B. S.; Friedl, J.; Kottisch, V.; Ibrahim, M.; Asano, M.; Keita, B.; Novitchi, G.; Lan, Y.; Powell, A.; Stimming, U.; Kortz, U. *Inorg. Chem.* **2014**, *53*, 5663. (d) Fang, X.; Speldrich, M.; Schilder, H.; Cao, R.; O'Halloran, K. P.; Hill, C. L.; Kögerler, P. *Chem. Commun.* **2010**, *46*, 2760. (e) Zheng, S.-T.; Zhang, J.; Li, X.-X.; Fang, W.-H.; Yang, G.-Y. *J. Am. Chem. Soc.* **2010**, *132*, 15102. (f) Rousseau, G.; Oms, O.; Dolbecq, A.; Marrot, J.; Mialane, P. *Inorg. Chem.* **2011**, *50*, 7376.

(5) (a) Wang, J.; Du, J.; Niu, J. *CrystEngComm* **2008**, *10*, 972. (b) Wang, J.; Ma, P.; Shen, Y.; Niu, J. *Cryst. Growth Des.* **2008**, *8*, 3130. (c) Zheng, S.-T.; Yuan, D.-Q.; Jia, H.-P.; Zhang, J.; Yang, G.-Y. *Chem. Commun.* **2007**, 1858. (d) Li, B.; Zhao, J.-W.; Zheng, S.-T.; Yang, G.-Y. *Inorg. Chem.* **2009**, *48*, 8294. (e) Mialane, P.; Dolbecq, A.; Marrot, J.; Rivière, E.; Sécheresse, F. *Chem. - Eur. J.* **2005**, *11*, 1771. (f) Artetxe, B.; Reinoso, S.; San Felices, L.; Lezama, L.; Pache, A.; Vicent, C.; Gutiérrez-Zorrilla, J. M. *Inorg. Chem.* **2015**, *54*, 409.

(6) (a) Clemente-Juan, J. M.; Coronado, E.; Gaita-Ariño, A. *Chem. Soc. Rev.* **2012**, *41*, 7464. (b) Kögerler, P.; Tsukerblat, B.; Müller, A. *Dalton Trans.* **2010**, *39*, 21.

(7) (a) Ritchie, C.; Ferguson, A.; Nojiri, H.; Miras, H. N.; Song, Y.-F.; Long, D.-L.; Burkholder, E.; Murrie, M.; Kögerler, P.; Brechin, E. K.; Cronin, L. *Angew. Chem., Int. Ed.* **2008**, *47*, 5609. (b) Compain, J.-D.; Mialane, P.; Dolbecq, A.; Mbomekalle, I. M.; Marrot, J.; Sécheresse, F.; Rivière, E.; Rogez, G.; Wernsdorfer, W. *Angew. Chem., Int. Ed.* **2009**, *48*, 3077. (c) Ibrahim, M.; Lan, Y.; Bassil, B. S.; Xiang, Y.; Suchopar, A.; Powell, A. K.; Kortz, U. *Angew. Chem., Int. Ed.* **2011**, *50*, 4708. (d) Sawada, Y.; Kosaka, W.; Hayashi, Y.; Miyasaka, H. *Inorg. Chem.* **2012**, *51*, 4824. (e) Fang, X.; Kögerler, P.; Speldrich, M.; Schilder, H.; Luban, M. *Chem. Commun.* **2012**, *48*, 1218. (f) Vonci, M.; Boskovic, C. *Aust. J. Chem.* **2014**, *67*, 1542. (g) Sato, R.; Suzuki, K.; Minato, T.; Shinoe, M.; Yamaguchi, K.; Mizuno, N. *Chem. Commun.* **2015**, *51*, 4081.

(8) (a) Special issue on polyoxometalates with catalytic and electrocatalytic properties: Hill, C. L. Ed., *J. Mol. Catal. A: Chem.* **2007**, *262*, 1. See also some recent examples.10.1016/j.molcata.2006.08.041 (b) Han, X.-B.; Li, Y.-G.; Zhang, Z.-M.; Tan, H.-Q.; Lu, Y.; Wang, E.-B. *J. Am. Chem. Soc.* **2015**, *137*, 5486. (c) Hao, H.-F.; Zhou, W.-Z.; Zang, H.-Y.; Tan, H.-Q.; Qi, Y.-F.; Wang, Y.-H.; Li, Y.-G. *Chem. - Asian J.* **2015**, *10*, 1676. (d) Huo, Y.; Huo, Z.; Ma, P.; Wang, J.; Niu, J. *Inorg. Chem.* **2015**, *54*, 406. (e) Von Allmen, K.; Moré, R.; Müller, R.; Soriano-López, J.; Linden, A.; Patzke, G. R. *ChemPlusChem* **2015**, *80*, 1389.

(9) Yin, Q.; Tan, J. M.; Besson, C.; Geletii, Y. V.; Musaev, D. G.; Kuznetsov, A. E.; Luo, Z.; Hardcastle, K. I.; Hill, C. L. *Science* **2010**, *328*, 342.

(10) (a) Amanchi, S. R.; Khenkin, A. M.; Diskin-Posner, Y.; Neumann, R. *ACS Catal.* **2015**, *5*, 3336. (b) Anderson, T. M.; Zhang, X.; Hardcastle, K. I.; Hill, C. L. *Inorg. Chem.* **2002**, *41*, 2477.

(11) See, for example, (a) Wang, X.-L.; Li, T.-J.; Tian, A.-X.; Li, N.; Yang, Y.; Ning, Y.-L.; Hou, X. *CrystEngComm* **2015**, *17*, 3257. (b) Yao, S.; Zhang, Z.; Li, Y.; Wang, E. *Dalton Trans.* **2010**, *39*, 3884. (c) Mitchell, S. G.; Khanra, S.; Miras, H. N.; Boyd, T.; Long, D.-L.; Cronin, L. *Chem. Commun.* **2009**, 2712. (d) Li, Y.-W.; Li, Y.-G.; Wang, Y.-H.; Feng, X.-J.; Lu, Y.; Wang, E.-B. *Inorg. Chem.* **2009**, *48*, 6452. (e) Boyd, T.; Mitchell, S. G.; Miras, H. N.; Long, D.-L.; Cronin, L. *Dalton Trans.* **2010**, *39*, 6460. (f) Mbomekalle, I. M.; Mialane, P.; Dolbecq, A.; Marrot, J.; Sécheresse, F.; Berthet, P.; Keita, B.; Nadjo, L. *Eur. J. Inorg. Chem.* **2009**, *2009*, 5194. (g) Ruhlmann, L.; Canny, J.; Contant, R.; Thouvenot, R. *Inorg. Chem.* **2002**, *41*, 3811. (h) Yao, S.; Zhang, Z.; Li, Y.; Wang, E. *Dalton Trans.* **2010**, *39*, 3884. (i) Zhang, Z.; Yao, S.; Qi, Y.; Li, Y.; Wang, Y.; Wang, E. *Dalton Trans.* **2008**, 3051.

(12) (a) Zhang, Z.; Qi, Y.; Qin, C.; Li, Y.; Wang, E.; Wang, X.; Su, Z.; Xu, L. *Inorg. Chem.* **2007**, *46*, 8162. (b) Mal, S. S.; Bassil, B. S.; Ibrahim, M.; Nellutla, S.; van Tol, J.; Dalal, N. S.; Fernández, J. A.; López, X.; Poblet, J. M.; Biboum, R. N.; Keita, B.; Kortz, U. *Inorg. Chem.* **2009**, *48*, 11636. (c) Nellutla, S.; van Tol, J.; Dalal, N. S.; Bi, L.-H.; Kortz, U.; Keita, B.; Nadjo, L.; Khitrov, G. A.; Marshall, A. G. *Inorg. Chem.* **2005**, *44*, 9795.

(13) (a) Mal, S. S.; Dickman, M. H.; Kortz, U.; Todea, A. M.; Merca, A.; Bögge, H.; Glaser, T.; Müller, A.; Nellutla, S.; Kaur, N.; van Tol, J.; Dalal, N. S.; Keita, B.; Nadjo, L. *Chem. - Eur. J.* **2008**, *14*, 1186. (b) Bi, L.-H.; Kortz, U.; Nellutla, S.; Stowe, A. C.; van Tol, J.; Dalal, N. S.; Keita, B.; Nadjo, L. *Inorg. Chem.* **2005**, *44*, 896.

(14) El Moll, H.; Rousseau, G.; Dolbecq, B.; Oms, O.; Marrot, J.; Haouas, M.; Taulelle, F.; Rivière, E.; Wernsdorfer, W.; Lachkar, D.; Lacôte, E.; Keita, B.; Mialane, P. *Chem. - Eur. J.* **2013**, *19*, 6753.

(15) Kubíček, V.; Kotek, J.; Hermann, P.; Lukeš, I. *Eur. J. Inorg. Chem.* **2007**, *2007*, 333.

(16) Mialane, P.; Marrot, J.; Rivière, E.; Nebout, J.; Hervé, G. *Inorg. Chem.* **2001**, *40*, 44.

(17) Bösing, M.; Loose, I.; Pohlmann, H.; Krebs, B. *Chem. - Eur. J.* **1997**, *3*, 1232.

(18) Sheldrick, G. M. *SADABS,* program for scaling and correction of area detector data; University of Göttingen: Germany, 1997.

(19) Blessing, R. *Acta Crystallogr., Sect. A: Found. Crystallogr.* **1995**, *A51*, 33.

(20) Sheldrick, G. M. *SHELX-TL,* version 5.03, Software Package for the Crystal Structure Determination, Siemens Analytical X-ray Instrument Division: Madison, WI, 1994.

(21) Borras-Almenar, J. J.; Clemente-Juan, J. M.; Coronado, E.; Tsukerblat, B. S. *J. Comput. Chem.* **2001**, *22*, 985.

(22) Woo, H. Y.; So, H.; Pope, M. T. *J. Am. Chem. Soc.* **1996**, *118*, 621.

(23) Bi, L. H.; Kortz, U. *Inorg. Chem.* **2004**, *43*, 7961.

(24) (a) Zheng, S. T.; Yuan, D. Q.; Zhang, J.; Yang, G. Y. *Inorg. Chem.* **2007**, *46*, 4569. (b) Pichon, C.; Mialane, P.; Dolbecq, A.; Marrot, J.; Rivière, E.; Keita, B.; Nadjo, L.; Sécheresse, F. *Inorg. Chem.* **2007**, *46*, 5292.

(25) Li, X. X.; Zheng, S. T.; Fang, W. H.; Yang, G.-Y. *Inorg. Chem. Commun.* **2011**, *14*, 1541.

(26) Mialane, P.; Dolbecq, A.; Marrot, J.; Rivière, E.; Sécheresse, F. *Angew. Chem., Int. Ed.* **2003**, *42*, 3523.

(27) Demoro, B.; Caruso, F.; Rossi, M.; Benítez, D.; González, M.; Cerecetto, H.; Galizzi, M.; Malayil, L.; Docampo, R.; Faccio, R.; Mombrú, Á. W.; Gambino, D.; Otero, L. *Dalton Trans.* **2012**, *41*, 6468.

(28) Weakley, T. J. R.; Finke, R. G. *Inorg. Chem.* **1990**, *29*, 1235.

(29) $R = [\sum(\chi MT_{\mathrm{calc}} - \chi MT_{\mathrm{obs}})^2/\sum(\chi MT_{\mathrm{obs}})^2]$.

(30) (a) Siedle, A. R.; Padula, F.; Barandwski; Goldstein, C.; DeAngelo, M.; Kokoszka, G. F.; Azevedo, L.; Venturini, E. L. *J. Am. Chem. Soc.* **1983**, *105*, 7447. (b) Stowe, A. C.; Nellutla, S.; Dalal, N. S.; Kortz, U. *Eur. J. Inorg. Chem.* **2004**, *2004*, 3792.

(31) Crawford, V. H.; Richardson, H. W.; Wasson, J. R.; Hodgson, D. J.; Hatfield, W. E. *Inorg. Chem.* **1976**, *15*, 2107.

(32) Ruiz, E.; Alemany, P.; Alvarez, S.; Cano, J. *J. Am. Chem. Soc.* **1997**, *119*, 1297.

(33) Thompson, L. K.; Mandal, S. K.; Tandon, S. S.; Bridson, J. N.; Park, M. K. *Inorg. Chem.* **1996**, *35*, 3117.

(34) Kahn, O. *Inorg. Chim. Acta* **1982**, *62*, 3.

(35) Escuer, A.; El Fallah, M. S.; Vicente, R.; Sanz, N.; Font-Bardia, M.; Solans, X.; Mautner, F. A. *Dalton Trans.* **2004**, 1867.

(36) (a) Keita, B.; Mbomekalle, I.-M.; Nadjo, L.; Contant, R. *Electrochem. Commun.* **2001**, *3*, 267. (b) Keita, B.; Abdeljalil, E.; Nadjo, L.; Contant, R.; Belgiche, R. *Electrochem. Commun.* **2001**, *3*, 56. (c) Mbomekalle, I.-M.; Keita, B.; Lu, Y. W.; Nadjo, L.; Contant, R.; Belai, N.; Pope, M. T. *Eur. J. Inorg. Chem.* **2004**, *2004*, 4132. (d) Jabbour, D.; Keita, B.; Nadjo, L.; Kortz, U.; Mal, S. *Electrochem. Commun.* **2005**, *7*, 841. (e) Nellutla, S.; van Tol, J.; Dalal, N. S.; Bi, L.-H.; Kortz, U.; Keita, B.; Nadjo, L.; Khitrov, G. A.; Marshall, A. G. *Inorg. Chem.* **2005**, *44*, 9795.

(37) Ruhlmann, L.; Nadjo, L.; Canny, J.; Contant, R.; Thouvenot, R. *Eur. J. Inorg. Chem.* **2002**, *2002*, 975.

(38) Rousseau, G.; Zhang, S.; Oms, O.; Dolbecq, A.; Marrot, J.; Liu, R.; Shang, X.; Zhang, G.; Keita, B.; Mialane, P. *Chem. - Eur. J.* **2015**, *21*, 12153.

Supporting Infomation at **DOI:** 10.1021/acs.inorgchem.5b02456.

ChemComm

ROYAL SOCIETY OF CHEMISTRY

COMMUNICATION

View Article Online
View Journal | View Issue

Cite this: *Chem. Commun.*, 2015, **51**, 2972

Received 15th December 2014,
Accepted 9th January 2015

DOI: 10.1039/c4cc09986a

www.rsc.org/chemcomm

Immobilization of polyoxometalates in the Zr-based metal organic framework UiO-67†

William Salomon,[a] Catherine Roch-Marchal,*[a] Pierre Mialane,[a] Paul Rouschmeyer,[a] Christian Serre,[a] Mohamed Haouas,[a] Francis Taulelle,[a] Shu Yang,[b] Laurent Ruhlmann[b] and Anne Dolbecq*[a]

The encapsulation of polyoxometalates within the large pores of the Zr(IV) biphenyldicarboxylate UiO-67 metal–organic framework has been achieved, for the first time, by direct solvothermal synthesis. The resulting POM@UiO-67 composite materials were fully characterized by XRPD, IR, MAS NMR, N_2 porosimetry measurements and cyclic voltammetry.

Polyoxometalates (POMs) are soluble early-transition-metal clusters with a large diversity of structures and compositions.[1] They possess redox and acid–base properties which can be exploited for catalytic applications.[2] However their low specific surface area, low stability under catalytic conditions and high solubility in aqueous solution constitute some of their drawbacks. The search for stable heterogeneous catalysts with a high surface area, which could combine the activity of the POMs with the advantages of heterogeneous catalysts, such as easier recovery and recycling, thus attracts a lot of interest. Encapsulation of POMs within the cavities of metal organic frameworks (MOFs)[3] constitutes a strategy to access to POMs-based heterogeneous catalysts.[4] The mesoporous M(III)-trimesate MIL-100 and -terephthalate MIL-101 families (M = Fe, Cr, Al; MIL stands for Material of Institut Lavoisier) have been the most investigated host matrices so far because of their very large pore sizes and surface areas and good chemical stability. Keggin-type as well as sandwich-type POMs have been incorporated either by impregnation or *in situ* during the MOF synthesis.[5] Besides the MIL families, Cu–BTC frameworks (BTC = 1,3,5-benzene-tricarboxylate), known as HKUST-1 (HKUST stands for Hong-Kong University of Science and Technology), have been the subject of intense research.[5] Due to the small size of the pores they can only accommodate Keggin anions by direct synthesis. However the poor aqueous stability of these copper carboxylate based MOFs might prevent their practical use. Among the few examples of a series of thermally, and chemically stable MOFs with high surface area, the UiO-66 to 68 family (UiO stands for University of Oslo), built up from $\{Zr^{IV}_6O_4(OH)_4\}$ oxocluster nodes and linear dicarboxylate linkers (with the general formulae $[Zr^{IV}_6O_4(OH)_4(\text{linker})_6]$), is one of the most studied MOFs.[6] These materials exhibit by themselves very promising catalytic properties.[7] In UiO-67 the inorganic octahedral Zr_6 units are bound to 12 other inorganic subunits through biphenyl dicarboxylate ligands forming a face-centered cubic (fcc) structure (a = 27.1 Å). This MOF exhibits two types of cages: supertetrahedral (∅ ∼ 11.5 Å) and superoctahedral (∅ ∼ 18 Å) accessible through microporous triangular windows (∅ ∼8 Å) (Fig. 1a), corresponding to the voids of the fcc packing. However, the incorporation of guest molecules within the pores of UiO MOFs has only been rarely studied[8] and, to our knowledge, there have been so far no reports of POM@UiO composites. Here we propose for the first time a synthetic method for the encapsulation within the pores of UiO-67

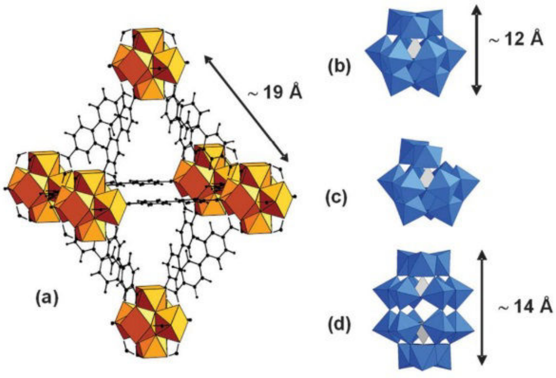

Fig. 1 Polyhedral representations of (a) the octahedral cages of UiO-67, (b) $[PW_{12}O_{40}]^{3-}$ (PW_{12}), (c) $[PW_{11}O_{39}]^{7-}$ (PW_{11}) and (d) $[P_2W_{18}O_{62}]^{6-}$ (P_2W_{18}); blue octahedra: WO_6, grey tetrahedra: PO_4, orange polyhedra: ZrO_8, black spheres: C, small black spheres: H.

---

[a] *Institut Lavoisier de Versailles, UMR 8180, Université de Versailles Saint-Quentin en Yvelines, 45 Avenue des Etats-Unis, 78035 Versailles cedex, France. E-mail: catherine.roch@uvsq.fr, anne.dolbecq@uvsq.fr*

[b] *Université de Strasbourg, Institut de Chimie, UMR CNRS 7177, Laboratoire d'Electrochimie et de Chimie Physique du Corps Solide, 4 rue Blaise Pascal, CS 90032, 67081 Strasbourg cedex, France*

† Electronic supplementary information (ESI) available: Detailed syntheses and characterizations. See DOI: 10.1039/c4cc09986a

of three representative examples of POMs: $[PW_{12}O_{40}]^{3-}$, $[PW_{11}O_{39}]^{7-}$ and $[P_2W_{18}O_{62}]^{6-}$ whose size (Fig. 1b–d) can fit in the microporous octahedral cavities of this MOF.

Attempts to incorporate POMs in the UiO-67 by an impregnation method, like for the MIL-101 materials,[5] have failed. This can be related to the narrow size of the windows. Thus a direct synthesis approach has been considered. A mixture of the pre-formed POM species ($H_3[PW_{12}O_{40}]$, $TBA_4H_3[PW_{11}O_{39}]$ or $TBA_6[P_2W_{18}O_{62}]$), zirconium tetrachloride, benzoic acid as a modulator,[9] and biphenyldicarboxylic acid was heated at 120 °C in dimethylformamide (DMF) (ESI†). Concentrated HCl was also added following previous reports.[6b,d] One would also expect that under the synthetic conditions used for the synthesis of UiO-67, the monolacunary PW_{11} POM would react with Zr(IV) ions to lead to the monomeric 1:1 complex $[PW_{11}O_{39}Zr(H_2O)_n]^{3-}$ (n = 2, 3), postulated by Kholdeeva *et al.*[10] Such a monomeric monosubstituted complex has also been evidenced in the Dawson[11] and Lindquist family.[12] The resulting insoluble microcrystalline materials, PW_{12}@UiO-67, $PW_{11}Zr$@UiO-67 and P_2W_{18}@UiO-67, respectively, were filtered and washed several times with DMF and acetone. Infrared (IR) spectra (Fig. 2) indicate the presence of both the POM and the MOF, with P–O and W–O vibration bands characteristic of the POM observed between 850 and 1100 cm^{-1} together with the carboxylate vibration bands of the linker between 1300 and 1600 cm^{-1}. The positions of the Bragg peaks are similar in the X-ray powder diffraction pattern of bare UiO-67 and of the POM@UiO-67 materials, confirming that the introduction of POMs in the synthetic medium does not perturb the formation of the MOF (Fig. S1, ESI†).

Elemental analysis combined with thermogravimetric analysis (TGA) measurements allows proposing the $[Zr_6O_4(OH)_{5.4}][C_{14}H_8O_4]_{5.3}$ formula for UiO-67, in agreement with the existence of linker defects occupied by hydroxide anions.[6b] One expects that for the POM@UiO-67 composites, the negative charges introduced by the POMs compensate, almost totally, the linker deficiencies. Note that the presence of tetrabutylammonium cations can be ruled out both by IR, elemental analysis and nuclear magnetic resonance (NMR). The TGA curves for UiO-67 and its composites (Fig. S2 and Table S1, ESI†) reveal steps that are attributed to water removal, linker decomposition and formation of inorganic oxides. Combined with elemental analyses, these results lead to the estimation of the following formulae $[Zr_6O_4(OH)_4][C_{14}H_8O_4]_{5.37}[PW_{12}O_{40}]_{0.42}$ (PW_{12}@UiO-67), $[Zr_6O_4(OH)_4][C_{14}H_8O_4]_{5.73}[PW_{11}O_{39}Zr]_{0.18}$ ($PW_{11}Zr$@UiO-67), and $[Zr_6O_4(OH)_{4.30}][C_{14}H_8O_4]_{5.10}[P_2W_{18}O_{62}]_{0.25}$ (P_2W_{18}@UiO-67) for the POM@UiO-67 composites. As there is one octahedral cavity per Zr_6 unit, these formulae indicate that approximately 1/2, 1/5 and 1/4 of the cavities are occupied by POMs in PW_{12}@UiO-67, $PW_{11}Zr$@UiO-67 and P_2W_{18}@UiO-67, respectively.

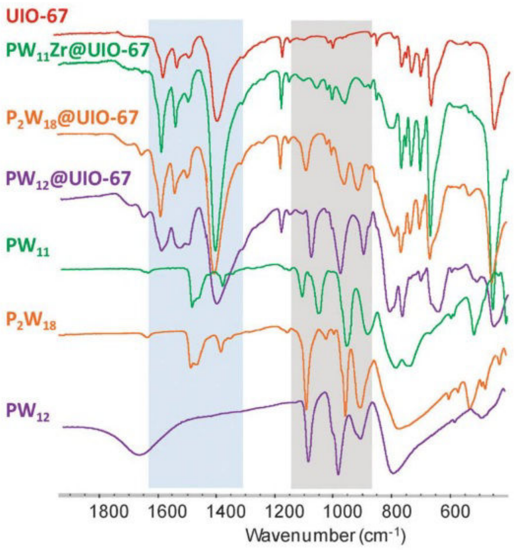

Fig. 2 IR spectra of POM@UiO-67 composites compared to that of the POM precursors and UiO-67. The regions with characteristic peaks of the POMs and of the MOF are highlighted in grey and light blue respectively.

N_2 sorption isotherms have been recorded for all the reported compounds (Fig. S3 and Table S2, ESI†). As expected, the surface area as well as the total pore volumes decrease from UiO-67 to POM@UiO-67 composites, as a consequence of the encapsulation of the POMs within the octahedral cavities, leaving however a significant porosity accessible to nitrogen. It should be noted that the values of the normalized specific surface area, taking into account the mass of UiO-67 in the composites samples, are significantly different from the value of UiO-67 (Fig. S3 and Table S2, ESI†), suggesting that the POMs are located inside the cavities and not at the surface of the material.

The ^{1}H MAS and $^{13}C\{^{1}H\}$ CPMAS NMR spectra of the three POM@UiO-67 (Fig. S4 and S5, ESI†) exhibit the characteristic resonances from the crystalline UiO-67. The Zr–OH hydroxyl protons from the hexameric unit lie in the 0–3.6 ppm range while the resonances of the linker, *i.e.* aromatic protons, are observed at 7.1 and 7.9 ppm. The aromatic carbon atoms (125, 130, 134, and 143 ppm) and the carbon atoms of the carboxylic function (172 ppm) are in the expected range.[8c] Noteworthily, broad components of all these resonances are observed and the general tendency showed that higher the amount of encapsulated POM larger the fraction of these broad resonances (23% in $PW_{11}Zr$@UiO-67, 54% in P_2W_{18}@UiO-67, and 68% in PW_{12}@UiO-67). This is assigned to structural disorder caused by the POM filling pores.

The ^{31}P MAS NMR spectra of PW_{12}@UiO-67 (Fig. S6a, ESI†) and P_2W_{18}@UiO-67 (Fig. 3a) show characteristic features of the POM precursors with signals at −15.2 and −12.9 ppm respectively, comparable to the literature values.[13] In contrast, the spectrum of $PW_{11}Zr$@UiO-67 (Fig. S7a, ESI†) exhibits a resonance at −13.2 ppm instead of −12.4 ppm expected for PW_{11}.[14] This shift is in perfect agreement with that determined for a mixture of PW_{11} and $ZrCl_4$ in DMF (Fig. S8, ESI†).

^{31}P NMR provides not only information about the structure of the POM but also some insights on location and host–guest interactions between the POM and the MOF. Indeed, the ^{1}H–^{31}P HETCOR (heteronuclear correlation) experiment enables us to probe the dipolar contact between the ^{31}P and ^{1}H nuclei. Correlations between the phosphorus atom of the POM and protons of the aromatic linkers as well as Zr–OH framework hydroxyl groups are observed in the three POM@UiO-67 composite materials. This unambiguously indicates the close proximity of the POM

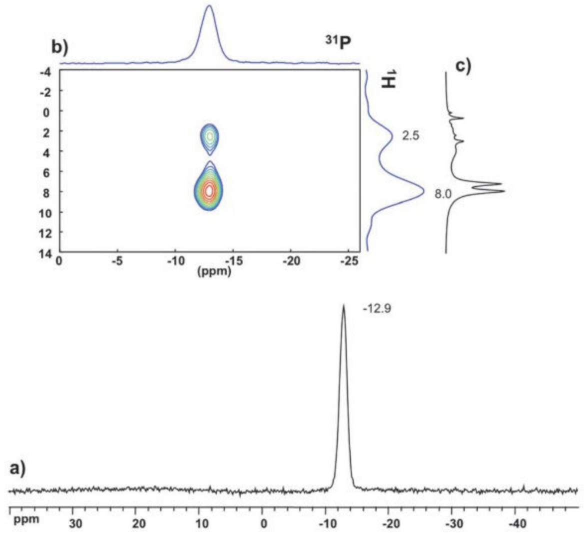

Fig. 3 Solid-state NMR spectra of P_2W_{18}@UiO-67: (a) $^{31}P\{^1H\}$ CPMAS; (b) ^1H–^{31}P HETCOR; (c) ^1H MAS.

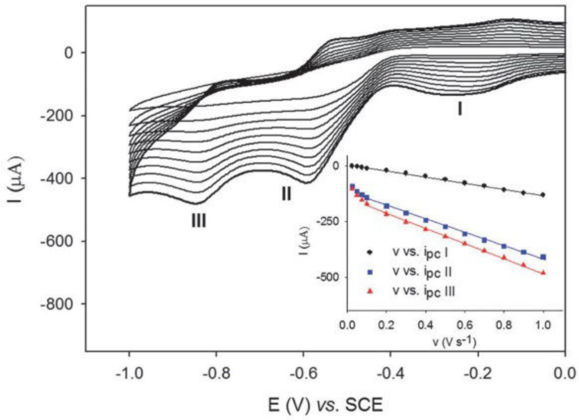

Fig. 4 Cyclic voltammograms of P_2W_{18}@UiO-67 immobilized at a PG electrode in a pH 2.5 H_2SO_4–Na_2SO_4 0.5 M buffer solution at different scan rates from 0.025 to 1.000 V s^{-1}. Inset: plots of I_{pc} *vs.* v for peaks I, II and III.

to the surface of the MOF inside the pores homogeneously as otherwise no such efficient dipolar transfer would be seen. Furthermore, the strength of the correlation with these protons appears varied from one POM to another. Indeed in P_2W_{18}@UiO-67 (Fig. 3b) and PW_{12}@UiO-67 (Fig. S6b, ESI†) the ^{31}P site correlates mainly with the aromatic resonance (8 ppm) while in $PW_{11}Zr$@UiO-67 (Fig. S7b, ESI†) the correlation mainly occurs with the hydroxyl group peak (2.5 ppm). This clearly indicates the preferential interaction of PW_{12} and P_2W_{18} with the organic linker, whereas $PW_{11}Zr$ should be closer to the inorganic node, suggesting interactions between the Zr(IV) ions inserted in the POM lacuna and the $\{Zr^{IV}_6O_4(OH)_4\}$ clusters. Finally, these correlations involve only the broad components of the ^1H spectra (as it could be compared with 1D MAS in Fig. 3c). This strongly suggests as stated above that the POMs are located in the distorted/disordered domain.

The electrochemical properties of the POM@UiO composite materials were also studied and compared to those of the POMs alone. The solids were first immobilized on the surface of the basal plane of the pyrolytic graphite disk (PG) and their electrochemical responses studied in pH 2.5 H_2SO_4–Na_2SO_4 0.5 M buffer solutions. PW_{12} and P_2W_{18} and their related POM@UiO-67 composites exhibit similar redox behaviors related to the $W^{VI/V}$ redox couples (Table S3, Fig. S9–S11, ESI† and Fig. 4), showing that when saturated POMs are encapsulated inside the cages they retain their electrochemical properties. It must be noted however that the first reduction process for P_2W_{18} is 175 mV higher for P_2W_{18}@UiO-67 than for P_2W_{18}.

In the case of $PW_{11}Zr$@UiO-67 the cyclovoltammogram clearly shows the complexation of the monolacunary PW_{11} with Zr(IV) and the formation of $PW_{11}Zr$ encapsulated in UiO-67 (Fig. S12 and S13, ESI†). Indeed, PW_{11} immobilized on the PG exhibits four successive waves at −0.450 V, −0.560 V, −0.694 V and −0.830 V *vs.* SCE respectively while only two waves are measured for $PW_{11}Zr$@UiO-67 at −0.713 V and −0.885 V. It should be noted that the electrochemical behaviors of the POM@UiO composites and of composites obtained by mechanical mixing of POMs and UiO (Fig. S14–S16) are different which confirm the encapsulation of the POMs inside the cavities and the transformation of PW_{11} into $PW_{11}Zr$. Finally, all peak current intensities vary linearly with the scan rate in the range 0.1–1.0 V s^{-1}, as expected for surface confined redox processes. This behavior is in agreement with the immobilization of the POMs inside the cavities of the MOF and contrasts with the observation of diffusion-controlled processes for PW_{11}@MIL-101(Cr) which were attributed to the mobility of the POMs.[15]

In conclusion, the immobilization of three polyoxotungstates in the largest pores of UiO-67(Zr) has been carried out for the first time, by a direct synthetic method. POM encapsulation compensates almost totally the linker deficiencies. The elaborated POM@UiO-67 composites have been thoroughly characterized. Cyclic voltammetry studies have confirmed the direct formation of $PW_{11}Zr$ during the synthetic process and the integrity of the saturated inserted POMs PW_{12} and P_2W_{18}. MAS NMR experiments provided essential information on the structure of the composites. First, they have shown interactions between the POMs and the framework, thus confirming the encapsulation within the structure. Moreover they highlighted the existence of disordered domains related to the presence of the POMs. Finally they evidenced specific interactions between the asymmetric $PW_{11}Zr$ POMs and the UiO framework. Noticeably, because of the small size of the cage windows, POM leaching cannot occur in these materials. The introduction of POMs might pave the way for future applications in catalysis. It may also greatly influence the hydrophilicity of the materials and thus their gas sorption properties. Future work will focus on these two applications.

This work was supported by CNRS, UVSQ, University of Strasbourg and the French National Research Agency (ANR) as part of the ''Investissements d'Avenir'' program no. ANR-11-IDEX-0003-02 and CHARMMMAT ANR-11-LABX-0039. Patricia Horcajada and Thomas Devic are gratefully acknowledged for fruitful discussions.

Notes and references

1 (*a*) H. N. Miras, L. Vilà-Nadal and L. Cronin, *Chem. Soc. Rev.*, 2014, **43**, 5679; (*b*) O. Oms, A. Dolbecq and P. Mialane, *Chem. Soc. Rev.*, 2012, **41**, 7497; (*c*) A. Proust, B. Matt, R. Villanneau, G. Guillemot, P. Gouzerh and G. Izzet, *Chem. Soc. Rev.*, 2012, **41**, 7605.

2 (*a*) H. Lv, Y. V. Geletii, C. Zhao, J. W. Vickers, G. Zhu, Z. Luo, J. Song, T. Lian, D. G. Musaev and C. L. Hill, *Chem. Soc. Rev.*, 2012, **41**, 7572; (*b*) A. Sartorel, M. Bonchio, S. Campagna and F. Scandola, *Chem. Soc. Rev.*, 2013, **42**, 2262; (*c*) N. Mizuno and K. Kamata, *Coord. Chem. Rev.*, 2011, **255**, 2358; (*d*) X.-B. Han, Z.-M. Zhang, T. Zhang, Y.-G. Li, W. Lin, W. You, Z.-M. Su and E.-B. Wang, *J. Am. Chem. Soc.*, 2014, **136**, 5359.

3 Special issue on Metal Organic Frameworks *Chem. Soc. Rev.*, 2014, **43**, 5415.

4 J. Juan-Alcañiz, J. Gascon and F. Kapteijn, *J. Mater. Chem.*, 2012, **22**, 10102.

5 See for example: (*a*) N. V. Maksimchuk, M. N. Timofeeva, M. S. Melgunov, A. N. Shmakov, Y. A. Chesalov, D. N. Dybtsev, V. P. Fedin and O. A. Kholdeeva, *J. Catal.*, 2008, **257**, 315; (*b*) L. Bromberg, Y. Diao, H. Wu, S. C. A. Speakman and T. A. Hatton, *Chem. Mater.*, 2012, **24**, 1664; (*c*) C. M. Granadeiro, A. D. S. Barbosa, P. Silva, F. A. Almeida Paz, V. K. Saini, J. Pires, B. de Castro, S. S. Balula and L. Cunha-Silva, *Appl. Catal., A*, 2013, **453**, 316; (*d*) J. Juan-Alcañiz, E. V. Ramos-Fernandez, U. Lafont, J. Gascon and F. Kapteijn, *J. Catal.*, 2010, **269**, 229; (*e*) A.-X. Yan, S. Yao, Y.-G. Li, Z.-M. Zhang, Y. Lu, W.-L. Chen and E.-B. Wang, *Chem. – Eur. J.*, 2014, **20**, 6927; (*f*) S. R. Bajpe, C. E. A. Kirschhock, A. Aerts, E. Breynaert, G. Absillis, T. N. Parac-Vogt, L. Giebeler and J. A. Martens, *Chem. – Eur. J.*, 2010, **16**, 3926; (*g*) J. Song, Z. Luo, D. K. Britt, H. Furukawa, O. M. Yaghi, K. I. Hardcastle and C. L. Hill, *J. Am. Chem. Soc.*, 2011, **133**, 16839; (*h*) J. J.-A. Alcañiz, M. Goesten, A. Martinez-Joaristi, E. Stavitski, A. V. Petukhov, J. Gascon and F. Kapteijn, *Chem. Commun.*, 2011, **47**, 8578. The complete list of references is given in the ESI† section.

6 (*a*) J. H. Cavka, S. Jakobsen, U. Olsbye, N. Guillou, C. Lamberti, S. Bordiga and K. P. Lillerud, *J. Am. Chem. Soc.*, 2008, **130**, 13850; (*b*) M. J. Katz, Z. J. Brown, Y. J. Colón, P. W. Siu, K. A. Scheidt, R. Q. Snurr, J. T. Hupp and O. K. Farha, *Chem. Commun.*, 2013, **49**, 9449; (*c*) J. E. Mondloch, M. J. Katz, N. Planas, D. Semrouni, L. Gagliardi, J. T. Hupp and O. K. Fahra, *Chem. Commun.*, 2014, **50**, 8944; (*d*) P. S. Barciá, D. Guimarães, P. A. P. Mendes, J. A. C. Silva, V. Guillerm, H. Chevreau, C. Serre and A. E. Rodrigues, *Microporous Mesoporous Mater.*, 2011, **139**, 67; (*e*) G. C. Schearer, S. Chavan, J. Ethiraj, J. G. Vitillo, S. Svelle, U. Olsbye, C. Lamberti, S. Bordiga and K. P. Lillerud, *Chem. Mater.*, 2014, **26**, 4068.

7 (*a*) F. Vermoortele, R. Ameloot, A. Vimont, C. Serre and D. De Vos, *Chem. Commun.*, 2010, **47**, 1521; (*b*) M. J. Katz, J. E. Mondloch, R. K. Totten, J. K. Park, S. T. Nguyen, O. K. Farha and J. T. Hupp, *Angew. Chem., Int. Ed.*, 2014, **53**, 497.

8 (*a*) S. Devautour-Vinot, C. Martineau, S. Diaby, M. Ben-Yahia, S. Miller, C. Serre, P. Horcajada, D. Cunha, F. Taulelle and G. Maurin, *J. Phys. Chem. C*, 2013, **117**, 11694; (*b*) J. He, J. Wang, Y. Chen, J. Zhang, D. Duan, Y. Wang and Z. Yan, *Chem. Commun.*, 2014, **50**, 7063; (*c*) C. Larabi and E. A. Quadrelli, *Eur. J. Inorg. Chem.*, 2012, 3014.

9 A. Schaate, P. Roy, A. Godt, J. Lippke, F. Waltz, M. Wiebcke and P. Behrens, *Chem. – Eur. J.*, 2011, **17**, 6643.

10 O. A. Kholdeeva, G. M. Maksmimov, R. I. Maksimovskaya, M. P. Vanina, T. A. Trubitsina, D. Y. Naumov, B. A. Kolesov, N. S. Antonova, J. J. Carbó and J. M. Poblet, *Inorg. Chem.*, 2006, **45**, 7224.

11 (*a*) M. N. Sokolov, N. V. Izarova, E. V. Peresypkina, D. A. Mainichev and V. P. Fedin, *Inorg. Chim. Acta*, 2009, **362**, 3756; (*b*) S. Vanhaecht, G. Absillis and T. N. Parac-Vogt, *Dalton Trans.*, 2013, **42**, 15437.

12 R. J. Errington, P. S. S. Petkar, P. S. Middleton and W. McFarlane, *J. Am. Chem. Soc.*, 2007, **129**, 12181.

13 (*a*) J. Chunjie, S. Shengnan, W. Xuyang, W. Xiangsheng, G. Hongchen, G. Xinwen and C. Lidong, *Acta Chim. Sin.*, 2013, **71**, 810; (*b*) S. Ribeiro, A. D. S. Barbosa, A. C. Gomes, M. Pillinger, I. S. Gonçalves, L. Cunha-Silva and S. S. Balula, *Fuel Process. Technol.*, 2013, **116**, 350.

14 G. Férey, C. Mellot-Draznieks, C. Serre, F. Millange, J. Dutour, S. Surblé and I. Margiolaki, *Science*, 2005, **309**, 2040.

15 P. M. Paes de Sousa, R. Grazina, A. D. S. Barbosa, B. de Castro, J. J. G. Moura, L. Cunha-Silva and S. S. Balula, *Electrochim. Acta*, 2013, **87**, 853.

Supporting Infomation at **DOI:** 10.1039/C4CC09986A.

ChemPubSoc Europe
DOI: 10.1002/chem.201600202
CHEMISTRY
A European Journal
Full Paper

Single-Molecule Magnets |*Hot Paper*|

Single-Molecule Magnet Behavior of Individual Polyoxometalate Molecules Incorporated within Biopolymer or Metal–Organic Framework Matrices

William Salomon+,[a] Yanhua Lan+,[b] Eric Rivière,[c] Shu Yang,[d] Catherine Roch-Marchal,[a] Anne Dolbecq,[a] Corine Simonnet-Jégat,[a] Nathalie Steunou,[a] Nathalie Leclerc-Laronze,[a] Laurent Ruhlmann,[d] Talal Mallah,*[c] Wolfgang Wernsdorfer,*[b] and Pierre Mialane*[a]

Abstract: The chemically and structurally highly stable polyoxometalate (POM) single-molecule magnet (SMM) $[(FeW_9O_{34})_2Fe_4(H_2O)_2]^{10-}$ (Fe_6W_{18}) has been incorporated by direct or post-synthetic approaches into a biopolymer gelatin (Gel) matrix and two crystalline metal–organic frameworks (MOFs), including one diamagnetic (UiO-67) and one magnetic (MIL-101(Cr)). Integrity of the POM in the Fe_6W_{18}@Gel, Fe_6W_{18}@UiO-67 and Fe_6W_{18}@MIL-101(Cr) composites was confirmed by a set of complementary techniques. Magnetic studies indicate that the POMs are magnetically well isolated. Remarkably, in Fe_6W_{18}@Gel, the SMM properties of the embedded molecules are close to those of the crystals, with clear quantum tunneling steps in the hysteresis loops. For the Fe_6W_{18}@UiO-67 composite, the molecules retain their SMM properties, the energy barrier being slightly reduced in comparison to the crystalline material and the molecules exhibiting a tunneling rate of magnetization significantly faster than for Fe_6W_{18}@Gel. When Fe_6W_{18} is introduced into MIL-101(Cr), the width of the hysteresis loops is drastically reduced and the quantum tunneling steps are smeared out because of the magnetic interactions between the antiferromagnetic matrix and the SMM guest molecules.

Introduction

Polyoxometalates (POMs) constitute a class of soluble anionic oxide clusters based on d-block transition metal ions in high oxidation states (e.g., W^{VI}, $Mo^{V,VI}$, $V^{IV,V}$).[1] They can incorporate a huge variety of organic or inorganic substrates enabling a diverse range of properties, including optical[2] to catalytic.[3] Focusing on their magnetic properties,[4] single-molecule magnets (SMMs) based on inorganic POMs are of particular interest. SMMs are bistable molecules that can be magnetized in a magnetic field, retain the magnetization when the external field is switched off, and therefore exhibit hysteresis loops in magnetization versus field experiments. Magnetic inorganic POMs offer the advantage of being structurally robust, preventing the deformation of the coordination sphere of the magnetic ions when the molecules are placed in various environments, a drawback from which SMMs with organic ligands can suffer. In addition, their thermal and chemical stabilities, even in reacting media containing coordinating ligands or metallic cations, are a main advantage for further processing of these species. Moreover, the bulky diamagnetic shell of vacant POMs efficiently isolates the magnetic cores of neighboring molecules from each other. Finally, these highly charged anionic species are able to strongly interact electrostatically with positively charged supports, leading to stable composite materials. Since the first discovery of a POM exhibiting SMM behavior in 2008,[5] there has been an increasing number of reports of SMM POMs[6] and more recently of mononuclear SMM[7a] POMs.[7b,c] However, although SMMs represent nanoscale magnetic objects that offer potential applications in the field of high-density information storage at the molecular level, molecular spintronics, and quantum computing,[8] these applications require their organization in 2D or 3D architectures in which each individual molecule can be used as a bit of information. Several approaches have been explored for the preparation of surface-supported SMMs,[9] such as electrostatic graft-

---

[a] *W. Salomon,+ Dr. C. Roch-Marchal, Dr. A. Dolbecq, Dr. C. Simonnet-Jégat,*
Prof. N. Steunou, Dr. N. Leclerc-Laronze, Prof. P. Mialane
Institut Lavoisier de Versailles, UMR CNRS 8180
Université Paris Saclay, Université de Versailles St-Quentin en Yvelines
45 Avenue des Etats-Unis, 78035 Versailles cedex (France)
E-mail: pierre.mialane@uvsq.fr

[b] *Dr. Y. Lan,+ Dr. W. Wernsdorfer*
CNRS and Université Grenoble Alpes, Institut Néel
38042 Grenoble (France)
E-mail: wolfgang.wernsdorfer@neel.cnrs.fr

[c] *Dr. E. Rivière, Prof. T. Mallah*
Institut de Chimie Moléculaire et des Matériaux d'Orsay
UMR 8182 CNRS, Université Paris Saclay
Université Paris Sud 11, 91405 Orsay cedex (France)
E-mail: talal.mallah@u-psud.fr

[d] *S. Yang, Prof. L. Ruhlmann*
Université de Strasbourg, Institut de Chimie, UMR CNRS 7177
Laboratoire d'Electrochimie et de Chimie Physique du Corps Solide
4 Rue Blaise Pascal, CS 90032, 67081 Strasbourg cedex (France)

[+] *Both authors contributed equally to this work*

Supporting information for this article can be found under http://dx.doi.org/10.1002/chem.201600202.

ing on carbon nanotubes[10] or covalent grafting onto an Au surface.[11] Immobilization in 3D materials has been performed through incorporation within polycarbonate matrices,[12] resins,[11] poly(methylmethacrylate)[13] or poly(ethylmethacrylate)[14] polymers, ordered mesoporous silica,[15] a 3D bimetallic oxalate network,[16] and a TaS_2-layered superconductor.[17] Very interestingly, the neutral mesoporous aluminum-based metal–organic framework (MOF) $[Al(OH)(SDC)]_n$ ($H_2SDC=4,4'$-stilbenedicarboxylic acid) was recently nanostructured with neutral SMM molecules.[18] However, these studies have mainly concerned Mn_{12} derivatives and none of them has dealt with POMs.

In 2009, we reported that the $[(FeW_9O_{34})_2Fe_4(H_2O)_2]^{10-}$ POM (abbreviated here as Fe_6W_{18}; Figure 1 a) exhibits SMM behavior with a large hysteresis in zero field.[19] Following our first study on the grafting of Fe_6W_{18} onto carbon nanotubes,[20] we report herein the organization of Fe_6W_{18} SMM molecules in two types of supports; gelatin (Gel) biopolymer and two distinct MOF materials. Gelatin (Figure 1 a), a cheap, abundant macromolecule obtained by hydrolytic degradation of mammalian or fish collagen, is widely used in food and pharmaceutical industries, and can form transparent and elastic gels. Gelatin has already proven a good matrix for the synthesis of bionanocomposites with diamagnetic POMs exhibiting topologies as different as heptamolybdate,[21] decavanadate,[22] Keggin-type,[23] or Keplerate and crown-shaped species.[24]

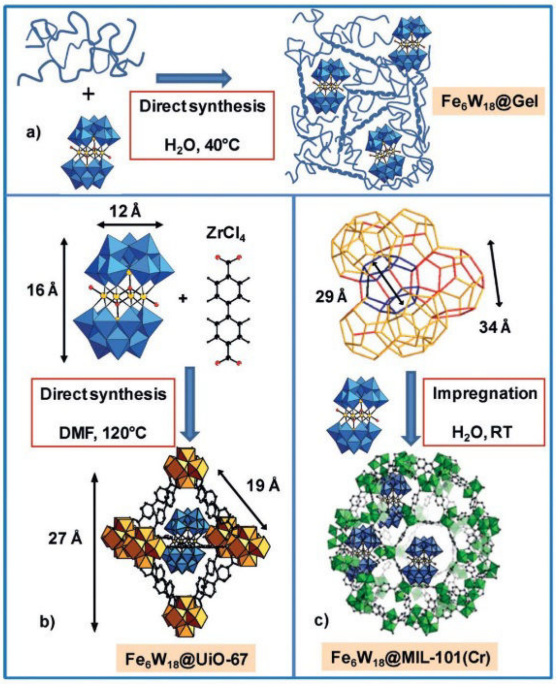

Figure 1. Representations of the POM SMM $[(FeW_9O_{39})_2Fe_4(H_2O)_2]^{10-}$ (Fe_6W_{18}), gelatin, UiO-67, MIL-101(Cr) and the synthetic routes to the three composite materials: a) Fe_6W_{18}@Gel; b) Fe_6W_{18}@UiO-67; c) Fe_6W_{18}@MIL-101(Cr); blue octahedra: WO_6, green octahedra: CrO_6, orange polyhedra: ZrO_8, yellow spheres: Fe, red spheres: O, black spheres: C, small black spheres: H.

MOFs are crystallized ordered materials in which isolated metal ions or clusters are connected by polydentate organic linkers to form hybrid structures with large pores.[25] In recent years, several studies devoted to the encapsulation of POMs in MOFs have been reported,[26] mainly for catalytic purposes. Based on the shaping of Fe_6W_{18}, we selected two MOFs, $[Zr^{IV}_6O_4(OH)_4(C_{14}H_8O_4)_6]$ (UiO-67; Figure 1 b)[27] and the mesoporous material $[Cr^{III}_3(H_2O)_3O(C_8H_4O_4)_3]NO_3$ (MIL-101(Cr); Figure 1 c).[28] Both are thermally and chemically stable, with high surface areas, and known abilities to encapsulate POMs.[26f,29] The nature of these three very different matrices (amorphous/crystalline, diamagnetic/paramagnetic) allows us to explore the influence of the host matrix on the magnetic properties of the SMM guests. Furthermore, UiO-67 and MIL-101(Cr) are solid powder samples, whereas gelatin offers the advantage of being easily processed as transparent and self-supporting films with good mechanical properties.

The three composite materials, denoted Fe_6W_{18}@Gel, Fe_6W_{18}@UiO-67, and Fe_6W_{18}@MIL-101(Cr), were thus assembled. The direct synthesis of Fe_6W_{18}@UiO-67 was possible only due to the high stability of the POM. To investigate the integrity of the guest POMs, the reported materials were all characterized by complementary techniques, including the preparation of robust and electrochemicaly stable pyrolytic graphite electrodes modified by Fe_6W_{18}@UiO-67 or Fe_6W_{18}@MIL-101(Cr), which proved easy and fast to perform. The magnetic properties of the three hybrid composites were thoroughly investigated and compared, to assess for each material whether the SMM character of the introduced POM had been conserved, and to what extent.

Results and Discussion

Synthesis and characterizations of the hybrid materials

Fe_6W_{18}@Gel was synthesized following a coacervation process previously described for the immobilization of POMs in gelatin matrix.[22–24] This process is mainly based on attractive electrostatic interactions between negatively charged POMs and positively charged gelatin chains. A solution of gelatin is added to a solution of POM at 40 °C. The physicochemical conditions (pH, temperature, POM and gelatin concentrations) are key parameters. In particular, the pH value of the solution must be lower than 4. Indeed, in this pH domain, gelatin macromolecules behave like weak cationic polyelectrolytes with fully protonated amine and carboxylic functions, giving rise to a global positive charge.[30] Furthermore, the temperature has to be higher than 30 °C due to the temperature-dependent sol–gel transition of gelatin. Conditions of pH 3 and $T=40$ °C were thus chosen for the experiment, considering also that Fe_6W_{18} is stable in acidic medium. Under these conditions, a viscous coacervate can be isolated from the supernatant solution. Upon drying, the viscous phase evolves to a glassy compound, owing to the vitreous transition of gelatin. As previously reported for other POM–gelatin bionanocomposites,[22–24] Fe_6W_{18} POMs are confined within a gelatin network composed of coils and triple helices. Its orange color suggests the presence of the POMs, which was confirmed afterwards by a series of characterizations.

The IR spectrum of Fe_6W_{18}@Gel can be seen as the superimposition of the IR spectra of the Fe_6W_{18} POM and gelatin (see the Supporting Information, Figure S1 a). The W–O vibration bands can be identified at 929 and 837 cm^{-1}. The vibration bands of the amino and carboxylate groups of amino acids at around 1400 cm^{-1} and the broad vibration band at 1625 cm^{-1}, which can be assigned to bands I and II of the amide groups, are also present in the spectrum of Fe_6W_{18}@Gel. It should also be noted that the C–N band at 1482 cm^{-1}, attributed to the tetramethylammonium (TMA^+) counter ions of the POM precursor, is absent in Fe_6W_{18}@Gel. This is consistent with a genuine encapsulation of the POM molecules into gelatin, driven by electrostatic interactions. The unit formula of Fe_6W_{18}@Gel was determined by a combination of elemental analyses (see Experimental section) and thermogravimetric analysis (TGA; see the Supporting Information, Figure S2), taking into account the charge of a gelatin chain and the content of counter ions as given by elemental analysis. At pH 3 the average charge of a gelatin chain was estimated to be 36+, considering that the positive charges of gelatin are mainly given by arginine and lysine amino acid residues.[24] Elemental analysis indicated that there are 5 POMs per formula unit and that the residual negative charge is compensated by sodium ions. TGA allowed determination of the water content. A formula of $Na_{14}(CH_{1.56}O_{0.42}N_{0.31})_{1625}(Fe_6W_{18})_5{\cdot}270\,H_2O$ was thus derived for Fe_6W_{18}@Gel. The POM loading in this composite is therefore equal to 35 wt%. XRPD experiments indicate that Fe_6W_{18}@Gel is amorphous, and it was not possible to detect Fe_6W_{18} domains by energy-dispersive X-ray (EDX) mapping (see the Supporting Information, Figure S3a). Note also that, owing to electrostatic interactions, the POMs are well isolated within such films by the long polymer chains of the gelatin.[23] This was confirmed by magnetization measurements, which indicated that the POM units in Fe_6W_{18}@Gel are magnetically isolated from each other (see below).

The UiO-67 MOF is built up of diamagnetic $\{Zr_6O_4(OH)_4\}$ oxo clusters connected by biphenyldicarboxylate linkers and incorporates two types of cages: supertetrahedral (Ø = 11.5 Å) and superoctahedral (Ø = 18 Å) connected by triangular windows (Ø = 8 Å). Each superoctahedral cavity can encapsulate one Keggin- or Dawson-type POM (Figure 1 b).[29] However, due to the narrow size of the windows, a direct synthesis approach must be used for the encapsulation of POMs inside this MOF. A mixture of the dioctadecyldimethylammonium ($DODA^+$, $(CH_3(CH_2)_{17})_2(CH_3)_2N^+$) salt of Fe_6W_{18}, zirconium tetrachloride, benzoic acid as a crystallization modulator, concentrated HCl, and biphenyl-4,4′-dicarboxylic acid was heated at 120 °C for 24 h in dimethylformamide, following our synthetic protocol developed for the incorporation of diamagnetic polyoxotungstates in UiO-67.[29] A combination of EDX and elemental analyses leads to the formula $[Zr_6O_4(OH)_4(C_{14}H_8O_4)_{5.5}][(FeW_9O_{39})_2Fe_4(H_2O)_2]_{0.1}(DMF)_{1.8}{\cdot}17\,H_2O$ for the Fe_6W_{18}@UiO-67 composite. The POM/UiO-67 ratio is equal to 1:10 and the POM loading in this composite amounts to 17 wt%. This implies also that one octahedral cavity in ten is occupied by the POM, the tetrahedral cages being too small to incorporate a Fe_6W_{18} unit. In this material, the negative charges introduced by the POMs compensate the biphenyldicarboxylate linker vacancies within the network. IR spectra (see the Supporting Information, Figure S1 b) indicate the presence of both POM and MOF, with W–O vibration bands characteristic of the POM observed between 800 and 1000 cm^{-1}, together with vibration bands of the linker between 1300 and 1600 cm^{-1}. Importantly, preformed UiO-67 and Fe_6W_{18} were mixed in experimental conditions analogous to those used for the synthesis of Fe_6W_{18}@UiO-67 (DMF, 120 °C, 24 h), and the obtained powder treated following the same workup as the one considered for the reported hybrid material. Analysis of this powder revealed the absence of any POM molecules and retention of the UiO-67 framework, again showing that the POMs in Fe_6W_{18}@UiO-67 are incorporated within the cavities and not adsorbed at the surface of the MOF.

The MIL-101(Cr) MOF is built up from trimers of Cr^{III} octahedra linked by terephtalate anions, which creates a 3D structure with two types of mesocages (Ø = 29 and 34 Å) accessible through micropore windows (Ø = 11 and 16 Å). Incorporation of POMs in the MIL-101 MOF can be performed either by impregnation[26d,f,31] or in situ during the MOF synthesis.[32] The conditions used for the former method are much milder (usually room temperature, rather than 220 °C) and are suitable for POMs that are soluble in water as well as in organic media. This approach was considered for the preparation of Fe_6W_{18}@MIL-101(Cr). The Fe_6W_{18} sandwich-type POM can only be incorporated in the largest cavities, the windows of the smallest cages being too small to allow the penetration of such entities (Figure 1 c).[26f] The encapsulation of Fe_6W_{18} results from anion exchange between the NO_3^- counter ions of the MOF and the negatively charged POMs due to strong electrostatic POM–matrix interactions. As the charge of Fe_6W_{18} is 10−, the maximum POM/MIL-101(Cr) ratio that can be attained is 1:10. Impregnation was performed with an initial POM/MIL-101(Cr) ratio of 1:4, that is, with a large excess of POM. Elemental analysis was in agreement with the formula $[Cr_3(H_2O)_3O(O_2CC_6H_4CO_2)_3][(FeW_9O_{39})_2Fe_4(H_2O)_2]_{0.083}(NO_3)_{0.17}{\cdot}30\,H_2O$. This indicates a POM/MIL-101(Cr) ratio of 1:12 in the Fe_6W_{18}@MIL-101(Cr) composite material, close to the maximum expected ratio. The POM loading is thus equal to 35 wt%.[33] These results are in very good agreement with our recent work on the introduction of $[Co_4(H_2O)_2P_2W_{18}O_{68}]^{10-}$ into the cavities of MIL-101(Cr),[26f] the cobalt and Fe_6W_{18} POMs having exactly the same charge and size. In the IR spectra, the intensity of the POM vibrations is stronger in the MIL-101(Cr) composite (see the Supporting Information, Figure S1 c) than in the UiO-67 composite, in accordance with a higher loading value (see above).

For both Fe_6W_{18}@UiO-67 and Fe_6W_{18}@MIL-101(Cr), the positions of the Bragg reflections are similar in the X-ray powder diffraction (XRPD) pattern of the Fe_6W_{18}@MOF composites and the MOF precursors, confirming the integrity of the MOF structure (see the Supporting Information, Figure S4). The intensity of the peaks at low angles decreases from MIL-101(Cr) to Fe_6W_{18}@MIL-101(Cr), in accordance with the presence of the

POM within the MOF cavities, as already observed for other POM@MIL materials.[26f,32] As expected, the surface area decreases from the MOF precursor to Fe_6W_{18}@MOF (Figure 2), albeit with a significant remaining porosity accessible to nitrogen.

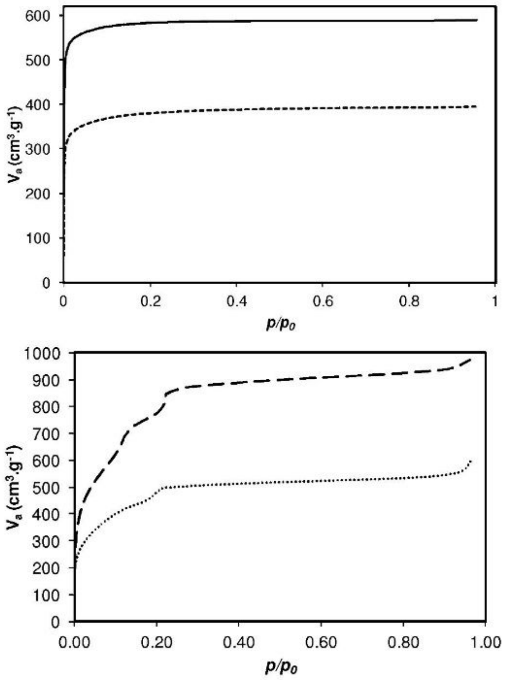

Figure 2. N_2 adsorption/desorption isotherms (77 K, $P_0 = 1$ atm). Top: UiO-67 (solid line) and Fe_6W_{18}@UiO-67 (dashed line). Bottom: MIL-101(Cr) (dashed line) and Fe_6W_{18}@MIL-101(Cr) (dotted line).

It was verified that the experimentally observed decrease in specific surface area is higher than the calculated value, taking into account the increase of the mass of the sample related to the POM loading.[34] This confirms the encapsulation of the POMs within the cavities. Modifications of total pore volume and of the pore size distributions also confirm the filling of the cavities. A significant shift to lower diameter and decrease of dV_P/dd_p, in which V_p is the pore volume and d_p is the pore diameter, is observed for Fe_6W_{18}@MIL-101(Cr), whereas only a decrease of dVP/ddp is found for Fe_6W_{18}@UiO-67 (see the Supporting Information, Figure S5 and Table S1). EDX mapping in the Fe_6W_{18}@UiO-67 (see the Supporting Information, Figure S3b) and Fe_6W_{18}@MIL-101(Cr) (see the Supporting Information, Figure S3c) composites shows an homogeneous distribution of the elements with appropriate Fe/W ratio within the materials, indicating a good dispersion of the POM within the MOFs.

Electrochemical studies of the Fe_6W_{18}@MOF composites

POMs are electroactive molecules and electrochemistry is one of the best techniques for probing a change in the electronic structure of a molecule subjected to different environments; it is used here to check the integrity of the POMs within the composite materials. The electrochemical properties of the three hybrids reported herein were studied and compared to Fe_6W_{18} alone in aqueous solution. The solids were first immobilized on the surface of the basal plane of the pyrolytic graphite disk (PG) and their electrochemical response studied in pH 2.5 (0.5 M H_2SO_4–Na_2SO_4) buffer solutions. It must be noted, however, that no electrochemical signal was detected in the case of Fe_6W_{18}@Gel, probably because of the insulating character of gelatin.

The Fe_6W_{18} POM precursor exhibits six successive reduction waves at −0.04 V, −0.18 V, −0.38 V, −0.53 V, −0.62 V and −0.68 V vs. SCE (see the Supporting Information, Table S2 and Figure S6). The first three waves (steps a, b, and c) correspond to the multistep reduction of iron centers ($Fe^{III/II}$ redox couple), whereas the last three waves (steps I, II and III) are attributed to the $W^{VI/V}$ couple, as previously reported.[20] The numbers of electrons exchanged at each Fe^{III} reduction step (steps a, b, and c) are 2, 1, and 1 respectively, attributed to the four sandwich Fe atoms, the two Fe heteroatoms in tetrahedral coordination being electrochemically inert.[19]

For Fe_6W_{18}@UiO-67 immobilized on the PG, cyclic voltammograms exhibit five successive waves at −0.02 V, −0.18 V, −0.44 V, −0.57 V and −0.65 V vs. SCE (see the Supporting Information, Table S2 and Figure S7) similar to the redox behavior of Fe_6W_{18}. All three successive waves of the reduction of the Fe atoms ($Fe^{III/II}$ redox processes) are observed. Furthermore, all peak current intensities vary linearly with the scan rate v in the range 0.1–1.0 V s^{-1}, as expected for surface-confined redox processes. The peak-to-peak separations (ΔE_p) are between 0.00 and 0.02 V and the ratio i_{pa}/i_{pc} (i_{pa} and i_{pc} are anodic and cathodic peak currents, respectively) is close to one. This behavior is in agreement with the immobilization of the Fe_6W_{18} POMs inside the cavities of the MOF and contrasts with the observation of diffusion-controlled processes reported for PW_{11}@MIL-101(Cr), which were attributed to the mobility of the POMs.[35] For the UiO-67 composite, only one POM can be trapped in the octahedral cavity and diffusion processes in the other cavities are not possible, owing to the small size of the triangular windows.

In the case of Fe_6W_{18}@MIL-101(Cr), the cyclic voltammogram also clearly shows similar redox behavior to Fe_6W_{18}. Indeed, Fe_6W_{18}@MIL-101(Cr) immobilized on the PG gives rise to four successive waves at −0.02 V, −0.38 V, −0.56 V and −0.65 V vs. SCE, the latter two waves corresponding to the $W^{VI/V}$ couple (Figure 3 and Table S2 in the Supporing Information). It must however be noted that the second step of the reduction of the Fe centers ($Fe^{III/II}$ couple, step b) measured at approximately −0.17 V for Fe_6W_{18} alone cannot be detected in the composite because of the rather weak electrochemical signal. Moreover, compared to the Fe_6W_{18} precursor, one additional reduction step is detected at 0.26 V vs. SCE, corresponding to the re-

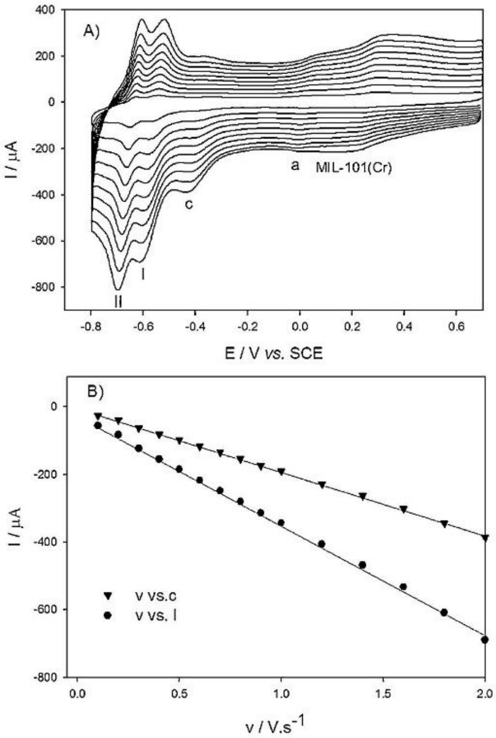

Figure 3. Top: cyclic voltammograms of Fe_6W_{18}@MIL-101(Cr) immobilized at a PG electrode in a 0.5 M pH 2.5 H_2SO_4–Na_2SO_4 buffer solution at 2.0, 1.8, 1.2, 1.0, 0.8, 0.6, 0.4, 0.2 and 0 V s^{-1} (from top to bottom). Bottom: plots of i_{pc} vs. v for peak c (third $Fe^{III/II}$ redox couple) and peak I (first $W^{VI/V}$ redox couple).

duction of the MIL-101(Cr) matrix.[35] Under the conditions used, a well-defined pair of peaks attributed to the $Cr^{III/II}$ redox process[36] is detected at $E_{pa} = 0.25$ V and $E_{pc} = 0.27$ V vs. SCE.

The electrochemical surface coverage (Γ) of the MIL-101(Cr)-modified electrode was calculated from the cathodic peak currents of peak c (third $Fe^{III/II}$ step) of the cyclic voltammograms according to the equation $\Gamma = (4 i_{pc} RT)/(n^2 F^2 \nu A)$, where i_{pc} is the cathodic peak current in amperes, $R = 8.314$ J K^{-1} mol^{-1}, $T = 298$ K, n is the number of electrons transferred (1 for Fe_6W_{18}),[20] F is Faraday's constant, ν is the scan rate in V s^{-1}, and A is the geometric area of the electrode (0.785 cm^2).[37] The i_p/v value, obtained from the plot of peak currents versus scan rate (0.1–2.0 V s^{-1}) was used to estimate the surface coverage, leading to $\Gamma = 2.63 \pm 0.19 \times 10^{-10}$ mol cm^{-2}, the number of electrons transferred being 1. The electrochemical surface coverage of the Fe_6W_{18}@UiO-67-modified electrode was also calculated. The cathodic peak currents of wave c (third $Fe^{III/II}$ redox process) were plotted against ν (0.1–1.0 V s^{-1}) and the values of i_p/v were considered; for this composite, $n = 1$ and $\Gamma = 2.58 \pm 0.21 \times 10^{-10}$ mol cm^{-2}. In short, this study establishes that the Fe_6W_{18} units encapsulated inside the cages of the UiO-67 or MIL-101(Cr) retain their electrochemical properties, confirming their integrity.

SMM behavior of the POM@matrix materials

The curves of magnetization (M) vs. the applied magnetic field ($\mu_0 H$) recorded on an array of micro-SQUIDs[38] in the 0.03–1.3 K temperature range and related to Fe_6W_{18}@Gel are depicted in Figure 4. These curves are characterized by stepped hystereses, demonstrating the occurrence of resonant quantum tunneling of magnetization (QTM). The coercive field decreases for increasing temperature with a blocking temperature of about 1.3 K at a sweep rate of 0.14 T s^{-1}. Moreover, the hysteresis loops are strongly field sweep rate dependent (see the Supporting Information, Figure S8) and temperature independent below 0.4 K, confirming the SMM and QTM behavior of Fe_6W_{18}@Gel. For an oriented single crystal, the value of the zero-field splitting parameter D that expresses the axial magnetic anisotropy can be obtained from the field interval between the zero-field step and the first step at non-zero field, which corresponds to resonant tunneling between the spin ground state and the first excited spin state. However, even a randomly oriented powder of crystallites shows steps in the hysteresis loops at the resonance fields H_n (see the details in the experimental section). In such a case, the value of D is given by the field value of the beginning of the first step at non-zero field, at which a rather large fraction of molecules are roughly aligned with the magnetic field. This non-zero field step has a shoulder towards high fields because of the non-aligned molecules. The beginning of this first step is located at around 0.5 T (see the Supporting Information, Figure S8a), leading to $|D| \approx 0.47$ cm^{-1}, in perfect agreement with the value determined for a single crystal of the Fe_6W_{18} complex. A similar set of parameters characteristic of the relaxation process (effective energy barrier $U_{eff}/k_B \approx 10.7$ K and $\tau_0 \approx 2 \times 10^{-6}$ s) is also obtained from the fit of the relaxation time vs. $1/T$ plot (see the Supporting Information, Figure S9b), the value of τ_0

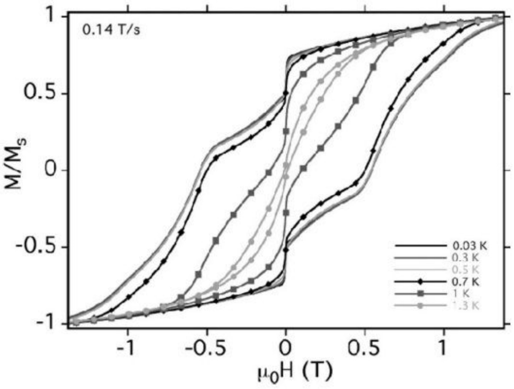

Figure 4. Magnetization vs. magnetic field hysteresis loops at the indicated temperatures and a sweep rate of 0.14 T/s for Fe_6W_{18}@Gel. The hysteresis loops are superimposed below 0.4 K establishing magnetization reversal through temperature-independent QTM. The magnetization is normalized to its saturation value M_s at 1.4 T.

being consistent with those expected for SMMs ($\tau_0 \approx 1\times10^{-5}$–$1\times10^{-11}$ s).[39]

Notably, the hysteresis loops are much smoother for Fe_6W_{18}@Gel than for the oriented crystals of Fe_6W_{18}, showing that as expected Fe_6W_{18} objects are randomly oriented in the gelatin matrix. Very importantly, the zero-field step is very narrow and at exactly $\mu_0H=0$ (see the Supporting Information, Figure S8 b), whereas the oriented crystals of Fe_6W_{18} have a rather broad zero-field step, which is shifted to negative fields by about 35 mT (see the Supporting Information, Figure S10). This establishes that the Fe_6W_{18} molecules are magnetically well isolated in the host material, which can be highlighted by plotting the $dM/dH = f(\mu_0H)$ curves. Indeed, a sharp peak at $\mu_0H=0$ is observed for the Fe_6W_{18} molecules isolated in the gelatin matrix, in strong contrast with the $dM/dH = f(\mu_0H)$ behavior of a single crystal or a powdered sample of F_6W_{18} (Figure 5). It also excludes the possibility of a measurable amount of microcrystals in the sample because randomly oriented microcrystals would have a broad zero-field step (see the Supporting Information, Figure S11 a). Overall, these results indicate that the Fe_6W_{18} molecules retain SMM behavior that is comparable to that of the single crystal when they are well isolated within the diamagnetic gelatin matrix.

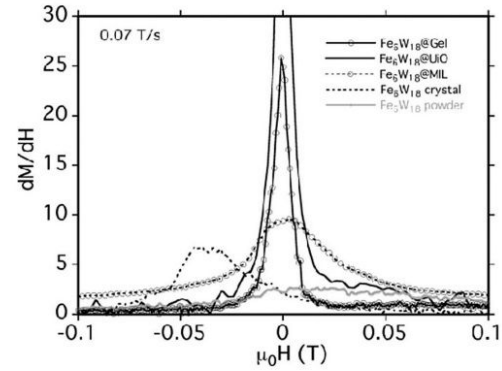

Figure 5. dM/dH vs. magnetic field at 0.03 K and a sweep rate of 0.07 T/s for a crystalline or a powdered sample of Fe_6W_{18} and for the three composites reported herein.

The M vs. μ_0H curves in the 0.03–1.3 K temperature range related to Fe_6W_{18}@UiO-67 are depicted in Figure 6. They are open at zero applied magnetic field below $T=1.3$ K and possess the stepped hysteresis loops expected for QTM, which characterize the SMM behavior. The zero-field step is also very narrow and at $\mu_0H=0$ (see the Supporting Information, Figure S12) showing that the Fe_6W_{18} SMMs are nicely decoupled in the matrix. The magnetization loops have a large step at $\mu_0H=0$ (Figure S12 and Figure 5) indicative of a very fast tunneling rate of magnetization. This observation is actually in agreement with the ac magnetic susceptibility measurements discussed below, where the fast tunneling can be slowed down as soon as a small field of 90 mT is applied. The width of the hysteresis loop has a clear dependence on temperature and field sweep rate (Figure 6 and Figure S12 in the Supporting Information), evidencing that the SMM character of the Fe_6W_{18} units is conserved once introduced in the UiO-67. Furthermore, the beginning of the first step in the hysteresis loop is located at around 0.5 T, leading to a magnitude of $|D|$ similar to that of the parent Fe_6W_{18} POM unit.

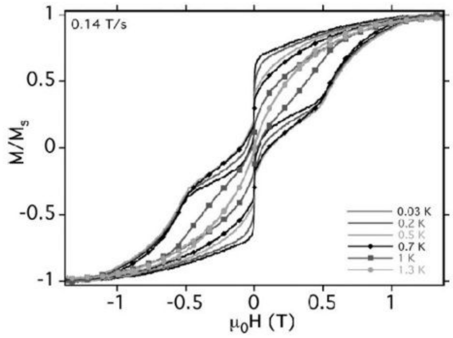

Figure 6. Magnetization vs. magnetic field hysteresis loops at the indicated temperatures and a sweep rate of 0.14 T/s for Fe_6W_{18}@UiO-67. The magnetization is normalized to its saturation value M_s at 1.4 T.

The frequency and temperature dependence of the in-phase χ'_M and out-of-phase χ''_M magnetic susceptibility plots[40] under the zero applied dc field are shown in Figure S13 (see the Supporting Information). Cole–Cole plots of χ'_M vs. χ''_M and the obtained fits using a Debye model[41] ($\alpha = 0.09$–0.25 in the $T=$ 2.0–3.0 K temperature range, α being the parameter determining the width of the distribution of relaxation times; Figure 7,

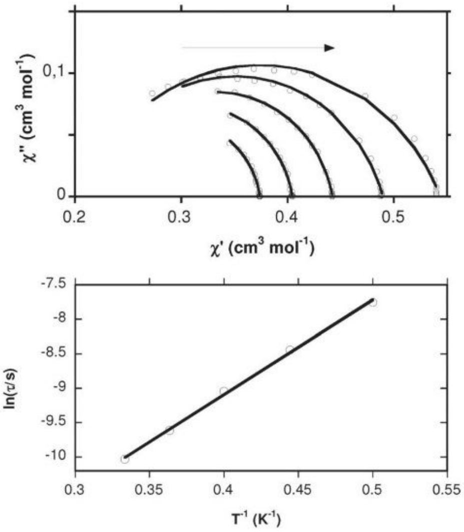

Figure 7. Top: Cole–Cole plots of Fe_6W_{18}@UiO-67 constructed from the measurement of the frequency and temperature dependence of the in-phase χ'_M and out-of-phase χ''_M magnetic susceptibility under the zero applied dc field at (from left to right) 3, 2.75, 2.5, 2.25 and 2 K. The solid lines are fits of the experimental data using a generalized Debye model. Bottom: magnetization relaxation time plotted as $\ln(\tau)$ vs. $1/T$ for Fe_6W_{18}@UiO-67. The solid line represents the fit to the Arrhenius law.

top) reveal flattened semicircular profiles, indicating a weak distribution of relaxation processes. The plot of ln(τ) vs. 1/T is linear in the considered temperature range (Figure 7, bottom). Fitting the data to the Arrhenius law $\tau = \tau_0 \exp(U_{\mathrm{eff}}/k_{\mathrm{B}}T)$ reveals an effective energy barrier of $U_{\mathrm{eff}}/k_{\mathrm{B}} \approx 13.8$ K and $\tau_0 \approx 4.6 \times 10^{-7}$ s.

We further measured the dynamic properties of Fe_6W_{18}@UiO-67 in the presence of a static applied magnetic field of 90 mT. The in-phase χ'_{M} and out-of-phase χ''_{M} magnetic susceptibility plots are shown in Figure S14 and Figure S15, top, respectively (see the Supporting Information). In such measurements, the degeneracy of the $\pm ms$ energy levels can be removed, strongly reducing the contribution of the tunneling process. The Cole–Cole plots can be constructed from these data and fitted (see the Supporting Information, Figure S15, bottom) to a generalized Debye model to determine α values and relaxation time in the temperature range 1.8–4.0 K. The α values, ranging from 0.17 to 0.23, indicate a narrow distribution of relaxation times. The plot of ln(τ) vs. 1/T in the considered temperature range (see the Supporting Information, Figure S16) is linear and fitting the data to the aforementioned Arrhenius law yielded $U_{\mathrm{eff}}/k_{\mathrm{B}} \approx 17.8$ K and $\tau_0 \approx 4.2 \times 10^{-7}$ s. The effective energy barrier was thus increased by 30% (17.8 K in comparison to 13.8 K) as a result of minimizing the QTM process. This barrier value is closer to the theoretical value (25 K), assuming $|D| = 0.5$ cm^{-1} and $S = 6$.

Comparison of these results with those obtained for pure Fe_6W_{18} ($\tau_0 \approx 3.7 \times 10^{-7}$ s^{-1} and $U_{\mathrm{eff}}/k_{\mathrm{B}} \approx 18.0$ K) measured in the presence of a dc field of 90 mT (see the Supporting Information, Figures S17 and S18) shows that the MOF has no obvious influence on the magnetic properties of the POM when a static magnetic field that minimizes the quantum tunneling relaxation process is applied. In short, the isolated Fe_6W_{18} units preserve their SMM behavior once dispersed into the cavities of the UiO-67 MOF. However, the Fe_6W_{18} SMMs tunnel faster in this matrix than in gelatin. This fact suggests that the symmetry of the molecule is reduced and/or there are interactions with the substrate.

Before discussing the magnetic properties of the Fe_6W_{18}@MIL-101(Cr) composite, we must describe the magnetic behavior of MIL-101(Cr), which, to our knowledge, has not previously been quantitatively investigated. The temperature dependence of $\chi_{\mathrm{M}}T$ for this MOF is shown in Figure S19 (see the Supporting Information). $\chi_{\mathrm{M}}T$ continuously decreases from 300 K ($\chi_{\mathrm{M}}T = 4.35$ cm^3 mol^{-1} K) to 2 K ($\chi_{\mathrm{M}}T = 0.370$ cm^3 mol^{-1} K), indicating that in MIL-101(Cr) the Cr$^{\mathrm{III}}$ centres are antiferromagnetically coupled, with a $S_T = {}^1/_2$ ground state. The magnetic data have been fitted considering that this MOF is built of isolated $[Cr^{III}_3(H_2O)_3O(C_8H_4O_4)_3]^+$ units in which the chromium ions form an equilateral triangle. The adapted Hamiltonian can thus be written as Equation (1) in which g is the Lande factor, β the Bohr Magneton, B the applied magnetic field, $\hat{S}$ the local spin operator and J the exchange interaction parameter.

$$\hat{H} = \beta B g\,(\hat{S}_{\mathrm{Cr1}} + \hat{S}_{\mathrm{Cr2}} + \hat{S}_{\mathrm{Cr3}}) - 2J\,(\hat{S}_{\mathrm{Cr1}}\hat{S}_{\mathrm{Cr2}} + \hat{S}_{\mathrm{Cr2}}\hat{S}_{\mathrm{Cr3}} + \hat{S}_{\mathrm{Cr1}}\hat{S}_{\mathrm{Cr3}}) \tag{1}$$

An excellent fit to the experimental $\chi_{\mathrm{M}}T$ data in the 300–2 K temperature range was obtained for $J = -9.4$ cm^{-1} (TIP $= 550 \times 10^{-6}$ cm^3 mol^{-1}, $g = 1.93$ and $R = 4.8 \times 10^{-5}$),[42] leading to a $S_T = {}^1/_2$ ground state with an $S = 3/2$ first excited state at 28.2 cm^{-1}. These results are in good agreement with those reported for the molecular complex $[Cr^{III}_3(H_2O)_3O(C_7H_5O_2)_3]^+$ ($J = -10.1$ cm^{-1}, TIP $= 550 \times 10^{-6}$ cm^3 mol^{-1}, $g = 1.97$), which possesses a highly related trinuclear magnetic core.[43] Magnetization vs. field experiments confirm the $S_T = {}^1/_2$ nature of the ground state, M tending to 1 Bohr Magneton at high field (see the Supporting Information, Figure S19, inset). The low-temperature hysteresis loop measurements show a very small hysteresis that might be due to spin frustration in the antiferromagnetic network (see the Supporting Information, Figure S20).

The $\chi_{\mathrm{M}}T$ vs. T curves for Fe_6W_{18}@MIL-101(Cr), MIL-101(Cr), and Fe_6W_{18} are shown in Figure 8, top. [$\chi_{\mathrm{M}}T$(Fe_6W_{18}@MIL-101(Cr))$-\chi_{\mathrm{M}}T$(MIL-101(Cr))] is close to the temperature dependence of $\chi_{\mathrm{M}}T$(Fe_6W_{18}), but the two curves are not superimposed, suggesting the presence of magnetic interactions between the inserted POM and the matrix. This is confirmed by the broad step around zero-field (Figure 8, bottom) in the M vs. μ_0H curve. The width of hysteresis loops characterizing Fe_6W_{18}@MIL-101(Cr) is drastically reduced (see the Supporting Information, Figure S21) compared to that of a powdered

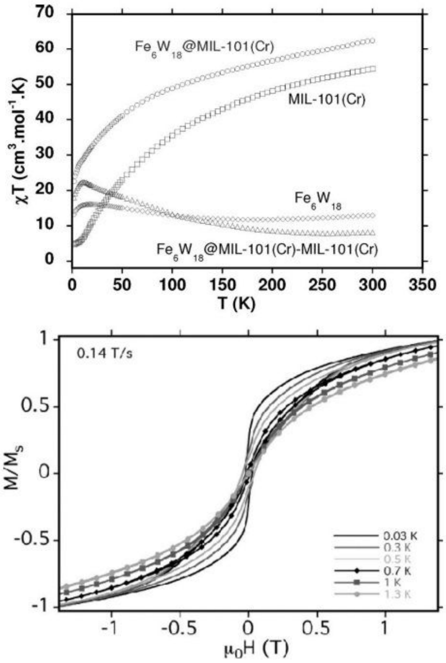

Figure 8. Top: temperature dependence of $\chi_{\mathrm{M}}T$ for MIL-101(Cr) (□), Fe_6W_{18}@MIL-101(Cr) (○), Fe_6W_{18} (◇), and [$\chi_{\mathrm{M}}T$(Fe_6W_{18}@MIL-101(Cr))$-\chi_{\mathrm{M}}T$(MIL-101(Cr))] (Δ). Bottom: magnetization vs. magnetic field hysteresis loops for Fe_6W_{18}@MIL-101(Cr) at the indicated temperatures and a sweep rate of 0.14 T/s. The contribution of the antiferromagnetic matrix was subtracted approximately. The magnetization is normalized to its saturation value M_s at 1.4 T.

sample of Fe_6W_{18} (see the Supporting Information, Figure S11), and the steps observed in the single crystals are smeared out due to the presence of magnetic interactions between the antiferromagnetic matrix and the SMM molecules. Additionally, the width of the hysteresis loop has a dependence on sweep rate and temperature (see the Supporting Information, Figure S20), suggesting that the SMM character of the Fe_6W_{18} units is retained. However, due to the cooperative effect between the inserted POM and the matrix it can be said that the SMM character of the Fe_6W_{18} units is not well conserved once introduced in the MIL-101(Cr) MOF.

Conclusion

The Fe_6W_{18} POM is chemically robust and electronically and structurally stable. The robustness of Fe_6W_{18} is mainly due to the structure of this molecule, in which the tungsten–oxo shell effectively protects the magnetic core from external structural perturbations that can distort the Fe ions coordination sphere and destroy the axial anisotropy of the Fe_6 cluster. It is thus able to retain its integrity when subjected to different environments. In diamagnetic matrices, the SMM behavior is retained mainly because the magnetic anisotropy of the molecules is not altered by their interaction with the host whether it is a soft amorphous one (gelatin) or a more rigid crystalline one (UiO-67). In contrast with pure Fe_6W_{18}, because the molecules are perfectly isolated from each other, the resonant quantum tunneling of magnetization occurs at exactly zero applied magnetic field, leading to a sharp step in the hysteresis loops. When the Fe_6W_{18} POM is encapsulated in an antiferromagnetic network, the zero-field step is strongly broadened because of the magnetic interactions that lead to faster relaxation of its magnetization and the SMM character is clearly reduced. Only very few SMMs retain an opening of the hysteresis loop when the molecules are isolated, which make the Fe_6W_{18} POM among the very few excellent candidates to be used in molecular quantum spintronic devices.[44]

Experimental Section

Materials

Commercial gelatin (Gel) extracted from porcine skin (type A with a bloom of ca. 175 g), corresponding to an average molecular weight of approximately 40 000 g mol^{-1} and an isoelectric point (IEP) of approximately 8 (according to the supplier) was purchased from Sigma–Aldrich. $Na_6(C_4H_{12}N)_4[(FeW_9O_{39})_2Fe_4(H_2O)_2]\cdot 45\,H_2O$[19] [$Na_6(TMA)_4[Fe_6W_{18}]\cdot 45\,H_2O$] and MIL-101(Cr)[26f] were synthesized as previously described. To aid the salt's solubility in DMF, the Na^+ and TMA^+ cations of $Na_6(TMA)_4[Fe_6W_{18}]\cdot 45\,H_2O$ were exchanged with $DODA^+$ according to procedure reported for $[Eu(BW_{11}O_{39})_2]^{15-}$.[45]

Fe_6W_{18}@Gel

This bionanocomposite was prepared according to the complex coacervation-based procedure previously reported for the preparation of POM–gelatin hydrogels.[22–24] First, a solution of gelatin (10 wt %, 2.5 mM in water) was prepared. Then, a 15 mmol L^{-1} solution of $Na_6(TMA)_4[Fe_6W_{18}].45\,H_2O$ (0.451 g, 7.5×10^{-5} mol) in water (5 mL) was also prepared. The pH of both solutions was adjusted to 3 with 1 M HCl solution. The solutions were heated at 40 °C in an oil bath. 2.5 mL of the gelatin solution was then added to the POM solution. An orange gel quickly formed. The gel was removed from the solution, left to dry in air for 2 hours and then plunged into liquid nitrogen to obtain the product as solid (0.220 g, 50 % yield based on gelatin). The chemical composition of Fe_6W_{18}@Gel was determined by a combination of TGA and elemental analysis, taking into account the chemical composition of gelatin $(CH_{1.56}O_{0.42}N_{0.31})_{1625}$ as previously reported.[24] Elemental analysis calcd (%) for $Na_{14}(CH_{1.56}O_{0.42}N_{0.31})_{1625}[(FeW_9O_{39})_2Fe_4(H_2O)_2]_5\cdot 270\,H_2O$ (FW = 69 871.58 g mol^{-1}): C 27.93, H 4.46, N 10.10, W 23.68, Fe 2.40, Na 0.46; found: C 28.33, H 4.51, N 10.41, W 22.48, Fe 2.77, Na 0.62.

Fe_6W_{18}@UiO-67

$ZrCl_4$ (0.116 g, 0.5 mmol), biphenyl-4,4′-dicarboxylic acid (0.121 g, 0.5 mmol), $DODA_{10}[Fe_6W_{18}]$ (0.126 g, 1.25×10^{-5} mol), and benzoic acid (1.83 g, 15 mmol, 30 equiv) were dissolved in DMF (10 mL) in a 23 mL polytetrafluoroethylene-lined stainless steel container. 37 % hydrochloric acid (83 μL) was then added to the solution. All reactants were stirred briefly before heating. The mixture was heated to 120 °C over a period of 1 h, kept at 120 °C for 24 h, and allowed to cool down to room temperature. The solid was removed by filtration and washed on the filter funnel with DMF (3 × 20 mL), chloroform (2 × 20 mL) and dry acetone (2 × 20 mL). The solid product was then dried in an oven at 90 °C overnight (0.112 g, 46 % yield based on Zr). Elemental analysis calcd (%) for $[Zr_6O_4(OH)_4(C_{14}H_8O_4)_{5.5}][(FeW_9O_{39})_2Fe_4(H_2O)_2]_{0.1}(DMF)_{1.8}\cdot 17\,H_2O$ (FW = 2931.18 g mol^{-1}): C 33.76, H 3.27, N 0.86; found: C 33.73, H 2.60, N 0.87. Metal composition was checked by EDX measurements.

Fe_6W_{18}@MIL-101(Cr)

$Na_6(TMA)_4[Fe_6W_{18}].45H_2O$ (0.177 g, 2.94×10^{-5} mol) was dissolved in water (8 mL). MIL-101(Cr) (0.100 g, 1.28×10^{-4} mol) was then added to the solution and the resulting mixture was stirred for 24 h at room temperature. The solid was gathered by centrifugation, washed with water (3 × 15 mL), ethanol (2 × 15 mL) and diethyl ether (15 mL), and then dried in an oven at 120 °C for 24 h (weight of the collected sample = 0.130 g, yield: 85% based on MIL-101(Cr)). Elemental analysis calcd (%) for $[Cr_3(H_2O)_3O(O_2CC_6H_4CO_2)_3][(FeW_9O_{39})_2Fe_4(H_2O)_2]_{0.083}(NO_3)_{0.17}\cdot 30\,H_2O$ (FW = 1192.0 g mol^{-1}): C 24.18, H 2.04, N 0.20, W 23.14, Fe 2.34, Cr 13.09; found: C 24.68, H 2.27, N 0.15, W 22.15, Fe 2.77, Cr 13.70.

Physical measurements

Elemental analyses were performed by the Service Central d'Analyses of CNRS —Institut des Sciences Analytiques (Villeurbanne, France). Infrared spectra were recorded on a Nicolet 30 ATR 6700 FT spectrometer. Powder diffraction data were obtained on a Bruker D5000 diffractometer using $Cu_{K\alpha}$ radiation (1.54059 Å). Thermogravimetric analyses (TGA) were performed on a Mettler Toledo TGA/DSC 1, STAR^e System apparatus under oxygen flow (50 mL min^{-1}) at a heating rate of 5 °C min$^-$1 up to 600 °C. SEM images were recorded on a JEOL Model JSM-7001F microscope equipped with an EDX spectrometer using gold-coated samples and a X-Max silicon drift detector (SDD) by Oxford. The EDX spectra were acquired with a voltage acceleration of 15 kV, an acquisition time of 120 s, and > 1000 counts. Specific surface area experiments were performed at 77 K on a Belsorp Mini apparatus using nitrogen as the probing gas, after a Belsorp pre-treatment overnight at 70 °C under primary vacuum (BEL Japan). Cyclovoltammograms were recorded at room temperature with an Autolab PGSTAT30 potentiostat (Eco Chemie, Holland) driven by a GPSE software running on a personal computer using a conventional three-electrode setup. The working electrode was basal plane pyrolytic graphite disk (PG, Pine, Ø = 5 mm) or a glassy carbon electrode (Ø = 3 mm), the counter electrode was platinum wire and the reference electrode was a saturated calomel electrode (SCE) connected through a salt bridge. The working cell was surrounded by a grounded Faraday cage and all studies were carried out at room temperature and under an argon flow. Ultrapure water (Millipore, 18.2 MΩ cm^{-1}, 25 °C) was used to prepare all electrolyte solutions. For electrochemical measurements, we used a H_2SO_4/Na_2SO_4 buffer solution (pH 2.5), which was prepared by mixing suitable volumes of 0.5 mol L^{-1} Na_2SO_4 and 0.5 mol L^{-1} H_2SO_4 solutions. The solutions were deaerated thoroughly by bubbling argon through the solution and kept under argon atmosphere during the whole experiment. The PG electrode was cleaned before each measurement according to the following procedure: Polishing on a microcloth polishing pad with aluminium oxide (0.3 µm particle size); washing with ethanol and ultrapure water; sonication in an ultrasonic bath for 5 min. Electrode modification consisted of depositing an appropriate amount of powder of each material on the PG surface (Ø = 5 mm). Magnetic susceptibility measurements on powdered samples were carried out with a Quantum Design SQUID Magnetometer. The independence of the susceptibility value with regards to the applied field was checked at room temperature. The susceptibility data were corrected from the diamagnetic contributions as deduced by using Pascal's constant tables. Magnetization measurements were performed with an array of micro-SQUIDs. This magnetometer works in the temperature range of 0.04 to ca. 7 K and in fields up to 1.4 T with sweep rates as high as 0.28 T s^{-1}. The time resolution is approximately 1 ms. The magnetic field can be applied in any direction of the micro-SQUID plane with precision much better than 0.1° by separately driving three orthogonal coils. To ensure good thermalization, each sample was fixed with apiezon grease.[38]

Calculation of the field position of the quantum resonances for a randomly oriented ensemble of SMMs

For a randomly oriented sample of SMMs, initially saturated in a field along the z axis, the initial magnetization at zero field is M_{in}. In this case, the probability dP to find a molecule oriented at an angle of θ degrees to the z axis is given by Equation (2).

$$dP = 2\sin(\theta)\,d\theta \quad \text{for } 0 < \theta < \pi/2 \tag{2}$$

Each molecule projects a cos(θ) magnetization along the z axis. Therefore, the contribution to the magnetization along the z axis is given by Equation (3).

$$dM_z = M_{in}\cos(\theta)\,dP = 2M_{in}\cos(\theta)\sin(\theta)\,d\theta \tag{3}$$

Furthermore, the field of the nth quantum resonance position H_n as a function of the angle θ is given by Equation (4) and the derivative with respect to the angle is given by Equation (5).

$$H = H_n/\cos(\theta) \tag{4}$$

$$dH = [H_n\sin(\theta)/\cos^2(\theta)]\,d\theta \tag{5}$$

Using Equations. (3), (4), and (5), we derive the fraction of magnetization, which is in the nth quantum resonance, in the interval from H to $H + dH$ [Eqs. (6) and ()].

$$dM_z = [2M_{in}H_n^2/H^3]\,dH \quad \text{for } |H| > H_n \tag{6}$$

$$dM_z = 0 \text{ for } |H| < H_n \tag{7}$$

Therefore, during a field sweep from negative fields to positive fields, the first quantum resonance at zero field is sharp, whereas the others resonances start at $H = H_n$ and then decrease rapidly (e.g., $1/H^3$ for $H > H_n$; Figure 9). Because the probability of reversal depends on the tunneling rate, which also depends on the transverse field component, it is more difficult to calculate the hysteresis loops. In addition, the jump-like behavior at H_n can be smeared out by dipolar fields, hyperfine fields, and distributions of anisotropy parameters, but the step-like features should be visible in the hysteresis loop. The field derivative of the magnetization should show maxima at H_n (Figure 9). This means that even a randomly oriented sample of SMMs shows steps in the hysteresis loops at the resonance fields H_n.

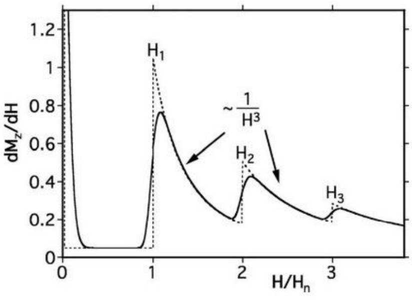

Figure 9. Schematic drawing of the field derivative of the magnetization of a randomly oriented ensemble of SMMs. The dotted line represents the behavior given by Equation (6). The solid line was broadened by dipolar and hyperfine fields.

Acknowledgements

This work was supported by the Ministère de l'Enseignement Supérieur et de la Recherche, the CNRS, the Université de Versailles Saint Quentin en Yvelines and a public grant overseen by the French National Research Agency (ANR) as part of the "Investissements d'Avenir" program nos. ANR-11-IDEX-0003-02 and CHARMMMAT ANR-11-LABX-0039. Y.L. and W.W. acknowledge the European Union for financial support within the FP7 FET-Proactive project MoQuaS no. 610449. Y.L., W.W., E.R., and T.M. thank the ANR for financial support (ANR-13-BS10-0001-03 MolQuSpin). L.R. thanks the Labex CSC of the University of Strasbourg for financial support.

Keywords: biopolymers · magnetic properties · metal–organic frameworks · polyoxometalates

[1] a) H. N. Miras, J. Yan, D.-L. Long, L. Cronin, *Chem. Soc. Rev.* **2012**, *41*, 7403; b) A. Proust, B. Matt, R. Villanneau, G. Guillemot, P. Gouzerh, G. Izzet, *Chem. Soc. Rev.* **2012**, *41*, 7605; c) A. Sartorel, M. Bonchio, S. Campagna, F. Scandola, *Chem. Soc. Rev.* **2013**, *42*, 2262; d) B. S. Bassil, U. Kortz, *Z. Anorg. Allg. Chem.* **2010**, *636*, 2222; e) A. Müller, P. Gouzerh, *Chem. Soc. Rev.* **2012**, *41*, 7431.

[2] a) T. Yamase, *Chem. Rev.* **1998**, *98*, 307; b) T. He, J. Yao, *Prog. Mater. Sci.* **2006**, *51*, 810; c) A. Wutkowski, B. R. Srinivasan, A. R. Naik, C. Schütt, C. Näther, W. Bensch, *Eur. J. Inorg. Chem.* **2011**, 2254; d) A. Saad, O. Oms, A. Dolbecq, C. Menet, R. Dessapt, H. Serier-Brault, E. Allard, K. Baczko, P. Mialane, *Chem. Commun.* **2015**, *51*, 16088.

[3] a) B. Keita, L. Nadjo, *J. Mol. Catal. A* **2007**, *262*, 190; b) R. Liu, S. Li, G. Zhang, A. Dolbecq, P. Mialane, B. Keita, *J. Cluster Sci.* **2014**, *25*, 711; c) J.-F. Lemonnier, S. Duval, S. Floquet, E. Cadot, *Isr. J. Chem.* **2011**, *51*, 290; d) H. Lv, Y. V. Geletii, C. Zhao, J. W. Vickers, G. Zhu, Z. Luo, J. Song, T. Lian, D. G. Musaev, C. L. Hill, *Chem. Soc. Rev.* **2012**, *41*, 7572; e) X.-B. Han, Z.-M. Zhang, T. Zhang, Y.-G. Li, W. Lin, W. You, Z.-M. Su, E.-B. Wang, *J. Am. Chem. Soc.* **2014**, *136*, 5359; f) M. Quintana, A. Montellano-López, S. Rapino, F. M. Toma, M. Iurlo, M. Carraro, A. Sartorel, C. Maccato, X. Ke, C. Bittencourt, T. Da Ros, G. Van Tendeloo, M. Marcaccio, F. Paolucci, M. Prato, M. Bonchio, *ACS Nano* **2013**, *7*, 811; g) G. Marcì, E. I. García-López, L. Palmisano, *Eur. J. Inorg. Chem.* **2014**, 21; h) A. Dolbecq, P. Mialane, B. Keita, L. Nadjo, *J. Mater. Chem.* **2012**, *22*, 24509.

[4] a) J. M. Clemente-Juan, E. Coronado, A. Gaita-Ariño, *Chem. Soc. Rev.* **2012**, *41*, 7464; b) S.-T. Zheng, G.-Y. Yang, *Chem. Soc. Rev.* **2012**, *41*, 7623; c) O. Oms, A. Dolbecq, P. Mialane, *Chem. Soc. Rev.* **2012**, *41*, 7497.

[5] C. Ritchie, A. Ferguson, H. Nojiri, H. N. Miras, Y.-F. Song, D.-L. Long, E. Burkholder, M. Murrie, P. Kögerler, E. K. Brechin, L. Cronin, *Angew. Chem. Int. Ed.* **2008**, *47*, 5609; *Angew. Chem.* **2008**, *120*, 5691.

[6] For a review, see: a) N. V. Izarova, P. Kögerler in *Trends in Polyoxometalates Research* (Eds.: L. Ruhlmann, D. Schaming), Nova Science Publishers, New York, **2015**, pp. 121–147. For some recent examples, see: b) Z.-M. Zhang, S. Yao, Y.-G. Li, H.-H. Wu, Y.-H. Wang, M. Rouzières, R. Clérac, Z.-M. Su, E.-B. Wang, *Chem. Commun.* **2013**, *49*, 2515; c) M. Ibrahim, Y. Lan, B. S. Bassil, Y. Xiang, A. Suchopar, A. K. Powell, U. Kortz, *Angew. Chem. Int. Ed.* **2011**, *50*, 4708; *Angew. Chem.* **2011**, *123*, 4805; d) X. Fang, P. Kögerler, M. Speldrich, H. Schilderb, M. Lubana, *Chem. Commun.* **2012**, *48*, 1218; e) H. El Moll, A. Dolbecq, J. Marrot, G. Rousseau, M. Haouas, F. Taulelle, G. Rogez, W. Wernsdorfer, B. Keita, P. Mialane, *Chem. Eur. J.* **2012**, *18*, 3845; f) M. Vonci, C. Boskovic, *Austr. J. Chem.* **2014**, *67*, 1542.

[7] a) G. A. Craig, M. Murrie, *Chem. Soc. Rev.* **2015**, *44*, 2135; b) M. A. AlDamen, J. M. Clemente-Juan, E. Coronado, C. Martí-Gastaldo, A. Gaita-Ariño, *J. Am. Chem. Soc.* **2008**, *130*, 8874; c) S. Cardona-Serra, J. M. Clemente-Juan, E. Coronado, A. Gaita-Ariño, A. Camón, M. Evangelisti, F. Luis, J. M. Martínez-Pérez, J. Sesé, *J. Am. Chem. Soc.* **2012**, *134*, 14982.

[8] a) F. Troiani, M. Affronte, *Chem. Soc. Rev.* **2011**, *40*, 3119; b) S. Sanvito, *Chem. Soc. Rev.* **2011**, *40*, 3336; c) L. Bogani, W. Wernsdorfer, *Nat. Mater.* **2008**, *7*, 179.

[9] A. Cornia, M. Mannini, P. Sainctavit, R. Sessoli, *Chem. Soc. Rev.* **2011**, *40*, 3076.

[10] C. Bosch-Navarro, E. Coronado, C. Martí-Gastaldo, B. Rodríguez-González, L. M. Liz-Marzán, *Adv. Funct. Mater.* **2012**, *22*, 979.

[11] L. Bogani, L. Cavigli, M. Gurioli, R. L. Novak, M. Mannini, A. Caneshi, F. Pineider, R. Sessoli, M. Clemente-León, E. Coronado, A. Cornia, D. Gatteschi, *Adv. Mater.* **2007**, *19*, 3906.

[12] D. Ruiz-Molina, M. Mas-Torrent, J. Gómez, A. I. Balana, N. Domingo, J. Tejada, M. T. Martínez, C. Rovira, J. Veciana, *Adv. Mater.* **2003**, *15*, 42.

[13] S. Willemin, B. Donnadieu, L. Lecren, B. Henner, R. Clérac, C. Guérin, A. Meyer, A. V. Pokrovskii, J. Larionova, *New. J. Chem.* **2004**, *28*, 919.

[14] F. Palacio, P. Oliete, U. Schubert, I. Mijatovic, N. Hüsing, H. Peterlik, *J. Mater. Chem.* **2004**, *14*, 1873.

[15] a) T. Coradin, J. Larionova, A. A. Smith, G. Togez, R. Clérac, C. Guérin, G. Blondin, R. Winpenny, C. Sanchez, T. Mallah, *Adv. Mater.* **2002**, *14*, 896; b) S. Willemin, G. Arrachart, L. Lecren, J. Larionova, T. Coradin, R. Clérac, T. Mallah, C. Guérin, C. Sanchez, *New J. Chem.* **2003**, *27*, 1533; c) M. Clemente-León, E. Coronado, A. Forment-Aliaga, P. Amorós, J. Ramírez-Castellanos, J. M. González-Calbet, *J. Mater. Chem.* **2003**, *13*, 3089; d) I. Kornarakis, G. Sopasis, C. J. Milios, G. S. Armatas, *RSC Adv.* **2012**, *2*, 9809.

[16] M. Clemente-León, E. Coronado, C. J. Gómez-García, M. López-Jordà, A. Camón, A. Repollés, F. Luis, *Chem. Eur. J.* **2014**, *20*, 1669.

[17] E. Coronado, C. Martí-Gastaldo, E. Navarro-Moratalla, E. Burzurí, A. Camón, F. Luis, *Adv. Mater.* **2011**, *23*, 5021.

[18] D. Aulakh, J. B. Pyser, X. Zhang, A. A. Yakovenko, K. R. Dunbar, M. Wriedt, *J. Am. Chem. Soc.* **2015**, *137*, 9254.

[19] J.-D. Compain, P. Mialane, A. Dolbecq, I.-M. Mbomekallé, J. Marrot, F. Sécheresse, E. Rivière, G. Rogez, W. Wernsdorfer, *Angew. Chem. Int. Ed.* **2009**, *48*, 3077; *Angew. Chem.* **2009**, *121*, 3123.

[20] A. Giusti, G. Charron, S. Mazerat, J.-D. Compain, P. Mialane, A. Dolbecq, E. Rivière, W. Wernsdorfer, R. Ngo Biboum, B. Keita, L. Nadjo, A. Filoramo, J.-P. Bourgoin, T. Mallah, *Angew. Chem. Int. Ed.* **2009**, *48*, 4949; *Angew. Chem.* **2009**, *121*, 5049.

[21] R. Guo, Y. Cheng, D. D. Ding, X. Li, L. Zhang, X. Jiang, B. Liu, *Macromol. Biosci.* **2011**, *11*, 839.

[22] F. Carn, O. Durupthy, B. Fayolle, T. Coradin, G. Mosser, M. Schmutz, J. Maquet, J. Livage, N. Steunou, *Chem. Mater.* **2010**, *22*, 398.

[23] B. Khadro, I. Baroudi, A.-M. Goncalves, B. Berini, B. Pegot, F. Nouar, T. N. H. Le, F. Ribot, C. Gervais, F. Carn, E. Cadot, C. Mousty, C. Simonnet-Jégat, N. Steunou, *J. Mater. Chem. A* **2014**, *2*, 9208.

[24] I. Baroudi, C. Simonnet-Jégat, C. Roch-Marchal, N. Leclerc-Laronze, C. Livage, C. Martineau, C. Gervais, E. Cadot, F. Carn, B. Fayolle, N. Steunou, *Chem. Mater.* **2015**, *27*, 1452.

[25] a) N. Stock, S. Biswas, *Chem. Rev.* **2012**, *112*, 933; b) M. Eddaoudi, D. F. Sava, J. F. Eubank, K. Adil, V. Guillerm, *Chem. Soc. Rev.* **2015**, *44*, 228; c) T. Devic, C. Serre, *Chem. Soc. Rev.* **2014**, *43*, 6097; d) J. Gascon, A. Corma, F. Kapteijn, F. X. Llabrés i Xamena, *ACS Catal.* **2014**, *4*, 361; e) *Metal–Organic Frameworks: Application from Catalysis to Gas Storage* (Ed.: D. Farrusseng), Wiley-VCH, Weinheim, **2010**.

[26] a) A.-X. Yan, S. Yao, Y.-G. Li, Z.-M. Zhang, Y. Lu, W.-L. Chen, E.-B. Wang, *Chem. Eur. J.* **2014**, *20*, 6927; b) J. Juan-Alcañiz, J. Gascon, F. Kapteijn, *J. Mater. Chem.* **2012**, *22*, 10102; c) D.-Y. Du, J.-S. Qin, S.-L. Li, Z.-M. Su, Y.-Q. Lan, *Chem. Soc. Rev.* **2014**, *43*, 4615; d) C. M. Granadeiro, P. Silva, V. K. Saini, F. A. Almeida Paz, J. Pires, L. Cunha-Silva, *Catal. Today* **2013**, *218*, 35; e) S. S. Balula, C. M. A. D. S. Granadeiro, I. C. Barbosa, M. S. Santos, L. Cunha-Silva, *Catal. Today* **2013**, *210*, 142; f) W. Salomon, F.-J. Yazigi, C. Roch-Marchal, P. Mialane, P. Horcajada, C. Serre, M. Haouas, F. Taulelle, A. Dolbecq, *Dalton Trans.* **2014**, *43*, 12698.

[27] J. H. Cavka, S. Jakobsen, U. Olsbye, N. Guillou, C. Lamberti, S. Bordiga, K. P. Lillerud, *J. Am. Chem. Soc.* **2008**, *130*, 13850.

[28] G. Ferey, C. Mellot-Draznieks, C. Serre, F. Millange, J. Dutour, S. Surblé, I. Margiolaki, *Science* **2005**, *309*, 2040.

[29] W. Salomon, C. Roch-Marchal, P. Mialane, P. Rouschmeyer, C. Serre, M. Haouas, F. Taulelle, S. Yang, L. Ruhlmann, A. Dolbecq, *Chem. Commun.* **2015**, *51*, 2972.

[30] F. Carn, N. Steunou, M. Djabourov, T. Coradin, F. Ribot, J. Livage, *Soft Matter* **2008**, *4*, 735.

[31] a) L. Bromberg, Y. Diao, H. Wu, S. A. Speakman, T. A. Hatton, *Chem. Mater.* **2012**, *24*, 1664; b) N. V. Maksimchuk, O. A. Kholdeeva, K. A. Kovalenko, V. P. Fedin, *Isr. J. Chem.* **2011**, *51*, 281.

[32] a) J. Juan-Alcañiz, M. Goesten, A. Martinez-Joaristi, E. Stavitski, A. V. Petukhov, J. Gascon, F. Kapteijn, *Chem. Commun.* **2011**, *47*, 8578; b) J. Juan-Alcañiz, E. V. Ramos-Fernandez, U. Lafont, J. Gascon, F. Kapteijn, *J. Catal.* **2010**, *269*, 229.

[33] R. Canioni, C. Roch-Marchal, F. Sécheresse, P. Horcajada, C. Serre, M. Hardi-Dan, G. Férey, J.-M. Grenèche, F. Lefebvre, J.-S. Chang, Y.-K. Hwang, O. Lebedev, S. Turner, G. Van Tendeloo, *J. Mater. Chem.* **2011**, *21*, 1226.

[34] Fe_6W_{18}@MIL-101(Cr) contains 62 wt% of MIL-101(Cr), S_{BET} (MIL-101(Cr)) = 3007 $m^2 g^{-1}$; calculated S_{BET} (POM + MIL-101(Cr)) = 0.62 × 3007 = 1864 $m^2 g^{-1}$ compared to the experimental S_{BET} (Fe_6W_{18}@MIL-101(Cr)) = 1750 $m^2 g^{-1}$. Fe_6W_{18}@UiO-67 contains 83 wt% of UiO-67, S_{BET} (UiO-67) = 2400 $m^2 g^{-1}$; calculated S_{BET} (POM + UiO-67) = 0.83 × 2400 = 1992 $m^2 g^{-1}$ compared to the experimental S_{BET} (Fe_6W_{18}@UiO-67) = 1480 $m^2 g^{-1}$.

[35] D. M. Fernandes, A. D. S. Barbosa, J. Pires, S. S. Balula, L. Cunha-Silva, C. Freire, *ACS Appl. Mater. Interfaces* **2013**, *5*, 13382.

[36] B. P. M. Paes de Sousa, R. Grazina, A. D. S. Barbosa, B. de Castro, J. J. G. Moura, L. Cunha-Silva, S. S. Balula, *Electrochim. Acta* **2013**, *87*, 853.

[37] D. M. Fernandes, C. M. A. Brett, A. M. V. Cavaleiro, *J. Solid State Electrochem.* **2011**, *15*, 811.

[38] a) W. Wernsdorfer in *Advances in Chemical Physics, Vol. 118* (Eds.: I. Prigogine, S. A. Rice), John Wiley & Sons, Hoboken, NJ, **2001**, pp. 99–190; b) W. Wernsdorfer, *Supercond. Sci. Technol.* **2009**, *22*, 064013.

[39] See for example E. Colacio, J. Ruiz-Sánchez, F. J. White, E. K. Brechin, *Inorg. Chem.* **2011**, *50*, 7268.

[40] D. Gatteschi, R. Sessoli, *Angew. Chem. Int. Ed.* **2003**, *42*, 268; *Angew. Chem.* **2003**, *115*, 278.

[41] D. Gatteschi, R. Sessoli, J. Villain, *Molecular Nanomagnets*, Oxford University Press, New York, **2006**.

[42] $R=[\Sigma(\chi_M T_{calc}-\chi_M T_{obs})^2/\Sigma(\chi_M T_{obs})^2]$.

[43] A. Figuerola, V. Tangoulis, S. Ribas, H. Hartl, I. Brüdgam, M. Maestro, C. Diaz, *Inorg. Chem.* **2007**, *46*, 11017.

[44] a) M. Urdampilleta, S. Klyatskaya, J.-P. Cleuziou, M. Ruben, W. Wernsdorfer, *Nat. Mater.* **2011**, *10*, 502; b) M. Ganzhorn, S. Klyatskaya, M. Ruben, W. Wernsdorfer, *Nat. Nanotechnol.* **2013**, *8*, 165; c) S. Thiele, F. Balestro, R. Ballou, S. Klyatskaya, M. Ruben, W. Wernsdorfer, *Science* **2014**, *344*, 1135.

[45] W. Li, S. Yin, J. Wang, L. Wu, *Chem. Mater.* **2008**, *20*, 514.

Received: January 15, 2016

Supporting Infomation at **DOI:** 10.1002/chem.2016002

UNIVERSITÉ DE STRASBOURG

YANG Shu

EDSC
Ecole Doctorale des
Sciences Chimiques

Réduction électrocatalytique des NO_x sur des nanoparticules métalliques stabilisées par des polyoxométallates

Résumé :

L'objet de ce travail est de développer des nouveaux catalyseurs pour réduire les ions nitrites (NO_2^- / HNO_2) et nitrates (NO_3^-) dans l'eau en étudiant les facteurs qui vont influencer leurs réductions catalytiques. On a montré que la présence de polyoxométallates (POMs) permet d'améliorer les propriétés catalytiques de l'électrode de Cu et d'Ag pour la réduction de ions nitrate et nitrite avec des conditions adaptées. Par la suite, des nanoparticules du cuivre (Cu@POM) ou d'argent (Ag@POM) ont été préparées par électroréduction of CuPOM *in situ* ou photocatalyse en présence d'ions POMs et Ag(I) respectivement. Leurs propriétés électrocatalytiques ont été étudiées. Six différents polyoxométallates substitués par des atomes de Cu^{II} (CuPOMs) ont montré de bonnes activités pour la réduction de nitrite à pH 1 et à pH 5. Deux activités sont observées : au potentiel de la réduction de Cu^{II} et au potentiel de réduction des W^{VI} du POM. Quant à la réduction du nitrate, $[Cu_4(H_2O)_2(P_2W_{15}O_{56})_2]^{16-}$ et $[(A\text{-}\beta\text{-}SiW_9O_{34})Cu_4(OH)_3(H_2O)(H_3N(CH_2)_3COO)_2]_3^{5-}$ peuvent catalyser la réduction du nitrate à un potentiel au-delà de la réduction du Cu^{II} à la réduction des W^{VI}. Par contre, dans le cas de $[(SbW_9O_{33})_2\{Cu(H_2O)\}_3]^{12-}$ aucune électrocatalyse n'est observée. Cela indique que le type de POM influence les propriétés catalytiques des nanoparticules. Pour le système Ag@POM photoréduit, un catalyseur hétérogène est préparé et stabilisé par une couche de Nafion. Les nanoparticules Ag@POM sont actives pour la réduction du nitrite et du nitrate et possèdent une activité meilleure que celle mesurée pour l'électrode d'Ag seule. Dans la dernière partie, une étude préliminaire de polyoxométallates encapsulés dans les 'Metal-Organic Framworks' (MOFs) est présentée. L'entité POM conserve ses propriétés électrochimiques et électrocatalytiques pour la réduction de nitrite après immobilisation dans la cage MOF.

Mots clés : polyoxométallates, nanoparticules, cuivre, argent, électrocatalyse, nitrate, nitrite

Summary:

The object of this work is to develop new catalysts to reduce nitrite ions (NO_2^- / HNO_2) and nitrate ions (NO_3^-) in water and also tried to understand the factors that will influence catalytic reductions. It has been shown that the presence of polyoxometalates makes it possible to improve the catalytic properties of the Cu and Ag bulk electrodes for the reduction of nitrate and nitrite ions under suitable conditions. Then, the copper or silver nanoparticles decorated with POMs, Cu@POM or Ag@POM), are formed with two different methods: electroreduction *in situ* of CuPOM or photocatalysis in the presence of POM and Ag(I) ions respectively). Their electrocatalytic properties are presented. Six different Cu-substituted polyoxometalates (CuPOMs) are active for nitrite reduction at pH 1 and pH 5. Two activities are observed at the potential of Cu^{II} reduction and at the potential of W^{VI} reduction in POM. $[Cu_4(H_2O)_2(P_2W_{15}O_{56})_2]^{16-}$ and $[(A\text{-}\beta\text{-}SiW_9O_{34})Cu_4(OH)_3(H_2O)(H_3N(CH_2)_3COO)_2]_3^{5-}$ catalyse the nitrate reduction at the potential beyond the reduction of Cu^{II} and at the reduction of W^{VI}. On the other hand, no catalysis efficiency was observed with $[(SbW_9O_{33})_2\{Cu(H_2O)\}_3]^{12-}$. This indicates the type of POM will influence the catalytic properties of nanoparticles. With the photoreduced Ag@POM nanoparticles, a heterogeneous catalyst is prepared and stabilized by a Nafion layer. Ag@POM nanoparticles are active for the reduction of nitrite and nitrate and have an activity better than the Ag electrode alone. In the last part, a preliminary study of polyoxometalates encapsulated in Metal-Organic Framworks (MOFs) is presented. POM retains its electrochemical and electrocatalytic properties toward the reduction of nitrite after immobilized in the cage of MOF.

Keywords: polyoxometalate, nanoparticles, copper, silver, electrocatalysis, nitrate, nitrite